Title

Surface Functionalization at the Nanoscale for Interfacing with Biological Systems

Author

Heidenreich, Liv Katherine

Publication Date

2024

Peer reviewed|Thesis/dissertation

UNIVERSITY OF CALIFORNIA

Los Angeles

Surface Functionalization at the Nanoscale for Interfacing with Biological Systems

A dissertation submitted in partial satisfaction of the requirements for the degree Doctor of Philosophy in Chemistry

by

Liv Katherine Heidenreich

2024

ABSTRACT OF THE DISSERTATION

Surface Functionalization at the Nanoscale for Interfacing

with Biological Systems

by

Liv Katherine Heidenreich

Doctor of Philosophy in Chemistry

University of California, Los Angeles, 2024

Professor Paul S. Weiss, Chair

With the development of technology to characterize and to manipulate objects at the nanoscale, our understanding of the world at the molecular level has opened the way for techniques to create functional surfaces that can interact with other small objects such as cells and biological molecules. The focus of the work embodied in this thesis is twofold: firstly, several devices with the intention of introducing genetic cargo into cells and secondly, aptamer field-effect biosensors to detect small molecules such as neurotransmitters. Both applications utilize aspects of chemical functionalization of surfaces at the nanoscale to imbue the desired properties of the devices.

Towards the goal of enhancing the throughput of gene therapies for genetic disorders, microfluidic devices assembled on piezoelectric substrates were created. We achieved cellular transfection on a model cell line through optimizing the acoustofluidic manipulation

of cells. A parallel approach with the same goal was to functionalize lipid bilayers to the walls of microfluidic cell-squeezing devices, another method of transfection. We demonstrated that lipid bilayers reduced the fouling of proteins and cellular debris in the flow channel which impacts device lifetime.

For small-molecule detection, an area of great interest is the study of neurotransmitters *in vivo*. In the developments of our biosensors, aptamers, or single stranded sequences of DNA, are functionalized to the surface of a semiconductor transistor using a series of organic chemical linkers. These sequences are designed to selectively bind to a target molecule of interest such as serotonin. The sensors monitor the electrical current between electrodes across the semiconductor, which is altered by the chemical binding. In my work, I aimed to enhance the time response for real-time monitoring by incorporating the sensors in a fluidic system to investigate aptamer binding kinetics. Custom electronics to measure the transistors were also built, with an emphasis on multiplexing and portability.

The dissertation of Liv Katherine Heidenreich is approved.

Steven J. Jonas

Harold G. Monbouquette

Justin R. Caram

Paul S. Weiss, Committee Chair

University of California, Los Angeles

2024

Table of Contents

CHAPTER 4: Acoustofluidic Sonoporation for Gene Delivery to Human Hematopoietic Stem and Progenitor Cells

CHAPTER 5: *In Situ* Shape Control of Thermoplasmonic Gold Nanostars on Oxide Substrates for Hyperthermia-Mediated Cell Detachment

CHAPTER 6: Microfluidic Platform for Studying the Reversibility and Kinetics of Aptamer-Target Binding

CHAPTER 7: Conclusions and Prospects

List of Figures and Tables

CHAPTER 2: Work Function Control of Germanium through Carborane-Carboxylic Acid Surface Passivation

CHAPTER 3: Lipid-Bicelle-Coated Microfluidics for Intracellular Delivery with Reduced Fouling

CHAPTER 4: Acoustofluidic Sonoporation for Gene Delivery to Human Hematopoietic Stem and Progenitor Cells

CHAPTER 5: *In Situ* Shape Control of Thermoplasmonic Gold Nanostars on Oxide Substrates for Hyperthermia-Mediated Cell Detachment

CHAPTER 6: Microfluidic Platform for Studying the Reversibility and Kinetics of Aptamer-Target Binding

Funding Sources

I acknowledge the funding sources for each of the projects discussed within this thesis.

Work Function Control of Germanium through Carborane-Carboxylic Acid Surface Passivation: U.S. Department of Energy Grant DE-SC-1037004.

Lipid-Bicelle-Coated Microfluidics for Intracellular Delivery with Reduced Fouling: National Institutes of Health: DP5 OD028181, National Institutes of Health: F31 HL149356, National Institutes of Health: R01 DA045550. Young Investigator funds awarded to S. J. Jonas from the Alex's Lemonade Stand Foundation for Childhood Cancer Research, the Hyundai Hope on Wheels Foundation for Pediatric Cancer Research, and the Tower Cancer Research Foundation.

Acoustofluidic Sonoporation for Gene Delivery to Human Hematopoietic Stem and Progenitor Cells: National Institutes of Health: K23 CA222659, National Institutes of Health: U54 HL119893, National Institutes of Health: R33 CA223908, National Institutes of Health: R01 GM127714, National Institutes of Health: F31 HL149356, National Institutes of Health: DP5 OD028181, National Institutes of Health: P30 CA016042, National Institutes of Health: P30 AI028697, National Institutes of Health: KL2 TR001882, National Institutes of Health: R01 GM132603, National Institutes of Health: UL1 TR001881, National Institutes of Health: T32 HL069766. Young Investigator funds awarded to S. J. Jonas from the Alex's

Lemonade Stand Foundation for Childhood Cancer Research, the Hyundai Hope on Wheels Foundation for Pediatric Cancer Research, and the Tower Cancer Research Foundation.

***In Situ* Shape Control of Thermoplasmonic Gold Nanostars on Oxide Substrates for Hyperthermia-Mediated Cell Detachment:** Young Investigator funds awarded to S. J. Jonas from the Alex's Lemonade Stand Foundation for Childhood Cancer Research, the Hyundai Hope on Wheels Foundation for Pediatric Cancer Research, and the Tower Cancer Research Foundation.

Microfluidic Platform for Studying the Reversibility and Kinetics of Aptamer-Target Binding: National Science Foundation: 1509794, National Science Foundation: CMMI-1636136, National Science Foundation: CBET1026592, National Science Foundation: CCF1518715, National Institutes of Health: GM104960, National Institutes of Health: DA045550.

Acknowledgments

I write this section with great difficulty- not in the sense of looking for inspiration but in terms of maintaining brevity. I am extremely lucky to have been encouraged throughout the past years by some amazing individuals. The list of people who have had an impact on my experiences is extensive, but I want to express a fraction of my gratitude here.

To my undergraduate advisors at the University of Wisconsin, Milwaukee who opened my eyes to the possibility of graduate studies- It's hard to believe, but I was already in my junior year of college before I was aware of grad school as a path forward. Prof. Joseph Aldstadt- an amazing mentor who taught me both the core principles of being a good scientist and of being a good lab mate. I'll never forget our first meeting in his office when he asked me, "Do you know how to juggle?"

Other mentors who broadened my view on the scientific approach to a holistic, interdisciplinary world were Prof. Gabriella Pinter and Prof. Istvan Lauko. I thank them for their passion and genuinely answering my questions of "why does this matter?"

I thank my graduate advisor Prof. Paul S. Weiss- it's been a journey, but having a mentor who was patient and believed that things would come together was integral to my success. Dr. Steven Jonas- truly a kind individual who exemplifies a tireless work ethic. I'm grateful to have worked with him. My committee members Prof. Justin Caram and Prof. Harold Monbouquette- both inspiring scientists willing to ask important, challenging questions. I would advise any future graduate students to seek out people like them and take the opportunity to learn from those involved with your graduate career.

I thank Dr. Leonardo Scarabelli and Dr. Naihao Chiang- some of the most brilliant people I've ever had the pleasure of meeting. Also, some of the funniest. Fellow group members Gail and Erin- it wouldn't be the same without them in our incoming class. Erin was an amazing roommate during the majority of grad school. I hope we can all get together again someday, whether that means having a bonfire at the beach, analyzing spectra, or making Leo watch a terrible movie. Other friends from grad school- Andrew, Andy, and Sophia made me glad to be a part of the chemistry department.

In my time tackling many electrical engineering problems, I was far from alone. I would like to thank Rahul Iyer for working many late nights despite having his own coursework, and Prof. Miguel Alcañiz Fillol, whom I met with countless times, often at an inconvenience to him due to the time difference between LA and Spain. He is a brilliant engineer and educator and was committed to helping me, even guiding my oscilloscope measurements over Skype calls. His students that I collaborated with were similarly wonderful. Specifically, Dr. Javier Monreal Trigo. I'm very proud to have been a part of his work and thankful for everything he taught me. Along with Dr. Martin Hartel, we worked tirelessly on the multi-FET hardware. Against all odds, we did some great experiments.

I would like to thank Dr. Olena Lukoyanova, a truly special woman. From the first time I met her, I knew she would be a great source of scientific insight as well as life advice. Sammy Mensah- you are missed. My memories of you are a bright spot in my time at UCLA.

Thank you to the CnSI Nanoscience outreach program- Prof. Sarah Tolbert, Dr. Rita Blaik, Dr. Cheylene Tanimoto, and Dr. Elaine Morita. Working with them instilled in me a deeper reverence for science education. I found a passion for teaching and it was fun, too.

I thank Dr. Jason Belling for everything- we quite literally stayed up all night, to the detriment of our health, whether working on stat. mech problem sets, running experiments, stressing over oral exams, or playing Slay the Spire. He and Dr. Geoffrey Pronovost became my family over the years and I will always laugh thinking of these memories.

My decision to attend UCLA for graduate studies was based on additional factors outside of academic interests. In particular, an amazing gaming community. When I first came to LA and didn't know anyone, it was the Super Smash Bros. Club where I first found a group of real, lasting friends. I'd like to thank Daniel, Sammy, Mustafa, Willa, Sunny, Olivia, George, Josh, Anthony, Preston, and the friends we made along the way. The list of people who made my time special could certainly go on. An additional thank you to Jed and Erin- I hope I can continue to be a part of their growing family.

Any time I felt discouraged, I thought of my friends and family back home who always believed in and supported me. Madeline, Jenny, Iris and Adam- I knew I couldn't let them down. I am also thankful to my cat James, the sweetest baby there ever was, who has kept me company throughout all of my education.

Ultimately, I would like to thank my family. My parents Wayne and Charlotte have always been there for me, free of judgment, happy for my successes, sympathetic in my struggles. My mom has been my number one, a phone call away when I didn't know what to do. My dad helped me find focus in tumultuous times and I can't thank him enough for

being there. I don't want to stop our writing sessions just because I'm finished with this project! My brother Daniel- I think of him all the time and hope that I will make him proud.

Liv Katherine Heidenreich

Education

BS Chemistry and BS Mathematics *December 2015*
University of Wisconsin - Milwaukee

MS Chemistry, Materials *March 2018*
University of California, Los Angeles

Publications

L. K. Heidenreich, J. Monreal-Trigo, M. C. Hartel, M. Alcañiz-Fillol and A. M. Andrews, Fully Integrated Measurement Platform for Real-Time Multiplexed Field-Effect Transistor Biosensors, *in press.*

J. N. Belling, L. K. Heidenreich, Z. Tian, A. M. Mendoza, T. Chiou, Y, Gong, N. Y. Chen T. D. Young, N. Wattanatorn, J. H. Park, L. Scarabelli, N. Chiang, J. Takahashi, S. G. Young, A. Z. Stieg, S. De Oliveira, T. J. Huang, P. S. Weiss and S. J. Jonas, Acoustofluidic Sonoporation for Gene Delivery to Human Hematopoietic Stem and Progenitor Cells, *PNAS* (2020*) 117* (20), 10976-10982.

J. N. Belling, L. K. Heidenreich, J. H. Park, L. M. Kawakami, J. Takahashi, I. M. Frost, Y. Gong, T. D. Young, J. A. Jackman, S. J. Jonas, N. Cho and P. S. Weiss, Lipid-Bicelle-Coated Microfluidics for Intracellular Delivery with Reduced Fouling, *ACS Applied Materials & Interfaces* (2020) *12* (41), 45744-45752.

G. A. Vinnacombe-Willson, N. Chiang, L. Scarabelli, Y. Hu, L. K. Heidenreich, X. Li, Y. Gong, D. T. Inouye, T. S. Fisher, P. S. Weiss and S. J. Jonas, *In Situ* Shape Control of Thermoplasmonic Gold Nanostars on Oxide Substrates for Hyperthermia-Mediated Cell Detachment, *ACS Central Science* (2020) *6* (11), 2105-2116.

A. C. Serino, M. E. Anderson, L. M. A. Saleh, R. M. Dziedzic, H. Mills, L. K. Heidenreich, A. M. Spokoyny and P. S. Weiss. Work Function Control of Germanium through Carborane-Carboxylic Acid Surface Passivation. *ACS Applied Materials & Interfaces* (2017) *9* (40), 34592-34596.

Awards

UCLA Chemistry and Biochemistry Excellence in Research Fellowship, Spring 2020

Recipient of the Hanson-Dow Excellence in Teaching Award in the UCLA Department of Chemistry and Biochemistry, April 22, 2019

Outstanding Performance in Inorganic Chemistry award from the UWM Department of Chemistry and Biochemistry, Spring 2015

Teaching Experience

University of California, Los Angeles
Teaching Assistant, General Chemistry I for Life Science Majors
General Chemistry I for Physical Science Majors
General Chemistry II for Physical Science Majors
Biochemistry I
General Chemistry Lab I for Physical Science Majors
Materials Characterization Training Program, Lab
Curricular Review, General and Organic Chemistry Lab II

California NanoSystems Institute
Applications of Nanoscience Summer Program Instructor

- 2-week program for high school students to learn nanoscience with hands-on experiments exploration of techniques
- Creation of class curriculum
- Mentoring for students

University of Wisconsin – Milwaukee
Tutor, Department of Mathematics
Teaching Assistant, General Chemistry I and Lab for Physical Science Majors
General Chemistry I for Life Science Majors

CHAPTER 1

Introduction

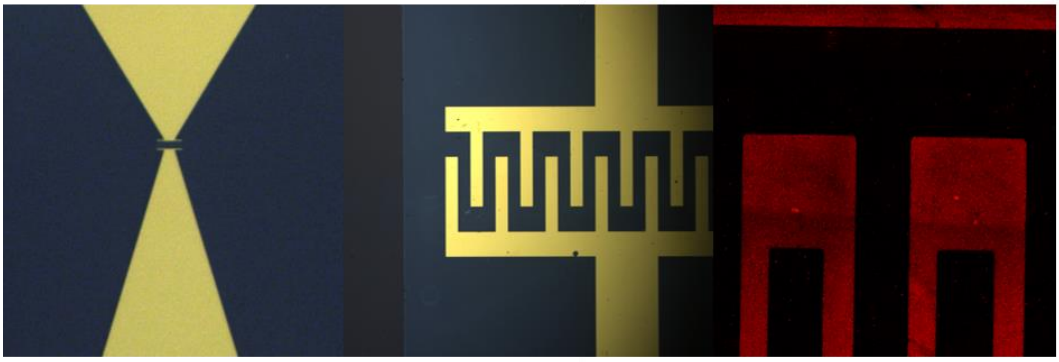

1.A An Introduction to Nanoscience

The world at the nanoscale, although unseen by our bare eyes, is ever-present and integral to life as we know it. The nanoscale refers to the size of 10^{-9} to 10^{-7} meters, and nanoscience is the field of research focusing on materials that possess these dimensions. Prior to what we practice as modern nanoscience, however, the nanoscale has long been a part of human art, medicine, and the very molecules that enable life.[1]

As far back as the 4th century, nanoparticles were a feature of artworks. The Roman artifact known as the Lycurgus Cup is a glass that contains silver and gold nanoparticles and

displays a bright red color when viewed with light passing through its center, but appears green when the light source is placed on the exterior.[2] The green color is due to light scattering from the nanoparticles and the phenomenon known as plasmon resonance, which occurs when a metal particle is small enough for incoming light waves to excite the electrons in the particle collectively. Hence, a specific wavelength is absorbed, responsible for the red color.[3] This observation is different from what one would expect to encounter when looking at bulk gold. This phenomenon is also seen in stained glass, where metal nanoparticles suspended within the glass do not lose their color over time despite being in direct sunlight for hundreds of years.[3] The unique properties of nanoscale metals were wholly unknown, yet utilized by ancient artisans.

Another example of size-dependent interactions of nanoscale objects and light is how the grooves on a butterfly's wings, spaced on the same order as the wavelengths of visible light, lead to diffraction and the beautiful colors one observes. Natural systems such as these have inspired scientists to make functional materials including architectures used for lenses, electronics, and sensors.[4]

Indirect methods and postulations about the nanoscale go back to 1857, when Michael Faraday, while working with gold leaf, happened to make a ruby-colored solution derived from rinsing the gold. He hypothesized correctly that this observed color was an effect of light interacting with particles too small to measure with the methods available to him.[5] Despite the history and presence of the nanoscale being all around us, the field we call nanoscience is relatively new. Widely renowned physicist and recipient of the 1965 Nobel Prize in physics, Richard Feynman theorized on the nature of things at continuously small scales in his lecture titled "There's Plenty of Room at the Bottom".[6] He famously asked in his

1959 lecture, “Why can’t we write the entire 24 volumes of the Encyclopedia Britannica on the head of a pin?”, and indeed if one could control the assembly of individual molecules this idea is not so absurd as it might have seemed at one time. The term “nanotechnology” was coined some time later in 1974 by Norio Taniguchi, who stated “nanotechnology mainly consists of the processing of separation, consolidation, and deformation of materials by one atom or one molecule.”[7] Both Feynman and Taniguchi emphasized the importance of not just observing but also having the ability to control systems at the nanoscale as crucial to advancements.

Naturally, the potential for experimentation on the nanoscale has grown alongside the inventions of advanced microscopy. The invention of the transmission electron microscope (TEM) in 1931 by Max Knoll and Ernst Ruska is still a prominent means of visualizing nanoscale features by measuring the scattering of electrons off of a solid.[8–10] Another system that uses a means of interrogation other than light is the scanning tunneling microscope (STM), invented in 1981 by Gerd Binnig and Heinrich Rohrer at the IBM Zurich Research Laboratory.[11,12] The principle of electron tunneling, where an electron has a probability of passing through an energy barrier that corresponds to its association with two distinct atoms, can be measured as a current through a probe tip, which has dimensions of only a few atoms at its apex when this tip is placed in very close proximity with a surface. This signal corresponds to the density of atoms on this surface, opening a new means of visualizing the world on the scale of individual atoms. In the case of the STM, individual atoms could even be manipulated, which was achieved in 1990 when Don Eigler and colleagues used a STM to pattern the letters “IBM” by moving individual xenon atoms on a nickel surface.[13] This process of positioning singular atoms is an example of a bottom-up

approach to creating materials at the nanoscale, and exhibits an impressive degree of control.[14]

Rather than having to influence individual atoms, however, a process at the chemical level to prepare surfaces at the nanoscale is self-assembly.[15] Self-assembly is the result of nanoscale interactions between molecules or nanoparticles which cause them to form structured formations and is a phenomenon that is featured prominently in this thesis.

In the following work, I discuss several projects whereby control of nanoscale reactions and surface functionalization enable the control of macroscopic properties and interfacing with various biological systems. The applications range from manipulating cells and permeabilizing them for the introduction of genetic material to developing surfaces that capture neurotransmitter molecules for chemical to electrical sensing.

1.B Thesis Research

To begin, I will discuss the functionalization of germanium surfaces with carborane isomers.[16] These molecules form self-assembled monolayers (SAMs) on germanium surfaces *via* the carboxylic acid functional group. Further, we investigated how carboranes with identical chemical formulas that differ in their dipole moment affect the work function, or the energy that is necessary to remove an electron from a surface. This investigation has applications in matching energy levels for low-resistance electronic contacts using functionalized semiconductors. Here, we see how the ability to manipulate matter at the nanoscale affects properties at the macroscale, as the measured work function is a property of the material rather than an individual molecule.

Transitioning to nanoscale interactions with biological systems, I will discuss several projects related to gene editing. The field of gene editing of human cells has grown in the past 50 years since it was proposed as a means to treat genetic disorders by Theodore Friedmann and Richard Roblin in 1972.[17] This manner of personalized medicine is an example of an area that has seen significant progress and since then, models have been developed to treat diseases such as HIV[18,19] and Hemophilia B.[20] In late 2023, two successful gene therapies were approved by the United States Food and Drug Administration to treat sickle cell disease.[39] In an *ex vivo* approach, a patient's own cells can be removed and genetic material can be introduced such that when the cells are cultured, a new population arises that expresses the corrected phenotypes to remedy the effects of the disease. Many edited cells are required to be transplanted into the patient in order to effectively change the body's environment and treat the expression of the disease, and a problem that precludes treatment is the need for higher efficiency of delivering the gene editing cargo.[21,22]

In my research, I have worked on two different gene-editing platforms with the aim of increasing cell throughput. Both of the devices utilize microfluidics and surface functionalization at the nanoscale. The first involves permeabilizing cells for the introduction of genetic cargo by squeezing them as they pass though constrictions a fraction of their diameter. We incorporate a lipid bilayer coating along the channel walls which aids in keeping the device operational by reducing clogging.[23] Secondly, we investigated the use of acoustic waves to manipulate cells within a microfluidic channel, subjecting them to pressure gradients and channel walls functionalized with genetic cargo.[24]

Some diseases, such as cancers, prove to be hard to treat and to detect in early stages due to the small number of cells that express the disease.[25] In the case of lung cancer, it was

reported in a 2014 study that the difference in detection at stage I versus stage IV could improve survival rates over a year by 70%.[26] To work towards technology that enables screening cells from small sample volumes, we developed a "catch and release" platform using gold nanoparticles.[27] Gold nanoparticles, which have extensively researched methods of synthesis,[38] have the advantages of being largely biologically inert when in the form of nanoparticles[28] along with thorough characterization of chemical reactions between gold and functional groups, specifically thiols.[29,30] These particles can then be functionalized with antibodies to capture markers expressed by the disease cells. In this project, I will discuss a microfluidic device wherein we synthesized gold nanostars directly to the channel walls. We then captured individual cells and used the plasmonic properties of the nanoparticles to convert near-infrared light to heat and to release the cells selectively. The ability to capture and to release cells can open the way for further studies of an individual's specific disease.[31]

In addition to the manipulation of cells in the interest of personalized medicine, another aspect of biology that occurs at the nanoscale is chemical signal transmission. Life as we understand it operates on a multitude of scales. Notably, nanoscale molecules are the building blocks of the ever-important proteins and nucleic acids that encode genes, with the radius of DNA curvature being 3-4 nm.[32] Small molecules are also means of chemical transmission in an organism and in the exploration of humanity, a key piece to the puzzle of understanding thought. A molecule such as serotonin, for example, is integral in the process of thought and emotion. Serotonin is also a metabolite of bacteria in the gut, and even spatially removed, factors in the digestive system have been shown to be capable of influencing behavior.[33] This demonstrates how vastly complicated the interactions of these molecules are in multicellular organisms.

In the final project I will discuss, I studied a method to detect a wide array of biological molecules including neurotransmitters by converting chemical binding to electrical signals. My research was mainly focused on serotonin and dopamine, measuring them in high ionic strength solutions that mimic biologically relevant environments such as the brain. Nanoscale objects have a high degree of surface area relative to their volume, and we utilize a thin film of indium oxide, a semiconductor, as the channel material of our field-effect transistors to enhance the sensitivity of our measurements.[34–36] Aptamers, which are single-stranded sequences of DNA that have been isolated to bind selectively to the neurotransmitter of interest, are chemically functionalized to the semiconductor surface and serve as our means of capturing the target molecule.[37] I will discuss our custom-built hardware to apply voltages and to measure multiple transistors simultaneously, greatly increasing our ability to characterize aptamer sequences and further pursue a robust analytical method.

In each topic of my research, chemical functionalization of surfaces at the nanoscale is utilized towards a wide range of ends. Studying and understanding how molecules interact at the nanoscale has led to advances in numerous applications that continue to broaden our scientific exploration and technological progress.

1.C References

(1) Bayda, S.; Adeel, M.; Tuccinardi, T.; Cordani, M.; Rizzolio, F. The History of Nanoscience and Nanotechnology: From Chemical-Physical Applications to Nanomedicine. *Molecules* **2020**, *25*, 1–15.

(2) Freestone, I.; Meeks, N.; Sax, M.; Higgitt, C. The Lycurgus Cup — A Roman Nanotechnology. *Gold Bull.* **2007**, *40*, 270–277.

(3) Molina Giralt, G.; Murcia, S.; Molera, J.; Roldán, C.; Crespo, D.; Pradell, T. Color and Dichroism of Silver-Stained Glasses. *J. Nanoparticle Res.* **2013**, *15, 1*–13.

(4) Butt, H.; Yetisen, A. K.; Mistry, D.; Khan, S. A.; Hassan, M. U.; Yun, S. H. Morpho Butterfly-Inspired Nanostructures. *Adv. Opt. Mater.* **2016**, *4*, 497–504.

(5) Faraday, M. The Bakerian Lecture. Experimental Relations of Gold (and Other Metals) to Light. *Philos. Trans. R Soc. Lond.* **1857**, *147*, 145–181.

(6) Feynman, R. P. There's Plenty of Room at the Bottom. *Eng. Sci.* **1960**, *23*, 22–36.

(7) Taniguchi, N.; A. C.; K. T. On the Basic Concept of Nano-Technology. *In Proceedings of the International Conference on Production Engineering, Tokyo, Japan* **1974**, 26–29.

(8) Knoll, M.; Ruska, E. Beitrag zur Geometrischen Elektronenoptik. I. *Ann. Phys.* **1932**, *404*, 607–640.

(9) Knoll, M.; Ruska, E. Beitrag zur Geometrischen Elektronenoptik. II. *Ann. Phys.* **1932**, *404*, 641–661.

(10) Sciau, Ph. Transmission Electron Microscopy: Emerging Investigations for Cultural Heritage Materials. *Adv. Imag. Elect. Phys.*, **2016**, *198*, 43–67.

(11) Binnig, G.; Rohrer, H.; Gerber, Ch.; Weibel, E. Tunneling through a Controllable Vacuum Gap. *Appl. Phys. Lett.* **1982**, *40*, 178–180.

(12) Binnig, G.; Rohrer, H.; Gerber, Ch.; Weibel, E. Surface Studies by Scanning Tunneling Microscopy. *Phys. Rev. Lett.* **1982**, *49*, 57–61.

(13) Eigler, D. M.; Schweizer, E. K. Positioning Single Atoms with a Scanning Tunneling Microscope. *Nature* **1990**, *344*, 524–526.

(14) Shimomura, M.; Sawadaishi, T. Bottom-up Strategy of Materials Fabrication: A New Trend in Nanotechnology of Soft Materials. *Curr. Opin. Colloid Interface Sci.* **2001**, *6*, 11–16.

(15) Amadi, E. V.; Venkataraman, A.; Papadopoulos, C. Nanoscale Self-Assembly: Concepts, Applications and Challenges. *Nanotechnology* **2022,** *33*, 132001.

(16) Serino, A. C.; Anderson, M. E.; Saleh, L. M. A.; Dziedzic, R. M.; Mills, H.; Heidenreich, L. K.; Spokoyny, A. M.; Weiss, P. S. Work Function Control of Germanium through Carborane-Carboxylic Acid Surface Passivation. *ACS Appl. Mater. Interfaces* **2017**, *9*, 34592–34596.

(17) Friedmann, T.; Roblin, R. Gene Therapy for Human Genetic Disease? *Science* **1972**, *175*, 949–955.

(18) Holt, N.; Wang, J.; Kim, K.; Friedman, G.; Wang, X.; Taupin, V.; Crooks, G. M.; Kohn, D. B.; Gregory, P. D.; Holmes, M. C.; Cannon, P. M. Human Hematopoietic Stem/Progenitor Cells Modified by Zinc-Finger Nucleases Targeted to CCR5 Control HIV-1 in Vivo. *Nat. Biotechnol.* **2010**, *28*, 839–847.

(19) Tebas, P.; Stein, D.; Tang, W. W.; Frank, I.; Wang, S. Q.; Lee, G.; Spratt, S. K.; Surosky, R. T.; Giedlin, M. A.; Nichol, G.; Holmes, M. C.; Gregory, P. D.; Ando, D. G.; Kalos, M.; Collman, R. G.; Binder-Scholl, G.; Plesa, G.; Hwang, W.-T.; Levine, B. L.; June, C. H. Gene

Editing of CCR5 in Autologous CD4 T Cells of Persons Infected with HIV. *N. Engl. J. Med.* **2014**, *370*, 901–910.

(20) Li, H.; Haurigot, V.; Doyon, Y.; Li, T.; Wong, S. Y.; Bhagwat, A. S.; Malani, N.; Anguela, X. M.; Sharma, R.; Ivanciu, L.; Murphy, S. L.; Finn, J. D.; Khazi, F. R.; Zhou, S.; Paschon, D. E.; Rebar, E. J.; Bushman, F. D.; Gregory, P. D.; Holmes, M. C.; High, K. A. *In Vivo* Genome Editing Restores Haemostasis in a Mouse Model of Haemophilia. *Nature* **2011**, *475*, 217–221.

(21) Cox, D. B. T.; Platt, R. J.; Zhang, F. Therapeutic Genome Editing: Prospects and Challenges. *Nat. Med*. **2015**, *21*, 121–131.

(22) Zhao, Y.; Stepto, H.; Schneider, C. K. Development of the First World Health Organization Lentiviral Vector Standard: Toward the Production Control and Standardization of Lentivirus-Based Gene Therapy Products. *Hum. Gene Ther. Methods* **2017**, *28*, 205–214.

(23) N. Belling, J.; K. Heidenreich, L.; Hyeon Park, J.; M. Kawakami, L.; Takahashi, J.; M. Frost, I.; Gong, Y.; D. Young, T.; A. Jackman, J.; J. Jonas, S.; Cho, N.-J.; S. Weiss, P. Lipid-Bicelle-Coated Microfluidics for Intracellular Delivery with Reduced Fouling. *ACS Applied Materials & Interfaces* **2020**, *12*, 45744–45752.

(24) Belling, J. N.; Heidenreich, L. K.; Tian, Z.; Mendoza, A. M.; Chiou, T.-T.; Gong, Y.; Chen, N. Y.; Young, T. D.; Wattanatorn, N.; Hyeon Park, J.; Scarabelli, L.; Chiang, N.; Takahashi, J.; Young, S. G.; Stieg, A. Z.; De Oliveira, S.; Jun Huang, T.; Weiss, P. S.; Jonas, S. J.; Doudna, J. A. Acoustofluidic Sonoporation for Gene Delivery to Human Hematopoietic Stem and Progenitor Cells. *Proc. Natl. Acad. Sci. U. S. A.* **2020**, *117*, 10976–10982.

(25) Knight, S. B.; Crosbie, P. A.; Balata, H.; Chudziak, J.; Hussell, T.; Dive, C. Progress and Prospects of Early Detection in Lung Cancer. *Open Biol*. **2017**, *7,* 1–12.

(26) Bannister, N.; Broggio, J. Cancer Survival by Stage at Diagnosis for England (Experimental Statistics): Adults Diagnosed 2012, 2013 and 2014 and Followed up to 2015. *Produced in collaboration with Public Health England* **2016**.

(27) A. Vinnacombe-Willson, G.; Chiang, N.; Scarabelli, L.; Hu, Y.; K. Heidenreich, L.; Li, X.; Gong, Y.; T. Inouye, D.; S. Fisher, T.; S. Weiss, P.; J. Jonas, S. In Situ Shape Control of Thermoplasmonic Gold Nanostars on Oxide Substrates for Hyperthermia-Mediated Cell Detachment. *ACS Cent. Sci.* **2020**, *6*, 2105–2116.

(28) Kus-liśkiewicz, M.; Fickers, P.; Ben Tahar, I. Biocompatibility and Cytotoxicity of Gold Nanoparticles: Recent Advances in Methodologies and Regulations. *Int. J. Mol. Sci.* **2021**, *22*, 10952.

(29) G. Warner, M.; M. Reed, S.; E. Hutchison, J. Small, Water-Soluble, Ligand-Stabilized Gold Nanoparticles Synthesized by Interfacial Ligand Exchange Reactions. *Chem. Mater.* **2000**, *12*, 3316–3320.

(30) H. Woehrle, G.; O. Brown, L.; E. Hutchison, J. Thiol-Functionalized, 1.5-Nm Gold Nanoparticles through Ligand Exchange Reactions: Scope and Mechanism of Ligand Exchange. *J. Am. Chem. Soc.* **2005**, *127*, 2172–2183.

(31) Liu, L.; Yu, L.; Li, Z.; Li, W.; Huang, W. Patient-Derived Organoid (PDO) Platforms to Facilitate Clinical Decision Making. *J. Transl. Med.* **2021**, *19*, 40.

(32) Vologodskii, A.; Frank-Kamenetskii, M. D. Strong Bending of the DNA Double Helix. *Nucleic Acids Research* **2013**, *41*, 6785–6792.

(33) Borrelli, L.; Aceto, S.; Agnisola, C.; De Paolo, S.; Dipineto, L.; Stilling, R. M.; Dinan, T. G.; Cryan, J. F.; Menna, L. F.; Fioretti, A. Probiotic Modulation of the Microbiota-Gut-Brain Axis and Behaviour in Zebrafish. *Sci. Rep.* **2016**, *6*, 30046.

(34) Chen, H.; Rim, Y. S.; Wang, I. C.; Li, C.; Zhu, B.; Sun, M.; Goorsky, M. S.; He, X.; Yang, Y. Quasi-Two-Dimensional Metal Oxide Semiconductors Based Ultrasensitive Potentiometric Biosensors. *ACS Nano* **2017**, *11*, 4710–4718.

(35) Kim, J.; Rim, Y. S.; Chen, H.; Cao, H. H.; Nakatsuka, N.; Hinton, H. L.; Zhao, C.; Andrews, A. M.; Yang, Y.; Weiss, P. S. Fabrication of High-Performance Ultrathin In_2O_3 Film Field-Effect Transistors and Biosensors Using Chemical Lift-off Lithography. *ACS Nano* **2015**, *9*, 4572–4582.

(36) Rim, Y. S.; Bae, S. H.; Chen, H.; Yang, J. L.; Kim, J.; Andrews, A. M.; Weiss, P. S.; Yang, Y.; Tseng, H. R. Printable Ultrathin Metal Oxide Semiconductor-Based Conformal Biosensors. *ACS Nano* **2015**, *9*, 12174–12181.

(37) Yang, K. A.; Pei, R.; Stojanovic, M. N. In Vitro Selection and Amplification Protocols for Isolation of Aptameric Sensors for Small Molecules. *Methods* **2016**, *106*, 58–65.

(38) Scarabelli, L.; Sánchez-Iglesias, A.; Pérez-Juste, J. M.; Liz-Marzán, L. A "Tips and Tricks" Practical Guide to the Synthesis of Gold Nanorods. *J. Phys. Chem. Lett.* **2015,** *6*, 4270–4279.

(39) National Heart, Lung, and Blood Institute. NIH Statement on New FDA-Approved Gene Therapies for Sickle Cell Disease. National Institutes of Health, December 8, 2023.

CHAPTER 2

Work Function Control of Germanium through Carborane-Carboxylic Acid Surface Passivation

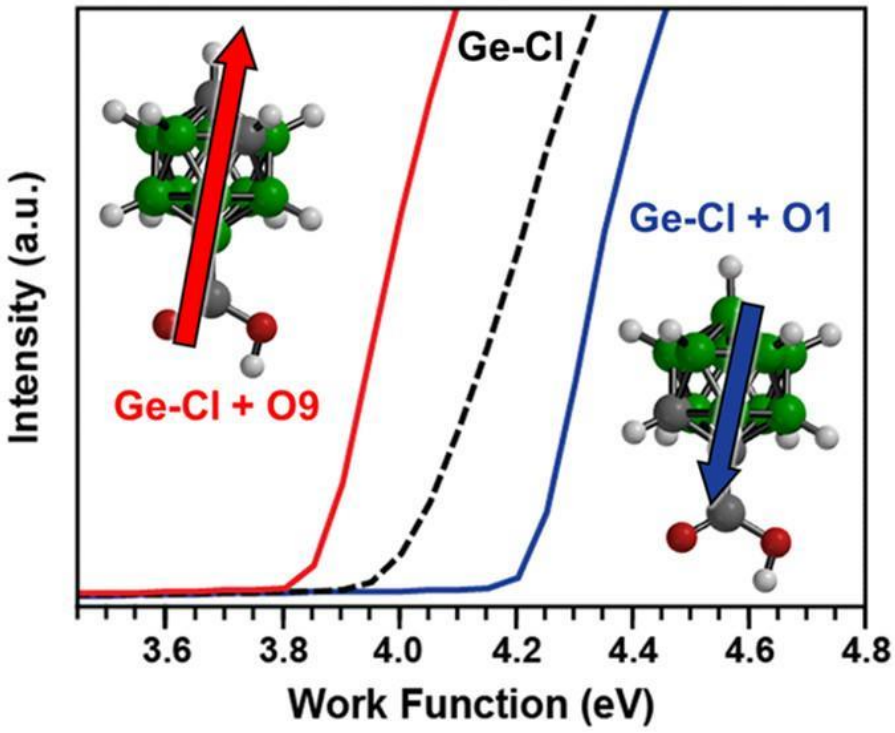

The information in this chapter was published in *ACS Applied Materials Interfaces* **2017**, *9*, 34592–34596 and is reproduced here with permission.

Authors: Serino, A. C.; Anderson, M. E.; Saleh, L. M. A.; Dziedzic, R. M.; Mills, H.; **Heidenreich, L. K.**; Spokoyny, A. M.; Weiss, P. S.

2.A Introduction

Recent advances in interface engineering for semiconductors have contributed to significant improvements for electronic devices such as transistors, photovoltaics, and sensors.[1-9] Many of these architectures require precise control of energy levels at the interfaces between materials. Alignment of these energy levels provides low-resistance contacts, whereas large misalignment causes band bending that generates internal electric fields. This internal field can be helpful for preventing electron–hole recombination in heterojunction photovoltaics. Band engineering can be accomplished by controlling surface work functions (WFs), which has been demonstrated by passivating surfaces with covalently bound organic monolayers possessing different dipole magnitudes and orientations.[2,3] However, these monolayers also often alter surface energy, adding complications to the device fabrication process by changing wetting or adhesive properties at the material interface.[7-9] The ability to tune energy level alignment with a simple and reliable method without influencing surface energy and wetting will reduce complications across industries.[10]

Our group modified gold and silver surfaces with carboranethiols to tune band alignment and thus interfacial charge-transfer resistance between metal contacts and a polymer semiconductor. The surface treatment had minimal effects on surface energy and wetting at the interface.[10] By changing both placement of carbon atoms within the carborane cluster and headgroup position on the carborane cage, it is possible to tune dipole moment magnitude and orientation while leaving the chemical environment identical between isomers.[11-14] This feature makes carboranes an attractive option for tuning surface WFs. Translating the carborane system from metal to semiconductor systems would aid in rapid-

prototyping of semiconductor devices by enabling precision band engineering with minimal impact on processing.[15]

Germanium is a promising candidate for semiconductor-based technologies because of its small band gap (0.67 eV) and high electron and hole mobilities, ~2.5× and ~4×, respectively, relative to silicon. These properties lead to faster devices and an absorption spectrum that extends into the infrared. Unfortunately, germanium's defect-rich, intrinsic oxide keeps it from having significant impact on today's devices.[16] Researchers have investigated methods for removing germanium's oxide layer, commonly through etching, and then depositing an organic monolayer to suppress oxide formation. Maboudian and co-workers demonstrated this removal by etching the oxide with hydrofluoric acid and simultaneously passivating the surface with hydrogen. Monolayers of 1-octadecanethiolate were subsequently formed by displacing surface hydrogens.[17] Bent and co-workers applied this alkanethiol deposition to halogenated Ge(111) and Ge(100) surfaces.[18] They removed germanium oxide by hydrogen peroxide (H_2O_2) and hydrochloric or hydrobromic acid etches (HCl or HBr), leaving behind halogen-passivated surfaces. The halogen layer was then displaced by octanethiol or octadecanethiol, resulting in organic monolayers that are stable in ambient conditions for several days. Many head groups have been explored for Ge, however, thiol passivation remains a prominent wet chemical method for organic self-assembled monolayer (SAM) formation.[19]

While exploring headgroup–surface interactions, Bent and co-workers revealed a significant difference in halogen and sulfur concentrations between Ge(100) and Ge(111) surfaces, which they attributed to the unique characteristics of the Ge(100) surface.[18-20] To reduce the number of dangling bonds, the Ge(100) surface reconstructs into a 2 × 1 structure,

resulting in the creation of surface dimers. The major difference in surface reactivity is attributed to the nucleophilic top Ge atom and the electrophilic bottom Ge atom. This reactivity difference has been studied with other possible headgroup chemistries on sputter-cleaned surfaces in ultrahigh vacuum. For example, alcohols and carboxylic acids were found to chemisorb selectively to Ge(100), and not Ge(111), through hydrogen dissociation and reaction between the oxygen and the electrophilic lower atom in the surface dimer.[21,22]

Herein, we investigate deposition of icosahedral carboranes with different head groups on Ge(100) surfaces using an H_2O_2 and HCl pretreatment. Specifically, boron clusters with thiol, hydroxyl, and carboxylic acid head groups attached at various vertices were studied in order to determine suitable headgroup chemistries for chemisorption of carborane monolayers on germanium with the ultimate goal of tuning the WF with minimal perturbations to surface energy.

2.B Experimental Methods

2.B.1 Surface Preparation

Single-side polished, undoped Ge(100) wafers (MTI Corporation, Richmond, CA) were cleaned by sonication in acetone and then rinsed with deionized water (18.2 MΩ-cm resistivity, Milli-Q from Millipore,Billerica, MA). The substrate was prepared for molecular deposition using an etch cycle of 30% H_2O_2, (Sigma Aldrich, St. Louis, MO) then 37% HCl (Sigma Aldrich) for 5 min each. This cycle was repeated a total of three times. After the last etch, samples were quickly dried under a nitrogen gas stream, and immediately transferred to a nitrogen glovebox with oxygen content ~0.1 ppm. The effects of the H_2O_2/HCl

pretreatment, are shown in **Figure 2.S9**, where X-ray photoelectron spectroscopy (XPS) reveals a reduction of the surface oxide layer.

The synthesis of the carbonane molecules with a variety of head groups is described in Supporting Information. All carborane films were formed using 1 mM solutions of carboranes dissolved in anhydrous benzene (Sigma Aldrich), which was purged with nitrogen for 30 min prior to use. The solutions were prepared in the glovebox and deposited on the germanium surfaces at room temperature for approximately 24. The functionalized germanium surfaces were held in solution until just before analysis, and immediately rinsed in benzene solely or benzene followed by anhydrous isopropanol (IPA, Sigma Aldrich), and dried with a nitrogen gas stream. Substrates were rinsed from the carborane solutions and dried three times.

2.B.2 Surface Characterization by X-Ray Photoelectron Spectroscopy

Samples were transferred from the glovebox to the XPS vacuum chamber (1 × 10-9 Torr) using a transfer vessel to maintain an air-free environment. Spectra were acquired using a Kratos Axis Ultra DLD photoelectron spectrometer (Kratos Analytical, Manchester, UK) with a monochromatic Al K α source at 300 W and a 300 μm × 700 μm spot size. A pass energy of 20 eV was used with a resolution of 0.1 eV for the high-resolution regions of Ge 2p, C 1s, Cl 2p, B 1s, and O 1s, using between 5 and 20 sweeps per region. Energy scales were corrected to the C-C binding energy of 284.8 eV. All peaks were analyzed using CasaXPS software, fit using Gaussian-Lorentzian line shapes with a Shirley background (fit lines were omitted for clarity) to determine peak positions, and finally smoothed using a Savotzky-Golay quadratic. The B 1s and Cl 2p peaks are normalized to the Ge.

2.B.3 Work Function Characterization by Ultraviolet Photoelectron Spectroscopy

Measurements were performed using a Kratos Axis Ultra DLD after XPS analysis, using a He I excitation source (21.2 eV). The spectra energy scales were calibrated to the Fermi level of freshly evaporated Au. To obtain clean germanium surfaces, chlorine terminated germanium surfaces were Ar ion etched using a 3.8 kV accelerating voltage, 100 μA extractor current, and a beam current of 1.159 μA.

2.B.4 Density Functional Theory

Dipole moment calculations were performed with ADF 2014 Suite version 2014.04[37-39] using TZP basis sets (Slater-type orbitals: double zeta core, triple zeta valence + 1 polarization function). Geometry optimizations and single point calculations were performed using PBE-D3(BJ),[40,41] B3LYP-D3(BJ),[40,42-44] PBE0,[45] and M06,[46] density functionals. Dipole moment calculations were performed with the substituted vertex and the antipodal vertex defining the Z-axis, and the YZ plane defining the mirror plane of each functionalized carborane as listed in **Table 2.S3**.

2.B.5 Contact Angle Goniometry

Dynamic contact angle measurements were obtained using an automated FTA1000 Analyzer System (First Ten Angstroms, Inc., Portsmouth, VA) equipped with a 500 μL gas tight #1750 syringe (Hamilton Co., Reno, NV) and a 27 gauge flat-tip stainless steel needle. Control and analysis software utilized was FTA32 version 2.1.

Using the dynamic sessile drop method, the sample was brought into close proximity to the substrate and a 4 μL droplet of deionized water is deposited on the sample with the

needle tip maintaining contact to the drop. To obtain advancing angle values, an additional 2.5 μL of deionized water is dispensed, then withdrawn to obtain receding angle values. The volume change occurs over a 1.25 sec time period followed by 8.75 sec when the drop is static. The advancing/receding cycle was repeated a total of 8 times with 5 photographs captured per second. The angle between the surface and the drop was analyzed for the final 6 cycles with 30 frames after each volume increase averaged to obtain advancing contact angle, likewise after each volume decrease to determine receding contact angle. The standard deviation for the majority of individual droplets throughout the analyzed cycles was found to be less than 1°. For comparison, the advancing and receding angles of an as-received Ge sample were 76.9° ± 0.44° and 50.6° ± 0.89°, respectively. The measure the effects of both 1-COOH-*o*-carborane (O1COOH) and 9-COOH-*o*-carborane (O9COOH) on surface wettability, four germanium substrates were passivated with each and characterized by dynamic contact angle goniometry with at least two droplets per sample analyzed to determine advancing and receding angles.

2.C Results and Discussion

While there are established methods for germanium SAM formation using thiol head groups,[16-19] our work indicates these are not suited for the carborane system and instead present evidence for carboxylic acid binding to the germanium surface. **Figure 2.1A** contains a schematic depicting the various head groups and carborane isomers used in this study. Initial experiments focused on binding positions where the headgroup was bound to boron vertices, specifically, 9-*o*-carborane (O9) and 9-*m*-carborane (M9), as this would reduce lateral dipole–dipole interactions that could aid in assembly and instead enable focus on

headgroup surface reactivity. X-ray photoelectron spectroscopy (XPS) was used to investigate head groups binding on germanium surfaces by taking high-resolution spectra of B 1s (**Figure 2.1B**) and S 2p (**Figure 2.S10**). For both 9-SH-*m*-carborane (M9SH) and 9-SH-*o*-carborane (O9SH), the lack of peaks in both the B 1s and S 2p spectra indicate that neither bind. Expanding to the two other possible head groups, (hydroxyl and carboxylic acid), we find that 9-OH-*m*-carborane (M9OH) did not show any evidence for binding, however, presence of boron for 9-COOH-*o*-carborane (O9COOH) suggests ultrathin film formation.

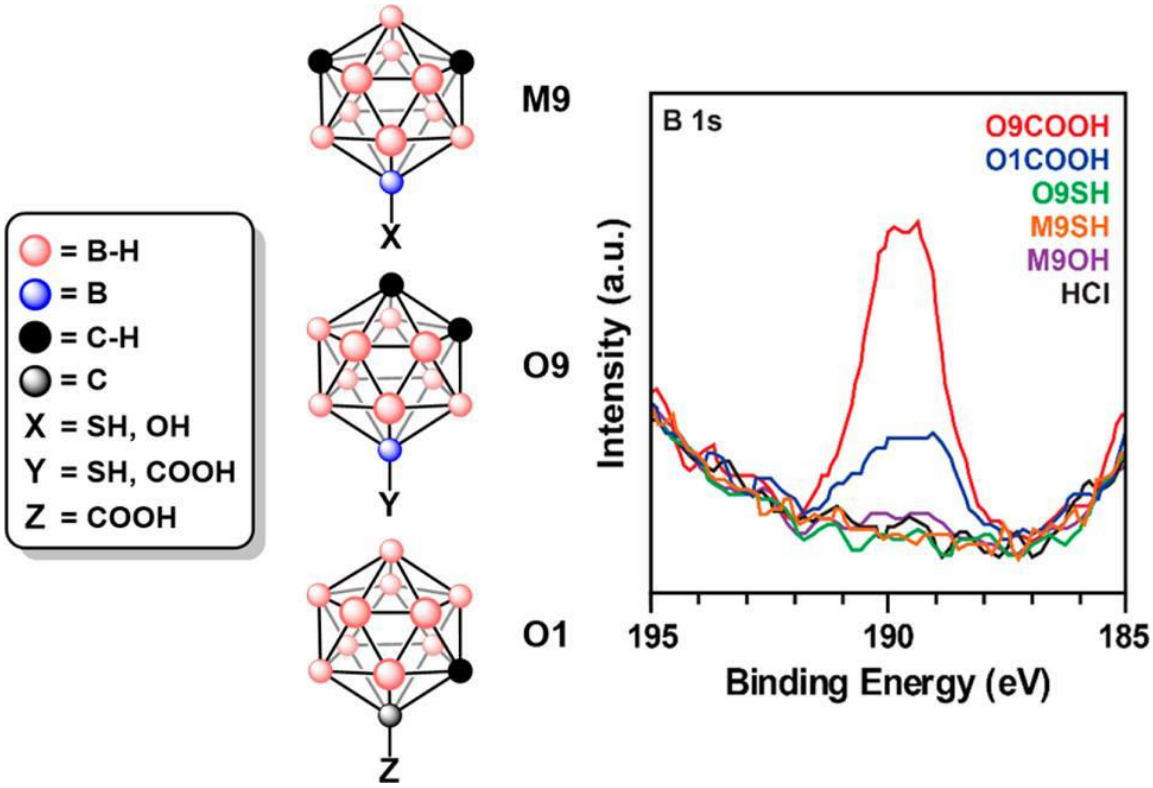

Figure 2.1. Schematic representation of 9-*m*-carborane (M9) with thiol and hydroxyl head groups (M9SH and M9OH, respectively), 9-*o*-carborane (O9) with thiol and carboxylic acid head groups (O9SH and O9COOH, respectively), and 1-*o*-carborane (O1) with a carboxylic acid headgroup (O1COOH). X-ray photoelectron spectra of the B 1s electron indicate only the presence of O9COOH and O1COOH on Ge(100).

With the success of O9COOH, we examined its isomer 1-COOH-*o*-carborane (O1COOH), where the headgroup is bound to a carbon vertex instead of boron. We hypothesize that a strong vertically oriented dipole moment might facilitate multilayering through head–tail attraction. To test this possibility, we rinsed O1COOH and O9COOH Ge surfaces with a polar solvent, isopropanol, after the benzene rinse to disrupt dipole–dipole interactions. This procedure resulted in decreases in B 1s signal for O9COOH (**Figure 2.2A**) so that both O1COOH and O9COOH are present in similar quantities, consistent with our multilayering hypothesis. After extensive rinsing with both polar and nonpolar solvents, the presence of boron suggests that the carborane carboxyl film is likely chemisorbed, through deprotonation analogous to work reported previously.[23-25]

High-resolution XPS spectra of carboxylic acid carborane films on germanium, shown in **Figure 2.2**, highlight the regions for **(A)** B 1s, **(B)** Cl 2p, **(C)** C 1s, **(D)** O 1s, and **(E)** Ge 2p. Ge(100) surfaces modified by HCl (black trace), O9COOH (red trace), and O1COOH (blue trace) are all shown for comparison, with fitted peak positions and relative elemental concentrations shown in the Supporting Information (**Tables 2.S1-S2**). These data show that the H_2O_2/HCl pretreatment successfully leaves a relatively oxide-free surface by etching away germanium oxide and passivating the germanium surface with chlorine atoms. **Figure 2.2B** highlights the chlorine region, showing that after deposition chlorine is still present on the surface, with Cl $2p_{1/2}$ and $2p_{3/2}$ XPS features at 198.6 and 200.3 eV, respectively. Note that there is overlap between Cl 2p peaks and the Ge 3s plasmon peak (fitted with purple dotted line). The chlorine peak decreases upon O1COOH and O9COOH film formation, relative to the Ge 3s plasmon background, while the chlorine peak position remains

unchanged. This reduction in signal could be a result of the displacement of chlorine ions with carboxylate groups, attenuation from the monolayer, or a combination of both.

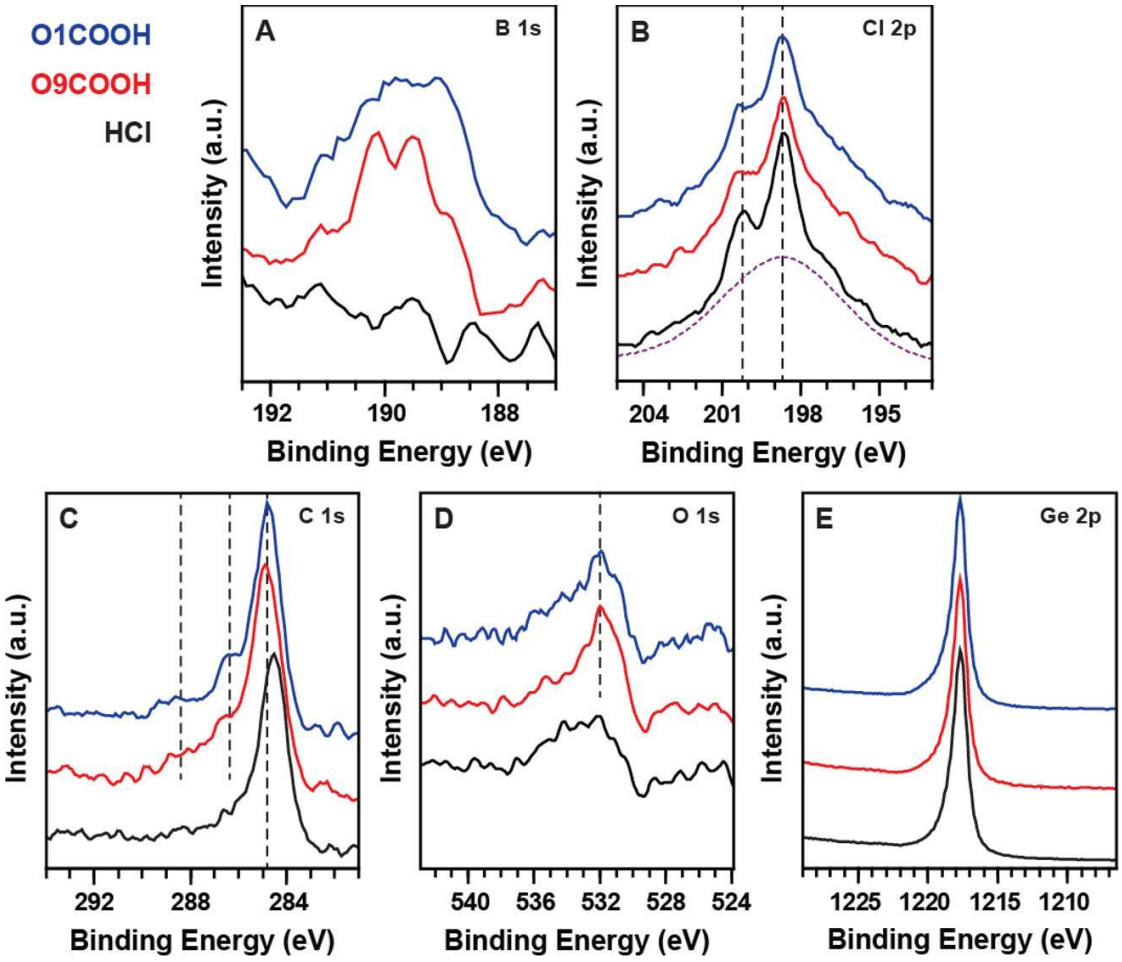

Figure 2.2. X-ray photoelectron spectroscopy of 1-COOH-*o*-carborane (O1COOH, blue trace), 9-COOH-*o*-carborane (O9COOH, red trace), and HCl etched (black trace) on Ge(100), highlighting the **(A)** B 1s, **(B)** Cl 2p, **(C)** C 1s, **(D)** O 1s, and **(E)** Ge 2p regions. Dotted purple line **(B)** outlines the Ge plasmon peak. Dotted black lines highlight specific peak positions.

The C 1s spectra (**Figure 2.2C**) indicate multiple carbon species on the surface. Presence of carbon on the HCl-treated sample is attributed to C–C/C–H bonds from adventitious carbon (284.5 eV). A similar carbon signal, slightly shifted to higher binding energies (284.8 eV), is

observed for both carborane isomers, which may be due to the higher electropositive nature of carboranes. In addition, the peaks at 286.4 and 286.5 eV for O1COOH and O9COOH, respectively, correspond to a C–B bond from the carborane cage.[26] The slight difference in binding energy between isomers may be a result of different bonding configurations. Peaks at 288.5 and 288.2 eV for O1COOH and O9COOH, respectively, are a result of the presence of the carboxylate functional group (O–C═O) on the surface. This small difference correlates to electronegativity difference between isomers, with the C–C bond in O1COOH increasing binding energy and C–B bond in O9COOH decreasing binding energy.

Both carborane systems change the O 1s spectra (**Figure 2.2D**) from the chlorine-passivated system in a similar fashion. The HCl-etched control sample shows a small amount of residual oxygen. After assembly of carborane films, there are increases in peak intensity at 531.7 and 531.6 eV for O1COOH and O9COOH, respectively, due to the presence of the carboxylate groups.[23] There is a prominent, but asymmetric Ge 2p peak at 1217.7 eV, corresponding to elemental Ge and possibly Ge–Cl (**Figure 2.2E**). The O1COOH and O9COOH samples show a slight shift in the peak onset to higher binding energy (**Figure 2.S11**) indicating Ge–O bond formation.[23,27] However, it is difficult to deconvolute peaks due to the small energy separation between oxidation states and the high concentration of bulk Ge.

Previous work with 11-mercaptoundecanoic acid has shown that the thiol group binds to Cl-terminated Ge(111) surfaces preferentially over the carboxyl group.[18,28] Preference of carboxylate over thiolate binding seen here may be the result of interplay between several factors, including the presence of surface dimers on the Ge(100) surface,[16,18,20,23,24] the electronic nature of the carborane cage,[29,30] the reduction in steric hindrance due to the size of the carboxylate group relative to the size of the carborane cage,

and a more energetically favorable Ge–O bond. To assess the contributions between these possible mechanisms, we deposited O1COOH on Ge(111) using similar surface preparation procedures, and characterized samples with XPS. The Ge(111) surface has a 1 × 1 structure, and therefore does not contain surface dimers. High-resolution spectra (**Figure 2.S12**) show that both boron and chlorine are still present on the Ge(111) surface, indicating surface dimers are not responsible for carboxylate binding.

Ultraviolet photoelectron spectroscopy (**Figure 2.3A**) was used to determine WF changes on the Ge(100) surface through the chemisorption of carborane carboxylic acid. The WF is calculated using **Equation 2.1**, where $h\nu$ is the excitation energy of the He I photon (21.2 eV) and E_{cutoff} is the high binding energy (BE) cutoff of the spectrum.[1] This sharp intensity drop in the spectrum corresponds to the energy level at which electrons can no longer escape.

$$WF = h\nu - E_{cutoff} \qquad \text{(Equation 2.1)}$$

The total WF change is a summation of both chemical bonding and molecular dipole effects, but due to the similarity of the binding between O1COOH and O9COOH isomers, we can directly compare how the molecular dipole affects surface WF. Using density functional theory (**Table 2.S3**) with B3LYP functional,[10] we determined dipole magnitudes and orientations to be 3.24 D oriented toward the headgroup for O1COOH (**Figure 2.3B**) and 5.14 D oriented away from the headgroup (**Figure 2.3C**) for O9COOH. These differences in dipole moment manifest themselves in a 5.22 pK_a difference between O1COOH and O9COOH, with O9COOH having a more electron-rich and O1COOH a more electron-poor headgroup.[30]

Although the net dipole of the molecules chemisorbed on the Ge surface will change, these values are useful in making qualitative comparisons.

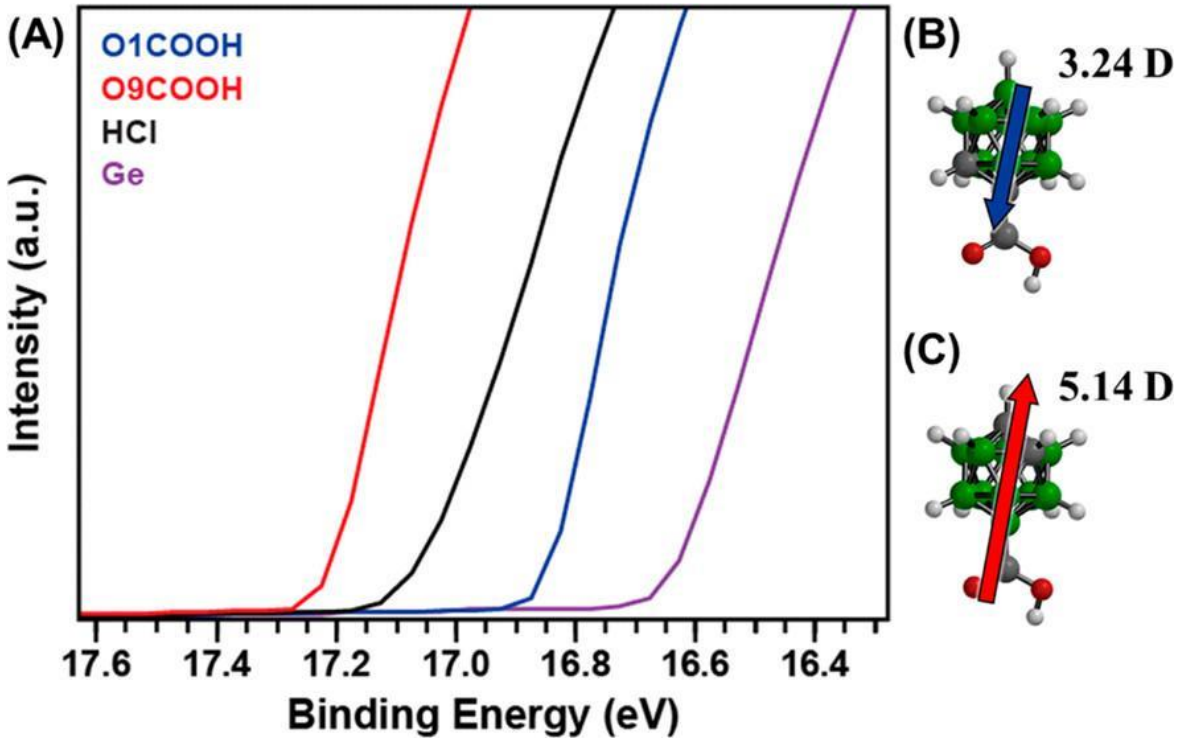

Figure 2.3. (A) Ultraviolet photoelectron spectroscopy of Ge(100) surfaces modified by 1-COOH-*o*-carborane (O1COOH, blue trace), 9-COOH-*o*-carborane (O9COOH, red trace), and chlorine (HCl, black trace), and Ar-ion-etched Ge(100) surface (Ge, purple trace). Surface modification by O1COOH and O9COOH show a shift of ±0.2 eV from chlorine passivated Ge with both shifted lower from germanium's native work function. Schematic representations of **(B)** O1COOH and **(C)** O9COOH with calculated dipole magnitudes and orientations.

All surface treatments (O1COOH, O9COOH, and HCl) examined here cause increases in the low-energy cutoff region of the spectra due to the strong effect that chemical binding has on the Ge WF.[3] For reference, clean Ge(100) surface and hydrochloric acid-etched Ge(100) surface exhibit a WF of 4.56 eV (BE of 16.65 eV) and 4.13 eV (BE of 17.08 eV), respectively. Upon modifying the hydrochloric acid-etched Ge(100) surface with O1COOH

and O9COOH films, the WF increased to 4.39 eV (BE of 16.82 eV) and decreased to 3.99 eV (BE of 17.22 eV), respectively. This result shows that the different dipoles of the carborane isomers influence the WF of the germanium surface in a similar fashion as on Au and Ag.[10] Relative to the Ge–Cl surface, the vertical component of O1COOH's dipole moment points into the surface increasing the WF by 0.26 eV, whereas the vertical component of the O9COOH's dipole moment points away from the surface decreasing the WF by 0.14 eV. These data indicate that the WF can shift by approximately ±0.2 eV relative to the Ge–Cl surface WF. The WF change with carborane dipole direction agrees with past work of carboranethiol SAMs on Au and Ag.[10] Additionally, following that work, these data suggest that a mixed monolayer of carborane carboxylates could tune the WF of Ge over a 0.4 eV range centered around 4.19 eV. Lastly, correlation between dipole orientation and WF change offers further verification that these carboranes are tethered to the surface through carboxylic acid head groups.

Advancing and receding contact angles for O1COOH and O9COOH (shown in **Table 2.1**), indicate that the wetting properties and surface energy of the two are not significantly different. The reported error is the standard deviation on the average advancing (or receding) contact angles for the nine droplets analyzed for each sample type. The O1COOH has the smaller contact angle and a smaller molecular dipole of the isomers used, consistent with data for M1 and M9 thiol on gold. Monolayers of M1 thiol on gold have a smaller dipole moment (1.06 D) relative to monolayers of M9 (4.08 D) thiol on gold, corresponding to static contact angles found to be 77.7° and 85.8°, respectively.[10] The reduced contact angle observed for the O1COOH and O9COOH may be due to substrate roughness,, lower molecular packing density, or differences in molecular orientation.[23,24] The nonpolar solvent

hexadecane was used as well, and similarly to the carboranethiol-Au system, the surface was completely wetted and no contact angle was attainable.[10]

Table 2.1 Advancing and receding contact angles for 1-COOH-*o*-Carborane (O1COOH), 9-COOH-*o*-Carborane (O9COOH) on Ge(100) surfaces.

	advancing θ	**receding θ**
O1COOH	56.8 ± 5.5°	39.9 ± 3.6°
O9COOH	59.5 ± 4.6°	42.3 ± 6.9°

The difference between the advancing and receding contact angle is hysteresis, which is indicative of the roughness. For both the O1COOH and O9COOH samples, the hysteresis is approximately 17°. This is only 2-3 times higher than what was observed for alkanethiols passivating germanium substrates using the facile water/ethanol solvent deposition method that is known to maintain the substrate roughness (~0.3 nm).[16] The similarity of the hysteresis values indicates that this roughening is consistent between the two samples.

2.D Conclusions and Prospects

In summary, carborane carboxylate monolayers were formed on germanium surfaces to modify surface WF with minimal effects to surface energy. We find that the carborane cluster affects headgroup binding, where carboxylic acid tethers successfully assemble and thiol and hydroxyl groups do not. This affinity for carboxylic acid is hypothesized to be induced by several factors, including steric effects, the unusual electronic character of the carborane cluster, and thermodynamic favorability. Carborane monolayers on Ge present the opportunity for the surface WF to be tailored over a 0.4 eV range while the integrity of surface properties, such as wetting and adhesion, are maintained. Potential challenges for

carborane films on Ge, such as air and thermal stability, are of interest to direct future research. Additionally, the effect binding angle may have on surface properties and stability, as well as whether this angle can be controlled with an annealing phase, are areas for further exploration.[23,24] Results presented herein motivate future experimental and theoretical investigations to understand how carborane clusters affect headgroup–surface binding chemistries, and whether other headgroup chemistries may be affected. Additionally, with the successful WF modulation presented here, it is worth exploring how carboranes may benefit other semiconductor device systems, such as silicon and metal oxides.

2.E Supplementary Materials

2.E.1 Synthesis of Molecules and Characterization by Nuclear Magnetic Resonance

1-COOH-*o*-carborane (O1COOH): Synthesis adapted from Kahl and co-workers.[31] ^{n}BuLi (4.8 mL, 7.7 mmol, 1.6 M in hexanes) was added dropwise to a cooled (-78 °C) solution of *o*-carborane (1.0 g, 6.9 mmol) in Et2 O (9.5 mL). The resultant solution was then stirred for 20 min at -78 °C, after which crushed dry ice (approx. 2.0-2.5 g) was quickly added to the reaction mixture and stirred at -78 °C for 1 h before warming to room temperature. All the volatiles were removed under reduced pressure and water was added to the remaining residue. Hexanes (2 × 15 mL) were added to the aqueous mixture to extract any unreacted *o*-carborane. Following this, the aqueous layer was acidified with 3 M HCl and the title compound was extracted with hexanes (4 × 15 mL). The combined organic phases were dried over Na_2SO_4 and all volatiles removed under reduced pressure to produce the title compound as a white solid (**Figures 2.S1 and 2.S2**).

Yield: 0.8 g (61%). ^{1}H NMR (500 MHz, $CDCl_3$): δ 1.50-3.20 (m, 10H, BH), 4.05 (s, 1H, $C_{carborane}$ -H) 8.59 (1H, COOH); ^{11}B NMR (160 MHz): δ -2.1 (d, 2B, ^{1}JBH = 148 Hz), -8.4 (d, 2B, ^{1}J BH = 152 Hz), -11.6 (d, 4B, ^{1}JBH = 173 Hz), -13.3 (d, 2B, ^{1}JBH = 178 Hz) Note: Due to the presence of acid in $CDCl_3$, the position for the resonance corresponding to COOH changes depending on the concentration of acid.

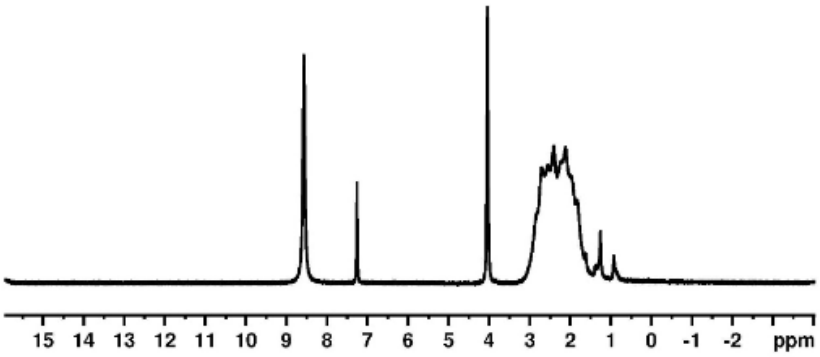

Figure 2.S1. ^{1}H NMR of 1-COOH-*o*-carborane in $CDCl_3$.

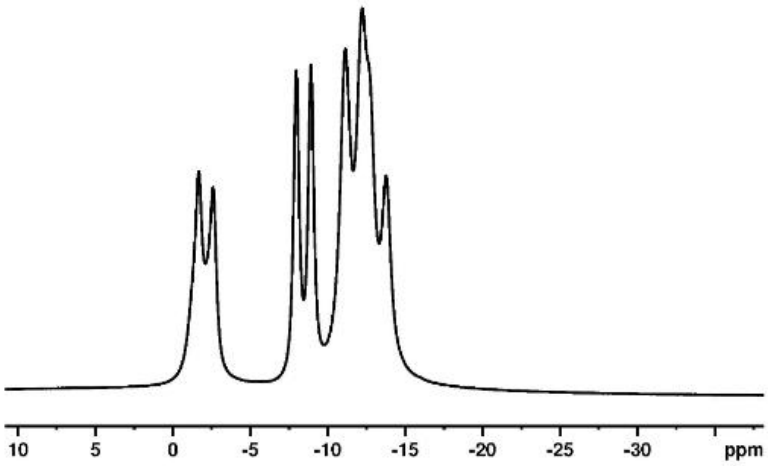

Figure 2.S2. ^{11}B NMR of 1-COOH-*o*-carborane.

9-COOH-*o*-carborane (O9COOH): Synthesis adapted from Craciun and Custelcean.[32] A 50 mL round-bottom flask containing a solution of 9-ethyl-*o*-carborane[33] (1.0 g, 5.8 mmol) in a mixture of glacial acetic acid (14 mL) and concentrated sulfuric acid (1.4 mL) was cooled in an ice bath (0 °C). CrO_3 (2.6 g, 32.5 mmol) was slowly added to the cold, stirring solution of 9-ethyl-*o*-carborane. After the addition of CrO_3 , the reaction mixture was stirred for 1 h at 0 °C, and subsequently heated for 2 h at 65 °C. After cooling to room temperature, the solution was poured into ice cold water (100 mL) immediately producing a white precipitate. The white precipitate was collected on a fritted glass funnel and washed with water (2 × 10 mL). The precipitate was further purified by dissolving the white crystals in a minimal amount of hot methanol and precipitated by adding water (20 mL). The precipitate was collected on a fritted glass funnel and dried under high vacuum to produce the title compound as a white powder (**Figures 2.S3 and 2.S4**).

Yield: 0.63 g (57%). ^{1}H NMR (400 MHz, DMSO-d_6): δ 1.24-3.02 (m, 9H, BH), 5.00 (s, 2H, $C_{carborane}$ -H), 11.39 (s, 1H, COOH); ^{11}B NMR (128 MHz): δ -0.5 (s, 1B), -3.4 (d, 2B, $^{1}J_{BH}$ = 148 Hz), -9.7 (d, 4B, $^{1}J_{BH}$ = 145 Hz), -14.6 (m, 6B)

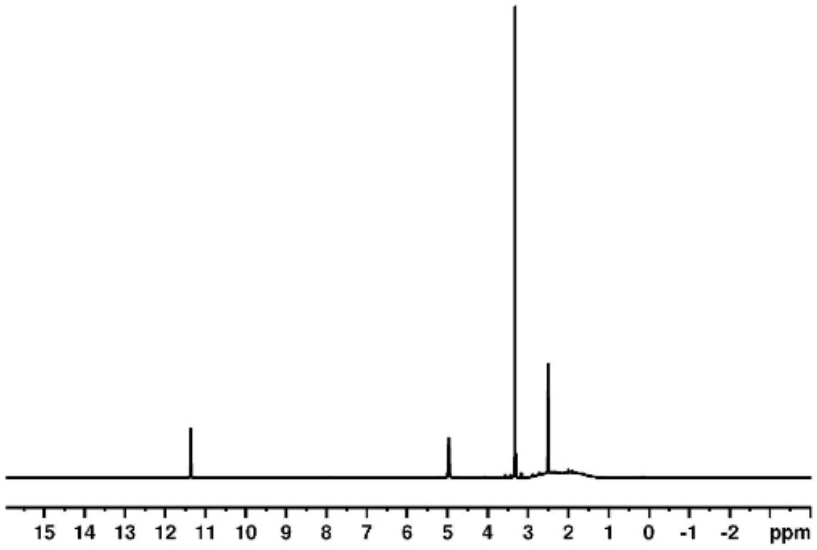

Figure 2.S3. ^{1}H NMR of 9-COOH-*o*-carborane in DMSO-d_6.

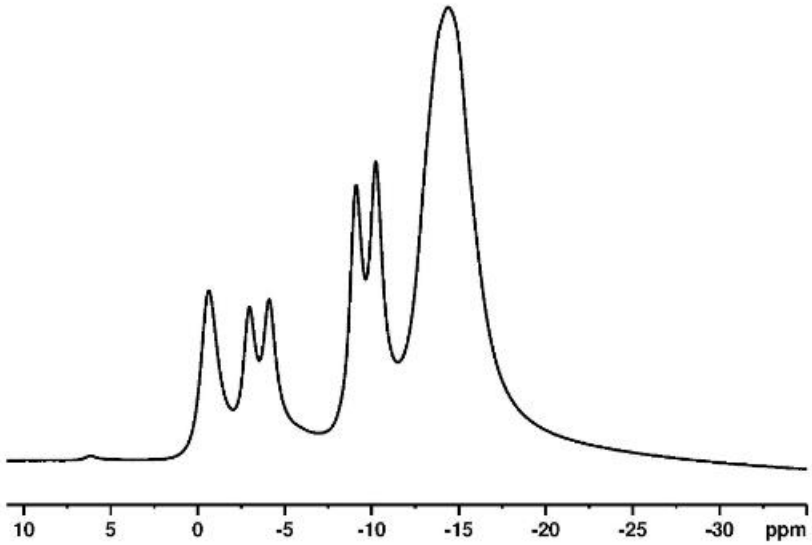

Figure 2.S4. ^{11}B NMR of 9-COOH-*o*-carborane.

9-OH-*m*-carborane (M9OH): Synthesis adapted from Spokoyny and co-workers.[34] SPhos (20.5 mg, 5 mol%), SPhos-Pd-G3 precatalyst (39.8 mg, 5 mol%), 9-Br-*m*-carborane (223 mg, 1 mmol) were added to an oven-dried reaction tube and sealed with a PTFE septum cap. The reaction tube was evacuated and backfilled with N_2 four times. 1,4-dioxane (2 mL) and a 1 M K_3PO_4 solution in water (2 mL, deoxygenated by sparging with N_2 for 30 min) were injected. The rapidly stirring reaction mixture was heated for 1 h in an 80 °C oil bath. Upon completion, the reaction mixture was extracted with Et_2O (4 × 5 mL), the organics were filtered through a silica plug and solvent removed under reduced pressure. The resulting dark brown oil was loaded onto a silica column and washed with a 1:1 CH_2Cl_2 :hexanes mixture, the product was eluted from the column using a 1:1 Et_2O:hexanes mixture. The product containing fractions were combined and solvent removed under reduced pressure to yield a white solid (**Figures 2.S5 and 2.S6**).

Yield: 83 mg (52%). ^{1}H NMR (500 MHz, $CDCl_3$): δ 1.40-3.10 (m, 9H, BH), 1.61 (s, 1H, -OH), 2.74 (s, 2H, $C_{carborane}$ -H); ^{11}B NMR (160 MHz): δ 8.6 (s, 1B), - 8.1 (d, 2B, ^{1}JBH = 162 Hz), -11.7 (d, 1B, ^{1}J BH = 151 Hz), -15.0 (d, 2B, ^{1}JBH = 162 Hz), - 16.9 (d, 2B, ^{1}JBH = 164 Hz), -20.5 (d, 1B, ^{1}JBH = 182 Hz), -27.1 (d, 1B, ^{1}JBH = 182 Hz).

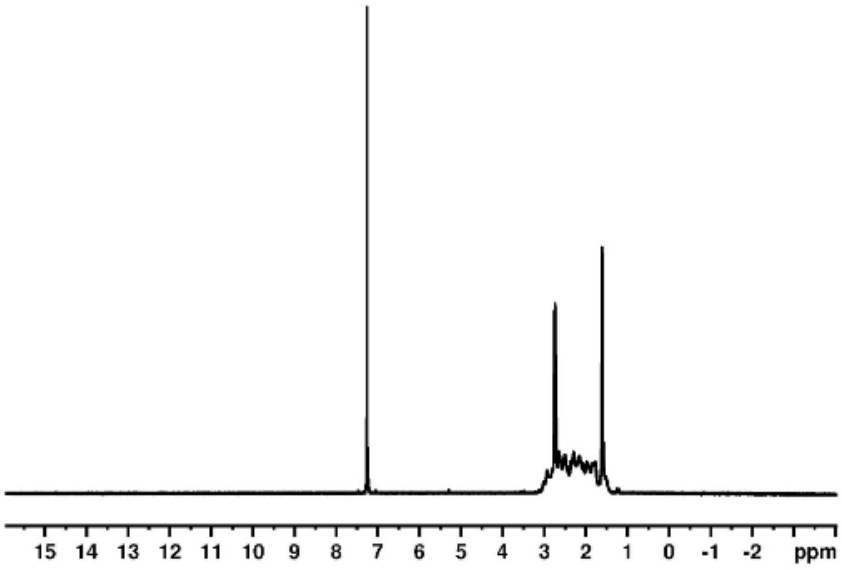

Figure 2.S5. ^{1}H NMR of 9-OH-*m*-carborane in $CDCl_3$.

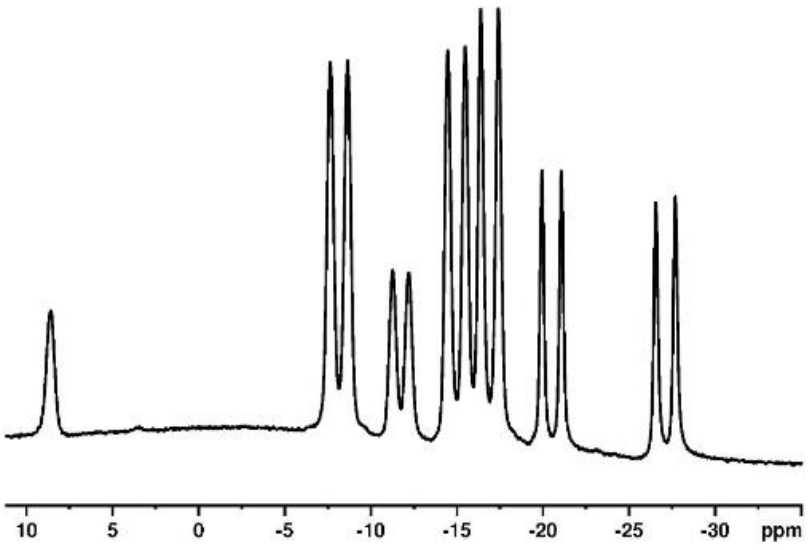

Figure 2.S6. ^{11}B NMR of 9-OH-*m*-carborane.

9-SH-*o*-carborane (O9SH): Synthesis adapted from Herňańek and collegues along with Mirkin and collegues.[35,36] To a suspension of *o*-carborane (1.44 g, 10.0 mmol) and $AlCl_3$ (1.33 g, 10.0 mmol) in 30 mL of anhydrous dichloromethane at -78 °C, a solution of sulfur monochloride (0.40 mL, 5.0 mmol) in anhydrous dichloromethane (5 mL) was added dropwise under an inert atmosphere. The reaction mixture was stirred at room temperature overnight. Then, the reaction mixture was quenched with water, the organic phase was separated from the aqueous phase, the organic layers were combined and the solvent was removed under reduced pressure. The resulting solids were resuspended in concentrated HCl prior to the careful introduction of zinc dust. After stirring overnight at room temperature, the reaction mixture was quenched with water and the resulting precipitates were filtered and purified via sublimation at 130 °C followed by silica gel column chromatography using 1:1 CH_2Cl_2:hexanes as the eluent. The product containing fractions were combined and solvent removed under reduced pressure to yield a white solid (**Figures 2.S7 and 2.S8**).

Yield: 194 mg (12%). ^{1}H NMR (400 MHz, CD_2Cl_2): δ 0.42(d, ^{2}JB-H = 4.05 Hz 1H, S-H), 1.6-3.1 (m, 9H, B-H), 3.5 (s, 1H, $C_{carborane}$ -H), 3.7 (s, 1H, $C_{carborane}$ -H); ^{1}B {^{1}H} NMR (128 MHz): δ -1.5 (1B), -8.0 (2B), -13.3 (2B), -14.3 (3B), -15.3 (2B).

Nuclear Magnetic Resonance Spectroscopy

^{1}H and ^{11}B NMR spectra were recorded on AV 500 and AV 400 spectrometers in ambient conditions at 298 K. Bruker Topspin V3.5 software was used to process the FID data and visualize the spectra. ^{1}H NMR spectra were referenced to residual solvent resonances in

deuterated solvents and are reported relative to tetramethylsilane (δ = 0 ppm). ^{11}B NMR spectra were referenced to $Et_2O{\cdot}BF_3$ in a sealed capillary (δ = 0 ppm).

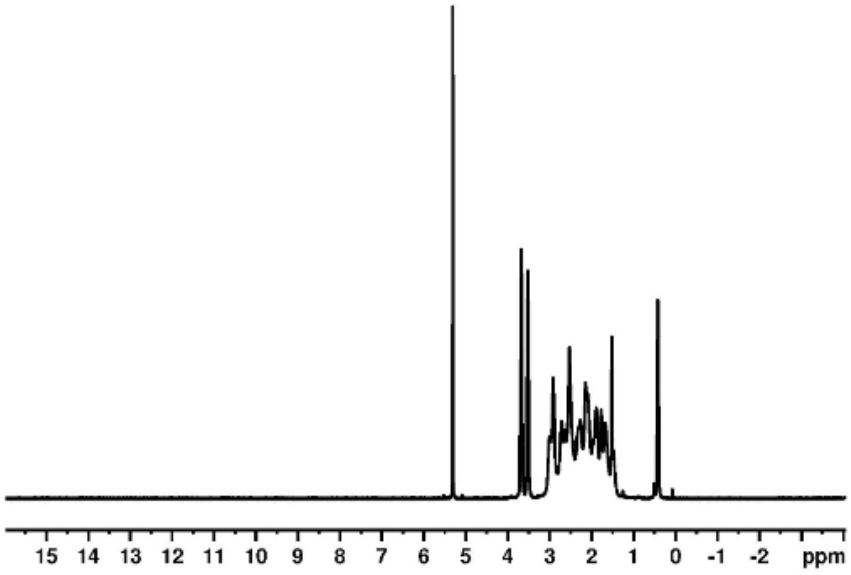

Figure 2.S7. ^1H NMR of 9-SH-*o*-carborane in CD_2Cl_2.

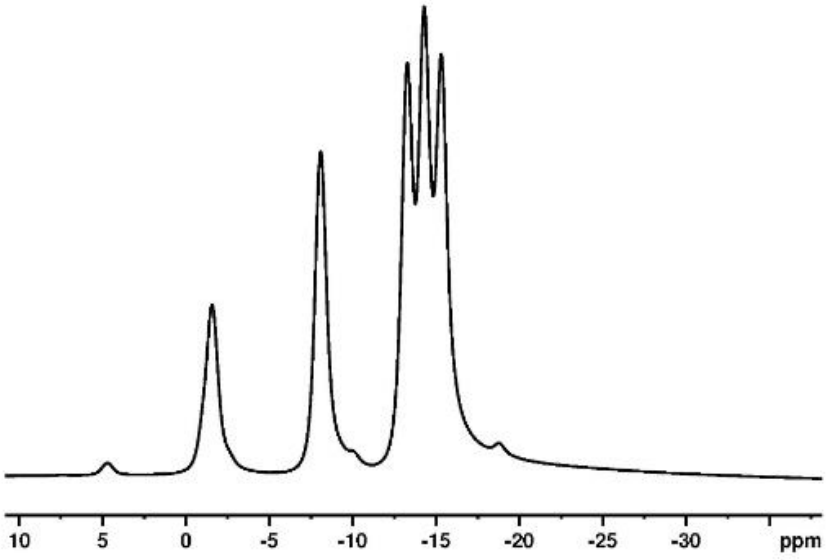

Figure 2.S8. ^{11} B {^{1}H}NMR of 9-SH-*o*-carborane.

2.E.2 X-Ray Photoelectron Spectra

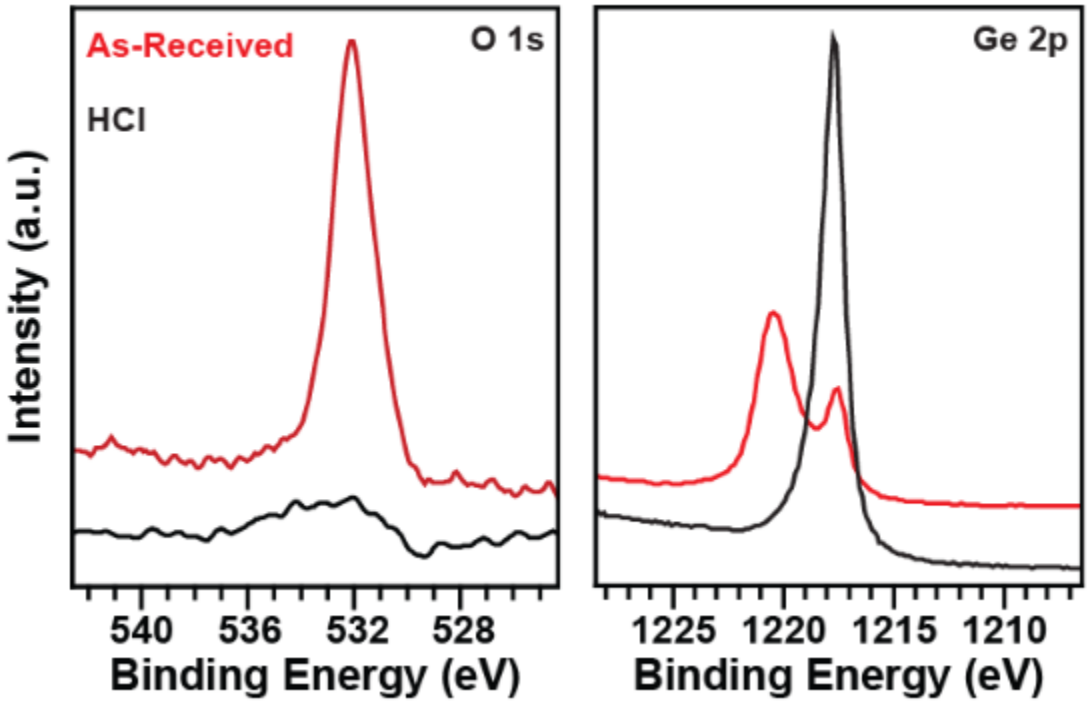

Figure 2.S9. High-resolution X-ray photoelectron spectroscopy highlighting the O 1s and Ge 2p regions for as-received (red trace) and H_2O_2/hydrochloric acid treated (HCl, black trace) Ge(100) wafers.

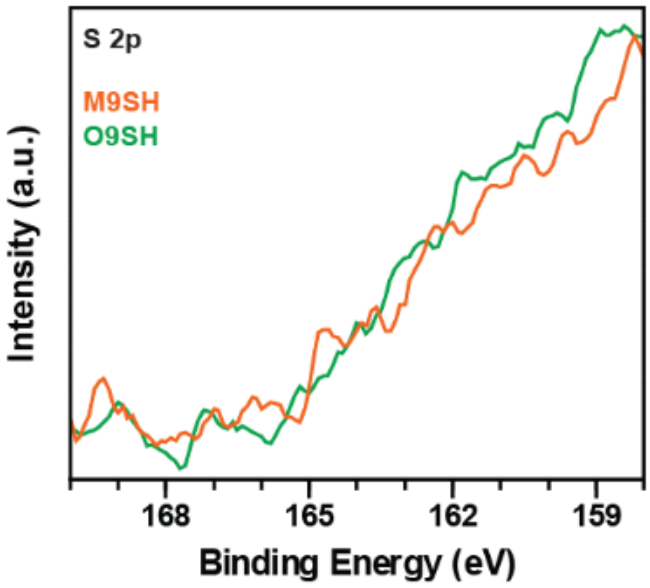

Figure 2.S10. X-ray photoelectron spectroscopy of M9SH and O9SH on Ge(100), highlighting the S 2p region. Any signal from the presence of sulfur is below instrument detection limits.

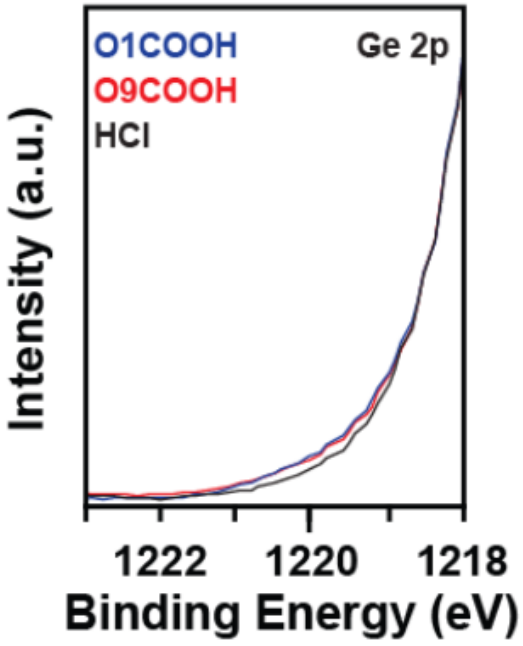

Figure 2.S11. High-resolution X-ray photoelectron spectroscopy highlighting the Ge 2p peak onset for 1-COOH-*o*-carborane (O1COOH, blue trace), 9-COOH-*o*-carborane (O9COOH, red trace), and chlorine (HCl, black trace) on Ge(100).

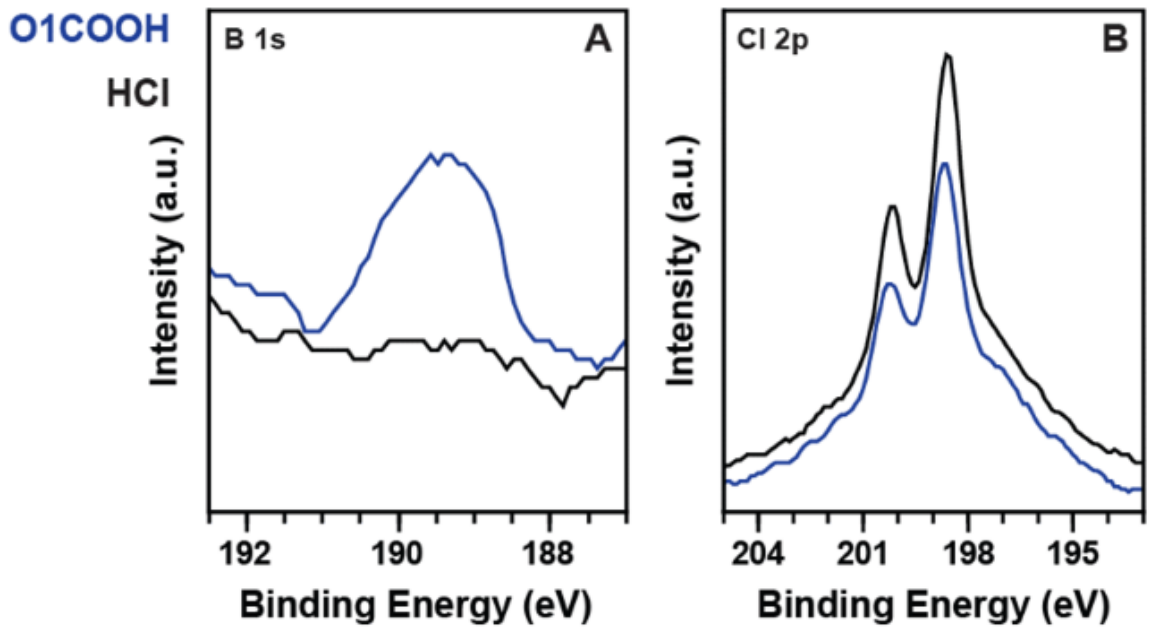

Figure 2.S12. X-ray photoelectron spectroscopy of 1-COOH-*o*-carborane (O1COOH, blue trace) and chlorine (HCl, black trace) modified Ge(111). (A) The B 1s region shows that O1COOH is present and (B) the Cl 2p region shows a relative decrease in intensity of Cl between Cl-passivated and O1COOH-passivated surfaces.

Table 2.S1. Summation of peak positions from X-ray photoelectron spectroscopy of hydrochloric acid-etched (HCl), 1-COOH-*o*-carborane (O1COOH), and 9-COOH-*o*-carborane (O9COOH) -passivated Ge(100) surfaces.

	B 1s	**O 1s**	**Ge 2p**	**Cl $2p_{1/2}$**	**C 1s**
HCl	–	–	1217.7 eV	198.6 eV	284.5 eV 286.0 eV
O1COOH	189.6 eV	531.7 eV	1217.7 eV	198.7 eV	284.8 eV 286.4 eV 288.5 eV
O9COOH	189.7 eV	531.6 eV	1217.7 eV	198.6 eV	284.8 eV 286.5 eV 288.2 eV

Table 2.S2. Percent elemental concentration of 1-COOH-*o*-carborane (O1COOH) and 9-COOH-*o*-carborane (O9COOH) on Ge(100).

	Ge 2p	O 1s	C 1s	Cl 2p	B 1s
O1COOH	86.40%	5.70%	7.10%	0.40%	0.50%
O9COOH	81.00%	7.80%	9.30%	1.60%	0.40%

2.E.3 Ultraviolet Photoelectron Spectroscopy

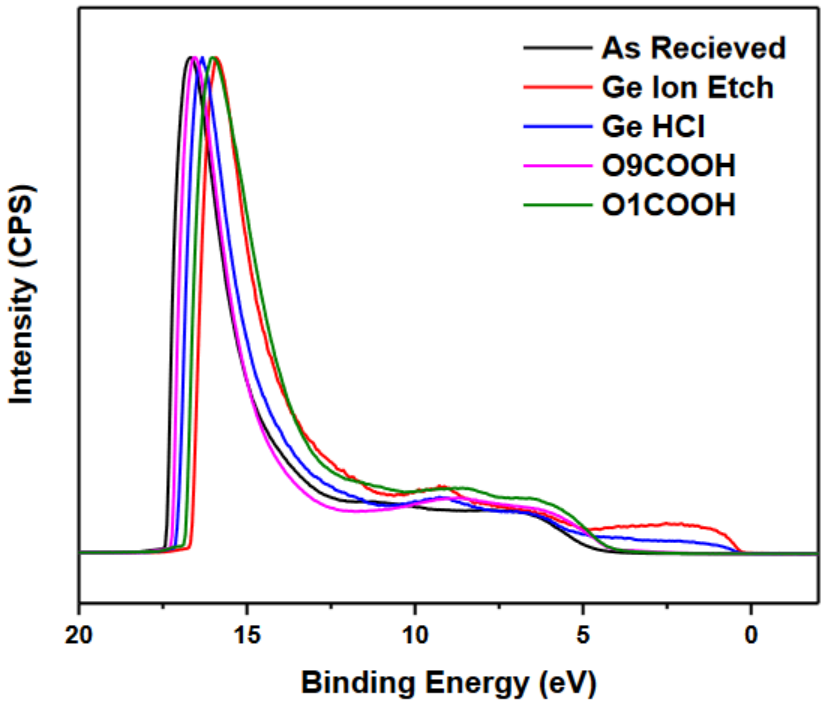

Figure 2.S13. Full ultraviolet photoelectron spectra of a new (as received, black trace), Ar-ion-etched (Ge Ion Etch, red trace), hydrochloric acid-etched (Ge HCl, blue trace), o-*9*-carborane carboxylic acid-passivated (O9COOH, pink trace), and o-*1*-carborane carboxylic acid-passivated (O1COOH, green trace) Ge(100) wafer surfaces.

2.E.4 Density Functional Theory Calculations

Table 2.S3. Dipole magnitudes and orientations calculated using density functional theory

O1	Dipole	[x]	[y]	[z]
SH				
PBE-D3(BJ)	3.75	0.69761753	-2.02337790	3.08190783
B3LYP-D3(BJ)	3.76	0.69857707	-2.03926806	3.07998822
PBE0	3.80	0.72607085	-2.05040678	3.12155451
M06	3.76	0.68633331	-1.96946353	3.13057304
COOH				
PBE-D3(BJ)	3.36	0.02519714	-0.67689966	3.29034758
B3LYP-D3(BJ)	3.24	-0.01342170	0.65789447	3.17322952
PBE0	3.37	0.01805419	-0.66460536	3.30156895
M06	3.37	0.00588162	-0.63440538	3.31077017
O9	**Dipole**	**[x]**	**[y]**	**[z]**
SH				
PBE-D3(BJ)	5.24	0.64446826	-2.36186256	4.63162036
B3LYP-D3(BJ)	5.44	0.65385386	-2.37582172	4.85123856
PBE0	5.43	0.69030422	-2.38601933	4.83088071
M06	5.11	0.59454144	-1.92794277	4.69062735
COOH				
PBE-D3(BJ)	5.02	-0.94344730	-1.43560061	4.71673395
B3LYP-D3(BJ)	5.04	-0.68261308	-1.15677534	4.95928961
PBE0	5.17	-0.89359993	-1.31769858	4.91653076
M06	4.97	-0.83310996	-1.20083782	4.74997079
M1	**Dipole**	**[x]**	**[y]**	**[z]**
SH				
PBE-D3(BJ)	1.96	0.52416668	-1.75154639	0.70188432
B3LYP-D3(BJ)	1.95	0.52204147	-1.76139729	0.66157757
PBE0	1.98	0.54561792	-1.77090327	0.68899967
M06	1.81	0.35575413	-1.59927981	0.76714709

M9	Dipole	[x]	[y]	[z]
SH				
PBE-D3(BJ)	3.41	0.38944325	-0.83447575	3.27979973
B3LYP-D3(BJ)	3.59	0.38465372	-0.84122027	3.47001511
PBE0	3.56	0.39787710	-0.82292237	3.43715650
M06	3.46	0.36310995	-0.85397928	3.33393794
Carborane	**Dipole**	**[x]**	**[y]**	**[z]**
ortho-CB				
PBE-D3(BJ)	4.23	0.00035560	-2.23669758	3.58883336
B3LYP-D3(BJ)	4.27	0.00169187	-2.25599379	3.62271532
PBE0	4.31	0.00164996	-2.27739567	3.66292793
M06	4.19	0.00004628	-2.21287112	3.56061348
meta-CB				
PBE-D3(BJ)	2.68	-0.00148343	-2.27703813	1.40894095
B3LYP-D3(BJ)	2.70	-0.00050187	-2.29386751	1.42176463
PBE0	2.73	-0.00002894	-2.32236334	1.43464539
M06	2.65	0.00142062	-2.24758244	1.39847908

Table 2.S4. The vertices that define the origin, Z axis, and YZ plane for DFT dipole moment calculations in the reported carborane molecules.

	[0,0,0]	[0,0,Z]	[0,Y,Z]
O1-R	B(12)	C(1)	C(2)
O9-R	B(9)	C(2)	C(1)
M1-R	B(12)	C(1)	C(7)
M9-R	B(9)	B(2)	B(3)
***o*-carborane**	B(12)	C(1)	C(2)
***m*-carborane**	B(12)	C(1)	C(7)

2.F References

(1) Greiner, M. T.; Helander, M. G.; Tang, W.-M.; Wang, Z.-B.; Qiu, J.; Lu, Z.-H. Universal Energy-Level Alignment of Molecules on Metal Oxides. *Nat. Mater.* **2011**, *11*, 76–81.

(2) He, T.; Ding, H.; Peor, N.; Lu, M.; Corley, D. A.; Chen, B.; Ofir, Y.; Gao, Y.; Yitzchaik, S.; Tour, J. M. Silicon/Molecule Interfacial Electronic Modifications. *J. Am. Chem. Soc.* **2008**, *130*, 1699–1710.

(3) Arefi, H. H.; Nolan, M.; Fagas, G. Role of the Head And/or Tail Groups of Adsorbed−[XHead Group]−Alkyl−[XTail Group] [X = O(H), S(H), NH(2)] Chains in Controlling the Work Function of the Functionalized H:Si(111) Surface. *J. Phys. Chem. C* **2015**, *119*, 11588–11597.

(4) Nishimura, T.; Kita, K.; Toriumi, A. A Significant Shift of Schottky Barrier Heights at Strongly Pinned Metal/Germanium Interface by Inserting an Ultra-Thin Insulating Film. *Appl. Phys. Express* **2008**, *1*, 051406.

(5) Mäkinen, A. J.; Kushto, G. P. Monolayer-Induced Band Bending in the Near-Surface Region of Ge(111). *Phys. Rev. B: Condens. Matter Phys.* **2011**, *83*, 245315.

(6) Hacker, C. A. Modifying Electronic Properties at the Silicon−Molecule Interface Using Atomic Tethers. *Solid-State Electron.* **2010**, *54*, 1657–1664.

(7) Paniagua, S. A.; Hotchkiss, P. J.; Jones, S. C.; Marder, S. R.; Mudalige, A.; Marrikar, F. S.; Pemberton, J. E.; Armstrong, N. R. Phosphonic Acid Modification of Indium−Tin Oxide Electrodes: Combined XPS/UPS/Contact Angle Studies. *J. Phys. Chem. C* **2008**, *112*, 7809–7817.

(8) Zhou, Y.; Fuentes-Hernandez, C.; Shim, J.; Meyer, J.; Giordano, A. J.; Li, H.; Winget, P.; Papadopoulos, T.; Cheun, H.; Kim, J.; Fenoll, M.; Dindar, A.; Haske, W.; Najafabadi, E.; Khan, T. M.; Sojoudi, H.; Barlow, S.; Graham, S.; Brédas, J.-L.; Marder, S. R.; Kahn, A.; Kippelen, B. A Universal Method to Produce Low–Work Function Electrodes for Organic Electronics. *Science* **2012**, *336*, 327–332.

(9) Giordano, A. J.; Pulvirenti, F.; Khan, T. M.; Fuentes-Hernandez, C.; Moudgil, K.; Delcamp, J. H.; Kippelen, B.; Barlow, S.; Marder, S. R. Organometallic Dimers: Application to Work-Function Reduction of Conducting Oxides. *ACS Appl. Mater. Interfaces* **2015**, *7*, 4320–4326.

(10) Kim, J.; Rim, Y. S.; Liu, Y.; Serino, A. C.; Thomas, J. C.; Chen, H.; Yang, Y.; Weiss, P. S. Interface Control in Organic Electronics Using Mixed Monolayers of Carboranethiol Isomers. *Nano Lett.* **2014**, *14*, 2946–2951.

(11) Hohman, J. N.; Zhang, P.; Morin, E. I.; Han, P.; Kim, M.; Kurland, A. R.; Mcclanahan, P. D.; Balema, V. P.; Weiss, P. S. Self-Assembly of Carboranethiol Isomers on Au{111}: Intermolecular Interactions Determined by Molecular Dipole Orientations. *ACS Nano* **2009**, *3*, 527–536.

(12) Grimes, R. N. Carboranes, 3rd ed.; Birtcher, K., Ed.; Academic Press: Cambridge, MA, 2016.

(13) Thomas, J. C.; Schwartz, J. J.; Hohman, J. N.; Claridge, S. A.; Auluck, H. S.; Serino, A. C.; Spokoyny, A. M.; Tran, G.; Kelly, K. F.; Mirkin, C. A.; Gilles, J.; Osher, S. J.; Weiss, P. S. Defect-Tolerant Aligned Dipoles within Two-Dimensional Plastic Lattices. *ACS Nano* **2015**, 9, 4734–4742.

(14) Schwartz, J. J.; Mendoza, A. M.; Wattanatorn, N.; Zhao, Y.; Nguyen, V. T.; Spokoyny, A. M.; Mirkin, C. A.; Baše, T.; Weiss, P. S. Surface Dipole Control of Liquid Crystal Alignment. *J. Am. Chem. Soc.* **2016**, *138*, 5957–5967.

(15) Yan, H.; Hohman, J. N.; Li, F. H.; Jia, C.; Solis-Ibarra, D.; Wu, B.; Dahl, J. E. P.; Carlson, R. M. K.; Tkachenko, B. A.; Fokin, A. A.; Schreiner, P. R.; Vailionis, A.; Kim, T. R.; Devereaux, T. P.; Shen, Z.-X.; Melosh, N. A. Hybrid Metal–organic Chalcogenide Nanowires with Electrically Conductive Inorganic Core through Diamondoid-Directed Assembly. *Nat. Mater.* **2017**, *16*, 349–355.

(16) Hohman, J. N.; Kim, M.; Bednar, H. R.; Lawrence, J. A.; McClanahan, P. D.; Weiss, P. S. Simple, Robust Molecular Self-Assembly on Germanium. *Chem. Sci.* **2011**, *2*, 1334–1343.

(17) Han, S. M.; Ashurst, W. R.; Carraro, C.; Maboudian, R. Formation of Alkanethiol Monolayer on Ge(111). *J. Am. Chem. Soc.* **2001**, *123*, 2422–2425.

(18) Ardalan, P.; Musgrave, C. B.; Bent, S. F. Formation of Alkanethiolate Self-Assembled Monolayers at Halide-Terminated Ge Surfaces. *Langmuir* **2009**, *25*, 2013–2025.

(19) Loscutoff, P. W.; Bent, S. F. Reactivity of the Germanium Surface: Chemical Passivation and Functionalization. *Annu. Rev. Phys. Chem*. **2006**, *57*, 467–495.

(20) Ardalan, P.; Sun, Y.; Pianetta, P.; Musgrave, C. B.; Bent, S. F. Reaction Mechanism, Bonding, and Thermal Stability of 1-Alkanethiols Self-Assembled on Halogenated Ge Surfaces. *Langmuir* **2010**, *26*, 8419–8429.

(21) Kachian, J. S.; Bent, S. F. Sulfur versus Oxygen Reactivity of Organic Molecules at the Ge(100)-2 × 1 Surface. *J. Am. Chem. Soc*. **2009**, *131*, 7005–7015.

(22) Lin, T.-H.; Lin, B.-Y.; Hao, T.; Chien, H.-Y.; Wang, J.-H.; Hung, W.-H. Adsorption and Thermal Reaction of Short-Chain Alcohols on Ge(100). *J. Phys. Chem. C* **2013**, *117*, 2760−2768.

(23) Filler, M. A.; Van Deventer, J. A.; Keung, A. J.; Bent, S. F. Carboxylic Acid Chemistry at the Ge(100)-2 × 1 Interface: Bidentate Bridging Structure Formation on a Semiconductor Surface. *J. Am. Chem. Soc.* **2006**, *128*, 770−779.

(24) Hwang, E.; Kim, D. H.; Hwang, Y. J.; Kim, A.; Hong, S.; Kim, S. Bidentate Structures of Acetic Acid on Ge(100): The Role of Carboxyl Oxygen. *J. Phys. Chem. C* **2007**, *111*, 5941−5945.

(25) Hwang, E.; Jung, S. J.; Kim, S.; Kim, D. H. Chemical Reaction of Benzoic Acid with Ge(100): Effect of a Phenyl Substituent. *J. Phys. Chem. C* **2016**, *120*, 14742−14748.

(26) Baše, T.; Bastl, Z.; Plzák, Z.; Grygar, T.; Plešek, J.; Carr, M. J.; Malina, V.; Šubrt, J.; Večerníková, J. B. E.; Kříž, O. Carboranethiol-Modified Gold Surfaces. A Study and Comparison of Modified Cluster and Flat Surfaces. *Langmuir* **2005**, *21*, 7776−7785.

(27) Bodlaki, D.; Yamamoto, H.; Waldeck, D. H.; Borguet, E. Ambient Stability of Chemically Passivated Germanium Interfaces. *Surf. Sci.* **2003**, *543*, 63−74.

(28) Cai, Q.; Xu, B.; Ye, L.; Tang, T.; Huang, S.; Du, X.; Bian, X.; Zhang, J.; Di, Z.; Jin, Q.; Zhao, J. Stable Functionalization of Germanium Surface and Its Application in Biomolecules Immobilization. *Appl. Surf. Sci.* **2014**, *316*, 46−53.

(29) DiBenedetto, S. A.; Facchetti, A.; Ratner, M. A.; Marks, T. J. Molecular Self-Assembled Monolayers and Multilayers for Organic and Unconventional Inorganic Thin-Film Transistor Applications. *Adv. Mater.* **2009**, *21*, 1407−1433.

(30) Bregadze, V. I. Dicarba-Closo-Dodecaboranes $C_2B_{10}H_{12}$ and Their Derivatives. *Chem. Rev.* **1992**, *92*, 209−223.

(31) Kasar, R. A.; Knudsen, G. M.; Kahl, S. B. Synthesis of 3-Amino-1-carboxy-o-carborane and an Improved, General Method for the Synthesis of All Three C-Amino-C-Carboxycarboranes. *Inorg. Chem*. **1999**, *38*, 2936-2940.

(32) Craciun, L.; Custelcean, R. Syntheses and Crystal Structures of 9-Acetyl- and 9-Cyano-1,2-dicarbadodecaborane: Supramolecular Association in Carboranyl C−H Hydrogen-Bonded α-Networks. *Inorg. Chem*. **1999**, *38*, 4916-4919.

(33) Zakharkin, L. I.; Kovredov, A. I.; Olshevskaya, V. A.; Shaugumbekova, Z. S. Synthesis of B-Organo-substituted 1,2-, 1,7-, and 1,12-Dicarbaclosododecaboranes(12). *J. Organomet. Chem.* **1982**, *226*, 217-222.

(34) Dziedzic, R.; Saleh, L.; Axtell, J.; Martin, J.; Stevens, S.; Royappa, A.; Rheingold, A.; Spokoyny, A. M. B−N, B−O, and B−CN Bond Formation via Palladium-Catalyzed Cross-Coupling of B-Bromo-Carboranes. *J. Am. Chem. Soc.* **2016**, *138*, 9081-9084.

(35) Plešěk, J.; Janouměk, Z.; Herŕmańek, S. Synthesis and Properties of Some Icosahedral Carborane B,B'-Dithiols. Collect. Czech. *Chem. Commun*. **1980**, *45*, 1775−1779.

(36) Spokoyny, A. M.; Machan, C. W.; Clingerman, D. J.; Rosen, M. S.; Wiester, M. J.; Kennedy, R. D.; Stern, C. L.; Sarjeant, A. A.; Mirkin, C. A. A Coordination Chemistry Dichotomy for Icosahedral Carborane-Based Ligands. *Nat. Chem.* **2011**, *3*, 590−596.

(37) Velde, G. te; Bickelhaupt, F. M.; Baerends, E. J.; Fonseca Guerra, C.; van Gisbergen, S. J. A.; Snijders, J. G.; Ziegler, T. Chemistry with ADF. *J. Comput. Chem*. **2001**, *22*, 931-967.

(38) Fonseca Guerra, C.; Snijders, J. G.; te Velde, G.; Baerends, E. J. Towards an Order-N DFT Methods. *Theor. Chem. Acc.* **1998**, *99*, 391-403.

(39) ADF2014, SCM, Theoretical Chemistry, Vrije Universiteit, Amsterdam, The Netherlands, http://www.scm.com.

(40) Grimme, S.; Huenerbein, R.; Ehrlich, S. On the Importance of the Dispersion Energy for the Thermodynamic Stability of Molecules. *Chem. Phys. Chem.* **2011**, *12*, 1258-1261.

(41) Perdew, J. P.; Burke, K.; Ernzerhof, M. General Gradient Approximation Made Simple. *Phys. Rev. Lett.* **1996**, *77*, 3865-3868.

(42) Lee, C.; Wang, W.; Parr, R. G. Development of the Colle-Salvetti Correlation-energy Formula into a Functional of the Electron Density. *Phys. Rev. B* **1998**, *37*, 785-789.

(43) Becke, A. D. Density-functional Thermochemistry. III. The Role of Exact Exchange. *J. Chem. Phys.* **1993**, *98*, 5648-5652.

(44) Stephens, P. J.; Devlin, F. J.; Chabalowski, C. F.; Frisch, M. J. Ab Initio Calculation of Vibrational Absorption and Circular Dichroism Spectra Using Density Functional Force Fields.

J. Phys. Chem. **1994**, *98*, 11623-11627.

(45) Adamo, C.; Barone, V. Toward Reliable Density Functional Methods Without Adjustable Parameters: The PBE0 Model. *J. Chem. Phys.* **1999**, *110*, 6158-6170.

(46) Zhao, Y.; Truhlar, D. G. The M06 Suite of Density Functional for Main Group Thermochemistry, Thermochemical Kinetics, Noncovalent Interactions, Excited States, and Transition Elements: Two New Functionals and Systematic Testing of Four M06-class Functionals and 12 Other Functionals. *Theor. Chem. Acc.* **2008**, *120*, 215-241.

CHAPTER 3

Lipid-Bicelle-Coated Microfluidics for Intracellular Delivery with Reduced Fouling

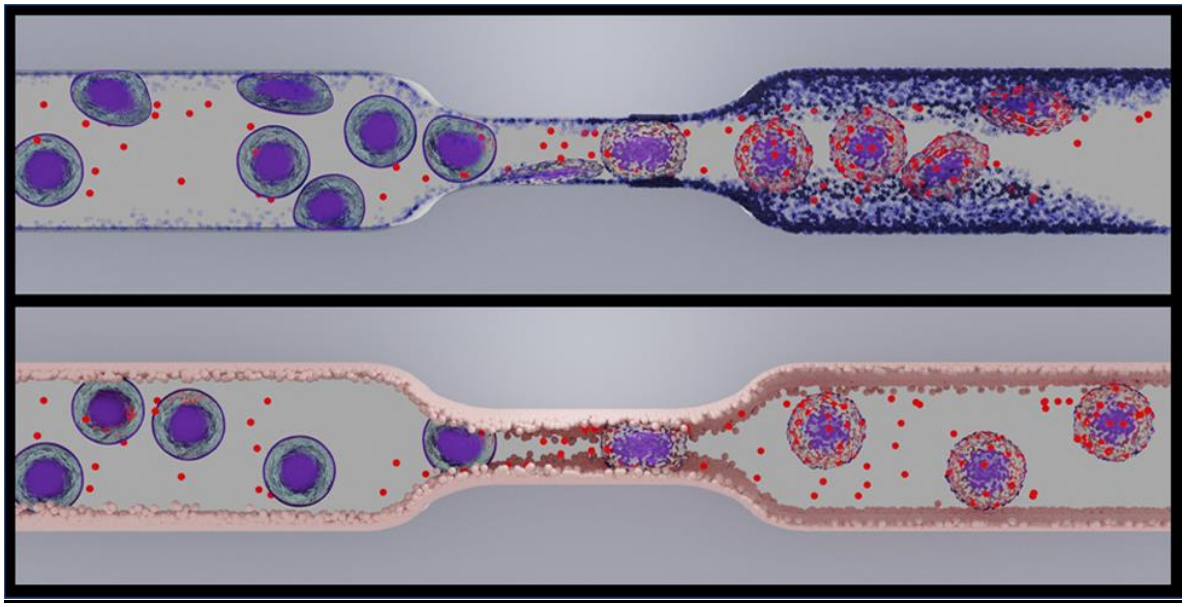

The information in this chapter was published in
ACS Applied Materials & Interfaces **2020**, *12*, 45744–45752 and is reproduced here with permission.

Authors: Belling, J. N.; **Heidenreich, L. K.**; Park, J. H.; Kawakami, L. M.; Takahashi, J.; Frost, I. M.; Gong, Y.; Young, T. D.; Jackman, J. A.; Jonas, S. J.; Cho, N. J.; Weiss, P. S.

3.A Introduction

Technology to transfect cells with genetic material has developed to include non-viral methods. These approaches are advantageous in that they circumvent the potential safety limitations and high costs of using viral vectors.[1] Some of the noninvasive gene-editing approaches that have gained in popularity include electroporation, sonoporation, which use electric fields and ultrasound, respectively, and platforms that physically squeeze cells.[2–4] Cell squeezing platforms have high throughput in that they send a large number of cells through a microfluidic channel. In work by Sharei *et al*., transfection was achieved when the cell diameter was larger than the width of the constriction in the microfluidic channel, which resulted in transient pores in the membrane through which the genetic material enters.[5] Using this mechanism, a range of material including DNA, RNA, and carbon nanotubes was delivered and the device could operate with a throughput of approximately 20,000 cells/s, outputting on the order of 1 million cells. The device lifetime is limited by cellular debris adhering to the sidewalls of the microfluidic constriction, which stops flow through the channel. With this clogging occurring over time, throughput was increased by adding more channels in parallel.[5]

Another variant of cell squeezing used a combination of both physical and electrical permeabilization to promote diffusion of plasmids into cells while increasing viability by using a faster flow rate. In this work, Ding *et al.* found that combining these two techniques enabled a greater degree of transfection and increased the amount and type of cargo that could be introduced to mammalian cells.[6] In Chapter 4, an alternative high-throughput strategy to deliver plasmids to human primary cells using an acoustofluidic sonoporation platform that maintains high levels of cell viability will be discussed.[7] Additional studies of

these physical transfection devices have shown their utility for studying membrane repair and for gene-editing and therapeutic applications.[8-11] Although there have been dramatic improvements in the permeabilization of cellular membranes with physical methods, most microfluidic designs remain limited by the fouling of the channel walls by cells and their secreted proteins. This fouling is due to the hydrophobicity of the channel materials that are typically combinations of polydimethylsiloxane (PDMS) and glass/silica, which are inexpensive and easy to fabricate with micron-scale features using lithography.[12,13] As such, the development of surface coatings that are biomimetic and prevent nonspecific adsorption of cells would increase microfluidic channel lifetime and throughput, independent of the application. A passivating layer would also increase the fraction of the biomolecules delivered to cells instead of adsorbed on the PDMS, improving control of the concentrations and delivery of biomolecular payloads.[14]

Indeed, a variety of approaches has been used to prevent nonspecific cell fouling in PDMS microchannels. An intuitive strategy is to examine the steric constraints on the system. For example, a "ratchet geometry" in the microfluidic channel can generate an oscillatory flow to sort and to separate circulating tumor cells according to their different deformability, with clogging occurring only when the device volume is filled.[15] A more common method is to use poly(ethylene glycol) polymer coatings to prevent fouling on PDMS and glass surfaces.[16] Others have used surfactant treatments, such as pluronic F68 or slippery liquid-infused porous surface(s) (SLIPS), to prevent protein adsorption and fibroblast adhesion to PDMS surfaces.[13,17] Self-assembled monolayers (SAMs) of siloxanes have also been used for preventing surface interactions between cells and proteins inside microfluidics. However, siloxane-based SAMs are difficult to characterize inside microfluidic channels due to the

indirect methods required to assess SAM uniformity, such as measuring functionalized flat substrates and extrapolating the coating thickness and uniformity to the interior of the channels.[18] Therefore, designing a system that enables *direct* characterization of the channel walls would be advantageous for engineering the physicochemical properties of uniform channel coatings.

Lipids can be coupled with fluorophores, have lateral mobility when configured into bilayer assemblies, and have controllable compositions that can be tailored to have a wide range of electrostatic or chemical interactions.[19-22] Exploiting these properties, the uniformity of supported lipid bilayers can be characterized using fluorescence microscopy and can be prepared simply with lipid bicelles as precursors. In previous work, coating channels with lipid bilayers increased resistance to antibody and protein adsorption by two orders of magnitude compared to bare surfaces, with the bilayers being stable for several weeks.[23,24] Other strategies for coatings include bovine serum albumin (BSA) passivation, since BSA is known to prevent nonspecific protein adsorption to surfaces. Chiu *et al.* utilized the non-adhesive nature of BSA coatings to make confluent patterns of cells in microfluidic channels.[25] It was demonstrated that cells do not adhere to bilayers in BSA-containing media.[25] However, the use of animal serum can stimulate fibronectin and vitronectin binding, resulting in integrin-dependent cell adhesion.[26] Supported lipid membranes can be designed to have protein-rich environments to mimic the rigidity of extracellular matrix and can be used as effective cell-culture platforms.[27,28] In applications where whole blood or protein-containing serum is needed, there may be nonspecific binding events that occur with the fabricated lipid membranes. Nevertheless, Persson *et al.* demonstrated that lipid bilayer coatings in nanofluidic channels outperformed BSA passivation in preventing interactions

between streptavidin-coated quantum dots, RecA proteins, and RecA-DNA complexes.[29] Groves *et al.* found that phospholipid bilayers patterned in corrals had no adhesion to HeLa cells except for lipid membranes containing phosphatidylserine.[30] Andersson *et al.* followed this work and showed supported lipid bilayers to be effective in preventing cell adhesion on SiO_2 and glass, even in protein-rich environments using egg yolk phosphatidylcholine.[31] Since phospholipid bilayers formed on solid supports prevent nonspecific protein and cell adhesion, have direct methods of characterization, and are naturally occurring in biological membranes, these molecules are excellent candidates for developing biomimetic engineering strategies to suppress cellular interactions with channel surfaces.

Here, we develop an anti-fouling passivation strategy for microfluidic channels that utilizes bicelle-mediated rupture to form a lipid bilayer coating. This coating can significantly reduce the nonspecific adsorption of protein and cell adhesion to microfluidic channel walls. This coating strategy was applied to microchannels with cell squeeze constrictions, which significantly reduced the accumulation of cell debris in the channels. We further tested the intracellular delivery performance of these coated microfluidic constrictions using 40 kDa fluorescently labeled dextran and an enhanced green fluorescent protein-expressing plasmid (eGFP) and observed successful intracellular delivery and protein expression with viability exceeding 70% for all samples. Taken together, this passivation strategy has great potential for reducing protein adsorption and cell attachment for a myriad of microfluidic applications.

3.B Experimental Methods

3.B.1 Bicelle Preparation Protocol

All lipids including 1,2-dioleoyl-*sn*-glycero-3-phosphocholine (DOPC), 1,2-dihexanoyl-*sn*-glycero-3-phosphocholine (DHPC), 1,2-dipalmitoyl-*sn*-glycero-3-phosphoethanolamine-*N* -(lissamine rhodamine B sulfonyl) were purchased from Avanti Polar Lipids. Small aliquots (1 mg) of DOPC and DHPC dissolved in chloroform were dried separately in test tubes under a gentle stream of nitrogen, while being rotated to make a lipid film at the bottom of the tube and the dried lipid film was placed in a vacuum desiccator overnight. Next, the DOPC film was hydrated in an aqueous TRIS (*tris*(hydroxymethyl)aminomethane) buffer (10 mM TRIS, 150 mM NaCl, pH 7.5) to a concentration of 63 μM to make a DOPC stock solution. The DOPC solution was subsequently used to hydrate the DHPC film to a final concentration of 252 μM, such that the molar ratio ("q-ratio") DOPC:DHPC is 0.25 between long- and short-chain lipids. The DOPC/DHPC mixture was transferred to a 50 mL falcon tube and a small hole was punctured on the top using a syringe needle to alleviate pressure. The sample was plunged into liquid nitrogen for 1 min, followed by 5 min incubation in a 60 °C water bath (prepared on a hotplate prior to hydration) and vortexing for 30 s. This freeze-thaw-vortex cycle was repeated five times.

3.B.2 Microfluidic Device Fabrication

Glass substrates were cleaned with piranha etch (piranha solution is a 3:1 mixture of concentrated sulfuric acid with 30% hydrogen peroxide). It is a corrosive liquid and strong oxidizer. Proper safety precautions should be applied before use followed by sonication in Millipore deionized water (18.2 MΩ·cm) for 5 cycles of 5 min. Polydimethylsiloxane channels

were fabricated with different dimensions, depending on the application. For fluidic devices designed to characterize lipid bilayer formation, straight channels were formed with a 2 mm × 27.5 mm × 0.05 mm silica mold that was fabricated using dry reactive etching. Constricted microfluidic channels for cell squeezing were designed to have a channel width of 25 μm that constricts to 5 μm for a 50 μm distance and expands back to 25 μm with a total volume of 2 mm × 25 μm × 30 μm in the expanded regions. Inlets and outlets were formed using a 0.75 mm biopsy punch (Robbins) to make small holes in the PDMS. The PDMS channels and glass substrates were exposed to an oxygen plasma (Harrick Plasma) for 90 s, at a power of 18 W with a chamber pressure of 10 psi, and were bound together immediately after being removed from the plasma chamber. The assembly was then placed in an oven set to 130 °C overnight. This plasma treatment and heating process enables a condensation reaction to occur between the plasma-activated glass and PDMS surfaces to form a covalent bond, sealing the microfluidic device. Polyethylene tubing (PE-50, Instech) was inserted into the inlet and outlet holes to form a tight.

3.B.3 Bilayer Formation

Rectangular microfluidic channels were initially hydrated with TRIS buffer for 10 min using a syringe pump (Chemyx Fusion 3000) with a flow rate of 20 μL/min. Bicelles or fluorescently labeled bicelles (where the long chain lipid consists of 99.5 mol % DOPC and 0.5 mol % 1,2-dipalmitoyl-*sn*-glycero-3-phos-phoethanolamine-*N*-(lissamine rhodamine B sulfonyl) lipid) were then flowed into the device with a flow rate of 20 μL/min for 30 min. In the constricted microfluidic channels, bilayer formation was significantly slower and required a flow rate of 5 μL/min for 12 h to ensure uniform coverage in the device. Lipid

bilayer formation was confirmed using fluorescence microscopy (Axio Observer Z1, Zeiss). This process was followed by a washing step with a constant flow of TRIS buffer (20 μL/min), for another 30 min. Note that maintenance of channel hydration was carefully monitored after the addition of each solution. If air bubbles were observed to enter the channel, the bilayer would be damaged and the formation protocol would have to be repeated to ensure a uniform bilayer coating.

3.B.4 Protein Adsorption Protocol

After washing the bilayer-coated channel with TRIS buffer, fluorescein isothiocyanate bovine serum albumin (FITC-BSA, Sigma) was prepared in TRIS at a concentration of 0.3 mg/mL and was flowed through channels at 20 μL/min for 30 min. The channels were subsequently washed with TRIS using a flow rate of 50 μL/min for 30 min. Protein adsorption on the channel walls was determined using fluorescence microscopy and taking micrographs of the assembled channel, and the PDMS and glass components after separating the two carefully with a razor blade. Relative fluorescence intensity of adsorbed FITC-BSA on each surface was quantified using ImageJ.[32]

3.B.5 Cell Culture

Jurkat cells (ATCC) and K562 3.21 cells generously provided by the Donald Kohn lab at UCLA were cultured in 1× RPMI 1640 with L-glutamine (Gibco) supplemented with 10% fetal bovine serum (Gibco) and 1% penicillin-streptomycin (10,000 units/mL penicillin and 10 mg/mL streptomycin) (Gibco). Human embryonic kidney cells (HEK 293T) were previously transfected to express fluorescent mitochondria as described previously[33] and were cultured using 1× Dulbecco's Modified Eagle Medium (DMEM) modified with D-glucose

and L-glutamine (Gibco) supplemented with 10% fetal bovine serum and 1% penicillin-streptomycin.

3.B.6 Cell Adhesion and Clogging

Jurkat cells and human embryonic kidney cells with fluorescent mitochondria were provided by the Satiro De Oliveira and Michael Teitell labs at UCLA, respectively. Jurkat cell nuclei were labeled with Hoescht 33342 (Sigma) by adding 1 μL of 1 mg/mL Hoescht solution to Jurkat cells in 1 mL of cell culture media. The cell mixtures were incubated for 15 min at 37 °C and were used immediately for the following steps. Irrespective of the cell type, fluorescent cells suspended in a cell culture medium were collected via centrifugation at 500× *g* for 5 min. The cell pellet was collected and dispersed in 1× phosphate-buffered saline solution (PBS, 137 mM NaCl, 2.7 mM KCl, 10 mM Na_2HPO_4, 1.8 mM KH_2PO_4, Gibco) at concentrations of 1, 10, or 100 million cells/mL and flowed into the characterization device using a syringe pump with a flow rate of 20 μL/min. Adhesion was quantified using fluorescence microscopy after washing with PBS buffer at 50 μL/min for 30 min. Cell adhesion was assessed by counting the cells that remained in the channel with ImageJ. For analyses of cell clogging in constricted microfluidic devices, Jurkat cells were dispersed in PBS buffer at 10 million cells/mL and flowed at 200 μL/min followed by a wash step at the same flow rate. Channel clogging was monitored by light microscopy and the area of cell debris remaining in the microfluidic device was quantified using ImageJ.[32]

3.B.7 Intracellular Delivery

Post-bilayer formation constricted microfluidic devices were pre-washed with 1× PBS at a flow rate of 50 μL/min for 15 min. Cells were then dispersed at a density of

5 million cells/mL in a delivery medium consisting of 1% (v/v) Pluronic F-68 (Gibco), 1× PBS, passed through a 40 μm mesh cell strainer (Fisher) and collected into a 50 mL falcon tube (Thermo Fisher). Next, a final concentration of 0.1 mg/mL of eGFP-expressing plasmid (pCMV-GFP, Plasmid #11153, Addgene) or 0.3 mg/mL of 40kDa fluorescein-isothiocyanate-labeled dextran (Invitrogen) was added to the delivery medium and collected into a 1 mL syringe. Cells were flowed through the microfluidic constrictions at 200 μL/min. An additional wash step of 1× PBS for 5 min followed and cells were incubated in the delivery medium for 10 min to facilitate membrane recovery and biomolecule diffusion. Cells were centrifuged at 500 *g* for 5 min and dispersed in their respective culture media for further analyses. Viability was determined using a Cell Countess II (Invitrogen) and 0.4% trypan blue (Invitrogen).

3.B.8 Flow Cytometry

Flow cytometry data were acquired and processed using an LSR Fortessa cytometer (BD Biosciences). Data analyses were performed using FlowJo software (FlowJo LLC). Fluorescence emission was stimulated using a 488 nm, 50 mW laser with a 505 nm long-pass filter and 515/20 nm bandpass filters for detecting green fluorescence.

3.B.9 Statistical and Image Analyses

One-way ANOVA analyses were performed using Origin 9.1 data analysis and graphing software. Student's T-test was performed using GraphPad software. Quantification of cell adhesion utilized Fiji image analysis software.[34]

3.C Results and Discussion

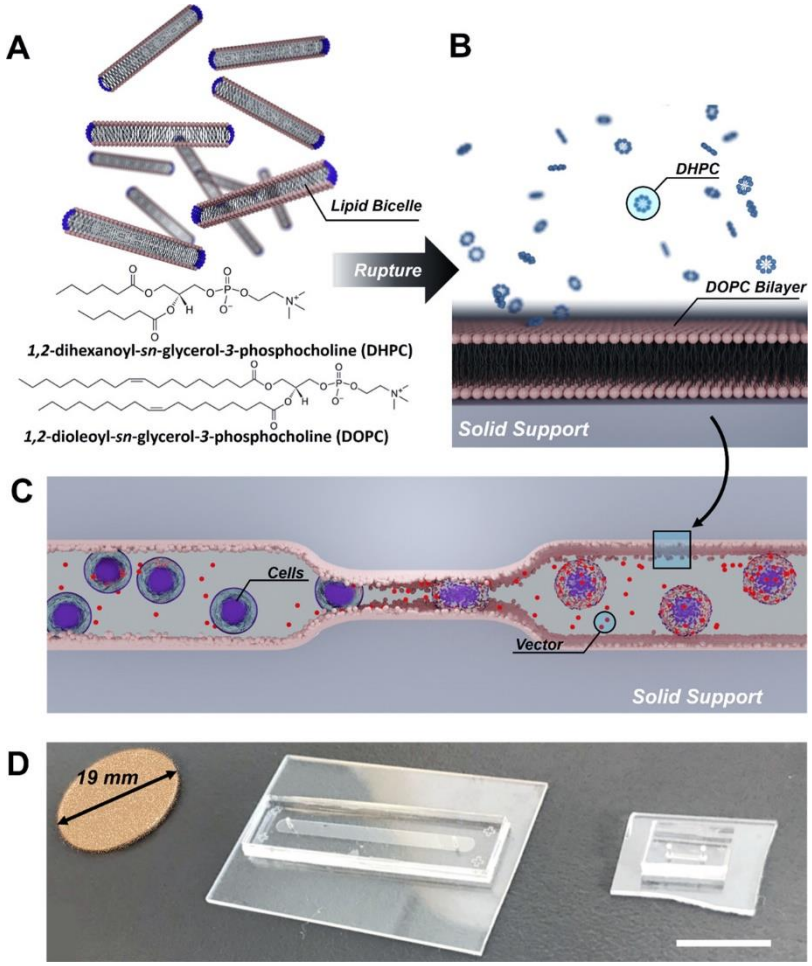

Figure 3.1. Schematic of bilayer formation and lipid bilayer microfluidic devices. **(A)** A schematic of lipid bicelles consisting of long (1,2-dioleoyl-*sn*-glycero-3-phosphocholine, DOPC) and short chain (1,2-dihexanoyl-*sn*-glycero-3-phosphocholine, DHPC) phospholipids. **(B)** Schematic of bicelles rupturing on a solid support to form a supported lipid bilayer, resulting in DHPC monomers and micelles released into the surrounding aqueous solution. **(C)** Schematic of a supported lipid bilayer coating a cell-squeezing device and depiction of cell squeezing. As cells pass through the microfluidic constriction the cells deform, causing transient pore formation and the delivery of biomolecular cargo (red) *via* diffusion. **(D)** Images of the characterization device and lipid-coated squeezing device (penny for scale). **(E)** Image of the characterization channel. **(F)** Image of the cell-squeezing channels. Scale bars are **(D)** 15 mm, **(E)** 500 m, and **(F)** 100 m.

Two different microfluidic devices were designed to evaluate the antifouling behavior of the lipid bilayer coating. First, a rectangular cross section microfluidic channel was used to characterize bilayer formation *via* bicelle-mediated rupture on solid supports and to determine the resistance of the lipid bilayer to nonspecific protein adsorption and cell attachment. Second, ten 5μm constrictions designed to induce cellular deformation for intracellular delivery were utilized to examine fouling in constricted microfluidic devices. (**Figure 3.1A-C**). The constriction dimensions were designed after previous reports that utilized squeezing for the delivery of biomacromolecules with increased accumulation of cell debris. These devices were fabricated using standard soft-lithographic strategies, binding a PDMS microfluidic channel to a clean glass substrate using plasma activation. (**Figure 3.1D-F**). Bicelles were formed using a freeze-thaw-vortex cycle that was optimized by Kohladouzan *et al.* and flowed into the microfluidic channel.[35] To characterize lipid bilayer formation in both devices, fluorescent bicelles were fabricated to have lipid compositions consisting of 1,2-dioleoyl-*sn*-glycero-3-phosphocholine (DOPC), 1,2-dihexanoyl-*sn*-glycero-3-phosphocholine (DHPC), and 1,2-dipalmitoyl-*sn*-glycero-3-phos-phoethanolamine-*N*-(lissamine rhodamine B sulfonyl) (Rhod-PE). Lipid bilayer formation was observed in each microfluidic device but the rate of its formation was found to differ based on channel geometry. Complete bilayer coverage in the rectangular microfluidic channel (**Figure 3.2A-B**) was observed after 45 min of bicelle exposure, whereas constricted microfluidic channels required longer exposure as described in the materials and methods. These lipid bilayer coating protocols were applied to each microfluidic device for fouling and intracellular delivery experiments.

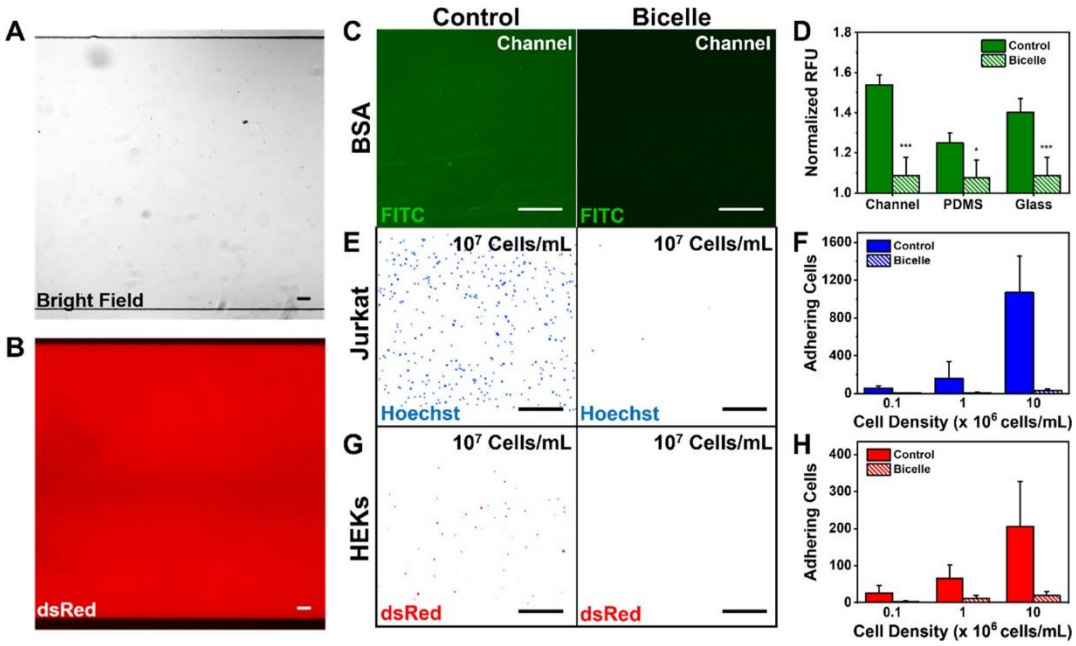

Figure 3.2. Analyses of protein adsorption and cell adhesion in lipid-coated and bare channels. **(A)** Brightfield image and **(B)** fluorescent micrograph of the microfluidic channel after the introduction of fluorescently labeled lipid bicelles. **(C)** Fluorescent micrographs of bare (Control) and bilayer-coated (Bicelle) microfluidic channels after the introduction of fluorescein-isothiocyanate (FITC, green) -labeled bovine serum albumin (FITC-BSA). **(D)** Normalized relative fluorescence intensity of adsorbed FITC-BSA for each component of the microfluidic characterization device including the fully assembled channel (Channel), the polydimethylsiloxane (PDMS), and the glass substrate (Glass) for Bicelle and Control samples. **(E)** Fluorescent micrographs after 10^7 suspension (Jurkat) cells/mL were flowed through the Control and Bicelle channels. **(F)** The number of adhered Jurkat cells as a function of initial cell density. **(G)** Fluorescent micrographs after 10^7 adherent human embryonic kidney cells (HEKs) were flowed in the Control and Bicelle channels. (H) Number of adhered HEKs as a function of initial cell density. Jurkat cell nuclei were stained with Hoechst (blue) before the cells were flowed into the channels. The HEKs were previously transfected to have fluorescently labeled mitochondria (dsRed, red). The data represent N=4 trials with standard deviations for error bars. Statistics were derived using a one-way ANOVA (Origin) and a Tukey test.

Fouling in microfluidics can occur when cells adhere to proteins that are secreted by the cell itself and adsorb to the channel wall. This protein-receptor interaction has been postulated as the primary mechanism for cell adhesion in polymer-based microfluidic

devices.[36,37] To determine the protein resistance of our lipid coating, we analyzed the adsorption of fluorescein-isothiocyanate-labeled BSA (FITC-BSA) on our lipid-coated rectangular microfluidic channel. It has been reported that FITC-BSA can fill in defects in a lipid bilayer due to its strong affinity for silica supports, and can be used as a metric for bilayer uniformity.[38] Initially, FITC-BSA was flowed into lipid bilayer-coated (Bicelle) and bare (Control) characterization devices and protein adsorption was quantified by measuring the fluorescence intensity in the channel (**Figure 3.2C**). These measurements were normalized to the devices' background fluorescence and each component of the microfluidic channel was also measured by separating the PDMS and glass with a razor blade. It was observed that lipid bilayer coatings resulted in >90% reduction in FITC-BSA adsorption on the assembled channel, the PDMS side walls, and the glass substrate (**Figure 3.2D**). This reduced protein adsorption confirmed a highly uniform lipid bilayer with few defects on all surfaces of the microfluidic device, and led to evaluations of cell attachment using our bilayer coating.

Suspension (Jurkat) and adherent (human embryonic kidney) cells were used to quantify cell attachment on both lipid bilayer-coated and bare microfluidic channels. The numbers of cells that attached to the channel walls were quantified using fluorescence microscopy. Jurkat cells were labeled with a live nuclear stain (Hoechst) and human embryonic kidney cells (HEKs) were transfected to have fluorescently labeled mitochondria. Both cell types were flowed into microfluidic channels for 30 min with cell densities ranging from 10^5-10^7 cells/mL. Individual cells were quantified using ImageJ analysis software. It was observed that cell attachment increased with increasing cell density. However, lipid

bilayer coatings resulted in >90% reductions in cell attachment for all cell densities tested and both cell types. (**Figure 3.2E-H**).

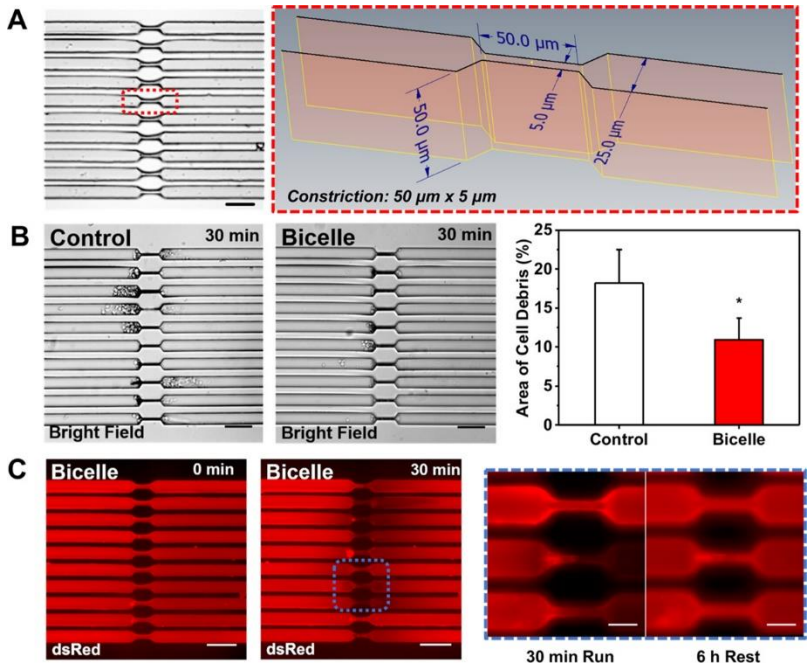

Figure 3.3. Characterization of cell debris in lipid-coated channels. **(A)** Image of the constricted microfluidic channel pre-cell treatment. (Red-dash Inset) Schematic of the microfluidic constriction dimensions. **(B)** Images of the cell-squeezing device post-cell treatment for bilayer-coated (Bicelle) and bare (Control) constricted channels. The percentages of adhered Jurkat cells and cell debris normalized to the device area after 25 million cells were flowed through Bicelle and Control microfluidic channels. **(C)** Fluorescent micrographs of fluorescently labeled bilayer-coated cell squeezing channels (Bicelle, dsRed) pre-cell treatment (0 min) and post-cell treatment (30 min). (Blue-dash Inset) High magnification (40×) fluorescent micrographs of the lipid bilayer-coated microfluidic constriction post-cell treatment and a buffer wash step (30 min Run) and 6 h after incubating the channel in phosphate-buffered saline (6 h Rest). The data represents N=4 trials with standard deviations for error bars. Statistics were derived using a Student's T-test and scale bars are 50 m.

Given our observations of reduced cell attachment with a lipid layer, we applied our lipid bilayer coating strategy to constricted microfluidic devices. Note that the nonspecific adhesion of cells is a major issue for device performance and lifetime and is dependent on the geometry of the device.[39-41] For a device that is designed to have a squeezing dimension,

the rate of cells that can be flowed through the constriction is limited. These constrictions result in objects that are larger than the squeezing dimension to clog and to disrupt flow through the device.[16] We investigated the ability of lipid bilayer coatings to reduce the accumulation of cell debris in our constricted microfluidic channels. Of note, the width of the channel was based on results from Han *et al.* who showed efficient intracellular delivery and high viability in 5-μm channel widths.[42] The length of the channel constriction (50 μm) was selected based on the results of Sharei *et al*. where a large amount of accumulated debris was observed in channels that had lengths larger than 30 μm (**Figure 3.3A**).[5] After 25 million cells were flowed through lipid bilayer-coated and bare microfluidic constrictions, the cell debris were quantified showing an average of 11% and 18% area of cell debris in lipid bilayer-coated and bare channels, respectively (**Figure 3.3B**). Evidence of cell debris in bilayer-coated constrictions led to additional evaluation of bilayer integrity after cell treatment using the fluorescent Rhod-PE bilayer composition. We observed reductions in fluorescence intensity at the microfluidic constriction outlet as a result of the bilayer being sheared away as cells pass through the constriction (**Figure 3.3C**). This decrease in fluorescence intensity in the sheared regions could be recovered by incubating the channel with buffer for 6 h, which we attribute to lipid lability that results in lipid bilayer reorganization and recovery of defects, enabling further use or reuse of devices made in this way.

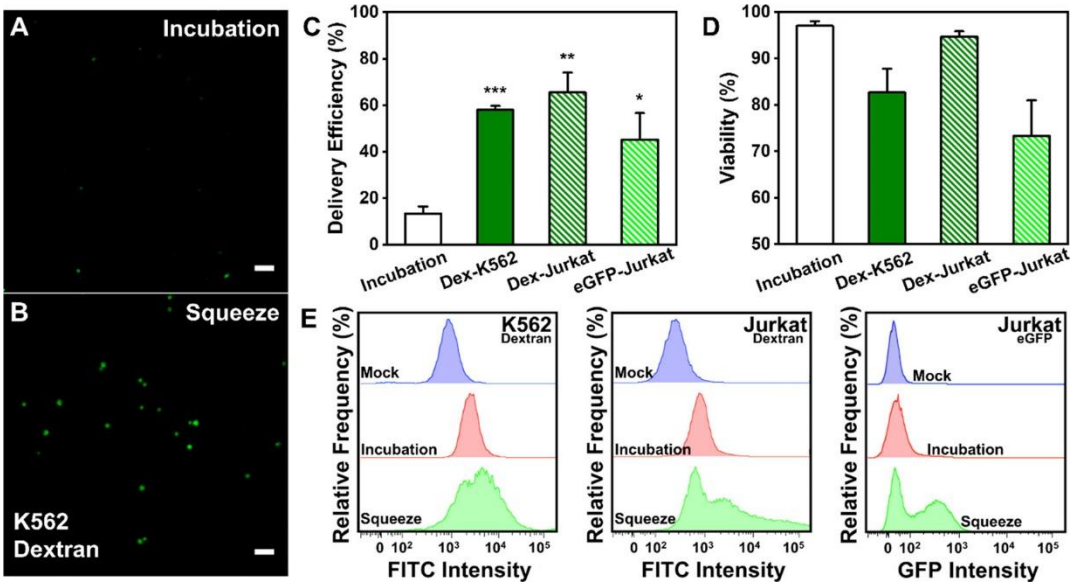

Figure 3.4. Transfection efficiency and viability of lipid bilayer-coated channels. **(A)** Confocal laser scanning micrograph of cells incubated with fluorescein-isothiocyanate-labeled 40 kDa dextran (FITC-Dex, green) and **(B)** K562 3.21 cells post-cell squeezing. **(C)** Delivery efficiency of FITC-Dex and enhance green fluorescent protein-expressing plasmid (eGFP) using bicelle-coated cell-squeezing devices with K562 3.21 and Jurkat cells. Dextran samples were measured 30 min post-cell squeezing whereas eGFP samples were measured 48 h later. (**D)** Cell viability at 30 min and 48 h post-cell squeezing of K562 3.21 and Jurkat cells using FITC-Dex and eGFP, respectively, as the biomolecular cargo. **(E)** Representative flow cytometry histograms for untreated cells (mock), or K562 3.21 and Jurkat cells that were incubated or squeezed with FITC-Dex or eGFP in the delivery medium. The data represents N=4 trials with standard deviations for error bars. Statistics were done using a one-way ANOVA (Origin) and a Tukey test and scale bars are 50 m.

To determine whether lipid bilayer-coated constrictions were effective for cell squeezing intracellular delivery, we tested the delivery of 40 kDa FITC-labeled dextran (FITC-Dex) to K562 3.21 and Jurkat cells, which are commonly used as lymphocyte models for gene-delivery applications. Fluorescence microscopy of K562 3.21 cells confirmed successful intracellular delivery of FITC-Dex showing bright fluorescence intensity as compared to the incubation control (**Figure 3.4A, B**). Jurkat cells incubated with FITC-Dex showed 13% fluorescent cells and was reported as the incubation control. Delivery of FITC-

Dex using lipid bilayer-coated constrictions showed 57% and 65% delivery to K562 3.21 and Jurkat cells, respectively. We further investigated this platform's potential for plasmid delivery using an eGFP-expressing plasmid and observed 45% protein expression in Jurkat cells 48 h post-squeeze treatment (**Figure 3.4C**). Additionally, viabilities of FITC-Dex samples were observed to be 83% and 94% in K562 3.21 and Jurkat cells, respectively, whereas eGFP samples showed a lower viability of 73% (**Figure 3.4D**). Flow cytometric analyses of successful intracellular delivery were applied with large shifts in fluorescence intensity for cells that were treated with constricted microfluidics (**Figure 3.4E**). These results are comparable to efficiencies and viabilities observed in previous cell squeezing work,[5,10] demonstrating that the lipid bilayer does not impede the formation of transient pores for intracellular delivery.

3.D Conclusions and Prospects

Collectively, we have demonstrated a strategy to coat lipid bilayers onto glass and polymeric microfluidic supports using lipid bicelles. This lipid bicelle-mediated bilayer coating technique has demonstrated >90% reduction of protein adsorption and cell attachment, which we applied to constricted microfluidic channels that physically permeabilize cell membranes for intracellular delivery. Channels were designed to promote fouling with longer constriction lengths, and significant reductions in cell debris were observed in lipid bilayer-coated channels. Lipid bilayer-coated devices showed intracellular delivery performances that are comparable to those in previous reports, without fouling and clogging issues. We find three main advantages of using lipid bicelles in cell-squeezing microfluidics applications for intracellular delivery. First, using lipid bicelles offers a facile

and versatile fabrication method for uniform lipid bilayer formation on standard microfluidic devices, requiring only freeze-thaw-vortex cycles and no special equipment. Second, the characterization of the devices can be easily made with standard fluorescence measurements, enabling direct observations of channel coating uniformity and integrity. Third, lipid bilayers formed through bicelle-mediated rupture show significant reductions in nonspecific protein adsorption and cell attachment in microfluidics that can be applied to cell applications beyond intracellular delivery. Future applications will explore improving the lipid bilayer stiffness thereby targeting reduced disruption of the lipid bilayer at the outlet of the microfluidic constrictions and reducing cell debris down to negligible amounts.

3.E Supplementary Materials

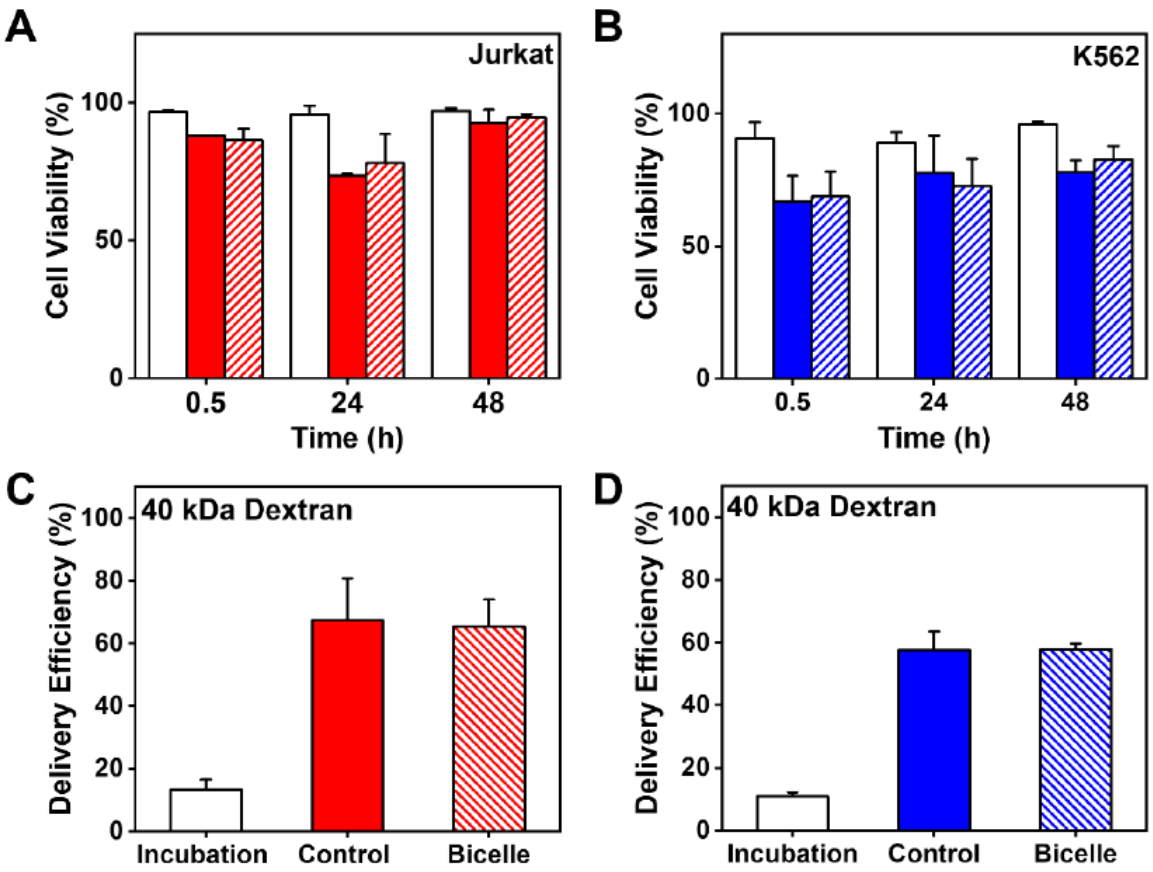

Figure 3.S1. Cell viability and delivery efficiency of bilayer coated and bare constricted devices. Cell viability at 30 min, 24 h and 48 h post-cell squeezing through bare (control) and bilayer-coated (bicelle) constricted devices to deliver 40 kDa fluorescein isothiocyanate labeleddextran (FITC-Dex) to **(A)** Jurkat and **(B)** K562 3.21 cells. Delivery efficiency of FITC-Dex using bicelle and control cell-squeezing devices to **(C)** Jurkat and **(D)** K562 3.21 cells. Samples were measured 30 min post-cell squeezing.

3.F References

(1) Stewart, M. P.; Sharei, A.; Ding, X.; Sahay, G.; Langer, R.; Jensen, K. F. *In Vitro* and *Ex Vivo* Strategies for Intracellular Delivery. *Nature* **2016**, *538*, 183–192.

(2) Carugo, D.; Ankrett, D. N.; Glynne-Jones, P.; Capretto, L.; Boltryk, R. J.; Zhang, X.; Townsend, P. A.; Hill, M. Contrast Agent-Free Sonoporation: The Use of an Ultrasonic Standing Wave Microfluidic System for the Delivery of Pharmaceutical Agents. *Biomicrofluidics* **2011**, *5*, 044108.

(3) Roth, T. L.; Puig-Saus, C.; Yu, R.; Shifrut, E.; Carnevale, J.; Li, P. J.; Hiatt, J.; Saco, J.; Krystofinski, P.; Li, H.; Tobin, V.; Nguyen, D. N.; Lee, M. R.; Putnam, A. L.; Ferris, A. L.; Chen, J. W.; Schickel, J. N.; Pellerin, L.; Carmody, D.; Alkorta-Aranburu, G.; Del Gaudio, D.; Matsumoto, H.; Morell, M.; Mao, Y.; Cho, M.; Quadros, R. M.; Gurumurthy, C. B.; Smith, B.; Haugwitz, M.; Hughes, S. H.; Weissman, J. S.; Schumann, K.; Esensten, J. H.; May, A. P.; Ashworth, A.; Kupfer, G. M.; Greeley, S. A. W.; Bacchetta, R.; Meffre, E.; Roncarolo, M. G.; Romberg, N.; Herold, K. C.; Ribas, A.; Leonetti, M. D.; Marson, A. Reprogramming Human T Cell Function and Specificity with Non-Viral Genome Targeting. *Nature* **2018**, *559*, 405–409.

(4) Stewart, M. P.; Langer, R.; Jensen, K. F. Intracellular Delivery by Membrane Disruption: Mechanisms, Strategies, and Concepts. *Chem. Rev.* **2018**, *118*, 409–7531.

(5) Sharei, A.; Zoldan, J.; Adamo, A.; Sim, W. Y.; Cho, N.; Jackson, E.; Mao, S.; Schneider, S.; Han, M.-J.; Lytton-Jean, A.; Basto, P. A.; Jhunjhunwala, S.; Lee, J.; Heller, D. A.; Kang, J. W.; Hartoularos, G.C. ; Kim, K.-S.; Anderson, D. G.; Langer, R.; Jensen, K. F. A Vector-Free Microfluidic Platform for Intracellular Delivery. *Proc. Natl. Acad. Sci. U. S. A.* **2013**, *110*, 2082–

2087.

(6) Ding, X.; Stewart, M. P.; Sharei, A.; Weaver, J. C.; Langer, R. S.; Jensen, K. F. High-Throughput Nuclear Delivery and Rapid Expression of DNA *via* Mechanical and Electrical Cell-Membrane Disruption. *Nat. Biomed. Eng.* **2017**, *1*, 39.

(7) Belling, J. N.; Heidenreich, L. K.; Tian, Z.; Mendoza, A. M.; Chiou, T.-T.; Gong, Y.; Chen, N. Y.; Young, T. D.; Wattanatorn, N.; Park, J. H.; Scarabelli, L.; Chiang, N.; Takahashi, J.; Young, S. G.; Stieg, A. Z.; De Oliveira, S.; Huang, T. J.; Weiss, P. S.; Jonas, S. J. Acoustofluidic Sonoporation for Gene Delivery to Human Hematopoietic Stem and Progenitor Cells. *Proc. Natl. Acad. Sci. U. S. A.* **2020**, 201917125.

(8) Sharei, A.; Poceviciute, R.; Jackson, E.; Cho, N.; Mao, S.; Hartaularos, G.; Jang, D.; Jhunjhunwala, S.; Eyerman, A.; Schoettle, T.; Langer, R.; Jensen, K. Plasma Membrane Recovery Kinetics of a Microfluidic Intracellular Delivery Platform. *Integr. Biol.* **2014**, *4*, 470–475.

(9) Ma, Y.; Han, X.; Quintana Bustamante, O.; Bessa De Castro, R.; Zhang, K.; Zhang, P.; Li, Y.; Liu, Z.; Liu, X.; Ferrari, M.; Hu, Z.; Carlos Segovia, J.; Qin, L. Highly Efficient Genome Editing of Human Hematopoietic Stem Cells *via* a Nano-Silicon-Blade Delivery Approach. *Integr. Biol. (United Kingdom)* **2017**, *9*, 548–554.

(10) DiTommaso, T.; Cole, J. M.; Cassereau, L.; Buggé, J. A.; Sikora Hanson, J. L.; Bridgen, D. T.; Stokes, B. D.; Loughhead, S. M.; Beutel, B. A.; Gilbert, J. B.; Nussbaum, K.; Sorrentino, A.; Toggweiler, J.; Schmidt, T.; Gyuelveszi, G.; Bernstein, H.; Sharei, A. Cell Engineering with Microfluidic Squeezing Preserves Functionality of Primary Immune Cells in Vivo. *Proc. Natl. Acad. Sci. U. S. A.* **2018**, *115*, E10907–E10914.

(11) Yuan, W.-M.; Shao, J.-Y.; Xue, C.-D.; Liu, B.; Qin, K.-R. A High-Throughput Microfluidic Device for Probing Calcium Dynamics of Single Cells Squeezing through Narrow Channels. *J. Micromechanics Microengineering* **2019**, *29*, 115014.

(12) Ocvirk, G.; Munroe, M.; Tang, T.; Oleschuk, R.; Westra, K.; Harrison, D.-J. Electrokinetic Control of Fluid Flow in Native Poly(dimethylsiloxane) Capillary Electrophoresis Devices. *Electrophoresis* **1999**, *21*, 107.

(13) Wu, M.-H. Simple Poly(dimethylsiloxane) Surface Modification to Control Cell Adhesion. *Surf. Interface Anal.* **2009**, *41*, 11–16.

(14) Boxshall, K.; Wu, M.-H.; Cui, Z.; Cui, Z.; Watts, J. F.; Baker, M. A. Simple Surface Treatments to Modify Protein Adsorption and Cell Attachment Properties within a Poly(dimethylsiloxane) Micro-Bioreactor. *Surf. Interface Anal.* **2006**, *38*, 198–201.

(15) Lee, W.; Tseng, P.; Di Carlo, D. Microfluidic Cell Sorting and Separation Technology. In *Microtechnology for Cell Manipulation and Sorting*. Lee, W., Tseng, P., Di Carlo, D. Eds.; Springer, Cham, **2017**; pp. 1–14.

(16) Kim, P.; Jeong, H. E.; Khademhosseini, A.; Suh, K. Y. Fabrication of Non-Biofouling Polyethylene Glycol Micro- And Nanochannels by Ultraviolet-Assisted Irreversible Sealing. *Lab Chip* **2006**, *6*, 1432–1437.

(17) Wong, T. S.; Kang, S.; Tang, S.; Smythe, E. J.; Hatton, B. D.; Grinthal, A.; Aizenberg, J. Bioinspired self-repairing slippery surfaces with pressure-stable omniphobicity. *Nature* **2011**, *477*, 443–447.

(18) Mukhopadhyay, R. When Microfluidic Devices Go Bad. *Anal. Chem.* **2005**, *77*, 429A–

432A.

(19) Sut, T. N.; Jackman, J. A.; Cho, N. J. Understanding How Membrane Surface Charge Influences Lipid Bicelle Adsorption onto Oxide Surfaces. *Langmuir* **2019**, *35*, 8436–8444.

(20) Sut, T. N.; Jackman, J. A.; Yoon, B. K.; Park, S.; Kolahdouzan, K.; Ma, G. J.; Zhdanov, V. P.; Cho, N. J. Influence of NaCl Concentration on Bicelle-Mediated SLB Formation. *Langmuir* **2019**, *35*, 10658–10666.

(21) Belling, J. N.; Cheung, K. M.; Jackman, J. A.; Sut, T. N.; Allen, M.; Park, J. H.; Jonas, S. J.; Cho, N. J.; Weiss, P. S. Lipid Bicelle Micropatterning Using Chemical Lift-Off Lithography. *ACS Appl. Mater. Interfaces* **2020**, *12*, 13447–13455.

(22) Jackman, J. A.; Cho, N. J. Supported Lipid Bilayer Formation: Beyond Vesicle Fusion. *Langmuir* **2020**, *36*, 1387–1400.

(23) Tinglu Yang; Seung-yong Jung; Hanbin Mao; Cremer, P. S. Fabrication of Phospholipid Bilayer-Coated Microchannels for On-Chip Immunoassays. *Anal Chem.* **2001**, *73*, 165-169.

(24) Makamba, H.; Kim, J. H.; Lim, K.; Park, N.; Hahn, J. H. Surface Modification of Poly(dimethylsiloxane) Microchannels. *Electrophoresis* **2003**, *24*, 3607–3619.

(25) Chiu, D. T.; Jeon, N. L.; Huang, S.; Kane, R. S.; Wargo, C. J.; Choi, I. S.; Ingber, D. E.; Whitesides, G. M. Patterned Deposition of Cells and Proteins onto Surfaces by Using Three-Dimensional Microfluidic Systems. *Proc. Natl. Acad. Sci. U. S. A.* **2000**, *97*, 2408–2413.

(26) Groves, J. T.; Dustin, M. L. Supported Planar Bilayers in Studies on Immune Cell Adhesion and Communication. *J. Immunol. Methods* **2003**, *278*, 19–32.

(27) Huang, C. J.; Cho, N. J.; Hsu, C. J.; Tseng, P. Y.; Frank, C. W.; Chang, Y. C. Type I Collagen-Functionalized Supported Lipid Bilayer as a Cell Culture Platform. *Biomacromolecules* **2010**, *11*, 1231–1240.

(28) Vafaei, S.; Tabaei, S. R.; Biswas, K. H.; Groves, J. T.; Cho, N.-J. Dynamic Cellular Interactions with Extracellular Matrix Triggered by Biomechanical Tuning of Low-Rigidity, Supported Lipid Membranes. *Adv. Healthc. Mater.* **2017**, *6*, 1700243.

(29) Persson, F.; Fritzsche, J.; Mir, K. U.; Modesti, M.; Westerlund, F.; Tegenfeldt, J. O. Lipid-Based Passivation in Nanofluidics. *Nano Lett.* **2012**, *12*, 2260–2265.

(30) Groves, J. T.; Mahal, L. K.; Bertozzi, C. R. Control of Cell Adhesion and Growth with Micropatterned Supported Lipid Membranes. *Langmuir* **2001**, *17*, 5129-5133.

(31) Andersson, A.-S.; Glasmästar, K.; Sutherland, D.; Lidberg, U.; Kasemo, B. Cell Adhesion on Supported Lipid Bilayers. *J. Biomed. Mater. Res. Part A* **2003**, *64A*, 622–629.

(32) Schneider, C. A.; Rasband, W. S.; & Eliceiri, K. W. NIH Image to ImageJ: 25 Years of Image Analysis. *Nature Methods* **2012**, *9*, 671–675.

(33) Miyata, N.; Steffen, J.; Johnson, M. E.; Fargue, S.; Danpure, C. J.; Koehler, C. M. Pharmacologic Rescue of an Enzyme-Trafficking Defect in Primary Hyperoxaluria 1. *Proc. Natl. Acad. Sci. U. S. A.* **2014**, *111*, 14406–14411.

(34) Schindelin, J.; Arganda-Carreras, I.; Frise, E.; Kaynig, V.; Longair, M.; Pietzsch, T.; Cardona, A. Fiji: An Open-Source Platform for Biological-Image Analysis. *Nature Methods* **2012**, *9*, 676–682.

(35) Kolahdouzan, K.; Jackman, J. A.; Yoon, B. K.; Kim, M. C.; Johal, M. S.; Cho, N. J. Optimizing the Formation of Supported Lipid Bilayers from Bicellar Mixtures. *Langmuir* **2017**, *33*, 5052–5064.

(36) Chen, C. S.; Mrksich, M.; Huang, S.; Whitesides, G. M.; Ingber, D. E. Geometric Control of Cell Life and Death. *Science* **1997**, *276*, 1425–1428.

(37) Liu, V. A.; Jastromb, W. E.; Bhatia, S. N. Engineering Protein and Cell Adhesivity Using PEO-terminated Triblock Polymers. *J. Biomed. Mater. Res.* **2002**, *60*, 126–134.

(38) Glasmästar, K.; Larsson, C.; Höök, F.; Kasemo, B. Protein Adsorption on Supported Phospholipid Bilayers. *J. Colloid Interface Sci.* **2002**, *246*, 40–47.

(39) Dressaire, E.; Sauret, A.; Kumar, A.; Ardekani, A. M.; Burr, T. J.; Hoch, H. C.; Wu, M.; Abdi, H.; Todenhöfer, T.; Bazov, J.; *et al.* Clogging of Microfluidic Systems. *Soft Matter* **2017**, *13*, 37–48.

(40) Hou, X.; Zhang, Y. S.; Santiago, G. T.; Alvarez, M. M.; Ribas, J.; Jonas, S. J.; Weiss, P. S.; Andrews, A. M.; Aizenberg, J.; Khademhosseini, A. Interplay between Materials and Microfluidics. *Nat. Rev. Mater.* **2017**, *2*, 17016.

(41) Green, J. V.; Kniazeva, T.; Abedi, M.; Sokhey, D. S.; Taslim, M. E.; Murthy, S. Effect of Channel Geometry on Cell Adhesion in Microfluidic Devices. *Lab Chip* **2009**, *9*, 677–685.

(42) Han, X.; Liu, Z.; Jo, M. C.; Zhang, K.; Li, Y.; Zeng, Z.; Li, N.; Zu, Y.; Qin, L. CRISPR-Cas9 Delivery to Hard-to-Transfect Cells via Membrane Deformation. *Sci. Adv.* **2015**, *1*, e1500454.

CHAPTER 4

Acoustofluidic Sonoporation for Gene Delivery to Human Hematopoietic Stem and Progenitor Cells

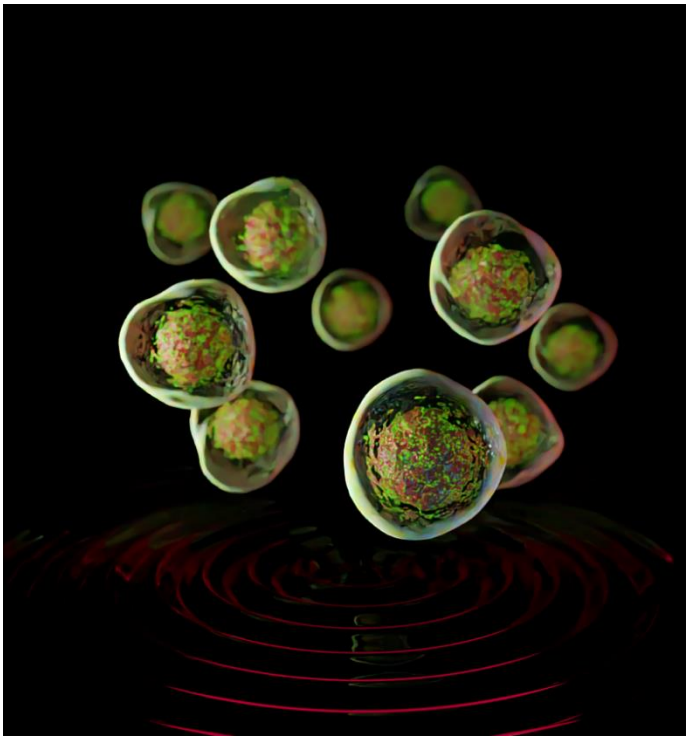

The information in this chapter was published in
Proceedings of the National Academy of Sciences **2020**, *117*, 10976–10982
and has been reproduced here with permission.

Authors: Belling, J. N.; **Heidenreich, L. K.**; Tian, Z.; Mendoza, A. M.; Chiou, T. T.; Gong, Y.; Chen, N. Y.; Young, T. D.; Wattanatorn, N.; Park, J. H.; Scarabelli, L.; Chiang, N.; Takahashi, J.; Young, S. G.; Stieg, A. Z.; De Oliveira, S.; Huang, T. J.; Weiss, P. S.; Jonas, S. J.

4.A Introduction

Intracellular delivery of plasmids to cells for gene modification is a critical step for treating genetic disorders in clinical and research applications. Of the variety of techniques that have been developed for inserting DNA or RNA into cells, viral-based delivery is the current standard for genetic engineering. Virus-based methods have been successful for establishing efficacious gene therapies for a range of diseases, including hemoglobinopathies and cancer.[1,2] However, viral carriers are expensive and are known to modify DNA semi-randomly. This indiscriminate chromosomal integration can lead to inefficient gene transfer and off-target effects, such as insertional mutations.[3] The recent emergence of targeted endonuclease gene-editing strategies (*e.g.*, clustered regularly interspaced palindromic repeats and Cas9 protein, CRISPR-Cas9) offer an exciting solution to investigate therapeutic approaches through coordinated gene disruption or insertion of new DNA sequences at preselected sites.[4] Yet, these gene-editing systems require alternative intracellular delivery strategies to overcome the size limitations of viral vectors for simultaneously encapsulating the editing enzymes and corrective DNA templates.[5,6] Engineered ribonucleoprotein complexes configured for base and prime editing could replace these templates, but similarly require alternative delivery strategies for effective genome editing because of the large fusion protein constructs used in these systems.[7,8]

Non-viral *ex vivo* transfection strategies have been employed in both commercial and research settings to circumvent the limitations of viral delivery.[9,10] However, improving the cost, safety, speed, throughput, and efficiency of non-viral transfection remains a challenge for the broader application of gene therapies to patient care. Of note, nanoparticle delivery, microinjection, electroporation, and lipofection are efficient techniques but vary in efficacy

and throughput, depending on the cell line or the platform.[11–13] Several clinical trials have shown that a minimum of 2 million cells/kg of body weight is needed for the effective engraftment of CD34+-selected hematopoietic stem cell populations used for gene therapies.[14] One such example is gene-modified treatments for inherited disorders such as adenosine deaminase–related severe combined immunodeficiency (ADA-SCID), which typically appears in the first years of life.[15] Assuming a pediatric patient weighs 12 kg, this therapy would thus require efficient processing of ~24 million cells, which is difficult to achieve quickly and efficiently with the aforementioned techniques. Cell-squeezing technologies, such as those discussed in Chapter 2, offer a promising alternative to address these throughput limitations, using constricted microchannels to form pores in cell membranes that enable biomolecule delivery.[16–18] Recent work has shown that these physical disruption strategies can preserve human T-cell function after the delivery of CRISPR-Cas9 biomolecules, with minimal aberrancies in transcriptional responses (compared with electroporation).[19]

In parallel with the success of membrane-disruption techniques, emerging acoustic methods can address the technical limitations of electroporation, lipofection, and viral vectors. Fechhemeimer et al. demonstrated the use of ultrasonic waves to deliver exogenous DNA to cell populations via sonoporation.[20] In the wake of this pioneering discovery, a variety of ultrasonic devices were developed, but they required ultrasound contrast agents (*e.g.*, Albunex) to stimulate microbubble formation for intracellular delivery.[21,22] The rapid expansion of microbubbles from ultrasonic perturbation is known to lead to a phenomenon known as cavitation, where bubble collapse results in high local temperatures and pressures that are detrimental to cell viability.[23] Contrast agent–free acoustofluidic systems have also

been explored, where cells are focused to nodal planes of pressure within a fluid from ultrasonic waves (enabling physical and spatial manipulation).[24] Notably, Rodamporn *et al.* demonstrated gene delivery using a bulk acoustic resonator with microfluidics that relied on radiation forces from standing waves, establishing parameters for gene delivery to HeLa cells.[25] Carugo *et al.* miniaturized these platforms for drug delivery to H9c2 cardiomyoblasts, optimizing frequency selection, device power, and flow conditions for increased cell viability.[26] Note that these bulk resonators operate in frequency regimes that do not completely suppress cavitation, which can be a mechanism of intracellular delivery using sonoporation. Recently, Yeo *et al.* demonstrated device architectures that utilize surface acoustic waves at high frequencies (>10 MHz) to suppress cavitation for gene delivery to human embryonic kidney cells and porcine tissue.[27,28] Zhang *et al.* explored even higher frequencies (GHz) with bulk acoustic resonators and demonstrated intracellular delivery of doxorubicin and plasmids with high efficiency.[29] As such, there is great promise in applying acoustic-based systems towards intracellular delivery to therapeutic and disease-relevant cell types (*e.g.*, T-cells, stem cells) with high throughput.

Within this work, we report the design and operation of an acoustofluidic device that delivers plasmid DNA to immortalized and primary human cell types with a throughput of 200,000 cells/min. These devices induce pores and permeability in cell membranes, enabling intracellular delivery without contrast agents. The mechanism of delivery was also explored, using Jurkat cells as a model system. AlexaFluor 546-labeled DNA (Cy3-DNA) was delivered and enabled device optimization of both plasmid delivery to Jurkat cells and nuclear membrane ruptures in mouse embryonic fibroblasts (MEFs). Optimized device parameters

showed successful delivery of an enhanced green fluorescent protein (eGFP)–expressing plasmid as well as nuclear membrane ruptures in acoustofluidic-treated cells. These results prompted additional experiments with plasmid delivery to human primary cells, including peripheral blood mononuclear cells (PBMCs) and umbilical cord blood CD34+ hematopoietic stem and progenitor cells (CD34+ HSPCs). All cell types tested showed eGFP-expression and >80% viability over 72 h, providing strong evidence for long-term protein expression. Altogether, these data indicate that this acoustofluidic-mediated gene-delivery approach could make it possible to manufacture gene-modified therapeutic cell products at doses appropriate for pediatric patients within 2 h, making it a viable approach for gene-editing applications. Further optimization with simultaneous cell processing in multiple, parallel channels has now been implemented in subsequent work as a natural direction for improving throughput.

4.B Experimental Methods

4.B.1 Surface Functionalization of Glass Microcapillaries

Square glass microcapillaries (Vitrocom) with 5 cm × 80 μm × 80 μm in internal dimensions were cleaned in piranha solution (3:1 concentrated sulfuric acid and 30% hydrogen peroxide) for 30 min to remove organic molecules while adding hydroxyl functionalities to the glass surface. Next, the capillaries were rinsed and sonicated in 18-MΩ deionized water (Millipore) for 5 cycles of 5 min and placed in a drying oven at 110 ˚C for 6 h. The dried capillaries were then dipped in a 5% (v/v) ethanolic solution of (3- aminopropyl)triethoxysilane (APTES, Sigma Aldrich) and placed in an oven at 60 ˚C for 5 min followed by 3 cycles of sonication in ethanol for 5 min to remove any passively

adsorbed APTES molecules from the channel walls. Clean functionalized capillaries were stored in ethanol until device assembly.

4.B.2 Device Fabrication

The acoustofluidic devices are comprised of a piezoelectric lead zirconate titanate (PZT) transducer (SMPL26W16T07111, StemInc), a functionalized glass microcapillary, and a glass slide that provides a supporting substrate. The PZT transducers were mounted onto the glass slide with a thin layer of Devcon 5-minute epoxy adhesive (300007-392, VWR) after soldering 30-gauge wire to the front and back electrodes of the PZT transducer. A functionalized glass microcapillary was attached onto the transducer with adhesive and cured for 30 min. Polyethylene tubing (PE-50, Instech) was connected to both ends of the microcapillary and sealed with small drops of epoxy. After curing, the tubing was secured to the glass slide with double-sided tape and tested for leaks. The resonant frequency for each device was determined with a vector network analyzer (VNA-120, Array Solutions).

4.B.3 Operation

The fabricated acoustofluidic devices were vertically aligned in a custom-built stage that aligned the cross section of the microfluidic channel within the optical path of a Nikon TE300 optical microscope. Tubing was connected to a syringe by inserting a 23-gauge needle adapter, and the flow rate was controlled with a syringe pump (Fusion 4000, Chemyx). The PZT transducers were excited with a sinusoidal wave at the desired frequency and an amplitude of 40 V peak-to-peak ($V_{p\text{-}p}$) with a signal generator (81150A, Agilent) and a broadband amplifier (25A250B, Amplifier Research).

4.B.4 DNA and Plasmid Delivery

The APTES-treated glass capillaries were pre-rinsed with 5 mL of 70% ethanol, followed by 3 mL of 1× phosphate-buffered saline solution (PBS, 137 mM NaCl, 2.7 mM KCl, 10 mM Na_2HPO_4, 1.8 mM KH_2PO_4, Gibco) before introducing plasmid DNA. The eGFP expression vector (pCMV-GFP, Plasmid #11153, Addgene) or Cy3-labeled DNA (Integrated DNA Technologies) was diluted to 50 ng/mL in 1× PBS and was zone-loaded with a flow a rate of 3.33 μL/min for 30 min with a 3-way valve (CMA 110, Harvard Apparatus) connected to the acoustofluidic device. Cells were then dispersed at a density of 3 million cells/mL (except for $CD34^+$ HSPCs) in a delivery medium consisting of 1% (v/v) Pluronic F-68 (Gibco), 1× PBS, and 0.1 mg/mL of eGFP-expressing plasmid and collected into a 1 mL syringe. Cells were introduced into the glass capillary at the designated flow rate, and acoustofluidic-treated cells were collected into a sterile tube. The $V_{p\text{-}p}$ was applied to the PZT transducer after the initial drop of solution was collected to ensure that cells were under continuous acoustofluidic treatment while passing through the device. Additional PBS was flowed through the device for 3 min after the cell syringe reached depletion to collect any remaining cells in the dead volume of the device. Upon collection, cells were incubated in the delivery medium for 10 min to facilitate membrane recovery and biomolecule diffusion. Cells were then centrifuged at 500 *g* for 5 min and dispersed in their respective culture media. Viability was determined using a Cell Countess II (Invitrogen).

4.B.5 Confocal Laser Scanning Microscopy

Cells were initially fixed *via* incubation in 0.5% paraformaldehyde (Sigma Aldrich) in 1× PBS solution. The cells were then spun down, dispersed in 1× PBS at a density of at least 1,000,000 cells/mL, plated on microscope slides (Denville) in a 2:7 mixture of cells to

ProLong diamond antifade mounting solution (Thermo Fisher Scientific), and mixed thoroughly using a P100 pipette (Gilson). A coverslip was carefully placed on top of the cell mixture and allowed to dry at room temperature for 1 h with foil covering the slides. Slides were stored at 4 °C and imaged within one week. Confocal laser scanning microscopy was performed with a confocal microscope (Zeiss, LSM 700) with Plan Apochromat 10×/0.45 and 20×/0.8 objectives. *Z*-stacks were acquired, and a maximum intensity projection was applied to each stack using Zeiss Zen Blue software.

4.B.6 Cell Culture

Jurkat cells (ATCC, Manassas VA) were cultured in 1× RPMI 1640 with L-glutamine (Gibco) supplemented with 10% fetal bovine serum (Gibco) and 1% penicillin-streptomycin (10,000 units/mL penicillin and 10 mg/mL streptomycin) (Gibco). Peripheral blood mononuclear cells were sourced from healthy donors and isolated by the University of California, Los Angeles (UCLA) Virology core and cultured with the aforementioned medium supplemented with 10 ng/mL of recombinant human IL-2 (Peprotech). Mouse embryonic fibroblasts with an NLS-GFP reporter were cultured and derived as described previously.[30] Staining with the γH2AX-antibody to identify DNA damage was described previously by Chen *et al*.[31] Mixed donor umbilical cord $CD34^+$ Hematopoietic stem and progenitor cells (Allcells Inc.) were thawed and pre-stimulated as described by Hoban *et al*.[32] Post-acoustofluidic treatment, HSPCs were cultured in X-VIVO 15 supplemented with 50 ng/μL of recombinant human SCF (Peprotech), 50 ng/μL of human recombinant Flt3-ligand (Peprotech), and 50 ng/μL of recombinant human TPO (Peprotech) in a 12-well plate at a density of 400,000 cells/mL for 24 h. The HSPCs were then spun down at 500 *g* for 5 min and

transferred to Iscove's Modified Dulbecco's Medium (IMDM, Thermo Fisher Scientific) supplemented with 50 ng/μL of recombinant human IL-3 (Peprotech), 50 ng/μL of recombinant human IL-6 (Peprotech), 50 ng/μL of human recombinant SCF (Peprotech), 1.5% bovine serum albumin (Sigma Aldrich), 20% fetal bovine serum, and 1% L-glutamine/penicillin/streptomycin (Gemini). For all cell types, cell culture media were changed every two days.

4.B.7 High-Speed Imaging

The high-speed imaging setup was described in detail in a previous work.[33] The frame rate of the camera is limited by the chosen pixel resolution (512 × 512 pixels resolution here). The resulting frame rate was 21,000 s^{-1} with an exposure time of 0.25 μs.

4.B.8 Flow Cytometry

Flow cytometry data were acquired and processed using an LSR Fortessa cytometer (BD Biosciences). Data analyses were performed using FlowJo™ software (BD Life Sciences). Fluorescence emission was stimulated using a 488 nm, 50 mW laser with a 505 nm long-pass filter and 515/20 nm bandpass filters for detecting green fluorescent protein.

4.B.9 Simulation

Commercial finite element analysis software, COMSOL Multiphysics, was used for simulating the pressure field in the glass capillary. A solid mechanics module was used to model the glass capillary with a density, Young's modulus, and Poisson's ratio set at 2,200 kg/m^3, 72 GPa, and 0.17 respectively. A pressure acoustic module was used to model the liquid medium by setting density and speed of sound at 1,000 kg/m^3 and 1,480 m/s respectively. Continuity boundary conditions are applied to the left and right boundaries of

the model and a harmonic force is applied to the top boundary of the glass capillary to simulate the excitation force from the lead zirconate titanate (PZT) transducer.

4.B.10 Statistical and Image Analyses

One-way ANOVA analyses were performed using Origin 9.1 data analysis and graphing software. Quantification of DAPI-GFP co-localization, and DNA damage utilized Fiji image analysis software and the cell counter plugin.[34]

4.C Results and Discussion

Acoustofluidic devices were designed to transduce acoustic pressure waves into a square glass microcapillary, physically shearing cell membranes against the capillary wall (**Figure 4.1A**). These waves are generated by applying a continuous sinusoidal electrical potential to a lead zirconate titanate piezoelectric (PZT) transducer at a resonance frequency

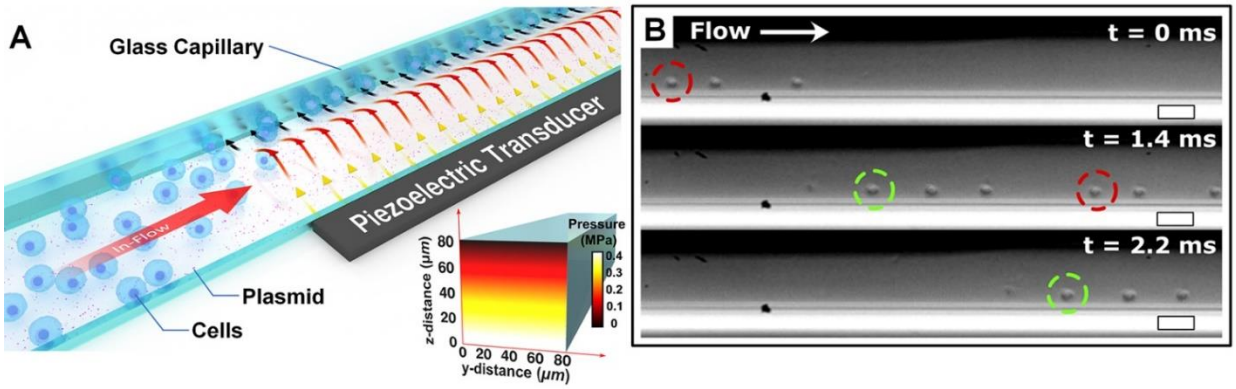

Figure 4.1. (A) Schematic of the device components and application, where target cells undergo acoustofluidic treatment *via* flow through a glass capillary over a piezoelectric transducer. (inset) Simulated acoustic pressure amplitude of the aqueous medium in the glass capillary showing minimum pressure presents at the wall farthest from the piezoelectric transducer at an excitation frequency of 3.3 MHz. **(B)** Sequential images taken with a high-speed camera at 0, 1.4, and 2.2 ms. Jurkat cells are observed to localize against a capillary wall and are pushed forward by laminar flow. Colored circles are used to track cells moving through the capillary. Scale bars are 50 μm.

(3.3 MHz) predetermined with a network analyzer. At this frequency, the inner width of the capillary is smaller than a quarter wavelength of the generated acoustic waves in the capillary medium, which results in a minimum Gor'kov potential farthest from the acoustic source.[35] Simulations of the generated acoustic pressure coincide with this potential minimum, with an amplitude gradient that decreases moving away from the PZT transducer (**Figure 4.S1A**). This acoustic pressure yields predictable cell movement towards the capillary wall opposite the transducer (**Figure 4.1B**).

To observe cell behavior within the cross-section of the glass capillary, acoustofluidic devices were vertically aligned with the optical path of a microscope (**Figure 4.S1A**). Images of Jurkat cells under acoustofluidic treatment without flow confirmed cell displacement away from the PZT transducer, pressing cells against the capillary wall due to the acoustic radiation force (Fig. S1B). Additional analyses of tracking cell displacement to the capillary wall with respect to time (Fig. S1C) enabled acoustic energy density measurements. This displacement analysis provided estimates for the maximum pressure amplitude (0.48 ± 0.04 MPa) (Fig. 1A, inset) and the acoustic radiation force (43 ± 10 pN) when applying an input voltage of 40 V peak-to-peak.

Cell movement under flow conditions (192 μL/min) was studied with a high-speed camera, enabling us to observe mobile Jurkat cells under acoustofluidic treatment (**Figure 4.1C**). Under these conditions, the cells experience a combination of forces that lead to sonoporation, including the shearing force induced by microscale acoustic streaming[36] and the acoustic radiation force that pushes the cells to the microcapillary wall. We also note that cavitation is not completely suppressed in our acoustofluidic platform, as the calculated

acoustic pressures fall within Krasovitski's theory of intramembranous cavitation (0.2-0.8 MPa), where membrane leaflets cyclically expand and contract, which results in increased cellular deformation, pore formation, and thus membrane permeability.[37]

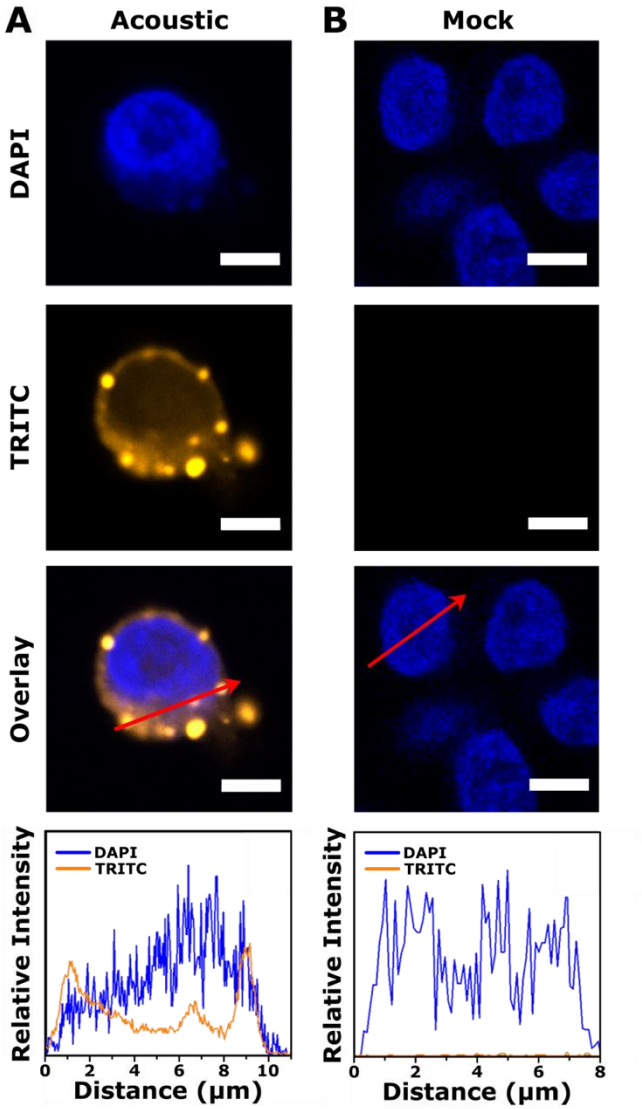

Figure 4.2. Confocal laser scanning micrographs for **(A)** acoustic-treated and **(B)** untreated Jurkat cells. Line profiles (red arrows) of DAPI and TRITC channels show fluorescence signal of Cy3-labeled DNA at the cell membrane, cytosol, and nucleus for acoustic-treated cells. Scale bars are 10 μm.

To examine whether intracellular delivery is achieved through cell membrane shearing, fluorescently labeled DNA (Cy3-DNA) was electrostatically tethered to the glass capillary by pre-functionalizing the surface with (3-aminopropyl)triethoxysilane (APTES). The Cy3-DNA was introduced into the glass capillary with a zone-loading technique using a three-way valve to prevent air from entering the capillary. Jurkat cells were flowed into the glass capillary at 192 μL/min and exposed to acoustic waves. Post-acoustofluidic treatment, cells were fixed and stained with 4′,6-diamidino-2-phenylindole (DAPI), enabling observations of acoustofluidic-mediated delivery by visualizing the distribution of Cy3-DNA around the cell nucleus with confocal laser scanning microscopy. Micrographs of the acoustofluidic-treated cells indicated delivery of Cy3-DNA into the cell cytosol, into the nucleus, and on the cell membrane (**Figures 4.2, 4.S2**). We characterized the Cy3-DNA distribution by plotting relative fluorescence intensity profiles across the red arrows and observed peak intensity maximums at the plasma membrane and nuclear membrane of the cell. These bright spots are postulated to represent formations of DNA aggregates that correspond to endosomal trafficking from the plasma membrane into the cell.[38,39]

Given the successful delivery of Cy3-DNA to Jurkat cells, the input voltage to the PZT transducer and the flow rate were optimized for both cell viability and gene expression. When applying $V_{p\text{-}p}$ up to 40 V, we observed cell viabilities that exceeded 90% (**Figure 4.3A**). This voltage was subsequently used as the standard input voltage. The effect of flow rate on cell viability was then studied over a range of 15 μL/min to 576 μL/min. Viability was found to exceed 90% at flow rates >192 μL/min **(Figure 4.3B),** showing viability to be inversely

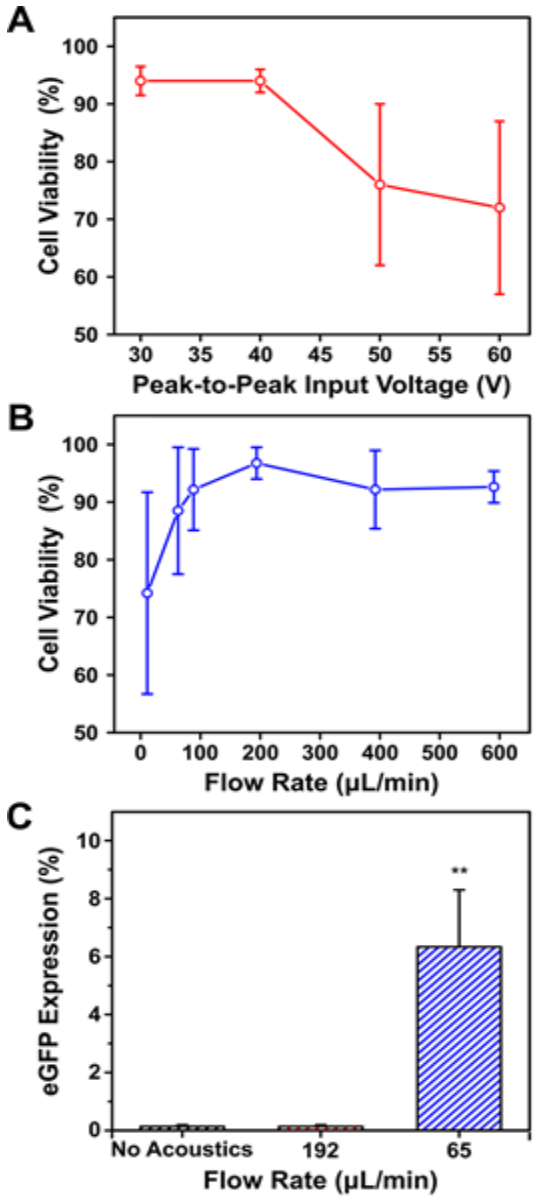

Figure 4.3. (A) Cell viability as a function of the applied $V_{p\text{-}p}$ to the piezoelectric transducer with a constant flow rate of 192 µL/min. **(B)** Cell viability as a function of flow rate through the glass capillary with a constant $V_{p\text{-}p}$ of 40 V. **(C)** Enhanced green fluorescent protein expression (eGFP) in Jurkat cells 24 h post-acoustofluidic delivery of an eGFP-expression plasmid. Protein expression is plotted as a function of flow rate and compared to a no acoustics control flowed at 65 µL/min. All cell viability measurements were assessed through trypan blue staining. Data are expressed as mean and standard deviation for N=3. Significance is determined using a one-way ANOVA and a Tukey means comparison test (**$p<0.01$).

related to the exposure time of acoustofluidic treatment. Following these observations, an

eGFP expression plasmid driven by a cytomegalovirus (CMV) promoter was tethered to the sidewalls of the channel and co-flowed with Jurkat cells (3 million cells/mL) to examine eGFP expression under different flow rates and acoustofluidic treatment. When reducing the flow rate to 65 μL/min, eGFP expression was observed after 24 h of incubation (**Figure 4.3C**). This density (3 million cells/mL) and flow rate (65 μL/min) established a processing throughput of 200,000 cells/min, which can meet the clinical throughput for pediatric patients within 2 h using a single channel. We also conducted additional viability experiments with an Annexin V-propidium iodide assay and flow cytometry using these device parameters. This assay showed ~77% live cells with <10% apoptotic cells 72 h after acoustofluidic treatment. (**Figure 4.S3**)

To exclude the possibility of endocytotic processes that may also lead to transfection, cells were flowed through a control device consisting of a glass capillary mounted on a glass scaffold with a tubing inlet and outlet. These control samples showed *no* evidence of eGFP expression and maintained viabilities equivalent to untreated cells, thereby establishing optimized input voltage (40 V peak-to-peak) and flow rate (65 μL/min) that were used for the rest of the work. Successful eGFP expression in Jurkat cells also provides the evidence of plasmid diffusion into the cell nucleus, since it is known that cytoplasmic nucleases can degrade free DNA, which would result in low gene expression.[40,41]

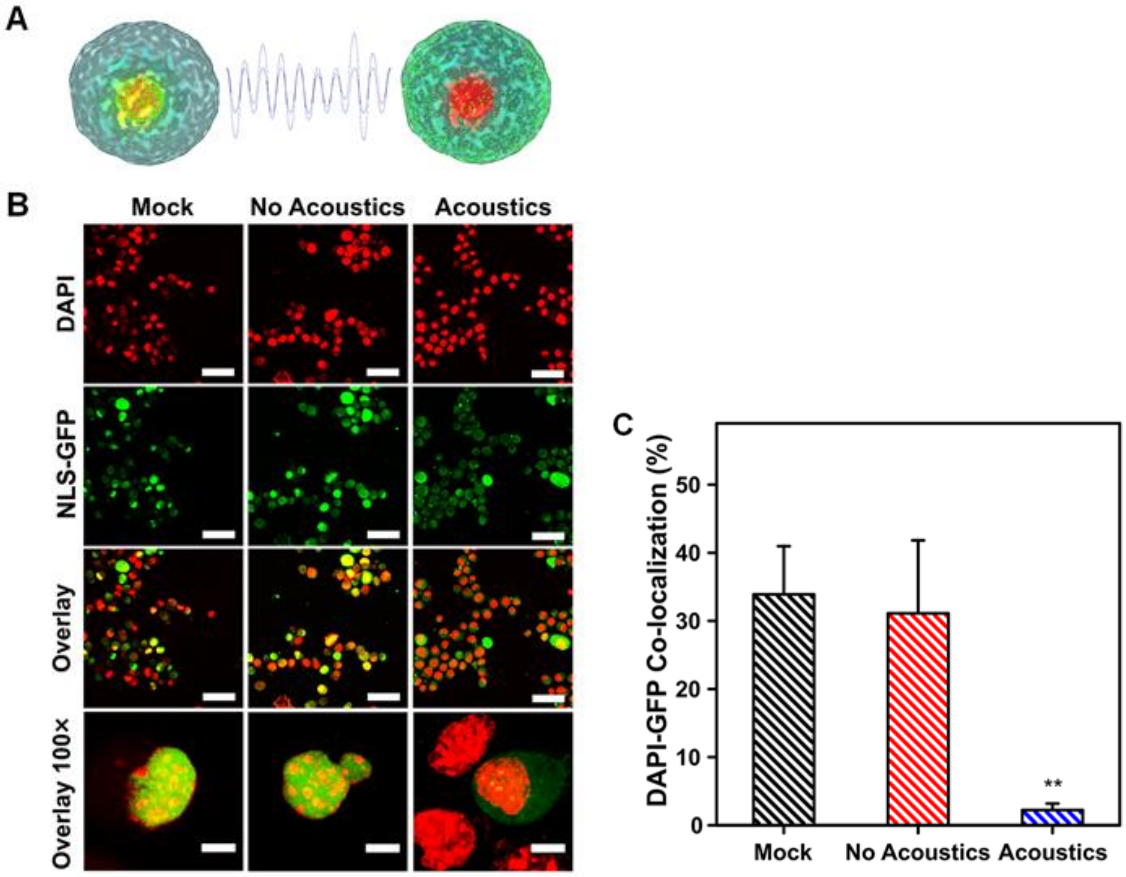

Figure 4.4. (A) A schematic of mouse embryonic fibroblasts (MEFs) green fluorescent protein fused to a nuclear localization signal (NLS-GFP) and acoustofluidic treatment inducing nuclear membrane rupture, resulting in dispersed NLS-GFP throughout the cell cytosol. **(B)** Confocal laser scanning micrographs of MEFs showing colocalization events of NLS-GFP and DAPI signals in the untreated (mock), no acoustics, and acoustics-treated samples. The MEFs are virally transduced to express GFP at their nuclei (green) and are stained post-acoustofluidic treatment with DAPI to label the cell nuclei (red). Co-localization of GFP and DAPI signals (yellow) are shown in the overlay and lack thereof is evidence of nuclear membrane rupture. **(C)** Quantification of co-localized DAPI and GFP signals for mock, no acoustic, and acoustic-treated cells. Data are expressed as mean and standard deviation for N=3 and significance is determined using a one-way ANOVA and Tukey's mean comparison test (**$p<0.01$). Co-localization % of DAPI and GFP signals are normalized to 60 cells for each condition. Scale bars are 50 μm for DAPI, NLS-GFP, and Overlay, and 10 μm for Overlay 100× micrographs respectively.

To determine the effects of acoustofluidic treatment (using the aforementioned parameters) on cell nuclei, we investigated nuclear membrane ruptures in MEFs (**Figure 4.4A**). Cells were first virally transduced with an NLS-GFP reporter (green fluorescent protein fused to a nuclear localization signal),[42] these cells constitutively express green fluorescent protein that localizes to the nuclear envelope and enables observations of perturbations on cell nuclei. These NLS-GFP MEFs were fixed and stained with DAPI immediately after acoustofluidic treatment for confocal laser scanning microscopy. A significant difference in the percentage of cells with nuclear membrane rupture was observed in acoustofluidic-treated cells compared with mock and no-acoustics controls, quantified by the numbers of cells with colocalization of DAPI and GFP signals (**Figures 4.4B**,**C 4.S4**). Notably, cells that underwent acoustofluidic treatment showed dispersed GFP throughout the cytosol and decreased nuclear fluorescence intensity, compared with untreated control (mock) and samples flowed through the control device (no acoustics). The displacement of nuclear localized GFP into the cytosol *via* acoustofluidic treatment provides evidence of nuclear envelope ruptures, which could enable diffusion of plasmid DNA into the nucleus. These results demonstrate the potential of the acoustofluidic platform as a tool to examine both cell membrane and nuclear membrane repair mechanics and for development of reagents that increase the entry of DNA into the nucleus. It is also possible that rupture of the nuclear envelope could be a driver for genomic instability and DNA damage.[43] Thus, we took an immunohistochemical approach to analyze DNA damage by staining NLS-MEFs with DAPI and a γH2AX-antibody immediately after acoustofluidic treatment. We determined highly damaged cells by counting cells that had >7 labeled DNA foci and found insignificant amounts of DNA damage when compared to untreated cells

(mock) (**Figure 4.S5**). The finding of nuclear membrane ruptures with insignificant DNA damage will make it possible to elucidate potential effects of acoustofluidic treatment on the genome, a relevant consideration for gene-editing applications.[44]

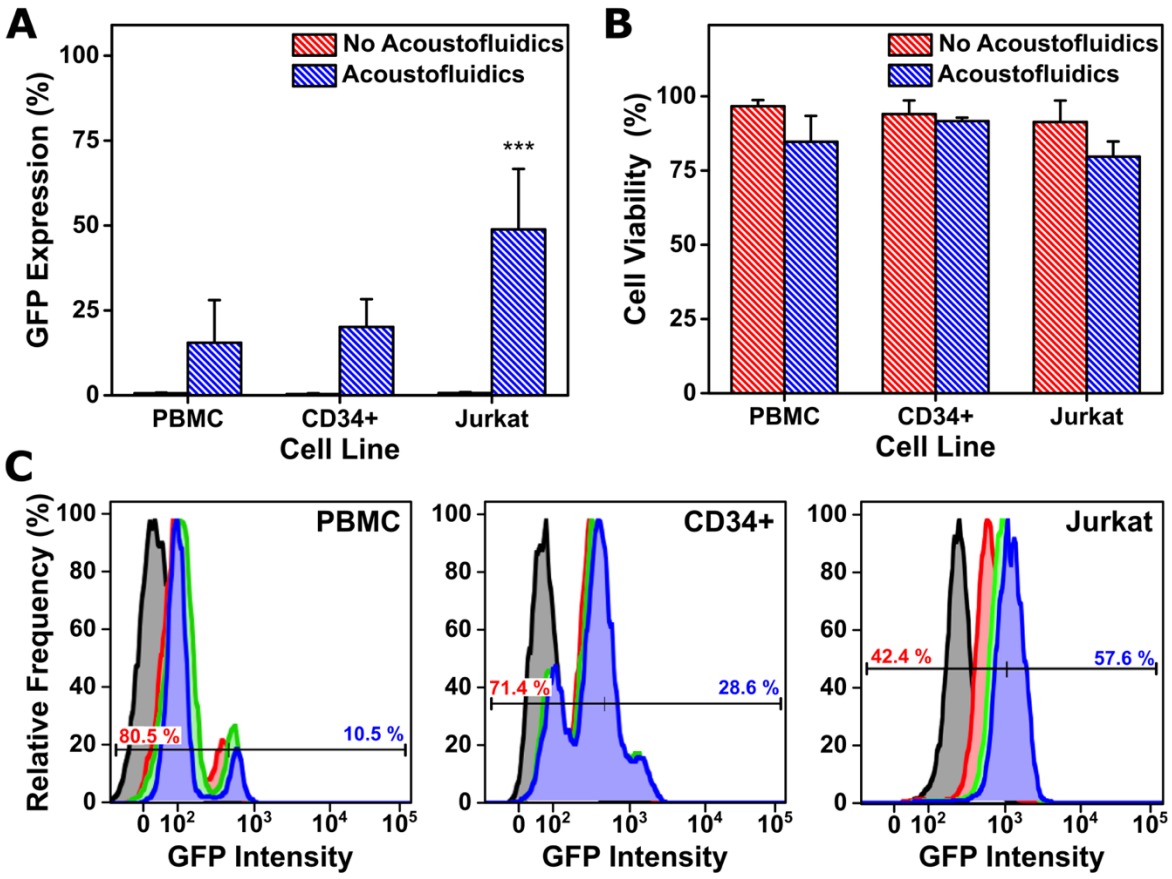

Figure 4.5. (A) Enhanced green fluorescent protein (eGFP) expression **(B)** and cell viability 72 h post-acoustofluidic delivery of an eGFP-expression plasmid to Jurkat, peripheral blood mononuclear cells (PBMC), and CD34+ hematopoietic stem and progenitor cells (CD34+). **(C)** Flow cytometry quantification of eGFP-expression over a 72-h period post-acoustofluidic delivery of an eGFP-expression plasmid. Histograms show relative frequency of detected eGFP events with time points defined as 0 h (black), 24 h (red), 48 h (green), and 72 h (blue). A representative bisector gate is overlaid on each histogram to show the flow cytometry gating for each cell type, with negative GFP populations in red text and positive in blue. Data are expressed as mean and standard deviation for N=5 for Jurkat and N=3 for PBMCs and CD34+. Statistical significance is determined using a Student's t-test (***$p<0.001$).

We explored the potential of this platform using the optimized device parameters (3 million cells/mL, 65 μL/min, and 40 V peak-to-peak) for therapeutic applications, in which an eGFP plasmid was delivered to Jurkat, PBMCs, and $CD34^+$ HSPCs. Protein expression was monitored at 24-, 48-, and 72-h time points with flow cytometry (assessing continued eGFP expression). Delivery to Jurkat cells revealed 6% eGFP expression after 24 h, increasing to 62% after 72 h. Primary human cells (mixed donor $CD34^+$ HSPCs derived from umbilical cord blood, PBMCs), demonstrated similar increases in transfection efficiency over time, with 15% and 20% eGFP expression and 85% and 92% viability, respectively, after 72 h (**Figure 4.5**). We also observed positive eGFP-expression in PBMCs 12 h post-acoustofluidic delivery (**Figure 4.S6**). Since there are a limited number of cells in a batch of mixed donor HSPCS, the cell density of $CD34^+$ HSPCs was reduced to 500,000 cells/mL in order to obtain data in triplicate. Fluorescence microscopy of $CD34^+$ HSPCs confirmed eGFP expression, revealing bright fluorescence intensity compared to the "no acoustofluidics" control (**Figure 4.S7**). Furthermore, the acoustofluidic treatment of Jurkat cells yielded comparable efficiencies to electroporation-mediated eGFP plasmid delivery.[45] While delivery to primary cell types showed lower efficiency, we expect that optimization of device parameters and delivery media for each cell type will enhance levels of gene expression.[46]

The high viabilities observed here indicate that cells could be circulated through multiple rounds of acoustofluidic treatment in order to boost efficiency further. Likewise, multiple parallel channels can be driven by a single acoustic source in order to increase throughput substantially. Avoiding viral methods increases safety, adds flexibility to the

biomolecular cargo delivered, and should significantly reduce the cost for clinical and research applications of gene delivery.

4.D Conclusions and Prospects

We developed a gene-delivery platform that utilizes acoustofluidic-mediated sonoporation to facilitate DNA uptake across the plasma membranes of target cells. With optimization of our device, we demonstrated plasmid delivery from model cells (Jurkat) to clinically relevant cell types (PBMCs, $CD34^+$ HSPCs) with throughputs of 200,000 cells/min and viabilities exceeding 80%. This device employs a facile and cost-effective design, taking advantage of a commercially available square glass capillary as the microfluidic channel, thereby circumventing the need for specialized facilities and complex microfluidic geometries. These data indicate scalable and economical acoustofluidic strategies for applications involving disease treatment. For example, successful eGFP expression in PBMCs suggests a strong potential to manufacture cells expressing chimeric antigen receptors (CAR) for cancer immunotherapies. Work by graduate student researcher Yao Gong following up on the aforementioned results aimed to adapt the platform for generating CAR T-cell populations. She integrated the use of supramolecular nanoparticle (SMNP) carriers to package the "sleeping beauty plasmids" designed to encode for expression of a Glypican-3 (GPC3)-targeting CAR.

Furthermore, analyses of intracellular delivery revealed disruptions of the cell membrane and the nuclear membrane of Jurkat and mouse embryonic fibroblasts, respectively. Further investigation of membrane disruption with our acoustofluidic platform will make it possible to examine membrane rupture, repair, and membrane mechanics in a

variety of cell types. These studies, along with the prospective delivery of CRISPR-Cas9 and other targeted nuclease systems, are important steps towards the implementation of the acoustofluidic platform for clinical applications of gene editing.

4.E Supplementary Materials

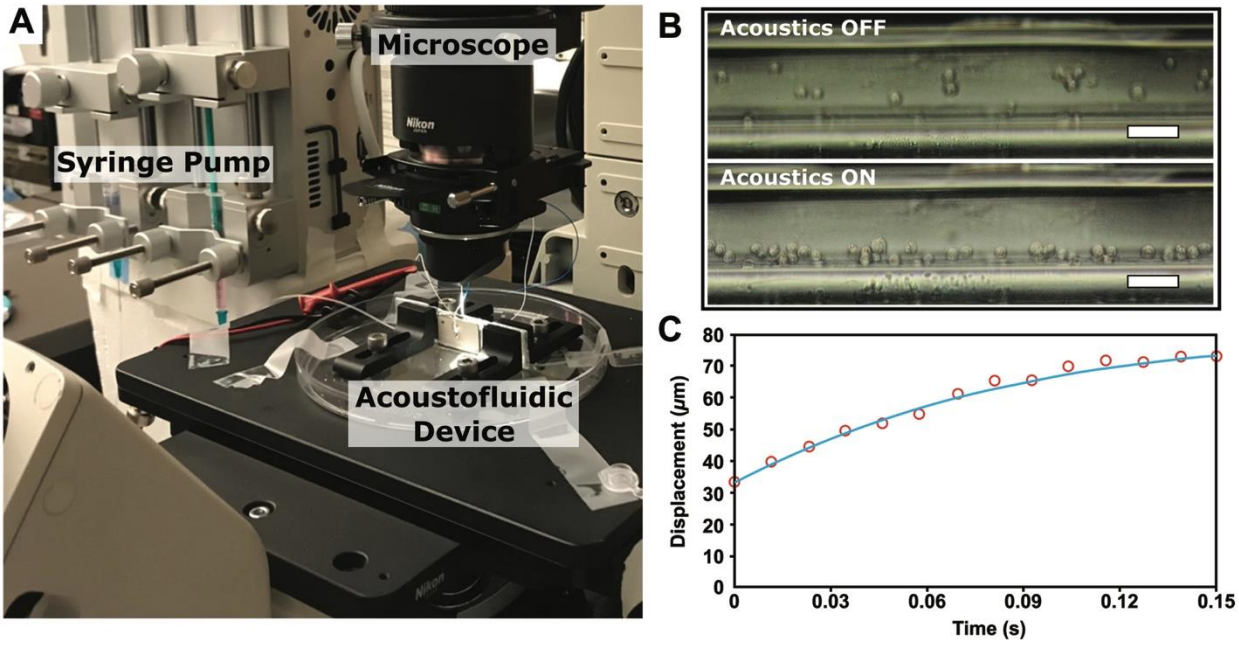

Figure 4.S1. (A) Custom stage setup to image the cross section of the glass capillary, where the acoustofluidic device is fixed vertically between two sliders that are attached to a Petri dish and placed above a microscope objective. **(B)** Images of Jurkat cells with (Acoustics ON) and without (Acoustics OFF) an applied electrical potential without flow. **(C)** Jurkat cell displacement from the transducer as a function of time. The red circles represent experimental data extracted from the recorded video of cell movement at the acoustic excitation frequency of 3.3 MHz with an amplitude of 40 V peak-to-peak. The solid line is obtained by fitting the experimental data to a theoretical cell displacement relation for resonator-based acoustic tweezers (39). From the fit curve, we can identify the acoustic energy density, and estimate the pressure amplitude and acoustic radiation force exerted on the cell. Scale bars are 50 μm.

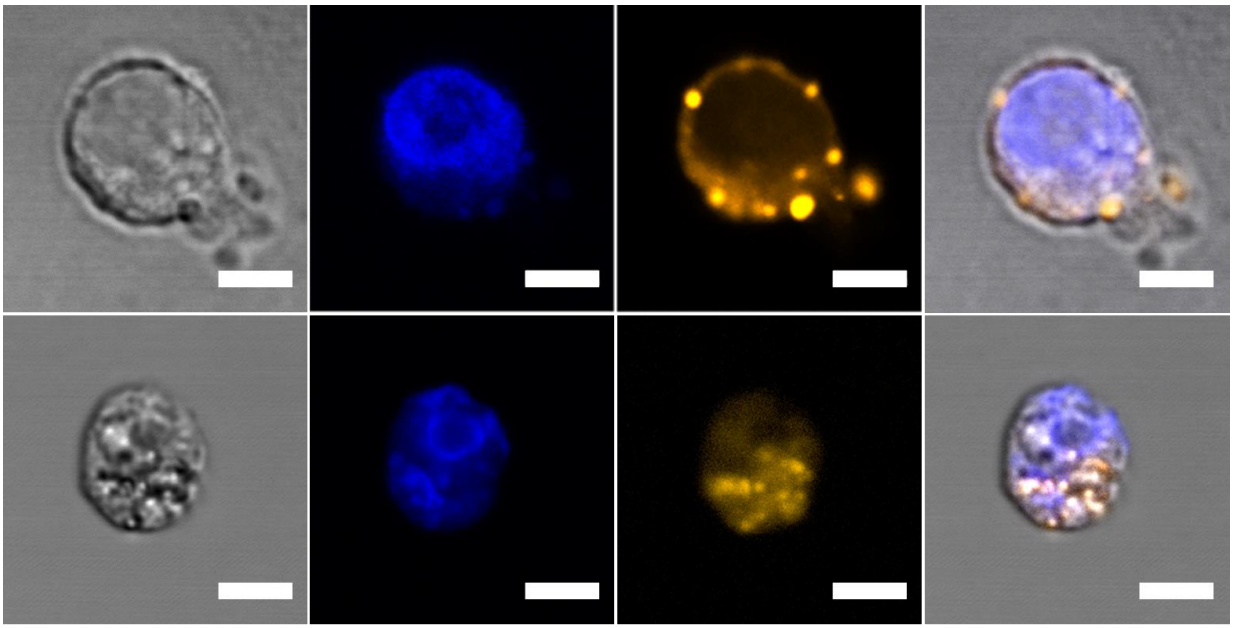

Figure 4.S2. Brightfield images and confocal laser scanning micrographs of Jurkat cells post-acoustofluidic delivery of Alexafluor 546-labeled DNA (Cy3-DNA). The Cy3-DNA (orange) is shown distributed throughout the cell cytosol, on the cell membrane, and at the cell nucleus that has been stained with DAPI (blue). Scale bars are 10 μm.

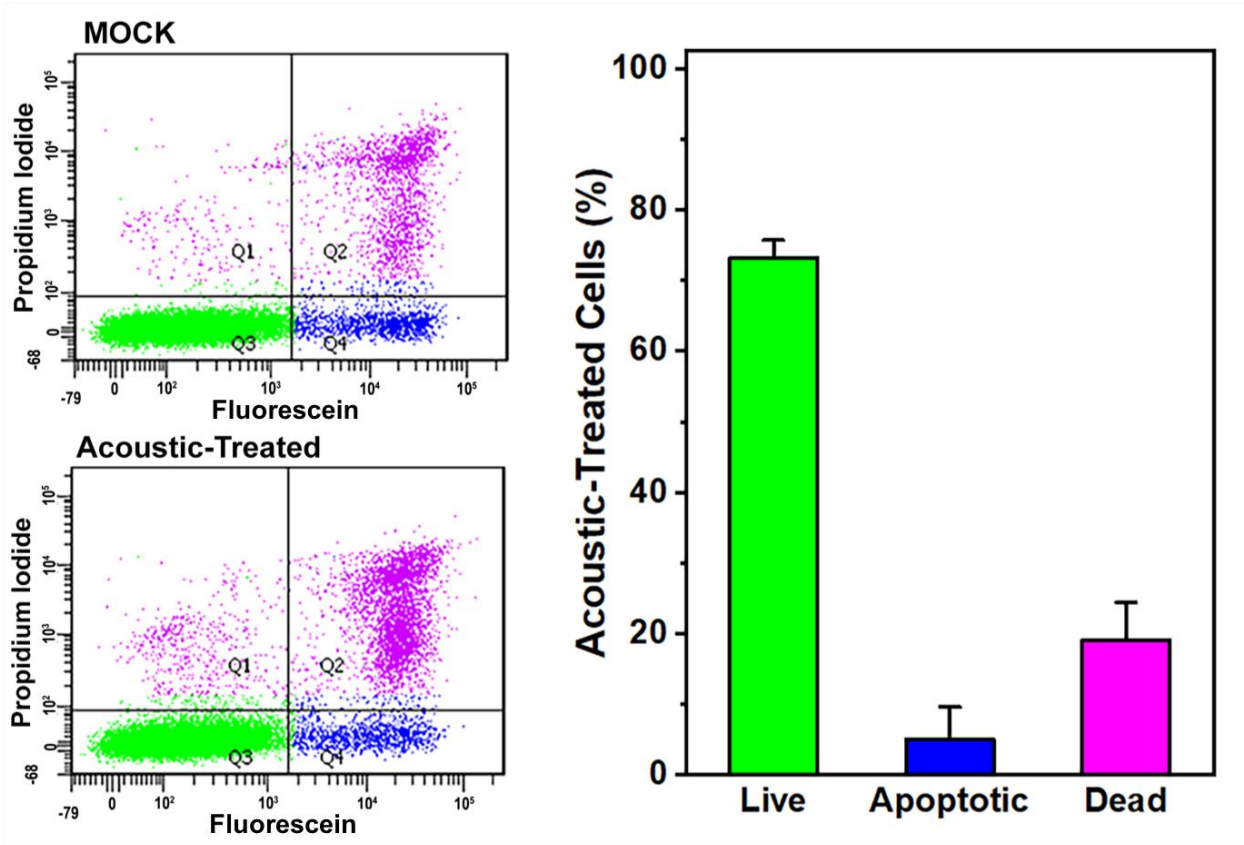

Figure 4.S3. Flow cytometric analysis of cell viability using an Annexin V-propidium iodide assay with untreated (mock) and post-acoustofluidic-treated Jurkat cells. Representative density plots with gating for mock and acoustic samples are shown on the left and the data are expressed as the mean and standard deviation for N=5.

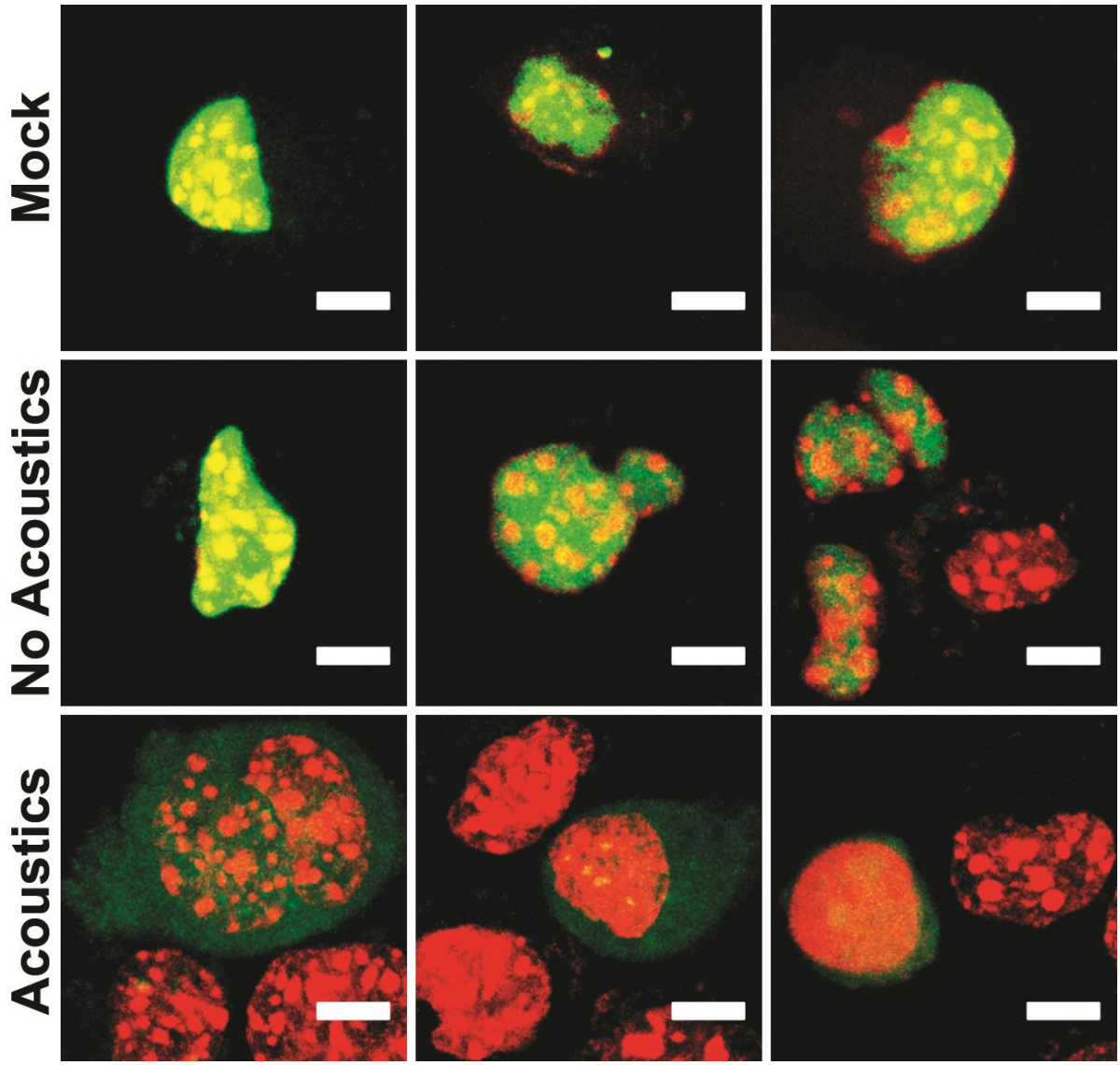

Figure 4.S4. Confocal laser scanning micrographs of mouse embryonic fibroblasts (MEFs) at 100× magnification, showing colocalization events of green fluorescent protein fused to a nuclear localization signal (NLS-GFP) and DAPI signals in the untreated (Mock), no acoustics (No Acoustics), and acoustic-treated (acoustics) samples. The MEFs are virally transduced to express GFP at their nuclei (green) and are stained post-acoustofluidic treatment with DAPI to label the cell nuclei (red). Co-localization of NLS-GFP and DAPI signals are shown in the overlay of the mock and no-acoustics samples and lack thereof (as shown in the acoustic-treated samples) is evidence of nuclear membrane rupture. Scale bars are 10 μm.

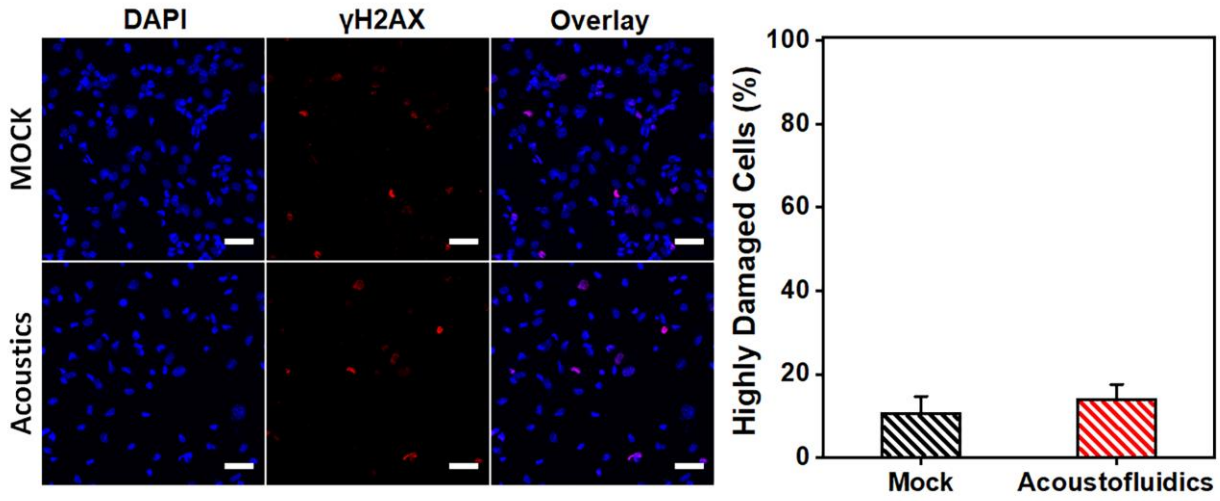

Figure 4.S5. Immunofluorescence microscopy of untreated (mock), and acoustofluidic-treated mouse embryonic fibroblasts that had been fixed and then stained with an antibody against the DNA damage marker γH2AX (red) and nuclear stain DAPI (blue). Highly damaged cells are identified as having >7 labeled DNA foci and data are expressed as mean and standard deviation for N=3. Scale bars are 50 μm.

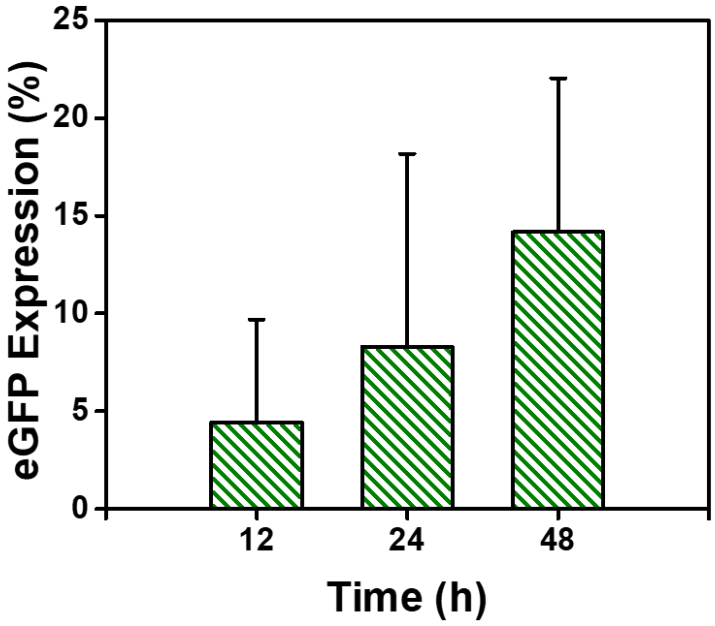

Figure 4.S6. Time response of enhanced green fluorescent protein (eGFP) expression measured over a 48 h period post-acoustofluidic delivery of an eGFP-expression plasmid to peripheral blood mononuclear cells. Data are expressed as mean and standard deviation for N=3.

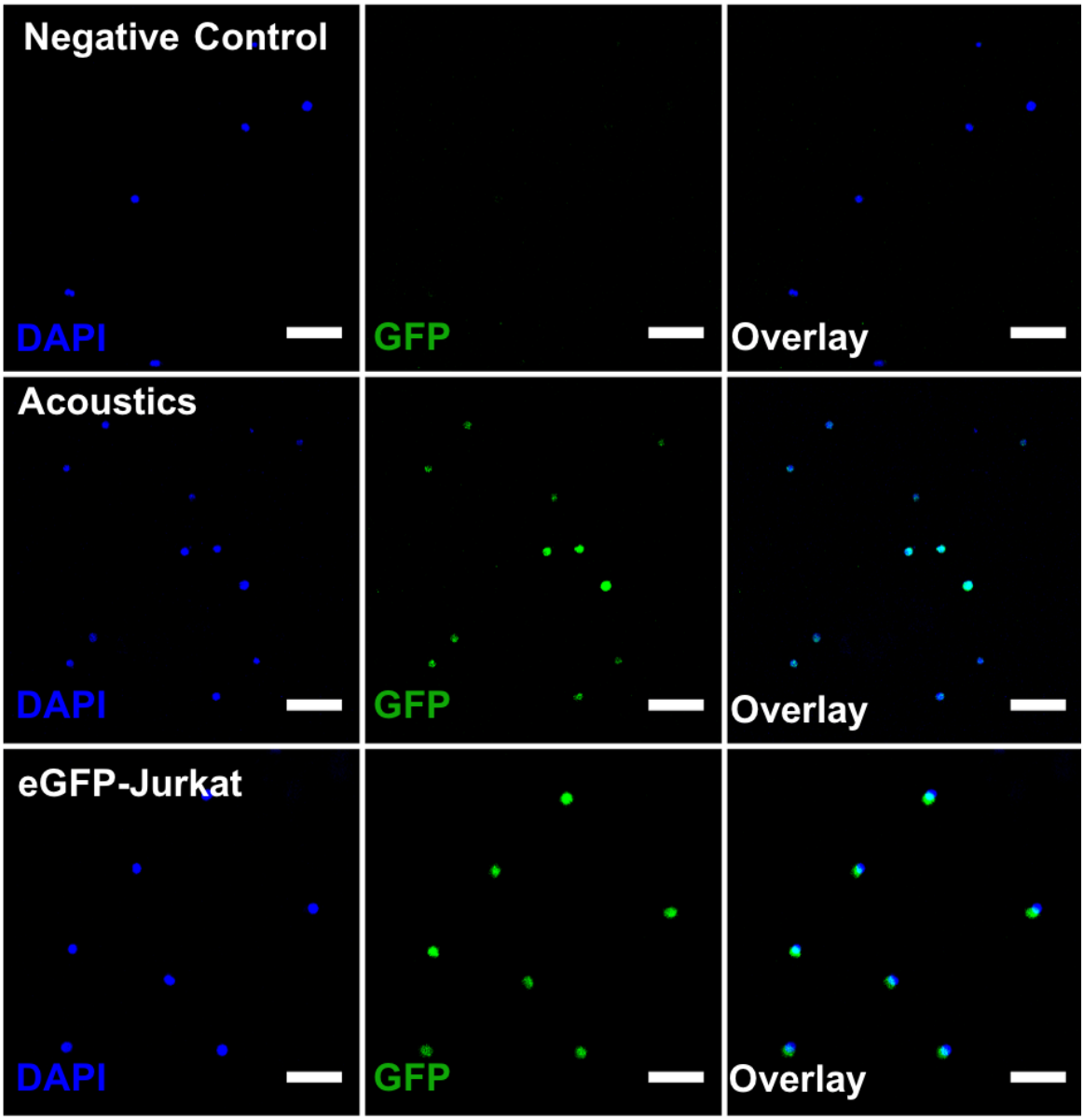

Figure 4.S7. Confocal laser scanning micrographs of untreated mixed donor umbilical cord blood $CD34^+$ hematopoietic stem and progenitor (CD34+) cells (Negative Control), 72 h post-acoustofluidic delivery of an enhanced green fluorescent protein-expressing plasmid (GFP) to CD34+ cells (Acoustics), and an eGFP-expressing Jurkat cell line (eGFP-Jurkat) as a positive control. A nuclear stain (DAPI) was used to determine cell location. Scale bars are 50 μm.

4.F References

(1) Hoban, M. D.; Bauer, D. E. A Genome Editing Primer for the Hematologist. *Blood* **2016**, *127*, 2525–2535.

(2) Dunbar, C. E.; High, K. A.; Joung, J. K.; Kohn, D. B.; Ozawa, K.; Sadelain, M. Gene Therapy Comes of Age. *Science* **2018**, *359*, eaan4672.

(3) Thomas, C. E.; Ehrhardt, A.; Kay, M. A. Progress and Problems with the use of Viral Vectors for Gene Therapy. *Nat. Rev. Genet.* **2003**, *4*, 346–358.

(4) Hsu, P. D.; Lander, E. S.; Zhang, F. Development and Applications of CRISPR-Cas9 for Genome Engineering. *Cell* **2014**, *157*, 1262–1278.

(5) Rui, Y.; Wilson, D. R.; Green, J. J. Non-Viral Delivery to Enable Genome Editing. *Trends Biotechnol.* **2018**, *37*, 281–293.

(6) Hu., J.; Davis, K.; Liu, D. Chemical Biology Approaches to Genome Editing: Understanding, Controlling, and Delivering Programmable Nucleases. *Cell Chem. Biol.* **2016**, *23*, 57–73.

(7) Rees, H. A.; Komor, A. C.; Yeh, W. H.; Caetano-Lopes, J.; Warman, M.; Edge, A. S. B.; Liu, D. R. Improving the DNA Specificity and Applicability of Base Editing through Protein Engineering and Protein Delivery. *Nat. Commun.* **2017**, *8*, doi: 10.1038/ncomms1.

(8) Anzalone, A. V.; Randolph, P. B.; Davis, J. R.; Sousa, A. A.; Koblan, L. W.; Levy, J. M.; Chen, P. J.; Wilson, C.; Newby, G. A.; Raguram, A.; Liu, D. R. Search-and-Replace Genome Editing without Double-Strand Breaks or Donor DNA. *Nature* **2019**, *576*, 149–157.

(9) Stewart, M. P.; Sharei, A.; Ding, X.; Sahay, G.; Langer, R.; Jensen, K. F. *In Vitro* and *Ex Vivo* Strategies for Intracellular Delivery. *Nature* **2016**, *538*, 183–192.

(10) Stewart, M. P.; Langer, R.; Jensen, K. F. Intracellular Delivery by Membrane Disruption: Mechanisms, Strategies, and Concepts. *Chem. Rev.* **2018**, *118*, 409–7531.

(11) Tabar, M. S.; Hesaraki, M.; Esfandiari, F.; Samani, F. S.; Vakilian, H.; Baharvand, H. Evaluating Electroporation and Lipofectamine Approaches for Transient and Stable Transgene Expressions in Human Fibroblasts and Embryonic Stem Cells. *Cell J.* **2015**, *17***,** 438–450.

(12) Mout, R.; Ray, M.; Tonga, G. Y.; Lee, Y. W.; Tay, T.; Sasaki, K.; Rotello, V. M. Direct Cytosolic Delivery of CRISPR/Cas9-Ribonucleoprotein for Efficient Gene Editing. *ACS Nano* **2017**, *11***,** 2452–2458.

(13) Q. Xu, Review of Microinjection Systems. Micromachines for Biological Micromanipulation, eds. M. Moldvai, B. Hal (Springer, Cham), **2018**, pp 15–47.

(14) Morgan, R. A.; Gray, D.; Lomova, A.; Kohn, D. B. Hematopoietic Stem Cell Gene Therapy: Progress and Lessons Learned. *Cell Stem Cell* **2017**, *21***,** 574–590.

(15) Shaw, K. L.; Garabedian, E.; Mishra, S.; Barman, P.; Davila, A.; Carbonaro, D.; Shupien, S.; Silvin, C.; Geiger, S.; Nowicki, B.; Smogorzewska, E. M.; Brown, B.; Wang, X.; De Oliveira, S.; Choi, Y.; Ikeda, A.; Terrazas, D.; Fu, P. Y.; Yu, A.; Fernandez, B. C.; Cooper, A. R.; Engel, B.; Podsakoff, G.; Balamurugan, A.; Anderson, S.; Muul, L.; Jagadeesh, G. J.; Kapoor, N.; Tse, J.; Moore, T. B.; Purdy, K.; Rishi, R.; Mohan, K.; Skoda-Smith, S.; Buchbinder, D.; Abraham, R. S.; Scharenberg, A.; Yang, O. O.; Cornetta, K.; Gjertson, D.;

Hershfield, M.; Sokolic, R.; Candotti, F.; Kohn, D. B. Clinical Efficacy of Gene-Modified Stem Cells in Adenosine Deaminase-Deficient Immunodeficiency. *J. Clin. Invest.* **2017**, *127*, 1689–1699.

(16) Sharei, A.; Zoldan, J.; Adamo, A.; Sim, W. Y.; Cho, N.; Jackson, E.; Mao, S.; Schneider, S.; Han, M. J.; Lytton-Jean, A.; Basto, P. A.; Jhunjhunwala, S.; Lee, J.; Heller, D. A.; Kang, J. W.; Hartoularos, G. C.; Kim, K. S.; Anderson, D. G.; Langer, R.; Jensen, K. F. A Vector-Free Microfluidic Platform for Intracellular Delivery. *Proc. Natl. Acad. Sci. U. S. A.* **2013**, *110*, 2082–2087.

(17) Han, X.; Liu, Z.; Jo, M. C.; Zhang, K.; Li, Y.; Zeng, Z.; Li, N.; Zu, Y.; Qin, L. CRISPR-Cas9 Delivery to Hard-to-Transfect Cells via Membrane Deformation. *Sci. Adv.* **2015**, *1*, e1500454.

(18) Ding, X.; Stewart, M. P.; Sharei, A.; Weaver, J. C.; Langer, R. S.; Jensen, K. F. High-Throughput Nuclear Delivery and Rapid Expression of DNA via Mechanical and Electrical Cell-Membrane Disruption. *Nat. Biomed. Eng.* **2017**, *1*, doi:10.1038/s41551-017-0039

(19) DiTommaso, T.; Cole, J. M.; Cassereau, L.; Buggé, J. A.; Sikora Hanson, J. L.; Bridgen, D. T.; Stokes, B. D.; Loughhead, S. M.; Beutel, B. A.; Gilbert, J. B.; Nussbaum, K.; Sorrentino, A.; Toggweiler, J.; Schmidt, T.; Gyuelveszi, G.; Bernstein, H.; Sharei, A. Cell Engineering with Microfluidic Squeezing Preserves Functionality of Primary Immune Cells in Vivo. *Proc. Natl. Acad. Sci. U. S. A.* **2018**, *115*, E10907–E10914.

(20) Fechheimer, M.; Boylan, J. F.; Parker, S.; Sisken, J. E.; Patel, G. L.; Zimmer, S. G.

Transfection of Mammalian Cells with Plasmid DNA by Scrape Loading and Sonication Loading. *Proc. Natl. Acad. Sci. U. S. A.* **1987**, *84*, 8463–8467.

(21) Bao, S.; Thrall, B. D.; Miller, D. L. Transfection of a reporter plasmid into cultured cells by sonoporation in vitro. *Ultrasound Med. Biol.* **1997**, *23***,** 953–959.

(22) Helfield, B.; Chen, X.; Watkins, S. C.; Villanueva, F. S. Biophysical Insight Into Mechanisms of Sonoporation. *Proc. Natl. Acad. Sci. U.S.A.* **2016**, *113***,** 9983–9988.

(23) Miller, D. L.; Pislaru, S. V.; Greenleaf, J. F. Sonoporation: Mechanical DNA Delivery by Ultrasonic Cavitation. *Somatic Cell Mol. Genet.* **2002**, *27***,** 115–134.

(24) Ozcelik, A.; Rufo, J.; Guo, F.; Gu, Y.; Li, P.; Lata, J.; Huang, T. J. Acoustic Tweezers for the Life Sciences. *Nature Methods* **2018**, *15*, 1021–1028.

(25) Rodamporn, S.; Harris, N. R.; Beeby, S. P.; Boltryk, R. J.; Sanchez-Eisner, T. HeLa Cell Transfection Using a Novel Sonoporation System. *IEEE Trans. Biomed. Eng.* **2011**, *58***,** 927–934.

(26) Carugo, D.; Ankrett, D. N.; Glynne-Jones, P.; Capretto, L.; Boltryk, R. J.; Zhang, X.; Townsend, P. A.; Hill, M. Contrast Agent-Free Sonoporation: The Use of an Ultrasonic Standing Wave Microfluidic System for the Delivery of Pharmaceutical Agents. *Biomicrofluidics* **2011**, *5*, 044108.

(27) Ramesan, S.; Rezk, A. R.; Dekiwadia, C.; Cortez-Jugo, C.; Yeo, L. Y. Acoustically-Mediated Intracellular Delivery. *Nanoscale* **2018**, *10***,** 13165–13178.

(28) Ramesan, S.; Rezk, A. R.; Yeo, L. Y. High Frequency Acoustic Permeabilisation of Drugs

Through Tissue for Localised Mucosal Delivery. *Lab. Chip* **2018**, *18***,** 3272–3284.

(29) Zhang, Z.; Wang, Y.; Zhang, H.; Tang, Z.; Liu, W.; Lu, Y.; Wang, Z.; Yang, H.; Pang, W.; Zhang, H.; Zhang, D.; Duan, X. Hypersonic Poration: A New Versatile Cell Poration Method to Enhance Cellular Uptake Using a Piezoelectric Nano-Electromechanical Device. *Small* **2017**, *13*, 1602962.

(30) Chen, N. Y.; Kim, P.; Weston, T. A.; Edillo, L.; Tu, Y.; Fong, L. G.; Young, S. G. Fibroblasts Lacking Nuclear Lamins Do Not Have Nuclear Blebs or Protrusions but Nevertheless Have Frequent Nuclear Membrane Ruptures. *Proc. Natl. Acad. Sci. U. S. A.* **2018**, *115*, 10100–10105.

(31) Chen, N. Y.; Yang, Y.; Weston, T. A.; Belling, J. N.; Heizer, P.; Tu, Y.; Kim, P.; Edillo, L.; Jonas, S. J.; Weiss, P. S.; Fong, L. G.; Young, S. G. An Absence of Lamin B1 in Migrating Neurons Causes Nuclear Membrane Ruptures and Cell Death. *Proc. Natl. Acad. Sci. U. S. A.* **2019**, *116*, 25870–25879.

(32) Hoban, M. D.; Romero, Z.; Cost, G. J.; Mendel, M.; Holmes, M.; Kohn, D. B. Delivery of Genome Editing Reagents to Hematopoietic Stem/Progenitor Cells. *Curr. Protoc. Stem Cell Biol.* **2016**, 5B.4.1-5B.4.10.

(33) Gossett, D. R.; Tse, H. T. K.; Lee, S. A.; Ying, Y.; Lindgren, A. G.; Yang, O. O.; Rao, J.; Clark, A. T.; Di Carlo, D. Hydrodynamic Stretching of Single Cells for Large Population Mechanical Phenotyping. *Proc. Natl. Acad. Sci. U. S. A.* **2012**, *109*, 7630–7635.

(34) Schindelin, J.; Arganda-Carreras, I.; Frise, E.; Kaynig, V.; Longair, M.; Pietzsch, T.; Cardona, A. Fiji: An Open-Source Platform for Biological-Image Analysis. *Nature*

Methods **2012**, *9*, 676–682.

(35) Guo, F.; Mao, Z.; Chen, Y.; Xie, Z.; Lata, J. P.; Li, P.; Ren, L.; Liu, J.; Yang, J.; Dao, M.; Suresh, S.; Huang, T. J. Three-Dimensional Manipulation of Single Cells Using Surface Acoustic Waves. *Proc. Natl. Acad. Sci. U. S. A.* **2016**, *113*, 1522–1527.

(36) Lentacker, I.; De Cock, I.; Deckers, R.; De Smedt, S. C.; Moonen, C. T. W. Understanding Ultrasound Induced Sonoporation: Definitions and Underlying Mechanisms. *Adv. Drug Delivery Rev.* **2014**, *72*, 49–64.

(37) Krasovitski, B.; Frenkel, V.; Shoham, S.; Kimmel, E. Intramembrane Cavitation as a Unifying Mechanism of Ultrasound-Induced Bioeffects. *Proc. Natl. Acad. Sci. U.S.A.* **2011**, *108*, 3258–3263.

(38) Delalande, A.; Kotopoulis, S.; Postema, M.; Midoux, P.; Pichon, C. Sonoporation: Mechanistic Insights and Ongoing Challenges for Gene Transfer. *Gene* **2013**, *525*, 191–199.

(39) Delalande, A.; Leduc, C.; Midoux, P.; Postema, M.; Pichon, C.; Efficient Gene Delivery by Sonoporation is Associated with Microbubble Entry into Cells and the Clathrin-Dependent Endocytosis Pathway. *Ultrasound Med. Biol.* **2015**, *41*, 1913–1926.

(40) Shah, P.; Wolf, K.; Lammerding, J. Bursting the Bubble - Nuclear Envelope Rupture as a Path to Genomic Instability? *Trends Cell. Biol.* **2017**, *27*, 546–555.

(41) Dean, D. A.; Strong, D. D.; Zimmer, W. E. Nuclear Entry of Nonviral Vectors. *Gene Ther.* **2005**, *12*, 881–890.

(42) Denais, C. M.; Gilbert, R. M.; Isermann, P.; McGregor, A. L.; te Lindert, M.; Weigelin, B.; Davidson, P. M.; Friedl, P.; Wolf, K.; Lammerding, J. Nuclear Envelope Rupture and Repair during Cancer Cell Migration. *Science* **2016**, *352*, 353–358.

(43) Cox, D. B. T.; Platt, R. J.; Zhang, F. Therapeutic Genome Editing: Prospects and Challenges. *Nat. Med.* **2015**, *21*, 121–131.

(44) Lim, S.; Quinton, R.; Ganem, N. Nuclear Envelope Rupture Drives Genome Instability in Cancer. *Mol. Biol. Cell* **2016**, *27*, 3210–3213.

(45) Li, L. H.; Shivakumar, R.; Feller, S.; Allen, C.; Weiss, J. M.; Dzekunov, S.; Singh, V.; Holaday, J.; Fratantoni, J.; Liu, L. N. Highly Efficient, Large Volume Flow Electroporation. *Technol. Cancer Res. Treat.* **2002**, *1*, 341–349.

(46) Jordan, E. T.; Collins, M.; Terefe, J.; Ugozzoli, L.; Rubio, T. Optimizing Electroporation Conditions in Primary and Other Difficult-to-Transfect Cells. *J. Biomol. Tech.* **2008**, *19*, 328–334.

CHAPTER 5

In Situ Shape Control of Thermoplasmonic Gold Nanostars on Oxide Substrates for Hyperthermia-Mediated Cell Detachment

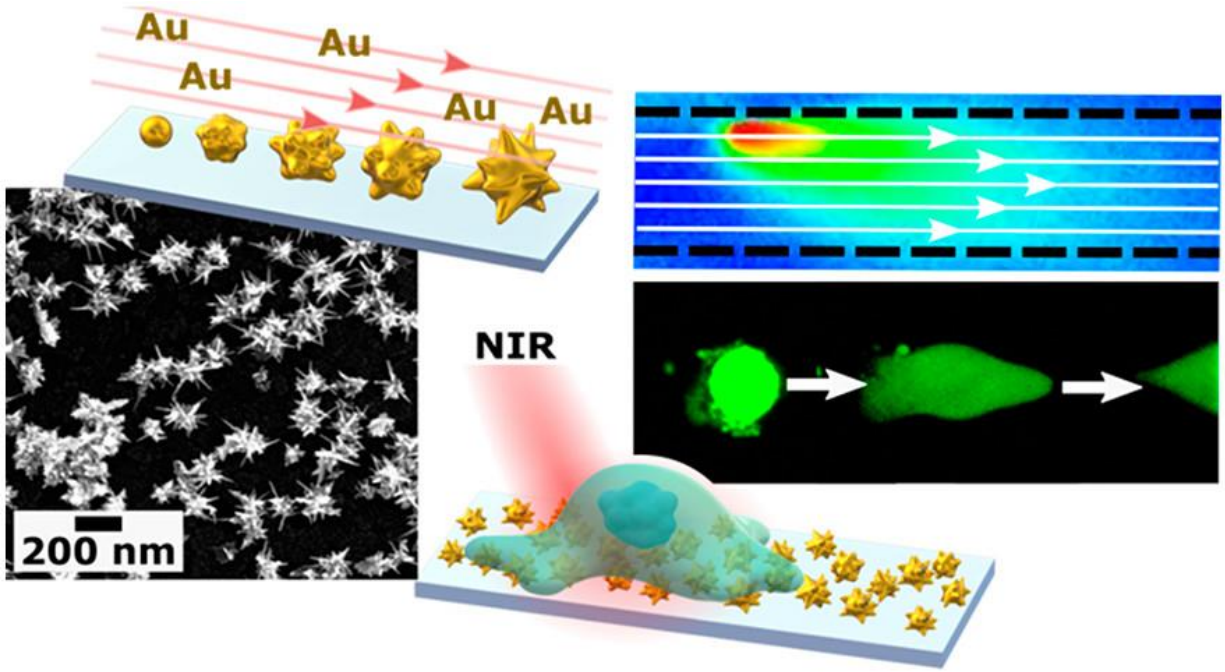

The information in this chapter was published in *ACS Central Science* **2020**, *11*, 2105–2116 and is reproduced here with permission.

Authors: Vinnacombe-Willson, G. A.; Chiang, N.; Scarabelli, L.; Hu, Y.; **Heidenreich, L. K.**; Li, X.; Gong, Y.; Inouye, D. T.; Fisher, T. S.; Weiss, P. S.; Jonas, S. J.

5.A Introduction

Gold nanoparticles (AuNPs) with dimensions smaller than the wavelengths of incident light can produce intense nanoscale electromagnetic field enhancement. Together with their biocompatibility and chemical stability, the plasmonic properties of AuNPs offer unique opportunities for a variety of biomedical applications.[1-3] When the AuNPs are illuminated with light of a frequency pertaining to their dimensions, there are collective excitations of the conduction electrons known as localized surface plasmon resonances (LSPRs). The plasmon resonance oscillation frequencies can be tuned by altering particle size, shape, and local dielectric environment.[4] Developments in bottom-up wet chemical synthetic methodologies, in particular the seed-mediated growth method, have improved the accessibility of uniform colloidal suspensions of nanoparticles with well-controlled shapes.[4-9] In a method known as seed-mediated growth, gold nucleation sites, or "seeds", are formed from gold salt reduction and are subsequently added to a growth solution that contains additional gold precursor and shape-directing reagents. This process produces colloidal suspensions of AuNPs with shapes such as rods, shells, cages, and stars, which have LSPRs in the near-infrared (NIR) biological window.[10] This range of wavelengths, from about 650 to 1350 nm, is also known as the therapeutic window and is of interest because these wavelengths of light have the greatest penetration depth in tissue.[77] Nonradiative plasmon-phonon coupling enables rapid local thermalization in these structures,[11] and this property has been leveraged for numerous studies focused on tissue-nanoparticle interactions.[12-15] Among these NIR-responsive morphologies, gold nanostars (AuNSTs) have gained particular

interest due to the significant electromagnetic field enhancement at their sharp points,[16,17] high NIR extinction, and large surface areas.[18,19]

Many researchers have integrated plasmonic nanostructures into solid-state systems such as sensors,[20-22] cargo delivery platforms,[23,24] substrates for light-responsive cell retrieval,[25,26] materials for combined cancer cell hyperthermia/chemotherapies,[12,27,28] and fundamental studies on phenomena resulting from plasmonic heating (*e.g.*, bubble generation).[29-31] There exist several strategies for the integration of nanoparticles into such systems. Common approaches toward achieving surface decoration with crystalline nanoparticle products include direct functionalization with presynthesized nanoparticles (*i.e.*, applying self-assembly, lithography, or a combination of the two)[32-36] and direct nanoparticle synthesis[37-43] on the desired substrate. Despite significant developments, nanoparticle integration approaches still face challenges accessing different substrate geometries, such as fluidic tubing and curved features, which are of broad interest for developing substrates that uniquely interact with light, microfluidic platforms, and plasmonic scaffolds for biological studies.[44] The development of a robust method for generating substrates functionalized with size and shape controlled nanoparticles at high density remains elusive and an active research challenge.[45]

Here, we report a facile method for the generation of AuNSTs on oxide substrates by applying a versatile silane functionalization method and bottom-up wet chemical synthesis. Protocols for the synthesis of AuNST colloidal suspensions were adapted by first grafting colloidally synthesized seeds and performing subsequent shape control *in situ* by submerging the functionalized surface in a growth solution. Within a microfluidic capillary, the flow rate and incubation time of the growth solution were used to control the

morphology and aspect ratio of the AuNSTs. Systematically varying flow parameters, we achieved highly branched nanostructures with configurable aspect ratios in the microfluidic capillary. These structures exhibit efficient light-to-heat conversion when irradiated with NIR light. The mesoscale heating of the microcapillary can be controlled by adjusting the laser power, as well as by flowing water into AuNST-decorated microcapillaries at different rates. Changes in the overall mesoscale temperature were correlated with phenomena at the local nanoscale environment through simultaneous thermal and surface-enhanced Raman scattering (SERS) measurements. Moreover, these nanostructures are interesting and useful for a variety of biomedical applications, such as photothermal therapy, due to their plasmonic response to NIR light and biocompatibility; thus, we applied this system to interrogate the response of adhered glioblastoma cells to AuNST localized heating and identified conditions that facilitate the systematic detachment of single cells from the capillary walls. Cellular responses, such as reshaping, necrosis/membrane permeabilization, and rapid cell ablation were dependent on local heating and flow conditions. Our results suggest that this plasmonic nanostructure-integrated microfluidic platform offers new solutions for small-molecule sensing,[20] intracellular delivery via cellular membrane poration,[24,46] or the targeted retrieval of single cells in adherent cultures, representing a starting point for the development of devices capable of cell capture and targeted, selective light-triggered release.[25,26]

5.B Experimental Methods

5.B.1 Materials

All analytical grade reagents, silver nitrate ($AgNO_3$; 99%, CAS: 7761-88-8), $HAuCl_4 \cdot 3H2O$ (99%, CAS: 16961-25-4) L-ascorbic acid (AA, 99%, CAS: 50-81-7), *N*-dodecyl-*N*,*N*-dimethyl-3-ammonio-1-propanesulfonate (LSB; 99%, CAS: D0431), hydrochloric acid (HCl; ACS Reagent 37%, CAS: 7647-01-0), (3-aminopropyl)triethoxysilane (APTES, 99%, CAS: 919-30-2), cetyltimethylammonium chloride (CTAC; 25 wt % in H2O, CAS: 112-02-7) and thiophenol (99%, CAS: 108-98-5) were purchased from Millipore Sigma. Piranha solution (3:1 98% sulfuric acid, CAS: 7664-93-9, and 30% hydrogen peroxide, CAS: 7722-84-1; Fisher Scientific) was used for cleaning glass capillaries. *Warning:* Piranha mixture is dangerous as it violently reacts with organics and should be handled with caution. High-performance liquid chromatography (HPLC)-grade sub-micron filtered water (CAS: 67-63-0) and 200 proof ethanol (CAS: 64-17-5) were obtained from Fisher Scientific. All glassware and magnetic stir bars used for synthesis were cleaned thoroughly with *aqua regia* (3:1 concentrated HCl to HNO_3, Millipore Sigma) and rinsed with HPLC-grade water before use (nitric acid: 15.8 M, Fisher Scientific, CAS: 7697-37-2). *Note: Aqua regia* solution is extremely corrosive and reactive. Care is needed in its preparation and usage.

5.B.2 Colloidal Gold Nanostar Synthesis

The gold nanostar (AuNST) synthesis was carried out using a seed-mediated growth method.[50] First, CTAC-capped seeds were prepared by adding 4.7 mL of 0.1 M CTAC with 25 µL $HAuCl_4$, followed by injection of 300 µL of 10 mM NaBH4 under vigorous magnetic stirring, yielding a light brown product. A separate growth solution containing 4 mL of 0.1 M

LSB, 60 μL of 50 mM $HAuCl_4 \cdot 3H2O$, 60 μL of 10 mM $AgNO_3$, and 40 μL of 1 M HCl was prepared. An aliquot of 200 μL of 100 mM AA was added to the solution and stirred by hand until the solution turned clear. This step is immediately followed by the addition of 8 μL of the seed solution and stirred by hand. The growth solution is then observed to turn from a clear color, to pink, purple, and finally to a dark blue color.

5.B.3 Preparation of Functionalized Glass Capillaries

Glass capillaries (VitroCom, Product No.: 5010-050) 1 mm × 100 μm were cleaned with piranha solution for 30 min, sonicated four times with HPLC-grade water, then once 5 min in ethanol (each sonication step for 5 min). The capillaries were then oven-dried. Due to the size of the capillaries, there is a chance that residual piranha might remain following the rinsing steps. To ensure that all of piranha solution is completely inactivated, the capillaries should be carefully dried at 60-120 °C for at least a day. Moreover, it is extremely important to ensure the capillaries are completely dry and free of any water prior to silane functionalization, otherwise the APTES will polymerize to a significant degree (leading to cloudy residue in the capillary). Once completely dried, the capillaries were functionalized with APTES by placing them in a vial containing APTES solution (5% v/v in ethanol), where the functionalization was performed at 60 °C for 5 min. Following functionalization, the capillaries were sonicated in ethanol three times for 5 min each and stored in ethanol as the functionalized capillaries will degrade over time if stored in air. Due to the small internal diameter of the microcapillaries, it is important to ensure that the solutions wet the entire length of the capillaries for each step. Brief sonication can be used to remove bubbles that may form internally during processing. Note that APTES is also air sensitive; for best results, the solution should be handled/stored under inert gas.

5.B.4 *In situ* Growth of Gold Nanostars in Glass Capillaries

The APTES-functionalized capillaries were dried with nitrogen before use, and 5-minute epoxy (Devcon, No. 14240) was used to secure tubing ~6 cm in length (Cole Parmer, Tygon S3-B-44-4X) onto each end of the capillary. The capillary was inserted ~1-2 mm into the tubing to prevent the epoxy from obstructing the microfluidic inlet and outlet. This assembly was secured to four glass slides to prevent the capillary from breaking during handling. The epoxy was allowed to dry overnight, and the capillary with tubing was rinsed twice by hand with a 5 mL syringe of HPLC water before the growth step. A solution of CTAC-coated seeds was flowed into the capillary at 0.1 mL/min using a syringe pump (Harvard, Chemyx 400) for 1 h. The capillary was then gently hand-rinsed with water using a syringe. The 4 mL growth solution (without seeds or AA) was prepared as described previously. The AA aliquot was added quickly and mixed well, at which point the solution appeared clear, as opposed to yellow (an indication the solution should be remade). Once combined, this growth solution was flowed through the capillary at the specified flow rate (0.63 mL/min – 0.5 mL/min). The growth was continued for 3 min after which the pump was stopped, and the capillaries were immediately rinsed with MilliQ water by hand two times using a syringe to remove any residual growth solution. During the flow step, the start of the growth time was recorded when the growth solution reached the capillary, which can take 15–30 s depending on the exact tubing length. During flow, the solution coming from the outlet was monitored to ensure it was clear, rather than red/blue, which would indicate nucleation in the solution due to insufficient rinsing of the seed solution out of the capillary. The final products appeared dark blue in color within the capillary.

5.B.5 Characterization of Gold Nanostars

An ultraviolet (UV)-visible spectrophotometer (Agilent, Cary 8454) was used for spectroscopic characterization of colloidal solutions and capillaries. Transmission electron microscopy (TEM; 120 kV, Technai T12) was used to determine the aspect ratio and distribution of products synthesized in solution. Samples were prepared by centrifuging 10 mL of the final solution at 15,000 rpm for 20 min, followed by removal of the supernatant.

Functionalization with thiolated 2000 MW poly(ethylene glycol) (PEG-SH) was performed as previously reported[50] for TEM grid preparation so that the nanoparticles could be washed multiple times without aggregating. The sample was redispersed in 10 mL of water and 1.0-1.1 mg of PEG-SH was added. The solution was left to stir on an orbital shaker for 2 h. Afterwards, the solution was washed by centrifuging 4 mL at 15,000 rpm for 20 min, removing the supernatant, and redispersing in 4 mL in milliQ water. After the final rinsing step, the particles were redispersed in 5 μL of milliQ water. A 400-mesh Cu grid with carbon support (Ted Pella, Inc., Part No.: 01844-F) was placed in a petri dish lined with parafilm, and a 5 μL drop of the washed AuNSTs was placed on the grid. The petri dish was closed and covered with parafilm to allow slow evaporation of the drop over 4 h. Scanning electron microscopy (SEM) was utilized to characterize the morphology and uniformity for the AuNSTs grown in capillaries (ZEISS Supra 40VP SEM, 3-10 kV). The AuNST on glass slides and microcapillaries were coated with an iridium thin film (~3 nm) using an Ion Beam Sputtering/Etching System (South Bay Technology, model number.) Carbon tape was used to secure the sample to the sample holder, along with copper tape to reduce charging.

5.B.6 Thermal and Surface-Enhanced Raman Scattering Measurements

Surface-enhanced Raman scattering (SERS) spectra were obtained utilizing a Renishaw InVia micro-Raman spectrometer (Renishaw PLC, Wotton-under-Edge, Gloucestershire, UK) equipped with a 1800 grooves mm^{-1} grating, Rayleigh line rejection edge filter, Peltier-cooled deep depletion CCD array detector (576 × 384 pixels). All SERS spectra were acquired with a 40× air objective and 785 nm continuous wave laser excitation with an approximate irradiation spot area of 34 μm^2 and maximum output power of about 25.0 mW. Simultaneous temperature measurements were obtained with a thermal camera (Flir A655sc, equipped with a 25 μm Close-up Infrared Lens, 25 frames per second) as shown in **Figure 5.S15**. A 5 mM solution of thiophenol in ethanol was flowed into the capillary at 0.1 mL/min over the course of 1 h to displace LSB. It is important to wait at least 8-24 h after the nanostar *in situ* growth prior to adding the thiophenol. If this step is performed immediately after growth, the nanostars may not have sufficient time to couple strongly with the APTES, which may lead to the nanostars being displaced by the thiol and washed out of the capillary.

5.B.7 Imaging Cells on Gold Nanostar Films

The cell grafting on the AuNSTs was characterized by SEM. First, the cells were fixed and stained following an established procedure.[76] Critical point drying of the cells was performed with a Tousimis Autosamdri-810 Critical Point Dryer and an iridium thin film was sputtered on the sample. Copper tape and carbon tape were again utilized to secure the sample to the substrate to improve conductivity.

5.B.8 Cell Release Studies

The LSB on the AuNSTs was displaced by flowing an ethanolic solution of 1-5 mM 11-mercapto-1-undecanol (MUD, 99%, CAS: 73768-94-2, Millipore Sigma) for 1 h into the capillary, followed by hand rinsing with MilliQ water three times. Then, 1 μg/mL fibronectin (0.1% solution, BioReagent, for cell culture, Millipore Sigma) in phosphate-buffered saline (DPBS no calcium or magnesium, Gibco™ 14190250, Fisher Scientific) was flowed into the capillary under the same flow conditions for 1 h, followed by three additional rinses with MilliQ water. Cell response to nanoscale heating was performed with the setup, shown in **Figure 5.S17**, with a Leica SP8 DIVE/FLIM laser scanning fluorescence confocal microscope (1.2×8–10 cm^2 spot area at 785 nm, 80 MHz rep rate, 35 fs pulse width; **Table 5.S2-3**) and simultaneous temperature measurements with a thermal camera (Fluke Fluke Ti450 Infrared Camera). Green fluorescent protein (GFP)-expressing U87 glioblastoma cells (U87 MG, cAP-0044) were cultured as per protocols from the American Type Culture Collection and following trypsinization were immediately introduced into the capillary (at ~103–105 cells/mL at a flow rate of 50 μL/min). The cells were allowed to incubate for at least 1 h prior to irradiation of the nanostructures. During cell release experiments under 50 μL/min flow, a bubble trap (Fluigent, CTQ-006BT) was used to prevent air bubbles from entering the capillary and removing the cells.

5.C Results and Discussion

5.C.1 *In Situ* Surface Growth of Gold Nanostars

Gold nanostars with high aspect ratios and numbers of branches efficiently produce intense localized heat in response to NIR light.[47,48] Of the various bottom-up wet-chemical

approaches for synthesizing branched nanoparticles, the seed-mediated growth method, where nucleation and growth steps are performed separately and sequentially, is one of the most promising approaches for precise nanoparticle shape control.[4-9] However, the immobilization of presynthesized nanoparticles on substrates can result in low surface density and inhomogeneous distributions.[41,45] To address this limitation, we developed a seed-mediated synthetic method, enabling direct growth of shape-controlled AuNPs uniformly on oxide substrates, based on recent methods utilized to achieve branched structures on surfaces using *in situ* shape control.[25,49] In particular, we modified a previously established batch seed-mediated growth protocol from Pallavicini and co-workers,[50] improving product reproducibility and reducing the impact of secondary nucleation (*i.e.*, uncontrolled formation of new nuclei after particle growth has already begun). In the original approach, zwitterionic surfactant LSB yields rapid growth of nanostars, utilizing kinetic control to achieve sharp tips. In their synthesis, the seeds were also capped with LSB, resulting in the requirement that reagents were kept at low temperature to avoid rapid aging and batch-to-batch variation in the position and intensity of the LSPR peaks. Therefore, we instead opted to utilize CTAC-capped seeds, which age more slowly and yield products with reproducible spectra (**Figure 5.S1**). Moreover, the addition of AA as a reducing agent in the absence of the seeds results in fast secondary nucleation, leading to the uncontrolled growth

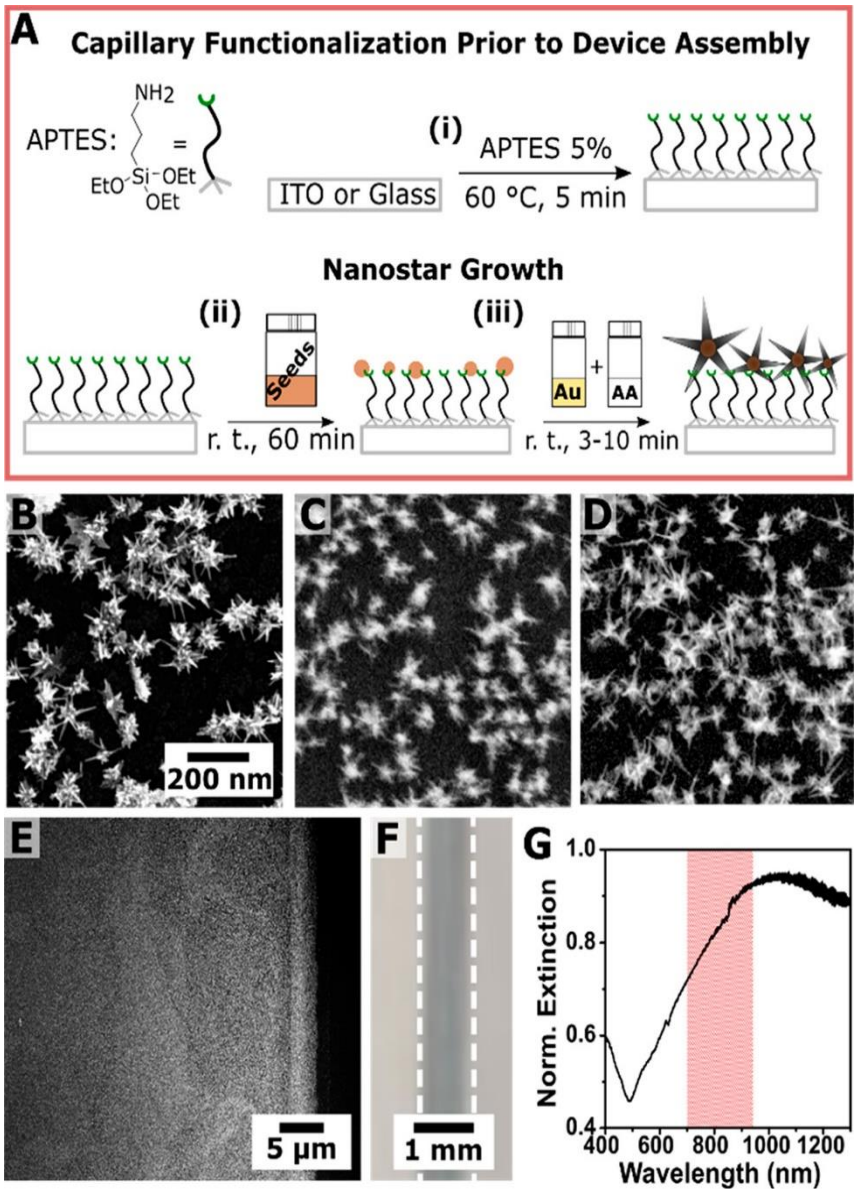

Figure 5.1. (A) Schematic of *in situ* seed-mediated gold nanostar growth: **(i)** indium tin oxide (ITO) and glass surface functionalization with aminopropyltriethoxysilane (APTES), **(ii)** attachment of catalytic seeds, and **(iii)** incubation (10 min) or flow (3 min) of growth solution containing tetrachloroauric acid, silver nitrate, laurylsulfobetaine (LSB), and ascorbic acid (AA). Scanning electron micrographs of gold nanostars on **(B)** ITO, **(C)** glass slides, and **(D, E)** within glass microcapillaries (all shown at the same scale). **(F)** Photograph showing blue capillary coloration following flow of growth solution and **(G)** ultraviolet–visible spectrum of the nanostar-coated capillary. The red area indicates the first near-infrared biological window.

of suboptimal morphologies. Thus, we further modified the growth solution through the

addition of hydrochloric acid (HCl) to slow secondary nanoparticle nucleation in solution. Ultraviolet– visible (UV-vis) kinetic data shown in **Figure 5.S2** indicate that significant nucleation does not occur for at least 20–40 min following AA addition, unless the gold seeds are added to the growth medium.

The final adjusted colloidal protocol produced three major products, as observed by transmission electron microscopy (TEM) and UV–vis spectroscopy: anisotropic spheroids, low-aspect ratio AuNSTs, and high-aspect ratio AuNSTs (**Figure 5.S3A-D**), exhibiting LSPR peaks at *ca*. 525, 650, and 875 nm, respectively. The corresponding yield of high-aspect ratio products was 20% (**Figure 5.S3E-G**). Addition of HCl slows the growth process and disfavors formation of highly branched and high aspect ratio products.[7] However, even without HCl addition, three different products are observed, indicating that the low yield of the desired products is likely due to inevitable secondary nucleation in solution. As discussed below, secondary nucleation is reduced by growing the branched structures directly on planar substrates.

The *in situ* seed-mediated AuNST growth strategy developed here takes advantage of the size of presynthesized seeds, which can be grafted easily onto a variety of oxide materials, followed by shape control *in situ*. Our *in situ* growth method approach is summarized in detail in **Figure 5.1**: (i) substrate chemical modification with APTES, (ii) grafting presynthesized gold seeds onto the APTES chemical anchor to serve as catalytic surfaces for the growth of AuNSTs, and (iii) subsequent introduction of a growth solution via incubation or flow. Attaching the smaller seed particles prior to AuNST growth, rather than tethering larger presynthesized nanostructures to the substrates, improves product density and limits the formation of byproducts resulting from secondary nucleation events that normally occur

during the colloidal growth step in solution. Moreover, our methodology can be applied to a variety of substrate geometries, including glass microcapillaries, enabling straightforward integration with microfluidic devices, which are increasingly applied for the development of biomedical devices and platforms.[44, 51-54]

Compared to previous work, the functionalization of our substrates with the plasmonic structures is rapid and applies only bottom-up wet-chemical techniques, avoiding the need for templating, printing, or thermal/electrochemical deposition. By translating optimized parameters for colloidal synthesis to substrate-mediated growth, we achieved uniform AuNST coatings on a variety of substrates, namely indium tin oxide (ITO) (**Figure 5.1B**), glass slides (**Figure 5.1C**), and along the internal walls of glass microcapillaries (**Figure 5.1D, E**). The final products yield films that appear blue in color with a broad LSPR peak at *ca*. 975 nm after flowing growth solution for 3 min (**Figure 5.1F, G**). Silver nitrate ($AgNO_3$) is known to play important roles in the shape control of anisotropic nanoparticles.[6] Reoptimization of the silver concentration in the growth solution confirmed that nanostructures giving the highest NIR extinction were produced with the same concentration used for the colloidal suspension (**Figure 5.S4**). This observation suggests that the optimal colloidal shape-directing reagent concentrations are directly translatable to growth in flow. The AuNSTs grown *in situ* were characterized by scanning electron microscopy (SEM) and were found to have branches with average aspect ratio of 3 ± 1, and an average of 7 ± 2 branches per AuNST without accounting for hyperbranching (n = 3, 150 nanoparticles each). Moreover, flow can increase the rate at which the gold precursor is delivered to the surface-bound seeds, therefore requiring shorter growth times (3 min) to achieve branched products in flow compared to the 10 min growth time necessary for slides

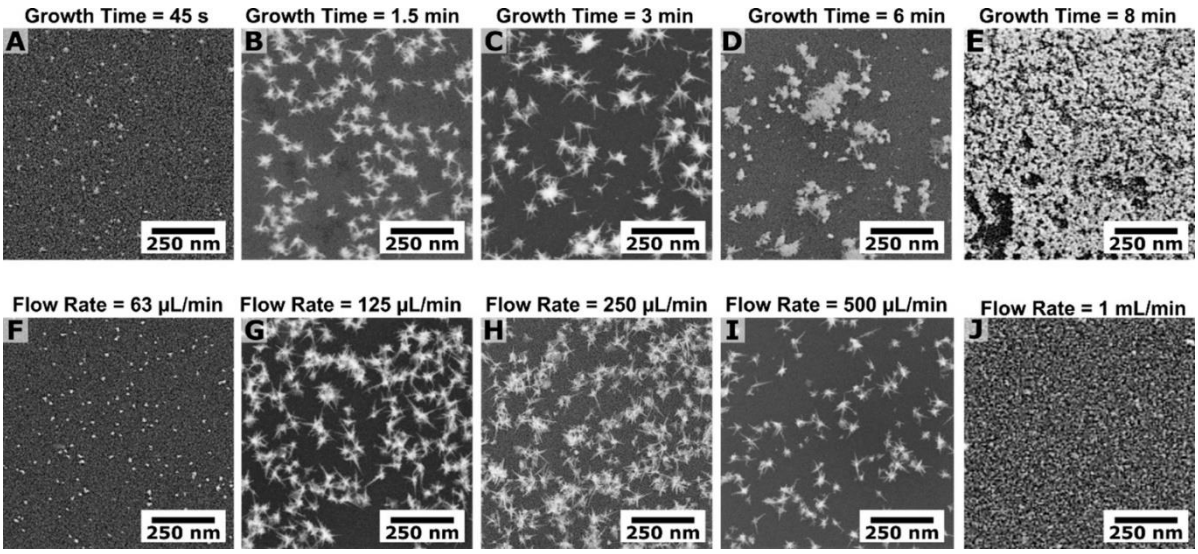

Figure 5.2. (A–E) Gold nanostars grown at the various growth times shown, all with flow rate 125 µL/min and **(F–J)** flow rates, all with 3 min growth times. Products shown in panels **C** and **H** represent the standard growth conditions.

or wafers (which incubate in a stationary solution). The AuNSTs grown *in situ* on flat substrates and in rectangular microcapillaries had 2.4× higher average aspect ratio and nearly twice the branching of those synthesized in solution (histograms of the *in situ*-grown AuNSTs are shown in **Figure 5.S5 and Table 5.S1**). On the substrate, the effective ratio of gold precursor to the seeds depends on factors absent in standard colloidal growth, including the yield of APTES functionalization and seed deposition. In the case of the microfluidic capillary, the flow profile and flow rate are additional considerations. Given these factors, the higher yield of high aspect ratio products on both the flat substrates and the capillary can be attributed to the spatial restrictions for growth from the surface-bound seeds. Furthermore, byproduct deposition is prevented by removal of the substrates from the growth solution or by flowing the growth solution out of the capillary prior to significant secondary nucleation.

As stated previously, when the synthesis is performed under flow, there are several factors affecting nanoparticle morphology, such as the volume of growth solution passed through the microfluidic channel, *i.e.*, the "growth time" (**Figure 5.2A-E**), and the flow rate used (**Figure 5.2F-J**). Nanostars grown over short time periods lacked branching, likely due to insufficient quantities of growth solution within the microcapillary (**Figure 5.2A**). Nanostructures grown for greater than 8 min at the same flow rate produced "overgrown" nanoparticle films, consistent with the introduction of excess gold precursor (**Figure 5.2E**). Conditions generating products shown in **Figure 5.2C,H** have 3 min growth times, which ensured that enough growth solution passed through the microfluidic system without leading to significant secondary nucleation (**Figure 5.S2**) and appear to yield the desired highly branched, high aspect ratio products more reproducibly than those grown at different flow rates (**Figure 5.S6**). Assuming lateral diffusion was negligible, the flow rate should dictate the deposition of gold atoms onto the seeds, where faster flow rates are expected to produce structures with the highest anisotropy and branching. However, both the lowest and highest flow rates yielded particles with minimal branching and low aspect ratio (**Figure 5.2F,J**). We expect that several factors affected the spatial distributions of the nanostructures, including variabilities in the flow rate and profile within the capillaries due to sample-to-sample differences in capillary positioning within the tubing, the yield of APTES functionalization, and seed anchoring. Specifically, the positioning of the capillary has the potential to affect the flow profile of the growth solution and the APTES layer is known to be inhomogeneous.[55] However, considering these effects, we achieve sufficient density of the nanostructures on the substrate (**Figure 5.1**). The branched particles were synthesized under laminar conditions based on the flow rate and capillary dimensions (Reynolds'

number, $R_e \sim 8.5$). We infer that the flow profile has a profound effect on AuNST morphology, since the products found at the outlet of the capillary have much less branching than those present at the inlet and center (**Figure 5.S7**). This observation suggests that an alternative flow profile (*i.e.*, that facilitates interaction of reagents with the internal capillary walls through mixing, or introducing lateral flows, such as Dean flow[56]) would likely offer improved control over product selection. This strategy will be tested in future studies through producing different microfluidic geometries.

Ultimately, the optimized *in situ* synthetic parameters provide a useful method for functionalizing oxide substrates of arbitrary geometries with dense coatings of shape-controlled products and demonstrate the potential for accessing different nanoparticle morphologies offered by the careful design and incorporation of fluid flow into the synthesis.

5.C.2 Plasmonic Activity and Photothermal Response Characterization

Cell hyperthermia can be broken down into temperature regimes giving rise to different biological phenomena: 37–41 °C is the diathermia range, where cells are able to maintain homeostasis and do not undergo significant damage due to heating; for 41–48 °C, cell death can be achieved and protein unfolding and aggregation occurs; 48–60 °C constitutes the ablation regime where thermalization yields DNA damage and rapid, irreversible protein denaturation.[57] Plasmonic heating is a near-field effect that can be detected by far-field temperature changes as heat is transferred from the nanoparticle to the surroundings.[58] We characterized the photothermal performance of the prepared substrates by measuring the mesoscale temperature using a thermal camera as the AuNST-coated microcapillary was irradiated at different laser power densities with a 785 nm continuous

wave (CW) laser and under different flow conditions. The thermal camera measures the temperature of the outer capillary surface because the infrared radiation inside the capillary does not transmit through the capillary wall. However, because the capillary wall is thin, the temperature gradient through the wall can be neglected, and the capillary surface temperatures are used to approximate the fluid temperatures inside the capillary. Temperature changes (ΔT) of *ca*. 40 °C were observed in "no flow" (stationary liquid) conditions (**Figure 5.3A**). When cooling (via flowing liquid) was applied at the same power density, temperature changes of 10 °C were observed (**Figure 5.3B**). Without flow, equilibrium temperature was reached after ~10 s of irradiation, compared to less than 1 s with flow. Rapid cooling occurred once laser irradiation was discontinued (**Figure 5.3C,D**). Negligible changes in temperature were measured when an unfunctionalized capillary was irradiated, consistent with the heating being due to the plasmonic response of the AuNSTs (**Figure 5.S8**).

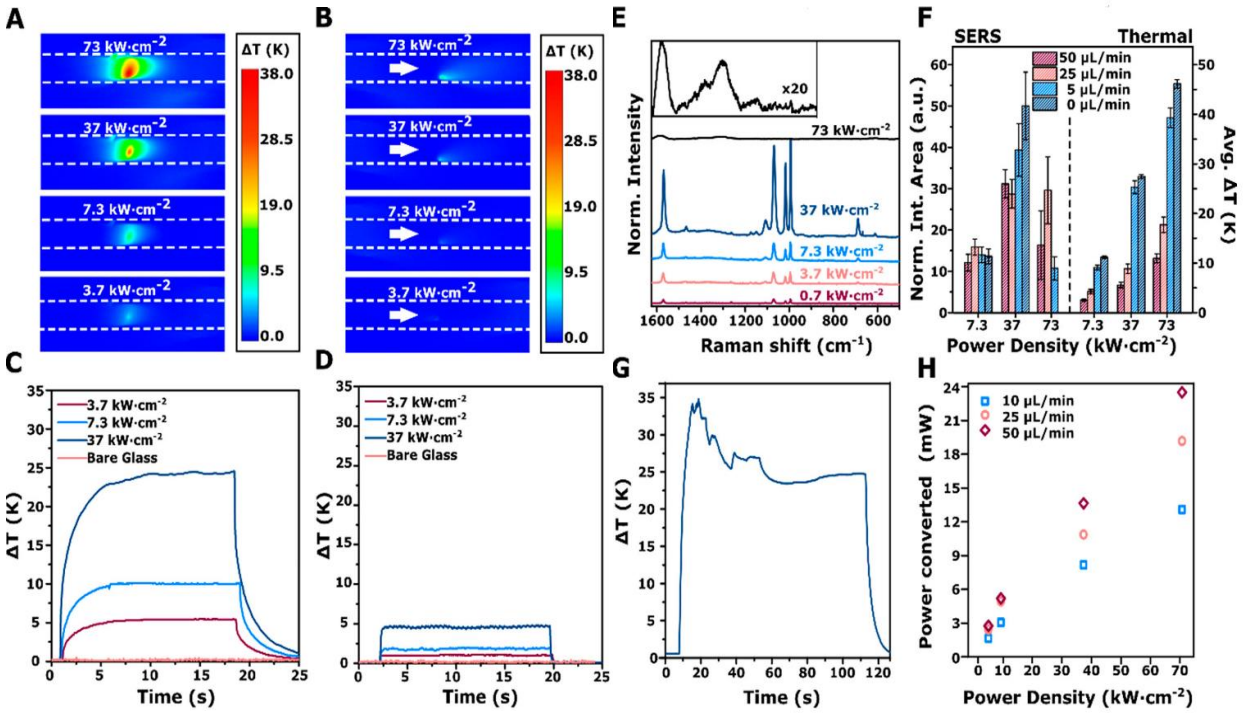

Figure 5.3. Thermal camera images of gold-nanostar-coated capillaries irradiated at different laser power in **(A)** no flow, and (**B**) 50 μL/min flow. The dotted line indicates the edges of the capillary (width: 1 mm) Heating curves in (**C**) no flow, and (**D**) 50 μL/min flow. (**E**) Surface-enhanced Raman spectra of thiophenol at various laser power (no flow), and the Raman spectra showing amorphous carbon obtained at 73 kW·cm^{-2} at 20× intensity (inset). (**F**) Comparison of Raman normalized integrated peak area at 1581 cm^{-1} and measured mesoscale heating at different flow conditions and laser power. (**G**) Heating profile of capillary at high power density. (**H**) Average power converted to heat at different laser power densities (maximum laser power is 25 mW). Laser wavelength: 785 nm. Waterfall plots of Raman spectra over a 5 min-period are shown in **Figure 5.S9** in the Supporting Information. Additional data on the thermal performance and scanning electron micrographs of products before and after reshaping are shown in **Figures 5.S10-S12**.

Because nanophotothermolysis is a near-field phenomenon, the measured macroscale or mesoscale temperatures are much lower than the temperature at the nanoparticle surface, which can exceed hundreds of degrees Celsius.[29] Rapid local thermalization can result in a number of events, including damage to molecules bound to the

nanostructures, nanoparticle reshaping, and vaporization/cavitation of fluid immediately surrounding the nanoparticles to produce nano- and microbubbles.[11,29-31,59,60] The plasmonic activity of the nanoparticles should not be affected by the presence of flowing water. Consequently, although the reported mesoscale temperatures in flow are lower than those seen under static conditions, we hypothesized that the nanoscale temperatures are comparable regardless of the flow. To test this hypothesis, we probed the near-field environment by measuring the SERS signal for AuNST-bound thiolated ligands. In fact, both the high SERS enhancement and the heat generation in branched AuNPs results from high electric field localization at sharp points.[17,61,62] Additionally, phenomena such as tip rounding and reshaping of the nanostructures, as well as damage to the ligand coating can occur at high temperatures, reducing both light-to-heat conversion and SERS intensity. Therefore, the combination of near-field and far-field optical measurements can lead to better assessment and understanding of the nanoscale effects of flow over the photothermal process. Such measurements are challenging to obtain simultaneously and in real-time; however, we have developed and set up experiments enabling us to do so (**Figures 5.S16, 5.S17**).

Experimentally, the LSB coating on the AuNSTs was displaced by thiophenol, a common nonresonant model system for SERS studies, taking advantage of the strong gold–thiol interaction. To track both the mesoscale temperature of the capillary (*i.e.*, probing the far field) and the SERS signal of the thiols bound to the nanostructures (*i.e.*, probing the near field), we incorporated concurrent thermal camera measurements along with the collection of SERS spectra in aqueous solution as well as in phosphate-buffered saline (PBS) and in cell culture medium, since these systems may be of interest for biological applications (**Figure 5.S9**). As expected, both temperature and SERS intensity increase with laser power (**Figure**

5.3A-E). Although the mesoscale temperature decreases significantly under flow, the SERS intensity remains comparable at flow rates ranging between 0 and 50 μL/min and at laser fluences up to the highest power density tested (73 kW·cm^{-2}; **Figure 5.3F**). However, under stationary conditions we observed the disappearance of the thiophenol fingerprints at the highest power density tested (73 kW·cm^{-2}) together with the appearance of the Raman spectra for amorphous carbon (*ca*. 1400 cm^{-1}, **Figure 5.3E**). The decrease in signal could be due to damage (*i.e*., breaking bonds within the molecule) or desorption of the molecule from the nanostars. Although desorption cannot be ruled out, the appearance of amorphous carbon peaks indicates that damage to the ligand does occur. Furthermore, at the same power density (73 kW·cm^{-2}, **Figure 5.3G**), we observed a decrease in ΔT over time, indicating that there was reduced light-to-heat conversion, pointing toward nanoparticle reshaping. Spatially correlated SEM measurements provide further evidence that nanoparticle restructuring occurs under these conditions (**Figure 5.S10C**). We conclude that the cooling effects of the fluid flow protect the nanostructures from thermally induced reshaping. Furthermore, we observed the formation of bubbles large enough (*i.e*., several microns in diameter based on the microscope images) to result in measurable mesoscale temperature fluctuations of a few degrees as they refill and coalesce with one another (**Figure 5.3G** shows the temperature fluctuations during this process).

The comparable SERS intensities observed under the various flow conditions indicate that although the presence of flowing liquid alters the mesoscale temperature, and flowing water can thereby reduce ligand damage or AuNST reshaping, it ultimately does not affect the near-field generation of heat. To test if the light-to-heat conversion is independent of the flow conditions (*i.e*., when damage to the plasmonic structures does not occur), we estimated

the heat q for different flow rates at multiple laser power settings (**Figures 5.S11, 5.S12**, with corresponding discussion). Based on the power of the laser source X (W), the power absorbed as heat is approximately q/X%. For different flow rates, the laser power converted into heat increases linearly with the percentage of the laser power and is comparable for the three different flow rates (**Figure 5.3H**). We estimate up to ~90% power conversion (based on the ~24 mW power converted compared to the max laser power of 25 mW) into heat from our estimation of the steady state ΔT at 50 μL/min flow rate, which lies within the expected performance previously reported for branched structures in colloidal suspension.[63,64] These results provide additional support that the flow conditions do not alter the plasmonic activity of the nanostructures within the capillary.

In summary, we demonstrate that these simultaneous SERS-thermal measurements can be correlated to far-field and near-field plasmonic responses of the AuNSTs and can be applied as tools for probing the nanoscale environment. In addition, we find that tuning the microfluidic flow rate enables finer control over total capillary heating without sacrificing plasmonic activity and has potential for protecting the nanostructures from temperature-induced morphological changes.

5.C.3 Nanophotothermolysis of Adherent Cells

Microfluidic systems have previously been proposed to confine adherent and suspension cells spatially to the same focal plane for performing fluorescence confocal microscopy studies on apoptosis and cell response to chemotherapeutics.[53,54,65] Fluorescence confocal cell imaging and simultaneous monitoring of the mesoscale temperature change have potential to offer new insight into the temperature dependence of cellular responses to plasmonic heating as they occur in real-time. Our setup enables us to use laser-scanning fluorescence confocal microscopy to visualize AuNST-cell interactions

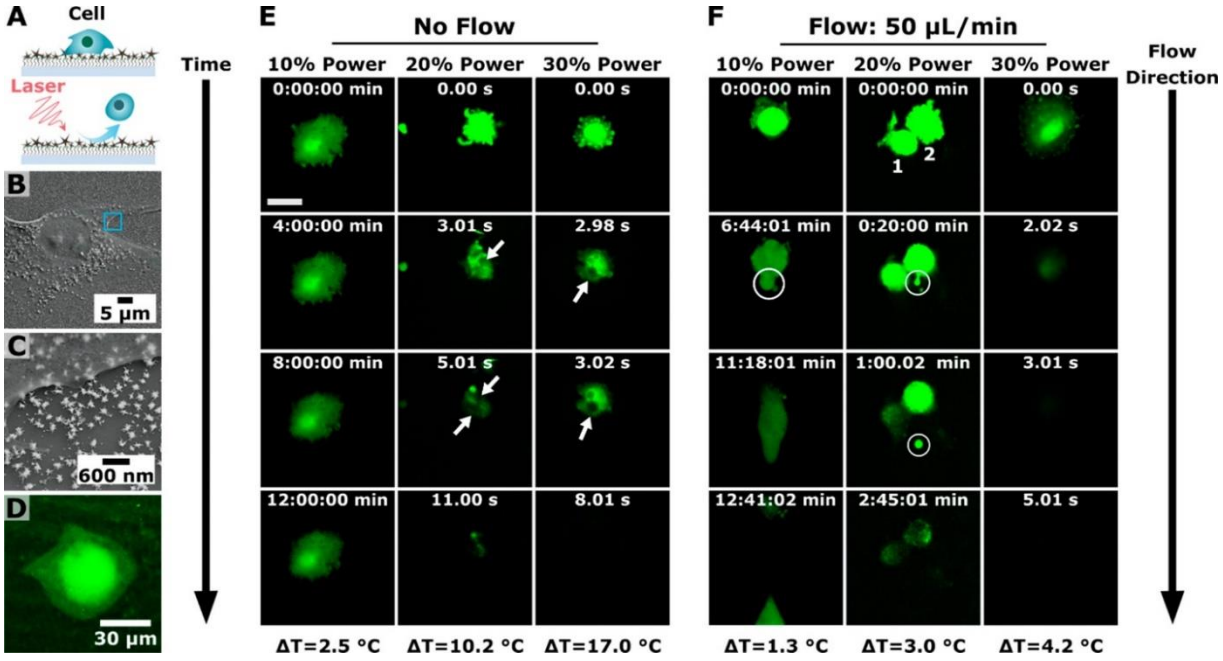

Figure 5.4. (**A**) Schematic of adherent cell attachment and light-activated removal. (**B, C**) Scanning electron micrographs (additional images shown in **Figure 5.S11**) and (**D**) scanning fluorescence confocal microscopy image of a green fluorescent protein (GFP)-expressing U-87 cell on gold nanostars. Scanning fluorescence confocal microscopy images of cell response at (**E**) different laser fluences, no flow (white arrows indicate microbubbles), and (**F**) 50 µL/min flow rate (white circles indicate blebs which caused leaking of intracellular contents (scale bar = 25 µm; parts **E** and **F** shown at the same scale. Laser wavelength: 785 nm. Maximum fluence = 17 mJ/cm^2 (**Tables 5.S2, 5.S3**).

with adherent cells while irradiating the AuNSTs with a NIR femtosecond pulsed laser and measuring capillary temperature (**Figure 5.S17**). Moreover, we demonstrated hyperthermia-mediated single-cell "point-and-shoot" release of grafted adherent cells (**Figure 5.4A**) and observed changes in cell morphology, appearance of necrotic protrusions known as "blebs", and microbubble formation, depending on the flow rate and temperature. First, we evaluated the adhesion of model cells onto AuNSTs by culturing them over a AuNST-coated substrate. Here, our goal was to functionalize the nanostructures with extracellular matrix proteins that promote cell growth and adherence. Thiols bind strongly to gold, and thus we used mercaptoundecanol (MUD) to ensure the displacement of LSB. Modification with MUD provides a hydroxyl functionality to facilitate coating with fibronectin in order to enhance cell interactions with the AuNSTs, which has a total thickness of ~25 nm.[66,67] After functionalization, the AuNST-capillary was split and an adherent glioblastoma cell line expressing green fluorescence protein (U-87 GFP) was incubated on the substrate in a well plate for 24 h (at 37 °C, 95% humidity, 5% CO_2). Scanning electron micrographs and fluorescence confocal microscopy images show that the cells spread over the functionalized substrate (**Figure 5.4B-D**). When cells were administered into the capillary via flow, spreading was observed within 60 min (**Figure 5.S12**). This analysis shows that the functionalization procedure enables direct interactions of the cell membrane with the local environment of the plasmonic nanostructures.

Plasmonic heating has previously been utilized to detach cells from planar substrates at time scales of up to ~1 h.[25,26] Our work builds upon these previous developments by applying the *in situ* growth method we developed to achieve point-and-shoot release of grafted cells with *single-cell* specificity. The point-and-shoot release triggered by the

localized heating demonstrates the plasmonic activity and the continued potential of our system for additional biological applications (**Figure 5.4A**). The cells were flowed into the capillary and incubated within the capillary for 60 min to facilitate attachment (based on the initial SEM/fluorescence confocal microscopy data, **Figure 5.S14**), then irradiated in the capillary. Though thermal measurements and microscopy imaging are generally performed separately,[68,69] here we apply the setup shown in **Figure 5.S17** to perform *simultaneous* thermal imaging and laser scanning confocal measurements while irradiating the capillary with a 785 nm femtosecond-pulse laser (80 MHz rep rate, 35 fs pulse width). This experimental setup enabled us to observe cell morphology changes, blebbing, loss of cytoplasmic material, bubble formation, and removal from the substrate of single cells in real time within a ΔT range from ~1 to 30 °C. We found that without fluid flow, cell removal occurs quickly with increased maximum temperature, where rapid cell ablation is observed within seconds as ΔT approaches 20 °C. Furthermore, if the irradiation area in the capillary temperature is increased by more than *ca*. 10 °C, we observed the formation of microbubbles (**Figure 5.4E**). Steam nanobubble generation and subsequent formation of microbubbles via diffusion of dissolved gases has been previously described for substrates (such as glass slides) decorated with thermoplasmonic nanoparticles, and their formation has been shown to play a role in causing mechanical damage to cell membranes.[13] Air bubble formation requires local temperatures near the spinodal temperature of water (277 °C) and consequently the local heat energy produced in this system is likely to exceed the measured mesoscale capillary heating greatly.[29,60] Bubble formation during nanophotothermolysis of cells induces significant mechanical stress, which likely plays major roles in the mechanism of cell removal under these circumstances.[59,70] As a control experiment, we observe no cell

damage, bubble formation, nor significant temperature change for at least 5 min irradiation time up to 30% of the fs-pulsed laser power (17 mJ/cm^2; **Tables 5.S2, 5.S3**) when AuNSTs are not present in the capillary (**Figure 5.S13**).

Under flow (**Figure 5.4F**), significant cell membrane damage occurs with temperature changes above 4 °C, and ablation leads to the loss of intracellular materials and near instantaneous removal from the substrate (*i.e.*, similar to what was observed at 17 °C without flow). At the fluences tested (5.7–17 mJ/cm^2), we do not observe microbubbles, which may be due to the flowing liquid carrying the bubbles downstream. However, even in the absence of microbubbles, cells exhibit membrane damage with changes in temperature of only 1–3 °C, leading to the rapid formation of blebs, with diameters in the tens of microns, which are precursors to the release of intracellular contents. The formation of blebs indicates rupture of the outer cell membrane and the nature of the blebbing can also indicate different mechanisms of cell death, such as apoptosis or necrosis, which have been observed previously with nanoparticle hyperthermia.[12,71-73] Apoptosis is a biologically controlled process, whereas necrosis is rapid cell death caused by external stimuli (*e.g.*, high local temperature in this case). The size and degree of blebbing indicates necrosis as the primary mechanism of cell removal and damage. Note that without flow, the formation of blebs is harder to detect using confocal microscopy, as the blebs quickly move out of the focal plane and do not move around nor detach from the main body of cells exposed to fluid flow.

The rate of local temperature increase is important to control when studying cell interactions with thermoplasmonic nanoparticles, where selection between apoptosis and necrosis can be achieved through careful control of the heating conditions. Furthermore, we leverage gradual heating to demonstrate controlled release of cultured cells from substrates

with branched thermoplasmonic structures.[25] In our system, we are able to tune both the flow and the laser fluence systematically to control the heating experienced by the cells. Although the laser fluences (11 mJ/cm^2) giving ΔT of 10 and 3 °C without and with flow, respectively, are the same, the cooling effects of flow mitigate damage to the cell, enabling cells to remain on the substrate substantially longer. With flow, we also do not observe bubble formation, likely because any bubbles generated are rapidly carried downstream. Both with and without flow, the cells exhibit significant membrane disruption, even at low overall capillary temperatures. In these experiments, we utilize a femtosecond-pulse laser to trigger the plasmonic response, which might result in more aggressive localized heating compared to CW illumination sources, where the energy deposition and generation of heat can be more efficiently controlled.[11,74,75] The SERS experiments (CW laser) and the cell experiments (femtosecond pulsed laser) exhibit similar photothermal phenomena (*i.e.*, bubble formation, AuNST reshaping), but we note that these systems are not directly comparable in their deposition of energy to the particles and therefore the mechanisms leading to the resulting phenomena likely differ between the two illumination conditions. Thus, building upon what was done here, one interesting avenue to pursue will be to compare temperature measurements, SERS spectra, and fluorescence confocal cell images collected simultaneously in real time with different illumination sources to probe phenomena that result from intense nanoscale heat generation.

5.D Conclusions and Prospects

We developed a seeded-growth method to achieve AuNST growth *in situ* on substrates with arbitrary geometries and that found this approach leads to improved

selection of highly anisotropic products. On the basis of this protocol, we developed a wet-chemical approach for growing shape-controlled nanoparticles not only on planar substrates but also on substrates with arbitrary geometries, such as glass microcapillaries using microfluidics. For the microfluidic growth, we demonstrate that both growth time and flow rate can be tuned to manipulate AuNST morphology. Our optimization of the branched structures in flow indicates that the rational design of flow profiles, rates, and growth times can be used to access different nanoparticle morphologies, offering the prospect of exploring new growth mechanisms for different shaped nanoparticles in microfluidics. Upon illumination, the AuNST coatings exhibit intense local heating, achieving up to ~40 °C mesoscale temperature increase, and flowing water acts as a heat sink, mitigating overall capillary heating. We developed an experimental setup for simultaneous measurement of thermal fluctuations and SERS signal and apply this system to monitor damage to ligands and heat-induced changes to AuNST morphology occurring at the nanoscale in real time. We have demonstrated light-triggered "point-and-shoot" selective removal of cells from the substrate and were able to observe cell necrosis, ablation, microbubble formation, and intact cell removal depending on flow conditions and laser fluence. With and without visibly evident microbubble formation, AuNST photothermal response leads to cell membrane damage, causing their rapid removal from the substrate. Due to the robustness of gold–thiol interactions, the use of thiolated antibodies to facilitate capture and selection of specific cell types adds additional experimental versatility and device capabilities while opening areas for future studies that apply our approach to biomedical applications. Although the presented studies on adherent cell interactions with AuNSTs in flow are preliminary, these data indicate that future studies elucidating the interplay between temperature, flow, and

cell-AuNST interaction strength can be leveraged to identify conditions that support controlled removal of intact, viable cells. Later designs of the platform will target soft-release of disease-relevant cells, incorporating systems for selective release and collection of specific cells from a large background cell population via localized heating to enable analysis of cell viability via colorimetric or flow cytometry-based assays and opportunities for clinical translation.

5.E Supplementary Materials

5.E.1 Colloidal Optimization

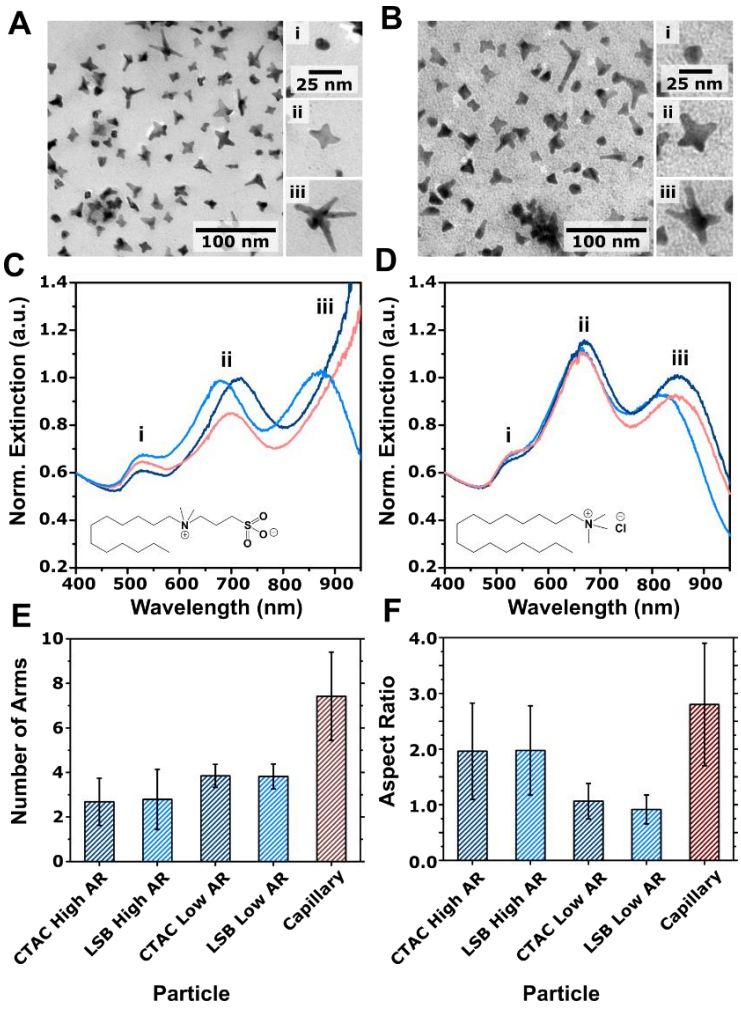

Figure 5.S1. Transmission electron microscopy images showing gold nanostar (AuNST) products synthesized utilizing (**A**) seeds capped with laurylsulfobetaine (LSB) and (**B**) cetyltrimethylammonium chloride (CTAC). Ultraviolet-visible spectra showing three repetitions of each synthesis, where (**C**) was performed with LSB-capped seeds and (**D**) was performed with CTAC-capped seeds. (**E**) The average number of arms obtained by analyzing 150 particles of each type. Low aspect ratio (AR) corresponds to product **A(ii)** and **B(ii)** for LSB- and CTAC-capped seeds, respectively. High AR corresponds to products shown in **A(iii)** and **B(iii)** for LSB- and CTAC-capped seeds, respectively. (**F**) The average aspect ratio (arm length/arm base width) for 150 of each product.

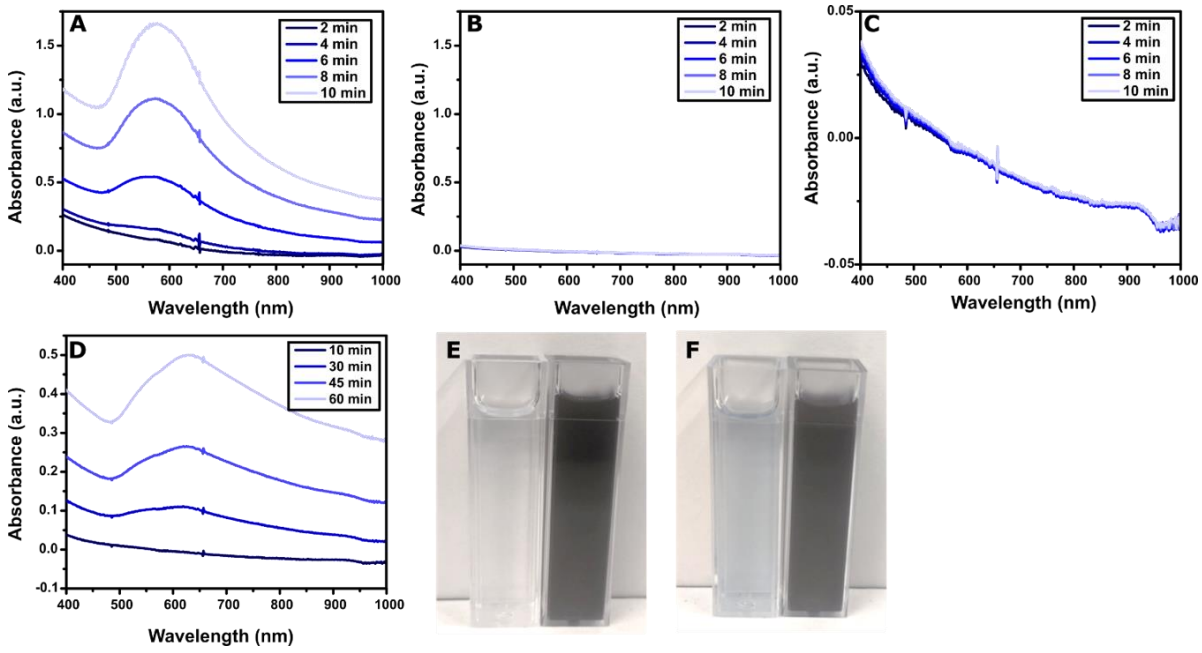

Figure 5.S2. Ultraviolet-visible spectra of (**A**) nucleation of nanoparticles in growth solution without HCl and (**B**) with 10 µL/mL 1 M HCl over 10 min without the addition of any seeds. (**C**) Scaled view of graph **B** and **D:** spectra of solution with HCl addition from 10 min to 60 min. Photographs of solutions after (**E**) 30 min and (**D**) 1 h; the solution with HCl is on the left in both pictures.

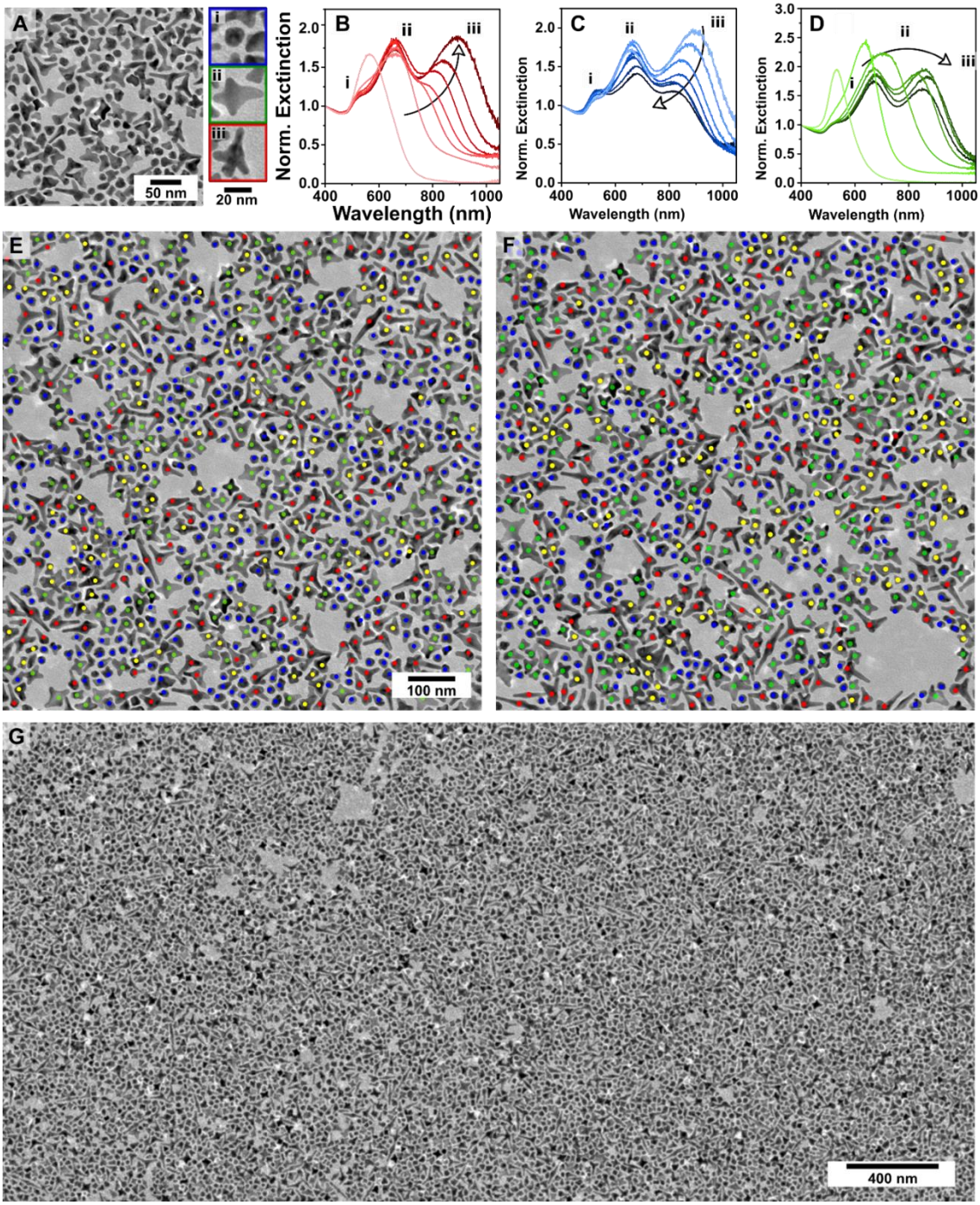

Figure 5.S3. (**A**) Transmission electron microscopy image of the three gold nanostar products (**i**) anisotropic spheroids. (**ii**) low aspect-ratio products, and (**iii**) high aspect-ratio products. Ultraviolet-visible spectra showing the effect of increasing (**B**) ascorbic acid, (**C**) hydrochloric acid, and (**D**) silver nitrate in the growth solution. Transmission electron micrographs (**E,F**) showing product identification for yield determination, and (**G**) large-scale view of final products yield: 42% spheroids (**i**), 24% low aspect ratio (**ii**), 20% high aspect ratio (**iii**), 14% unidentified.

5.E.2 *In Situ* Growth Optimization

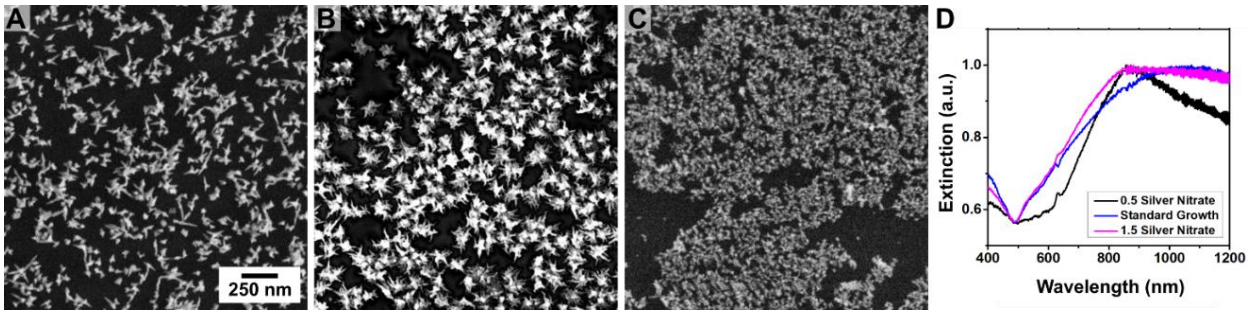

Figure 5.S4. Scanning electron microscopy images showing products with (**A**) 33 μM (0.5 silver nitrate), (**B**) 75 μM (standard), (**C**) 108 μM (1.5 times silver nitrate) silver nitrate in the growth solution, and (**D**) the corresponding ultraviolet-visible spectra.

5.E.3 Comparison of Colloidal and *in Situ* Nanostar Branching and Aspect Ratio

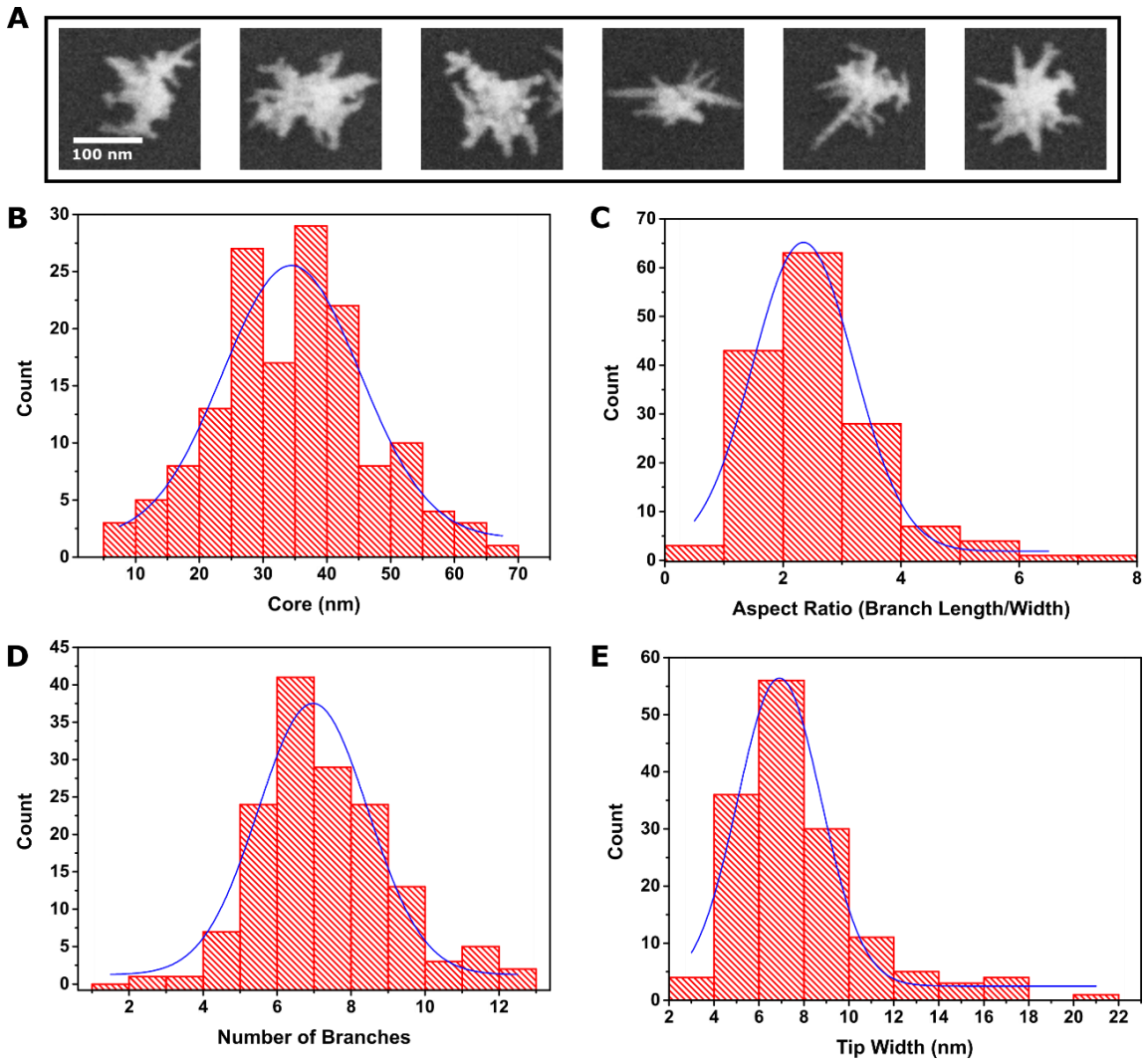

Figure 5.S5. (**A**) Scanning electron micrographs of representative gold nanostars grown *in situ* on a glass capillary. Histograms showing measurements (150 nanoparticles for each) of the nanostars' (**B**) core diameter, (**C**) aspect ratio, (**D**) number of branches, and (**E**) tip width.

Table 5.S1. Branching of Particles Prepared by Colloid and Microfluidic Syntheses
CTAC: Cetyltrimethylammonium chloride; LSB: Laurylsulfobetaine

Particle	Growth Method	Seed Capping Ligand	Core (nm)	Aspect Ratio (arm length/base)	Branches
Spheroids	Colloid	LSB	13 ± 2	--	--
Low Aspect Ratio	Colloid	LSB	13 ± 3	0.9 ± 0.3	3.8 ± 0.6
High Aspect Ratio	Colloid	LSB	14 ± 3	2.0 ± 0.8	3 ± 1
Spheroids	Colloid	CTAC	12 ± 2	--	--
Low Aspect Ratio	Colloid	CTAC	16 ± 3	1.1 ± 0.3	3.8 ± 0.5
High Aspect Ratio	Colloid	CTAC	16 ± 3	2.2 ± 0.9	3 ± 1
High Aspect Ratio	Microfluidic	CTAC	40 ± 10	3 ± 1	7 ± 2

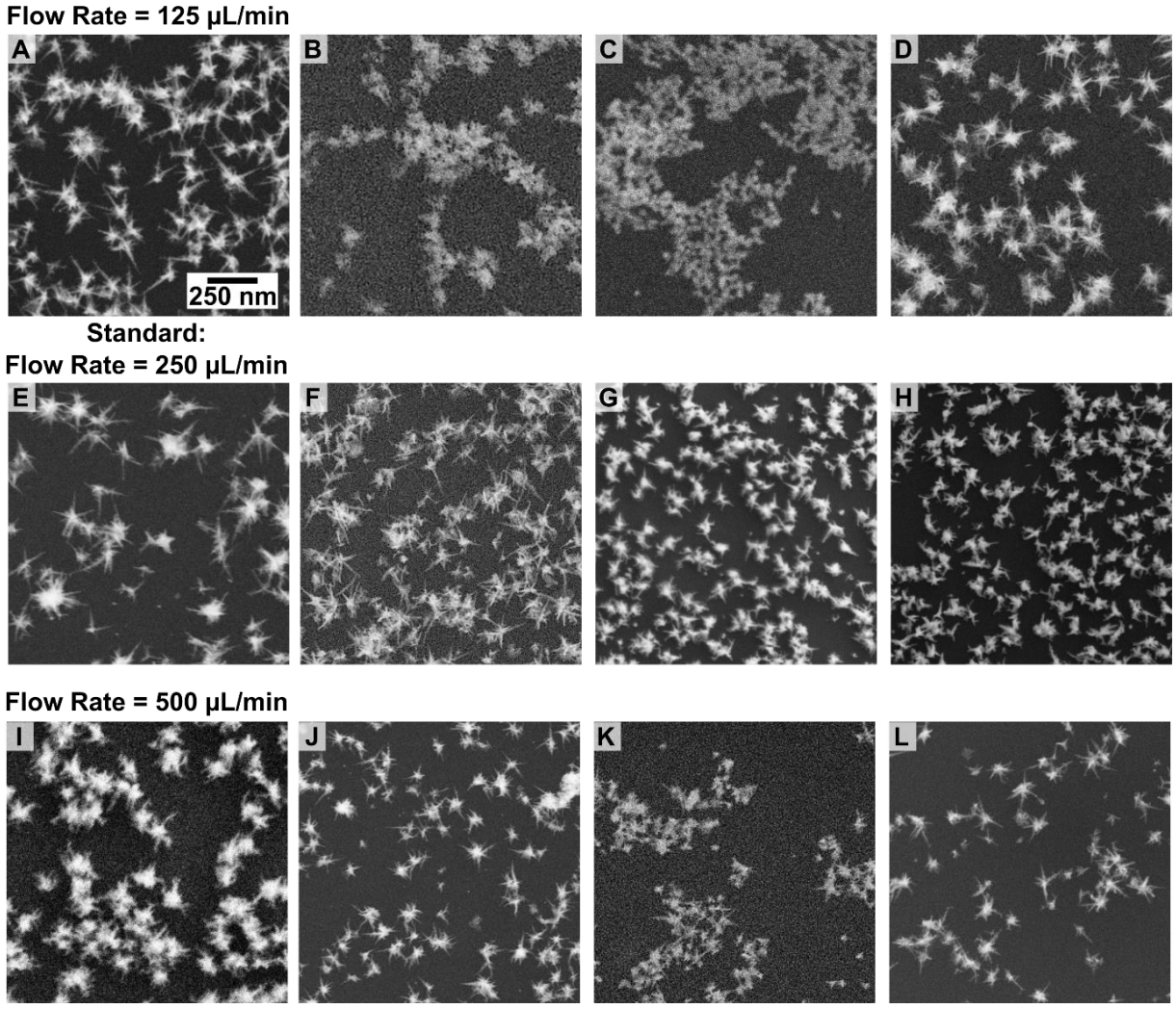

Figure 5.S6. Scanning electron microscopy images showing the products grown in four different capillaries for each flow rate shown: **A-D:** Samples grown at half the standard rate, **E-H:** samples prepared under "standard" flow conditions, and **I-L:** samples prepared using double the standard flow rate. Growth solution was flowed through the capillary for ~3 min (± 30 s) for each sample. All images are shown at the same magnification.

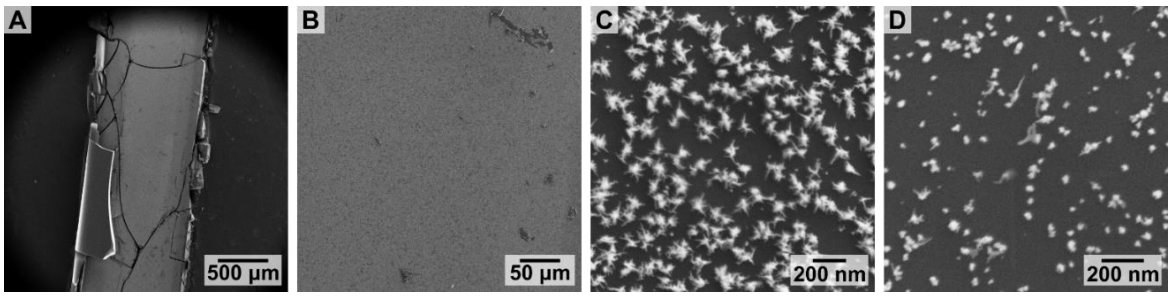

Figure 5.S7. Scanning electron micrographs of a split capillary at **A,B:** lower magnification, and at higher magnification (**C**) showing products in the first *ca*. two-thirds of the capillary and (**D**) products near the outlet of the same capillary.

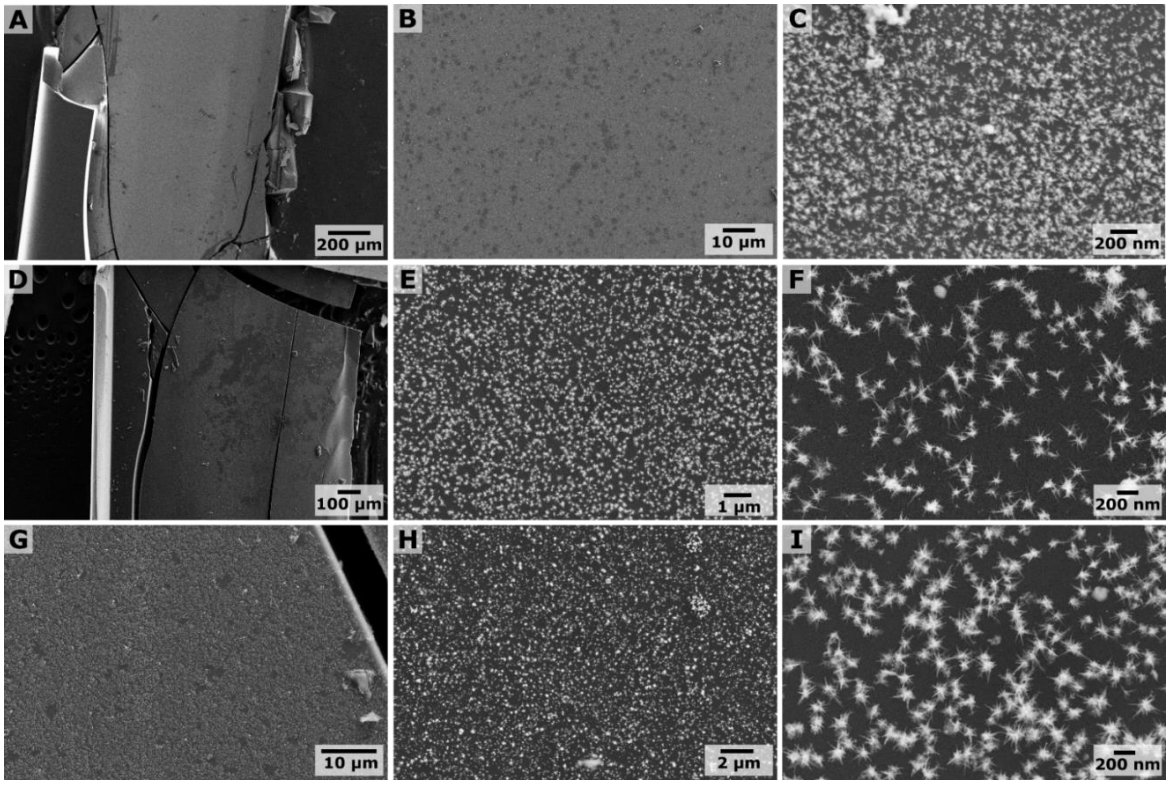

Figure 5.S8. Scanning electron micrographs showing three different capillaries prepared under standard growth conditions (3 min, 250 µL/min flow; one row=one sample) at different magnifications.

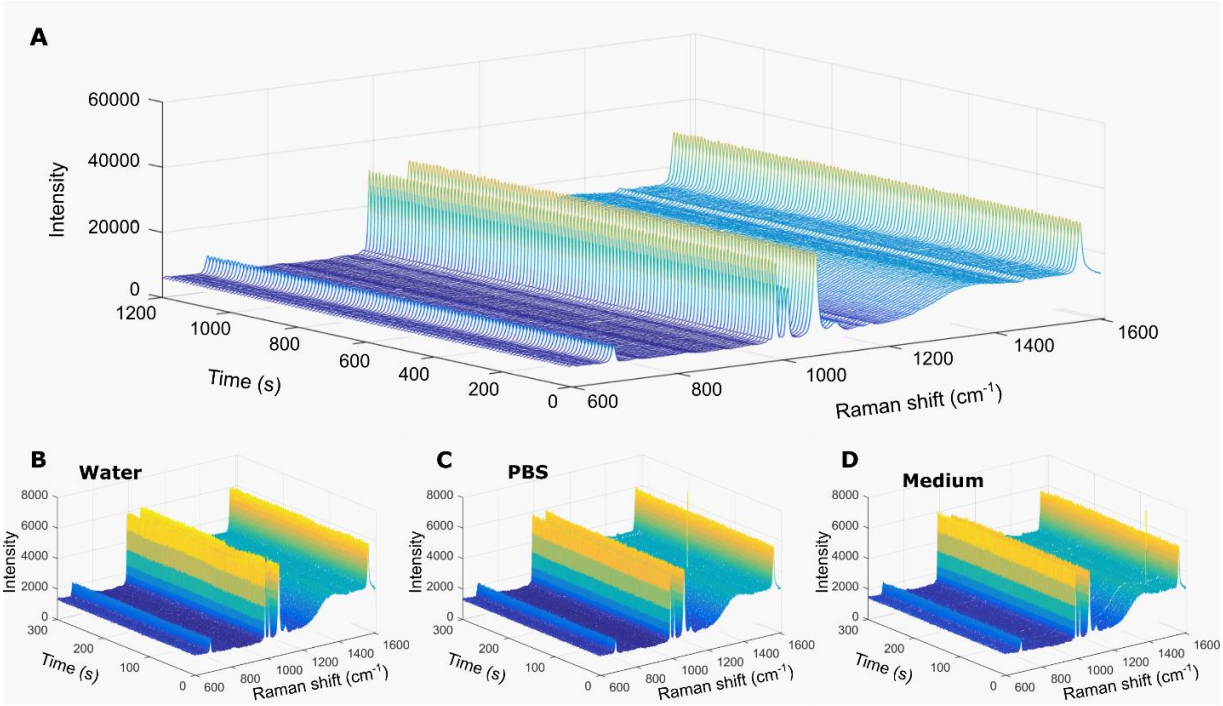

Figure 5.S9. (**A**) Surface-enhanced Raman spectra for thiophenol measured in a gold nanostar capillary at 55 W/cm^2 over 20 min. **B-D:** Comparison of surface-enhanced Raman spectra measured in flowing water, phosphate-buffered saline (PBS), and cell culture medium (Dulbecco's Modified Eagle's Medium; DMEM; used to culture U87-GFP cells) over 5 min.

Figure 5.S9A shows the surface-enhanced Raman scattering spectra of thiophenol over 20 min at 55 W/cm^2. Based on these data, the device should be operable for long periods of time at 55 W/cm^2 power density or lower, which accommodates the temperature changes studied for cell removal using our system. With the spectra shown in **Figure 5.S9B-D**, we compare water and various solutions of potential interest for biological applications, including phosphate-buffered saline and DMEM cell culture medium. Spectra for **Figure 5.S9B-D** were obtained with irradiation at 28 kW/cm^2, representing a laser power applied within the range presented in the main manuscript (37-0.7 kW/cm^2) achieving relevant temperature changes for cell removal. Moreover,

as dilute aqueous solutions containing salts, vitamins, and amino acids, both PBS and DMEM are thermally similar to water. Therefore, we also do not expect the localized heating effect to differ significantly between the three environments.

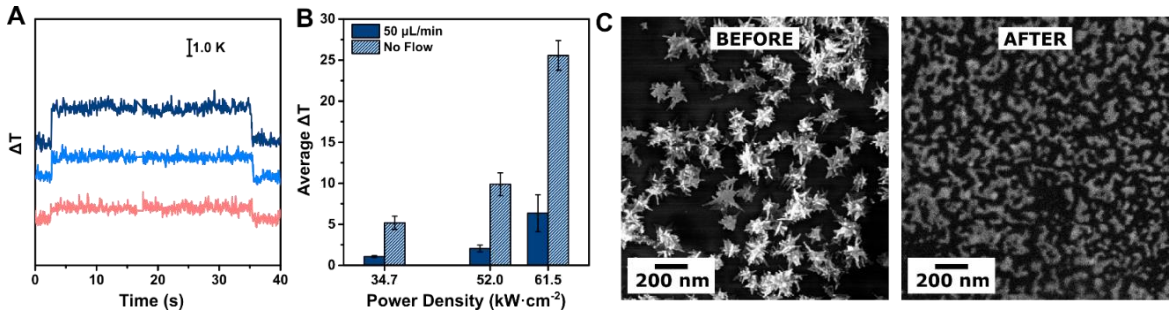

Figure 5.S10. (**A**) Heating curves obtained at different spots in the capillary under 50 µL/min flow at the same power density (34.7 kW·cm^{-2}). (**B**) Average temperature between three different capillaries prepared with standard growth conditions (3 min, 250 µL/min flow). (**C**) Scanning electron micrograph of capillary irradiated at high laser power density (73.3 mW/cm^2) before and after irradiation, corresponding to the heating curve shown in **Figure 4.3G** of the main text.

5.E.4 Laser Absorption Analysis using Energy Balance in Flow Conditions

We employ conservation of energy to estimate the power converted from laser to heat. Consider the control volume shown in **Figure 5.S9A**. Because the temperature rise (typically less than 5 ℃) is relatively low; we neglect heat loss to the ambient air. In addition, because the thermal conductivity of the capillary tube is low (1.2 W·m^{-1}K^{-1}) we neglect heat losses *via* capillary conduction. Therefore, the laser power converted to heat is approximately represented by the temperature difference of water between the inlet and the outlet of the control volume. Because the capillary wall is thin (0.070 mm thickness), we also neglect the temperature difference between the inner and outer surface of the capillary; consequently, the temperature of the water is approximated by

the temperature of the outer surface of the capillary. Capillary surface temperatures were recorded by an infrared (IR) camera (A655sc, 25 μm close-up lens), and an IR image for the capillary with water flow under laser heating is shown in **Figure 5.S9B**.

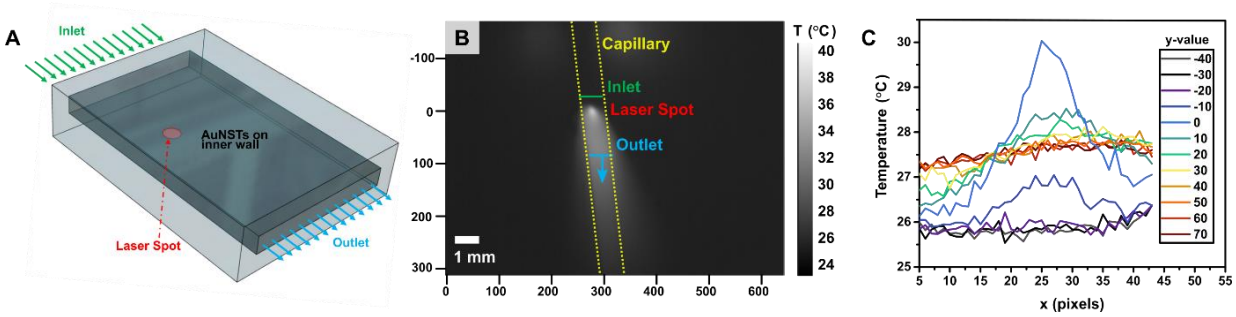

Figure 5.S11. (**A**) Schematic of system. (**B**) Thermal image showing capillary under irradiation. (**C**) Temperature profiles at *y*-values from -40 to 70 pixels for determination of outlet.

Consider the control volume shown in **Figure 5.S10A**. We denote the volumetric flow rate as $\dot{V}$, and the temperature difference between the inlet and outlet as ΔT. At steady state, the laser power converted into heat q can be estimated using **Equation 5.S1**:

$$q = \dot{V}\rho C_l \Delta T \qquad (5.S1)$$

where ρ indicates water density and C_l indicates water specific heat. $\dot{V}$ was controlled by the syringe pump, and ρ and C_l are both known constants. We need to measure ΔT to estimate q and rely on IR thermography to determine the former quantity.

Figure 5.S10B shows a temperature field measured by the IR camera (x and y axis units in pixels). We use y = 0 to indicate the plane exposed to the laser. Steady-state temperature distributions at several y locations on the capillary surface are shown in **Figure 5.S9C**. Positive y values indicate capillary positions downstream of the laser spot whereas negative y values indicate upstream positions of the laser spot. To determine ΔT,

we first determine the inlet and outlet boundaries of the control volume (shown in **Figure 5.S9A**), and corresponding temperatures at these boundaries. Based on **Figure 5.S10C**, either y = -40 or y = -30 can be used as the boundary for the flow inlet, because the temperatures at these y locations do not vary significantly along the x-direction. Similarly, y = 50, 60, or 70 can be used as the boundary for the flow outlet. The stable temperature profiles at different y locations indicate steady-state flow and also supports the assumption of neglecting heat loss because temperature decreases little in the y direction within the capillary region. We use the mean value along the x-axis of the capillary to indicate the temperature at y = -30 and y = 50 (**Figure 5.S11A**). We extract the temperatures at steady state as shown in **Figure 5.S11B**, and the temperature difference between inlet and outlet is shown in Figure S10C. ΔT is calculated using the mean value of the temperature differences.

The source code for the absorption calculation has been published online at: https://github.com/yuanyuansjtu/Nanostar/

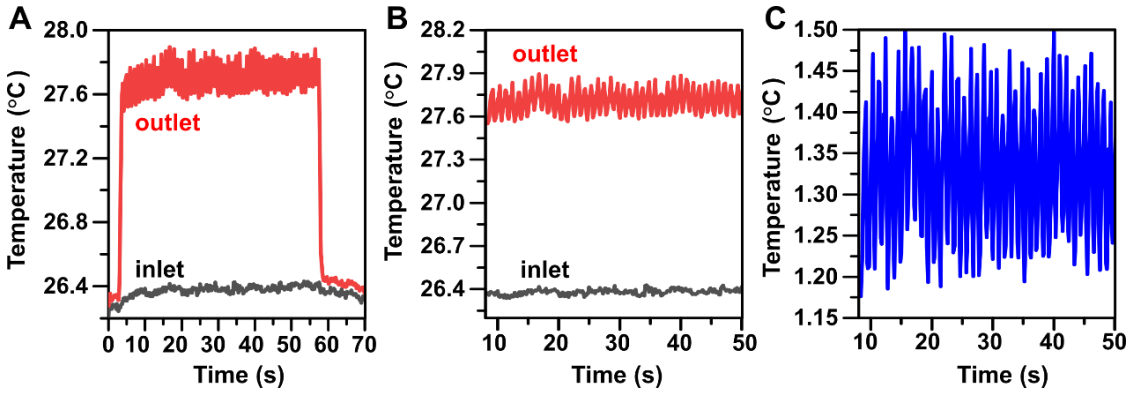

Figure 5.S12. (**A**) Mean temperature at the inlet and outlet. (**B**) Isolation of steady-state temperatures. (**C**) Temperature difference of inlet and outlet.

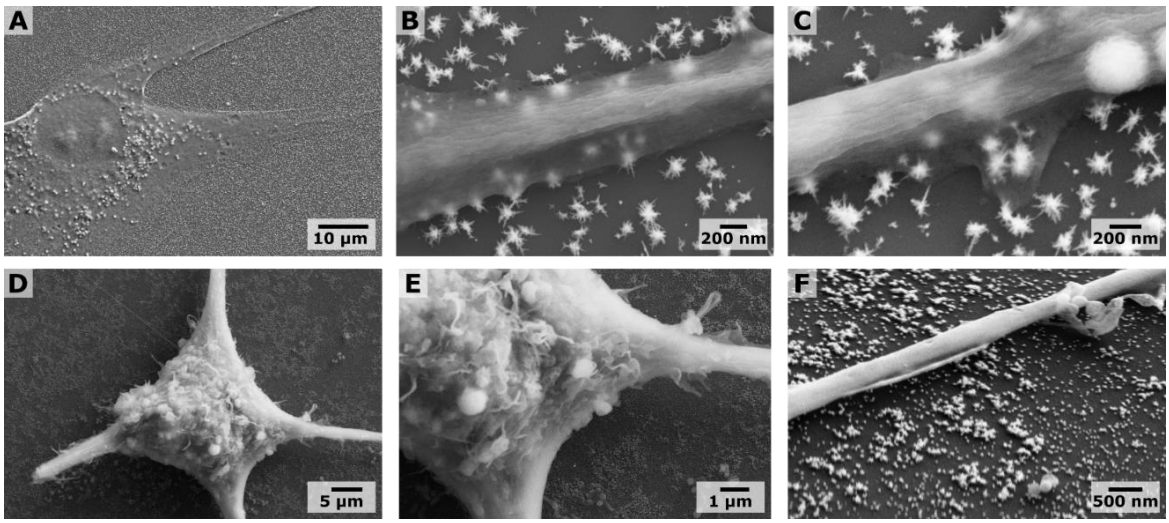

Figure 5.S13. Additional scanning electron microscopy images of cells cultured on gold nanostar substrates. **A-C** are images of the same cell. **D-F** are a different cell. Differences in contrast of cells can occur based on the success of osmium staining. A cell with a higher degree of staining will appear opaque as in **D-F**.

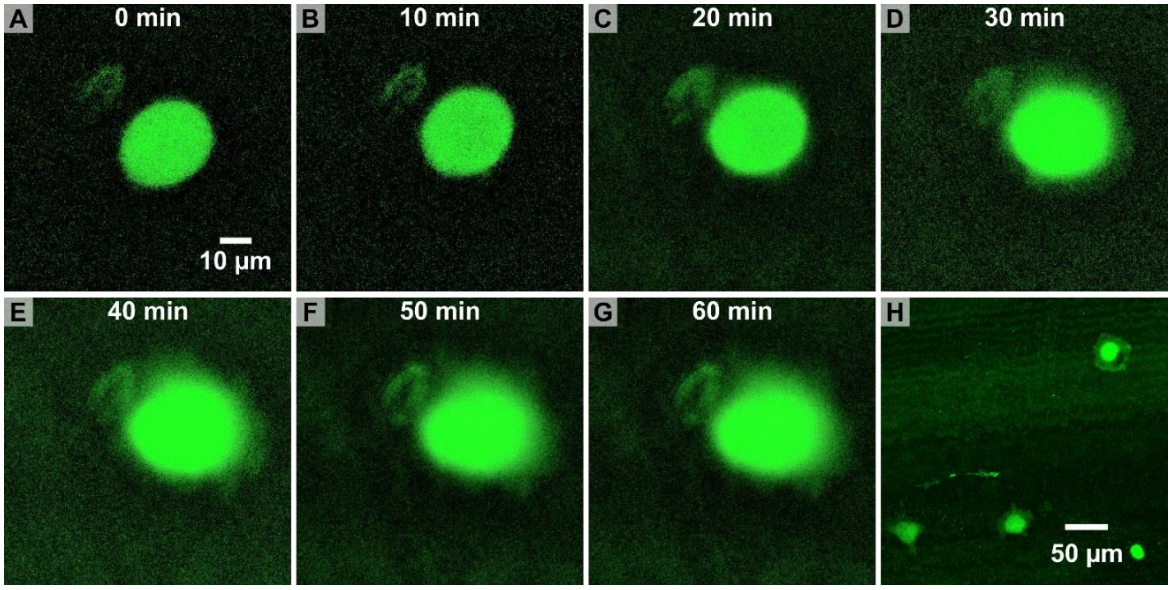

Figure 5.S14. Fluorescence scanning confocal microscopy images showing **A-G:** the same green fluorescent protein (GFP)-expressing U87 cell spreading over the course of 60 min within a gold nanostar-decorated capillary, and (**H**) image of multiple cells following incubation for 60 min.

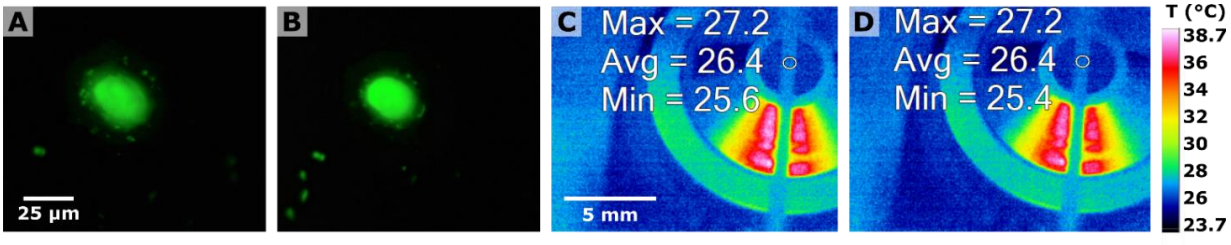

Figure 5.S15. Laser scanning confocal microscopy images of green fluorescent protein-expressing U87 cells (**A**) before irradiation and (**B**) after 5 min of irradiation at 17 mJ/cm^2 (30% power, no flow). Thermal camera images of capillary (**C**) before and (**D**) during irradiation with a fs-pulsed laser. Max, Avg, and Min temperatures are shown in °C for the circular region of interest.

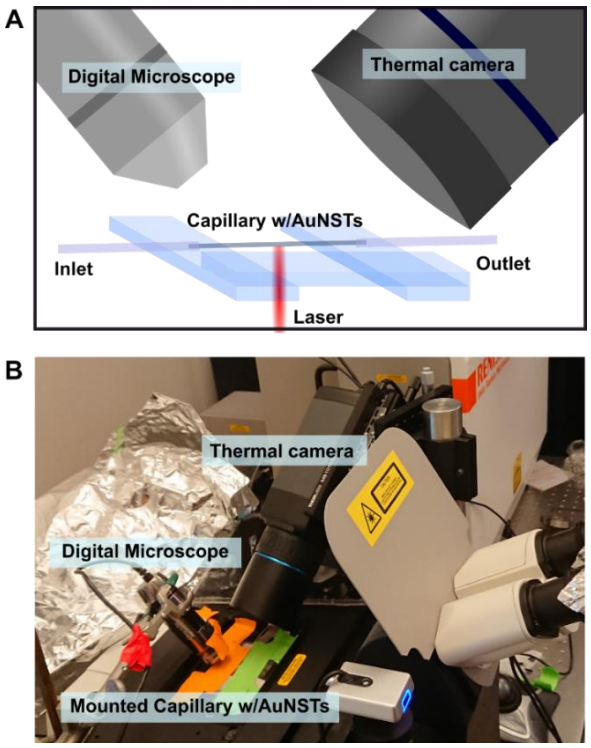

Figure 5.S16. (**A**) Schematic of instrumentation setup for the simultaneous thermal camera/surface enhanced Raman scattering (SERS) measurements. The camera and digital microscope are placed at an angle to prevent damage from the laser. (**B**) Photograph of the experimental setup.

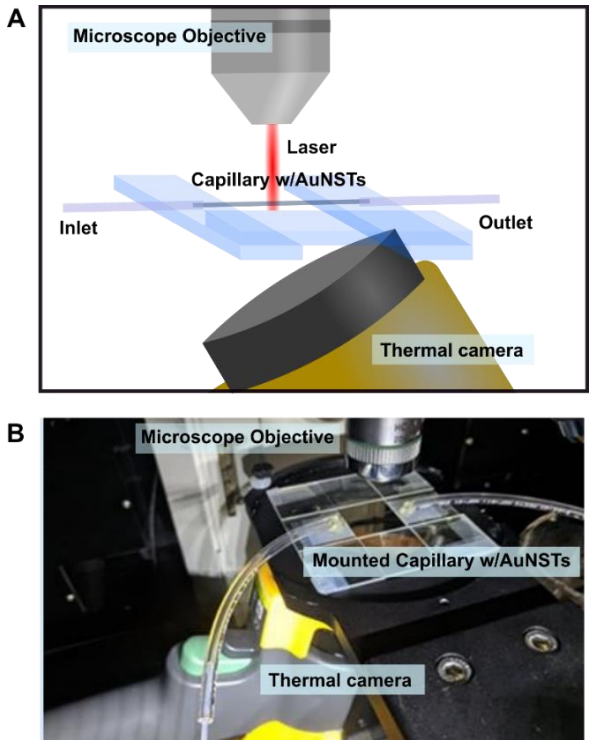

Figure 5.S17. (**A**) Schematic of instrumentation set up for the simultaneous thermal/fluorescence scanning confocal microscopy measurements. (**B**) Photograph of the experimental setup.

5.E.5 Femtosecond-Pulsed Laser Power Measurement and Fluence Calculation

Incident laser power from the femtosecond-pulsed laser was measured at low power percentage using a power meter (Thorlabs PM120V; S120UV Sensor, 200-1100 nm). Laser spot size (785 nm) was calculated from the factory reported size at a wavelength of 488 nm (7.48×10^{-13} m^2) as 1.2×10^{-12} m^2.

Table 5.S2. Measured Power

Percent Laser Power	Measured Power (mW)	Residual
0	0	--
1	0.027	0.03
1.5	0.068	0.01
2	0.135	0.03

Table 5.S3. Extrapolated Power

Percent Laser Power	Power (mW)	Calculated Fluence (mJ/cm^2)
10	5.5 ± 0.1	5.7
15	8.3 ± 0.1	8.6
20	11.0 ± 0.1	11
25	13.8 ± 0.1	14
30	16.5 ± 0.1	17

5.F References

(1) Hu, X.; Kwon, N.; Yan, K.; Sedgwick, A. C.; Chen, G.; He, X.; James, T. D.; Yoon, J. Bio-Conjugated Advanced Materials for Targeted Disease Theranostics. *Adv. Funct. Mater.* **2020**, *30*, 1907906.

(2) Langer, J.; Jimenez de Aberasturi, D.; Aizpurua, J.; Alvarez-Puebla, R. A.; Auguié, B.; Baumberg, J. J.; Bazan, G. C.; Bell, S. E. J.; Boisen, A.; Brolo, A. G.; Choo, J.; Cialla-May, D.; Deckert, V.; Fabris, L.; Faulds, K.; García de Abajo, F. J.; Goodacre, R.; Graham, D.; Haes, A. J.; Haynes, C. L.; Huck, C.; Itoh, T.; Käll, M.; Kneipp, J.; Kotov, N. A.; Kuang, H.; Le Ru, E. C.; Lee, H. K.; Li, J.-F.; Ling, X. Y.; Maier, S. A.; Mayerhöfer, T.; Moskovits, M.; Murakoshi, K.; Nam, J.-M.; Nie, S.; Ozaki, Y.; Pastoriza-Santos, I.; Perez-Juste, J.; Popp, J.; Pucci, A.; Reich, S.; Ren, B.; Schatz, G. C.; Shegai, T.; Schlücker, S.; Tay, L.-L.; Thomas, K. G.; Tian, Z.-Q.; Van Duyne, R. P.; Vo-Dinh, T.; Wang, Y.; Willets, K. A.; Xu, C.; Xu, H.; Xu, Y.; Yamamoto, Y. S.; Zhao, B.; Liz-Marzán, L. M. Present and Future of Surface-Enhanced Raman Scattering. *ACS Nano* **2020**, *14*, 28–117.

(3) Guerrero-Martínez, A.; Barbosa, S.; Pastoriza-Santos, I.; Liz-Marzán, L. M. Nanostars Shine Bright for You. *Curr. Opin. Colloid Interface Sci.* **2011**, *16*, 118–127.

(4) Scarabelli, L. Recent Advances in the Rational Synthesis and Self-Assembly of Anisotropic Plasmonic Nanoparticles. *Pure Appl. Chem.* **2018**, *90*, 1393–1407.

(5) Niu, W.; Zhang, L.; Xu, G. Seed-Mediated Growth of Noble Metal Nanocrystals: Crystal Growth and Shape Control. *Nanoscale* **2013**, *5*, 3172–3181.

(6) Personick, M. L.; Langille, M. R.; Zhang, J.; Mirkin, C. A. Shape Control of Gold Nanoparticles by Silver Underpotential Deposition. *Nano Lett.* **2011**, *11*, 3394–3398.

(7) Xia, Y.; Xia, X.; Peng, H.-C. Shape-Controlled Synthesis of Colloidal Metal Nanocrystals: Thermodynamic versus Kinetic Products. *J. Am. Chem. Soc.* **2015**, *137*, 7947–7966.

(8) Xia, Y.; Gilroy, K. D.; Peng, H.-C.; Xia, X. Seed-Mediated Growth of Colloidal Metal Nanocrystals. *Angew. Chem., Int. Ed.* **2017**, *56*, 60–95.

(9) Grzelczak, M.; Pérez-Juste, J.; Mulvaney, P.; Liz-Marzán, L. M. Shape Control in Gold Nanoparticle Synthesis. *Chem. Soc. Rev.* **2008**, *37*, 1783–1791.

(10) Lohse, S. E.; Burrows, N. D.; Scarabelli, L.; Liz-Marzán, L. M.; Murphy, C. J. Anisotropic Noble Metal Nanocrystal Growth: The Role of Halides. *Chem. Mater.* **2014**, *26*, 34–43.

(11) Baffou, G.; Quidant, R. Thermo-Plasmonics: Using Metallic Nanostructures as Nano-Sources of Heat. *Laser Photonics Rev.* **2013**, *7*, 171–187.

(12) Ali, M. R. K.; Wu, Y.; El-Sayed, M. A. Gold-Nanoparticle-Assisted Plasmonic Photothermal Therapy Advances toward Clinical Application. *J. Phys. Chem. C* **2019**, *123*, 15375–15393.

(13) Huang, X.; El-Sayed, I. H.; Qian, W.; El-Sayed, M. A. Cancer Cell Imaging and Photothermal Therapy in the Near-Infrared Region by Using Gold Nanorods. *J. Am. Chem. Soc.* **2006**, *128*, 2115–2120.

(14) Dam, D. H. M.; Lee, R. C.; Odom, T. W. Improved *in Vitro* Efficacy of Gold Nanoconstructs by Increased Loading of G-Quadruplex Aptamer. *Nano Lett.* **2014**, *14*, 2843–2848.

(15) Loo, C.; Lowery, A.; Halas, N.; West, J.; Drezek, R. Immunotargeted Nanoshells for Integrated Cancer Imaging and Therapy. *Nano Lett.* **2005**, *5*, 709–711.

(16) Hao, F.; Nehl, C. L.; Hafner, J. H.; Nordlander, P. Plasmon Resonances of a Gold

Nanostar. *Nano Lett.* **2007**, *7*, 729–732.

(17) Barbosa, S.; Agrawal, A.; Rodríguez-Lorenzo, L.; Pastoriza-Santos, I.; Alvarez-Puebla, R. A.; Kornowski, A.; Weller, H.; Liz-Marzán, L. M. Tuning Size and Sensing Properties in Colloidal Gold Nanostars. *Langmuir* **2010**, *26*, 14943–14950.

(18) Rodríguez-Oliveros, R.; Sánchez-Gil, J. A. Gold Nanostars as Thermoplasmonic Nanoparticles for Optical Heating. *Opt. Express* **2012**, *20*, 621–626.

(19) Hua, Y.; Chandra, K.; Dam, D. H. M.; Wiederrecht, G. P.; Odom, T. W. Shape-Dependent Nonlinear Optical Properties of Anisotropic Gold Nanoparticles. *J. Phys. Chem. Lett.* **2015**, *6*, 4904–4908.

(20) Bhamidipati, M.; Cho, H.-Y.; Lee, K.-B.; Fabris, L. SERS-Based Quantification of Biomarker Expression at the Single Cell Level Enabled by Gold Nanostars and Truncated Aptamers. *Bioconjugate Chem.* **2018**, *29*, 2970–2981.

(21) Pallavicini, P.; Donà, A.; Taglietti, A.; Minzioni, P.; Patrini, M.; Dacarro, G.; Chirico, G.; Sironi, L.; Bloise, N.; Visai, L.; Scarabelli, L. Self-Assembled Monolayers of Gold Nanostars: A Convenient Tool for near-IR Photothermal Biofilm Eradication. *Chem. Commun.* **2014**, *50*, 1969–1971.

(22) Osinkina, L.; Lohmüller, T.; Jäckel, F.; Feldmann, J. Synthesis of Gold Nanostar Arrays as Reliable, Large-Scale, Homogeneous Substrates for Surface-Enhanced Raman Scattering Imaging and Spectroscopy. *J. Phys. Chem. C* **2013**, *117*, 22198–22202.

(23) Zhang, B.; Shi, Y.; Miyamoto, D.; Nakazawa, K.; Miyake, T. Nanostraw Membrane Stamping for Direct Delivery of Molecules into Adhesive Cells. *Sci. Rep.* **2019**, *9*, 6806–6814.

(24) Man, T.; Zhu, X.; Chow, Y. T.; Dawson, E. R.; Wen, X.; Patananan, A. N.; Liu, T. L.; Zhao, C.; Wu, C.; Hong, J. S.; Chung, P.-S.; Clemens, D. L.; Lee, B.-Y.; Weiss, P. S.; Teitell, M. A.; Chiou,

P.-Y. Intracellular Photothermal Delivery for Suspension Cells Using Sharp Nanoscale Tips in Microwells. *ACS Nano* **2019**, *13*, 10835–10844.

(25) Giner-Casares, J. J.; Henriksen-Lacey, M.; García, I.; Liz-Marzán, L. M. Plasmonic Surfaces for Cell Growth and Retrieval Triggered by Near-Infrared Light. *Angew. Chem., Int. Ed.* **2016**, *55*, 974–978.

(26) Lv, S.-W.; Liu, Y.; Xie, M.; Wang, J.; Yan, X.-W.; Li, Z.; Dong, W.-G.; Huang, W.-H. Near-Infrared Light-Responsive Hydrogel for Specific Recognition and Photothermal Site-Release of Circulating Tumor Cells. *ACS Nano* **2016**, *10*, 6201–6210.

(27) Hirsch, L. R.; Stafford, R. J.; Bankson, J. A.; Sershen, S. R.; Rivera, B.; Price, R. E.; Hazle, J. D.; Halas, N. J.; West, J. L. Nanoshell-Mediated Near-Infrared Thermal Therapy of Tumors under Magnetic Resonance Guidance. *Proc. Natl. Acad. Sci. U. S. A.* **2003**, *100*, 13549–13554.

(28) Huang, X.; El-Sayed, I. H.; Qian, W.; El-Sayed, M. A. Cancer Cell Imaging and Photothermal Therapy in the Near-Infrared Region by Using Gold Nanorods. *J. Am. Chem. Soc.* **2006**, *128*, 2115–2120.

(29) Baffou, G.; Polleux, J.; Rigneault, H.; Monneret, S. Super-Heating and Micro-Bubble Generation around Plasmonic Nanoparticles Under cw Illumination. *J. Phys. Chem. C* **2014**, *118*, 4890–4898.

(30) Neumann, O.; Urban, A. S.; Day, J.; Lal, S.; Nordlander, P.; Halas, N. J. Solar Vapor Generation Enabled by Nanoparticles. *ACS Nano* **2013**, *7*, 42–49.

(31) Fang, Z.; Zhen, Y.-R.; Neumann, O.; Polman, A.; García de Abajo, F. J.; Nordlander, P.; Halas, N. J. Evolution of Light-Induced Vapor Generation at a Liquid-Immersed Metallic Nanoparticle. *Nano Lett.* **2013**, *13*, 1736–1742.

(32) Wang, D.; Bourgeois, M. R.; Guan, J.; Fumani, A. K.; Schatz, G. C.; Odom, T. W. Lasing

from Finite Plasmonic Nanoparticle Lattices. *ACS Photonics* **2020**, *7*, 630–636.

(33) Gisbert Quilis, N.; Lequeux, M.; Venugopalan, P.; Khan, I.; Knoll, W.; Boujday, S.; Lamy de la Chapelle, M.; Dostalek, J. Tunable Laser Interference Lithography Preparation of Plasmonic Nanoparticle Arrays Tailored for SERS. *Nanoscale* **2018**, *10*, 10268–10276.

(34) Khabbaz Abkenar, S.; Tufani, A.; Ozaydin Ince, G.; Kurt, H.; Turak, A.; Ow-Yang, C. W. Transfer Printing Gold Nanoparticle Arrays by Tuning the Surface Hydrophilicity of Thermo-Responsive Poly *N*-Isopropylacrylamide (PNIPAAm). *Nanoscale* **2017**, *9*, 2969–2973.

(35) Velleman, L.; Sikdar, D.; Turek, V. A.; Kucernak, A. R.; Roser, S. J.; Kornyshev, A. A.; Edel, J. B. Tuneable 2D Self-Assembly of Plasmonic Nanoparticles at Liquid | Liquid Interfaces. *Nanoscale* **2016**, *8*, 19229–19241.

(36) Hamon, C.; Novikov, S.; Scarabelli, L.; Basabe-Desmonts, L.; Liz-Marzán, L. M. Hierarchical Self-Assembly of Gold Nanoparticles into Patterned Plasmonic Nanostructures. *ACS Nano* **2014**, *8*, 10694–10703.

(37) Ali Umar, A.; Oyama, M. Growth of High-Density Gold Nanoparticles on an Indium Tin Oxide Surface Prepared Using a “Touch” Seed-Mediated Growth Technique. *Cryst. Growth Des.* **2005**, *5*, 599–607.

(38) Kambayashi, M.; Zhang, J.; Oyama, M. Crystal Growth of Gold Nanoparticles on Indium Tin Oxides in the Absence and Presence of 3-Mercaptopropyl-Trimethoxysilane. *Cryst. Growth Des.* **2005**, *5*, 81–84.

(39) Osinkina, L.; Lohmüller, T.; Jäckel, F.; Feldmann, J. Synthesis of Gold Nanostar Arrays as Reliable, Large-Scale, Homogeneous Substrates for Surface-Enhanced Raman Scattering Imaging and Spectroscopy. *J. Phys. Chem. C* **2013**, *117*, 22198–22202.

(40) Kumar, S.; Yang, H.; Zou, S. Seed-Mediated Growth of Uniform Gold Nanoparticle Arrays. *J. Phys. Chem. C* **2007**, *111*, 12933–12938.

(41) Fortuni, B.; Fujita, Y.; Ricci, M.; Inose, T.; Aubert, R.; Lu, G.; Hutchison, J. A.; Hofkens, J.; Latterini, L.; Uji-i, H. A Novel Method for *in Situ* Synthesis of SERS-Active Gold Nanostars on Polydimethylsiloxane Film. *Chem. Commun.* **2017**, *53*, 5121–5124.

(42) Cataldi, U.; Caputo, R.; Kurylyak, Y.; Klein, G.; Chekini, M.; Umeton, C.; Bürgi, T. Growing Gold Nanoparticles on a Flexible Substrate to Enable Simple Mechanical Control of Their Plasmonic Coupling. *J. Mater. Chem. C* **2014**, *2*, 7927–7933.

(43) Zhang, Q.; Xu, J.-J.; Liu, Y.; Chen, H.-Y. *In-Situ* Synthesis of Poly(Dimethylsiloxane)–Gold Nanoparticles Composite Films and Its Application in Microfluidic Systems. *Lab Chip* **2008**, *8*, 352–357.

(44) Jalali, M.; AbdelFatah, T.; Mahshid, S. S.; Labib, M.; Sudalaiyadum Perumal, A.; Mahshid, S. A Hierarchical 3D Nanostructured Microfluidic Device for Sensitive Detection of Pathogenic Bacteria. *Small* **2018**, *14*, 1801893.

(45) Li, Z.; Huang, X.; Lu, G. Recent Developments of Flexible and Transparent SERS Substrates. *J. Mater. Chem. C* **2020**, *8*, 3956–3969.

(46) Xiong, R.; Raemdonck, K.; Peynshaert, K.; Lentacker, I.; De Cock, I.; Demeester, J.; De Smedt, S. C.; Skirtach, A. G.; Braeckmans, K. Comparison of Gold Nanoparticle Mediated Photoporation: Vapor Nanobubbles Outperform Direct Heating for Delivering Macromolecules in Live Cells. *ACS Nano* **2014**, *8*, 6288–6296.

(47) Vanrompay, H.; Bladt, E.; Albrecht, W.; Béché, A.; Zakhozheva, M.; Sánchez-Iglesias, A.; Liz-Marzán, L. M.; Bals, S. 3D Characterization of Heat-Induced Morphological Changes of Au Nanostars by Fast *in Situ* Electron Tomography. *Nanoscale* **2018**, *10*, 22792–22801.

(48) Maestro, L. M.; Haro-González, P.; Sánchez-Iglesias, A.; Liz-Marzán, L. M.; García Solé, J.; Jaque, D. Quantum Dot Thermometry Evaluation of Geometry Dependent Heating Efficiency in Gold Nanoparticles. *Langmuir* **2014**, *30*, 1650–1658.

(49) Su, Q.; Ma, X.; Dong, J.; Jiang, C.; Qian, W. A Reproducible SERS Substrate Based on Electrostatically Assisted APTES-Functionalized Surface-Assembly of Gold Nanostars. *ACS Appl. Mater. Interfaces* **2011**, *3*, 1873–1879.

(50) Casu, A.; Cabrini, E.; Donà, A.; Falqui, A.; Diaz-Fernandez, Y.; Milanese, C.; Taglietti, A.; Pallavicini, P. Controlled Synthesis of Gold Nanostars by Using a Zwitterionic Surfactant. *Chem. Eur. J.* **2012**, *18*, 9381–9390.

(51) Dhar, M.; Lam, J. N.; Walser, T.; Dubinett, S. M.; Rettig, M. B.; Di Carlo, D. Functional Profiling of Circulating Tumor Cells with an Integrated Vortex Capture and Single-Cell Protease Activity Assay. *Proc. Natl. Acad. Sci. U. S. A.* **2018**, *115*, 9986–9991.

(52) Che, J.; Yu, V.; Dhar, M.; Renier, C.; Matsumoto, M.; Heirich, K.; Garon, E. B.; Goldman, J.; Rao, J.; Sledge, G. W.; Pegram, M. D.; Sheth, S.; Jeffrey, S. S.; Kulkarni, R. P.; Sollier, E.; Di Carlo, D. Classification of Large Circulating Tumor Cells Isolated with Ultra-High Throughput Microfluidic Vortex Technology. *Oncotarget* **2016**, *7*, 12748–12760.

(53) Zhao, L.; Cheng, P.; Li, J.; Zhang, Y.; Gu, M.; Liu, J.; Zhang, J.; Zhu, J.-J. Analysis of Nonadherent Apoptotic Cells by a Quantum Dots Probe in a Microfluidic Device for Drug Screening. *Anal. Chem.* **2009**, *81*, 7075–7080.

(54) Komen, J.; Wolbers, F.; Franke, H. R.; Andersson, H.; Vermes, I.; van den Berg, A. Viability Analysis and Apoptosis Induction of Breast Cancer Cells in a Microfluidic Device: Effect of Cytostatic Drugs. *Biomed. Microdevices* **2008**, *10*, 727–737.

(55) Kyaw, H. H.; Al-Harthi, S. H.; Sellai, A.; Dutta, J. Self-Organization of Gold

Nanoparticles on Silanated Surfaces. *Beilstein J. Nanotechnol.* **2015**, *6*, 2345–2353.

(56) Stoecklein, D.; Di Carlo, D. Nonlinear Microfluidics. *Anal. Chem.* **2019**, *91*, 296–314.

(57) Baffou, G. *Thermoplasmonics: Heating Metal Nanoparticles Using Light*; Cambridge University Press: Cambridge, U.K., 2017; pp 224–230.

(58) Jauffred, L.; Samadi, A.; Klingberg, H.; Bendix, P. M.; Oddershede, L. B. Plasmonic Heating of Nanostructures. *Chem. Rev.* **2019**, *119*, 8087–8130.

(59) Hou, L.; Yorulmaz, M.; Verhart, N. R.; Orrit, M. Explosive Formation and Dynamics of Vapor Nanobubbles around a Continuously Heated Gold Nanosphere. *New J. Phys.* **2015**, *17*, 013050.

(60) Kotaidis, V.; Dahmen, C.; von Plessen, G.; Springer, F.; Plech, A. Excitation of Nanoscale Vapor Bubbles at the Surface of Gold Nanoparticles in Water. *J. Chem. Phys.* **2006**, *124*, 184702.

(61) Jimenez de Aberasturi, D.; Serrano-Montes, A. B.; Langer, J.; Henriksen-Lacey, M.; Parak, W. J.; Liz-Marzán, L. M. Surface Enhanced Raman Scattering Encoded Gold Nanostars for Multiplexed Cell Discrimination. *Chem. Mater.* **2016**, *28*, 6779–6790.

(62) Meng, X.; Dyer, J.; Huo, Y.; Jiang, C. Greater SERS Activity of Ligand-Stabilized Gold Nanostars with Sharp Branches. *Langmuir* **2020**, *36*, 3558–3564.

(63) Bi, C.; Chen, J.; Chen, Y.; Song, Y.; Li, A.; Li, S.; Mao, Z.; Gao, C.; Wang, D.; Möhwald, H.; Xia, H. Realizing a Record Photothermal Conversion Efficiency of Spiky Gold Nanoparticles in the Second Near-Infrared Window by Structure-Based Rational Design. *Chem. Mater.* **2018**, *30*, 2709–2718.

(64) Espinosa, A.; Silva, A. K. A.; Sánchez-Iglesias, A.; Grzelczak, M.; Péchoux, C.; Desboeufs, K.; Liz-Marzán, L. M.; Wilhelm, C. Cancer Cell Internalization of Gold Nanostars

Impacts Their Photothermal Efficiency *in Vitro* and *in Vivo*: Toward a Plasmonic Thermal Fingerprint in Tumoral Environment. *Adv. Healthcare Mater.* **2016**, *5*, 1040–1048.

(65) Muñoz-Pinedo, C.; Green, D. R.; van den Berg, A. Confocal Restricted-Height Imaging of Suspension Cells (CRISC) in a PDMS Microdevice during Apoptosis. *Lab Chip* **2005**, *5*, 628–633.

(66) Slaughter, L. S.; Cheung, K. M.; Kaappa, S.; Cao, H. H.; Yang, Q.; Young, T. D.; Serino, A. C.; Malola, S.; Olson, J. M.; Link, S.; Häkkinen, H.; Andrews, A. M.; Weiss, P. S. Patterning of Supported Gold Monolayers via Chemical Lift-off Lithography. *Beilstein J. Nanotechnol.* **2017**, *8*, 2648–2661.

(67) Malmsten, M. Ellipsometry Studies of Fibronectin Adsorption. *Colloids Surf., B* **1995**, *3*, 371–381.

(68) Wang, H.; Zhou, S.; Guo, L.; Wang, Y.; Feng, L. Intelligent Hybrid Hydrogels for Rapid *in Situ* Detection and Photothermal Therapy of Bacterial Infection. *ACS Appl. Mater. Interfaces* **2020**, *12*, 39685–39694.

(69) Moise, S.; Byrne, J. M.; El Haj, A. J.; Telling, N. D. The Potential of Magnetic Hyperthermia for Triggering the Differentiation of Cancer Cells. *Nanoscale* **2018**, *10*, 20519–20525.

(70) Zharov, V. P.; Mercer, K. E.; Galitovskaya, E. N.; Smeltzer, M. S. Photothermal Nanotherapeutics and Nanodiagnostics for Selective Killing of Bacteria Targeted with Gold Nanoparticles. *Biophys. J.* **2006**, *90*, 619–627.

(71) Vo-Dinh, T. Shining Gold Nanostars: From Cancer Diagnostics to Photothermal Treatment and Immunotherapy. *J. Immunol. Sci.* **2018**, *2*, 1–8.

(72) Crawford, B.; Shammas, R.; Fales, A.; Brown, D.; Hollenbeck, S.; Vo-Dinh, T.; Devi, G.

Photothermal Ablation of Inflammatory Breast Cancer Tumor Emboli Using Plasmonic Gold Nanostars. *Int. J. Nanomed.* **2017**, *12*, 6259–6272.

(73) Pérez-Hernández, M.; del Pino, P.; Mitchell, S. G.; Moros, M.; Stepien, G.; Pelaz, B.; Parak, W. J.; Gálvez, E. M.; Pardo, J.; de la Fuente, J. M. Dissecting the Molecular Mechanism of Apoptosis during Photothermal Therapy Using Gold Nanoprisms. *ACS Nano* **2015**, *9*, 52–61.

(74) Díaz-Núñez, P.; González-Rubio, G.; Prada, A.; González Izquierdo, J.; Rivera, A.; Bañares, L.; Guerrero-Martínez, A.; Peña-Rodríguez, O. Using Femtosecond Laser Irradiation To Grow the Belly of Gold Nanorods. *J. Phys. Chem. C* **2018**, *122*, 19816–19822.

(75) Yan, J.; Zhu, D.; Xie, J.; Shao, Y.; Xiao, W. Light Tailoring of Internal Atomic Structure of Gold Nanorods. *Small* **2020**, *16*, 2001101.

(76) Heckman, C.; Kanagasundaram, S.; Cayer, M.; Paige, J. Preparation of Cultured Cells for Scanning Electron Microscope. *Protoc. Exch.* **2007**. DOI: 10.1038/nprot.2007.50

(77) Smith, A. M.; Mancini, M. C.; Nie, S. Bioimaging: Second Window for *in Vivo* Imaging. *Nat. Nanotechnol.* **2009**, *4*, 710–711.

CHAPTER 6

Microfluidic Platform for Studying the Reversibility and Kinetics of Aptamer-Target Binding

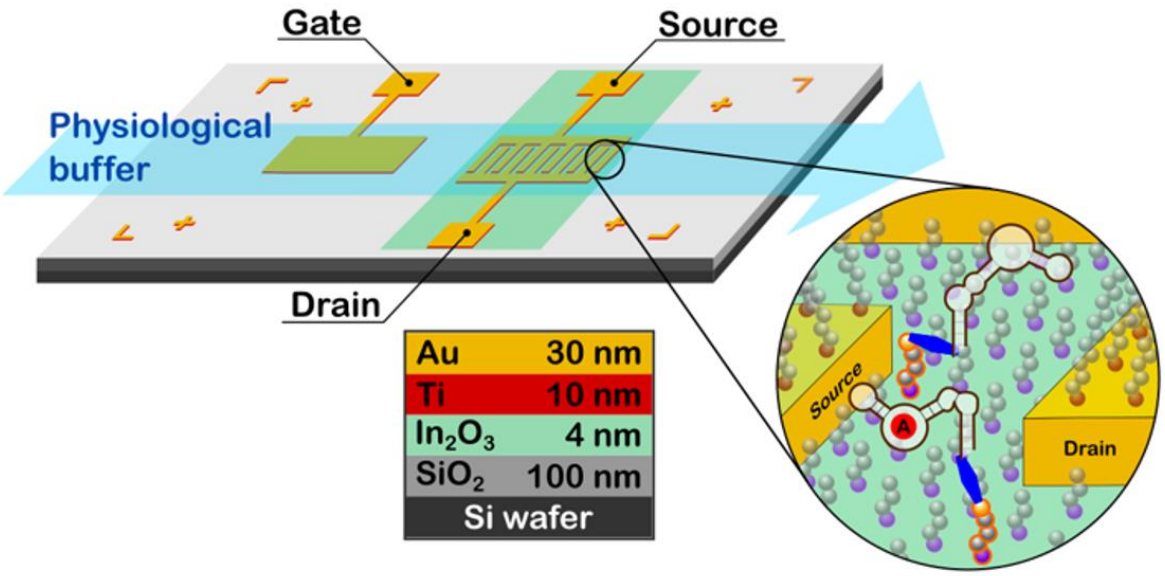

6.A Introduction

In our quest to explore the processes behind the seemingly infinite complexity of the human brain, we study an aspect that is integral to its function: chemical signaling. In addition to the electrical waveforms that fire in response to sensory information, impulses associated with cognition occurring on the order of 100 ms,[1] neurotransmission occurs at multiple spatial and temporal scales. The flux of neurotransmitters through a synaptic cleft, a distance of only about 20 nm,[2] can take place over 0.1-1 ms,[3,4] however other processes, such as nonsynaptic diffusion neurotransmission (NDN) or the tonic release of molecules, can influence neuromodulation over the course of a day or even weeks.[5,6]

Measuring small molecules in the brain presents numerous challenges. The high ionic strength environment has mM concentrations of sodium, calcium, and magnesium ions.[7] Furthermore, molecules of interest have many metabolites and structurally similar analogs, such as dopamine compared to norepinephrine, which differ by only a hydroxyl group.[8] The size and materials of the instrumentation are a consideration as well, as less invasive techniques limit the damage done to surrounding tissue.[9,10] We are also interested in measuring low concentrations of molecules, specifically requiring sensitivity capable of discerning changes in the range of nM for serotonin.[11,12] Various analytical techniques have been utilized to measure neurotransmitters *in vivo* using animal models to gain understanding of the correlations of chemical signaling in relation to behavior.

A widely used technique is fast-scan cyclic voltammetry (FSCV),[13–15] which has been used to provide insights on correlating dopamine release with the expectancy of reward.[16–18] Voltammetry is a primary method, deriving a signal from the transfer of charge at an electrode as a species is oxidized or reduced. Although individual data points are not

collected as rapidly as with a method such as constant potential amperometry, advances in voltage waveforms[19,20] and signal analysis[21] give FSCV the advantage of increased specificity, allowing differentiation of serotonin and dopamine. A typical scan frequency of 10 Hz[22,90] provides sufficient response time to resolve dynamics of dopamine neurotransmission on the order of seconds. One aspect that must be considered when putting FSCV into practice is that the target molecules must be electrically active at a sufficiently low voltage (namely below 1.5 V, above which water begins to oxidize at the carbon electrode).[23]

Other techniques for measuring neurotransmitters include electrochemical enzymatic sensors[24] and microdialysis.[11] Electrochemical enzymatic biosensors (EEB), which measure the product of an analyte after its reaction with the target specific enzyme, measure at time scales comparable to FSCV. In this type of sensor, a molecule that is not electroactive may be measured instead by a secondary product.[25] In the case of an EEB for glutamate, L-glutamate oxidase catalyzes the formation of hydrogen peroxide (H_2O_2), the oxidation of which provides the signal.[26] An advantage of silicon probes is the advanced state of fabrication techniques for this material, and typical silicon probe sizes are ~150 μm, onto which arrays of electrodes can be patterned.[27] In work by Wassum et al., EEBs featuring four electrodes were applied to study fluxes in glutamate levels in the amygdala of awake rats as they engaged in tasks, with a sample averaging time of 0.25 s.[28] The Monbouquette group at UCLA has also fabricated probes with their own iridium oxide (IrOx) reference electrode, eliminating the need for an external silver/silver chloride (Ag/AgCl) reference electrode and displaying reduced noise in the signal compared to a deposited Ag/AgCl film.[29] Apart from the strengths of EEBs, one aspect that limits the scope of targets is that the existence of a suitable enzyme precludes the development of sensors of this type.

In the case of microdialysis, the highly selective method of high-performance liquid chromatography (HPLC) serves as the detector, offering low detection limits and the ability to discern structurally similar analogs.[30] Some drawbacks of microdialysis are that the implanted probe sizes are generally hundreds of microns[31] and requires sampling time on the order of minutes[32] to allow molecules to diffuse though the microdialysis membrane into the perfusate. In work by the Andrews lab at UCLA, reducing the sampling time from 20 min to 3 min revealed more features of the dynamic changes in serotonin levels in mice over the course of hours, which were obscured when sample rates were spaced farther apart.[32] This work highlights the importance of both selectivity and time resolution when aiming to resolve chemical events in the brain.

Lastly, optogenetics is a growing field for its application in measuring neurotransmitters, as the method enables cite-specific monitoring by genetically modifying individual receptors. A method to measure acetylcholine, a target that is difficult to measure physiologically in part due to low concentrations, has been developed using this approach.[33] In another example, *in vivo* measurements of dopamine using the genetically modified receptor DA1h have achieved sensitivities of 10-100 nM concentrations with a rise time of ~100 ms,[34] however optogenetics is as of yet limited by the available means of modifying receptors in order to expand the variety of targets as well as the depth of light penetration into brain tissue.[91]

Working to develop an analytical method that has optimal temporal resolution for resolving transient neurotransmission events while also being highly selective and sensitive to the molecules of interest has led to the emergence of aptamer-based biosensors. Aptamers, or single-stranded oligonucleotides, offer an approach as highly selective

recognition units for many hard to measure targets. The aptamers are identified and isolated by systematic evolution of ligands by exponential enrichment (SELEX).[35] In this method, sequences of nucleotides are combinatorically synthesized, then tethered to a column. The target molecule of interest is then flowed through the column, which results in the elution of sequences which have high binding affinity to the molecule such that aptamers undergo a stem-loop closure upon target binding to destabilize the bond between the aptamer and the column. The sequences are then amplified and further characterized for their selectivity relative to structurally similar analogs. In the work carried out for this project, aptamers were isolated and characterized for their affinity and selectivity by collaborators Milan Stojanovic and Kyung-Ae Yang at Columbia University.[36,37] Aptamers can be identified for many difficult-to-measure targets that are not electroactive or charged,[36,38] offering promising recognition units to differentiate molecules *in vivo*.

Aptamers interact on a molecular level, but the means of measuring the molecular binding events can be done electronically. The earliest example of an electrochemical aptamer-based (E-AB) biosensor was prepared by Ikebukuro and colleagues in 2004 to measure thrombin.[39] The general operating principle of an E-AB is to couple a redox reporter to the aptamer. The reporter is responsible for electron transfer to the electrode upon target binding.[40] In our approach, we do not rely on binding additional electroactive species to the aptamers and measure direct charge transfer, but rather measure the current across a field-effect transistor (FET). We utilize indium oxide (In_2O_3) as a high-mobility *n*-type semiconductor for the channel material of our FETs,[41] deposited in nanometer-thick layers giving a high surface-to-volume ratio, on top of which gold electrodes apply the voltage bias between these "source" and "drain" electrodes (V_{ds}).[42,43] A third electrode, the "gate"

electrode, applies a potential relative to the source (V_{gs}), which modulates the transconductance of the semiconductor and thus the magnitude of the current which passes between the source and drain electrode. As mentioned, the In_2O_3 layer is very thin, ~4 nm,[43,44] which means that the number of surface atoms relative to the bulk is significant and small changes in the electronic environment at the surface results in measurable changes of the transconductance.[42–44] As the aptamers (which themselves are composed of charged oligonucleotides) bind with a target molecule, the signal is obtained by monitoring the current at the drain electrode (I_d) (**Figure 6.1**).

The FETs are patterned on silicon wafers using fabrication techniques including photolithography. The FETs can be produced at small scales for use on implantable probes. In the Andrews group, probes have been made with two FETs side by side on a 50 μm tip. A picture of one such "neuroprobe" mounted on a printed circuit board (PCB) for electrical contacts is shown in **Figure 6.S1**.

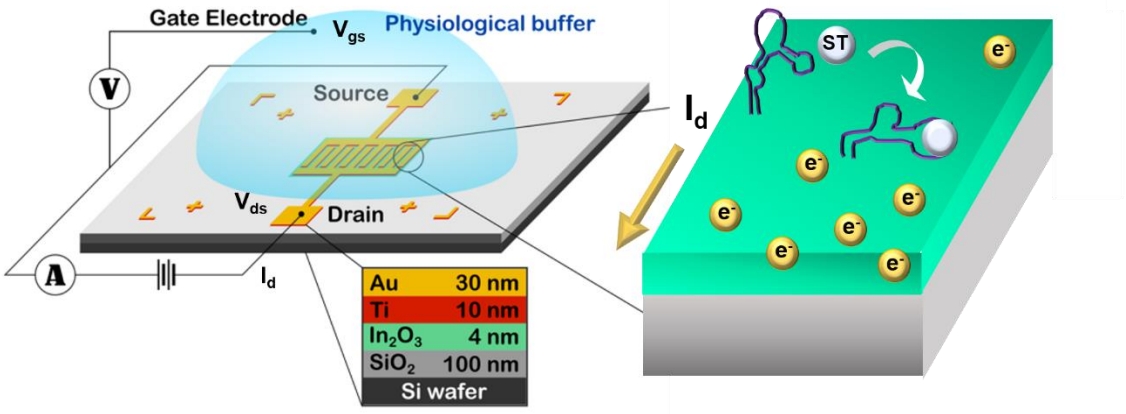

Figure 6.1. Schematic of field-effect transistor (FET) operation, where a bias is applied between gate and source electrodes (V_{gs}) through solution and between drain and source electrodes (V_{ds}) through the semiconductor channel. Changes in the electric environment at the surface of the semiconductor, such as from a conformational change of aptamers upon target (ST) binding, causes a change in the current measured at the drain electrode, I_d.

In previous work within the Andrews lab, aptamer-FETs functionalized with aptamers selective for serotonin, dopamine,[43] glucose, phenylalanine,[45] and cortisol[46] have been reported.[38] Specifically, the serotonin aptamer FETs boast detection limits down to fM levels while measuring in 1 × strength artificial cerebrospinal fluid (aCSF) solution.[38] This high sensitivity of the aptamer FET surface to bound targets (using the serotonin aptamer which has a K_D of 30 nM measured in solution) was hypothesized to be due to the enhanced sensitivity of the nano-thickness In_2O_3 along with the conformational changes induced by the target binding to these aptamers. In the same study, this FET architecture, including functionalization chemistry (described in experimental methods), was also shown to be capable of measuring chemical binding events occurring beyond the Debye length relative to the semiconductor surface, which is to say the high ionic strength environment of the

solution did not shield the material from experiencing changes in transconductance. In addition, data demonstrating an effective glucose aptamer-FETs further reinforced the ability to measure non-charged species with this approach.

To expand upon this previous work, my goal was to characterize the temporal limits of our aptamer FETs. To do so, I designed the FET geometry and a fluidics platform to monitor FET response in real time. These FETs featured three sets of interdigitated electrodes, as well as an IrOx "on-chip" gate electrode, prepared in collaboration with the Monbouquette lab,[29] allowing for the 3-point FET measurements to be carried out within a closed flow cell.

The changes in current in response to aptamer-target binding at biologically relevant concentrations can be small, on the order of nA or even pA, so the measurement must be done with minimal noise. As an analytical technique, it is desirable to have multiple FETs for replicates, controls for drift, and measurement of multiple targets simultaneously. Commercial instrumentation for these electrical measurements amounts to large, costly instrument stations. We aimed to develop custom hardware for measuring our FETs with simultaneous, low noise measurements. In collaboration with the lab of Miguel Alcañiz-Fillol at the Universidad Politécnica de Valencia in Valencia, Spain, we developed a platform that enabled simultaneous measurement of 4 FETs, along with custom software to program voltage sweeps and analyze data in real time.

6.B Experimental Methods

6.B.1 Materials

Chemicals were purchased from Sigma-Aldrich Co. (St. Louis, MO). Polydimethylsiloxane (PDMS) used to create microfluidic channels was prepared with SYLGARD 184 (Dow Corning Corporation, Midland, MI). All water used in solution preparation, functionalization, and rinsing substrates was deionized (18.2 MΩ) by a Milli-Q system (Millipore, Billerica, MA).

6.B.2 Field-Effect Transistor Fabrication

For measurements carried out in the reversibility and kinetics studies, FETs were fabricated using a spin-coating method to deposit In_2O_3 in films of about 4 nm in thickness. Heavily doped silicon wafers (University Wafer, Boston, MA or WaferPro, San Jose, CA) with a 100 nm thermally grown oxide layer were spin-coated with a 0.1 M aqueous solution of indium(III) nitrate hydrate ($In(NO_3)_3 \bullet xH_2O$, 99.999%) at 3000 rpm for 30 s. Substrates were then heated at 150 °C for 10 min followed by 3 h of annealing at 350 °C.[1,2] Three pairs of interdigitated source and drain electrodes along with an additional non-interdigitated electrode for the gate were patterned using a second shadow mask and deposition of a 10 nm titanium (Ti) adhesion layer followed by 50 nm gold (Au) *via* electron-beam evaporation (CHA Solution electron beam). The IrOx on-chip gate electrode was deposited electrochemically using a method described in Tolosa et al.[29]

To fabricate the FETs used in the multi-FET studies where we investigated simultaneous FET measurements, we employed a dual shadow mask approach to create a 4-FET chip. First, In_2O_3 rectangles (3.3 mm × 2.1 mm) were deposited *via* RF sputtering

(Denton Discovery 550 sputtering system) to serve as the semiconducting channel material. The thickness was set at 16 nm by controlling the sputtering time. This thickness was determined to be optimal for high sensitivity to ionic (pH) changes while maintaining film uniformity.[47] The In_2O_3 rectangles were spaced 6.6 mm apart such that individual FETs were not on a continuous layer to prevent crosstalk between FETs when undergoing simultaneous monitoring. Source and drain electrodes were patterned in the same method described previously. The dimensions of both geometries of FETs and effective sensing areas between interdigitations are shown in **Figures 6.S2-6.S3.**

6.B.3 Surface Functionalization

Once isolated *via* the SELEX method,[36,37] the aptamer oligonucleotides were purchased from Integrated DNA Technologies (Coralville, IA). These sequences were thiolated at the 5' end to enable our coupling chemistry with a maleimide molecule.[48] The sequences used are shown in supporting information. Our first step in the functionalization procedure was to expose the FET substrates to UV light for 10 min. The UV exposure serves to clean the surface and activate hydroxyl groups on the In_2O_3 layer to enhance reactivity.[49] The substrates were then immediately moved to a vacuum flask containing a mixture of (3-aminopropyl)trimethoxysilane (APTMS) and trimethoxy(propyl)silane (PTMS) in a 1:9 v/v ratio and held at 40 °C for 1 h to carry out a vapor-phase deposition to the oxide layer. The substrates were then triple rinsed with isopropyl alcohol, then annealed on a hot plate for 10 minutes at 95 °C. To passivate the Au electrodes with a monolayer of alkanethiol to decrease leakage current through solution while measuring the FETs, the substrates were placed in a 1 mM ethanolic solution of 1-dodecanethiol (C12SH) for 1 h.[50] After rinsing with

ethanol, the substrates were then incubated with a 1 mM solution of 3-maleimidobenzoic acid *N*-hydroxysuccinimide ester (MBS) in 1:9 (v/v) dimethyl sulfoxide and phosphate-buffered saline (1× PBS, pH 7.4) for 30 min. The aptamer sequences were diluted to 1 μM in nuclease-free water (Sigma Aldrich, 7732-18-5) and the solution was heated for 5 min at 95 °C followed by rapid cooling in an ice bath in order to reduce nonspecific interactions between aptamer strands.[51] The aptamer solution was then drop-cast over the FETs for 24 h, after which the substrates were rinsed with deionized water and dried under N_2 gas. A schematic of the organic coupling chemistry to functionalize aptamers to the In_2O_3 surface is shown in **Figure 6.2**.

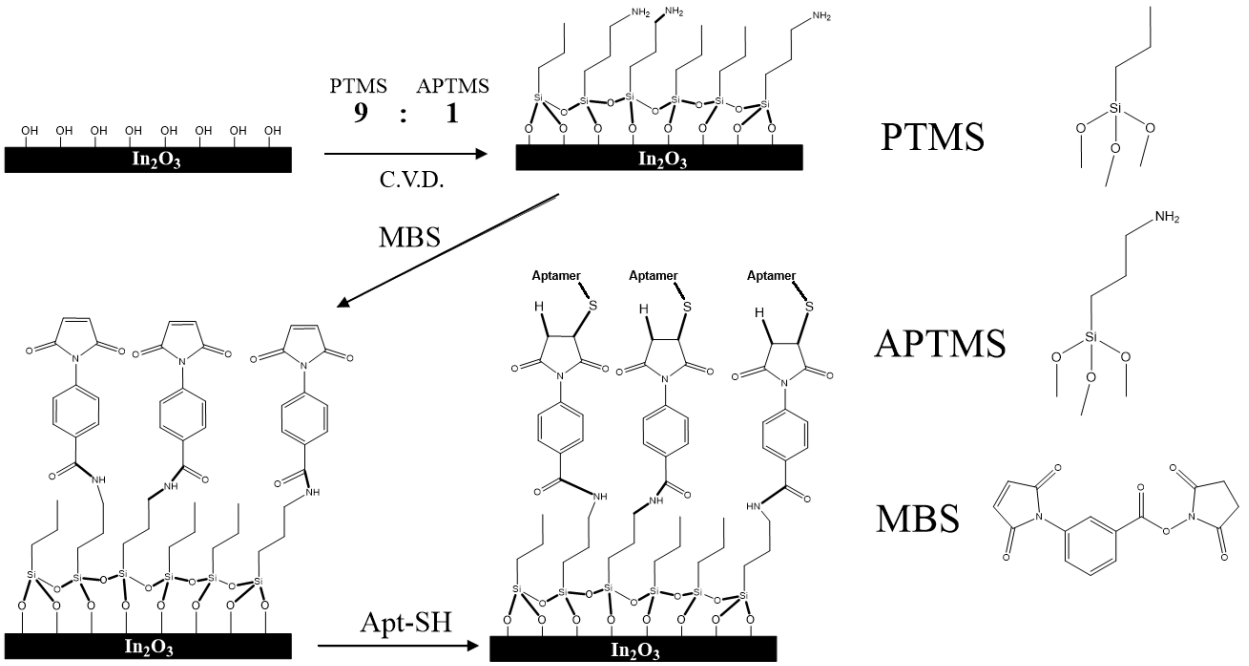

Figure 6.2. Schematic of organic linker molecules to functionalize indium oxide (In_2O_3) with aptamers. A mixture of trimethoxy(propyl)silane (PTMS) and (3-aminopropyl)trimethoxysilane (APTMS) in a 9:1 v/v ratio is deposited *via* chemical vapor deposition (C.V.D.), followed by the addition of 3-maleimidobenzoic acid *N*-hydroxysuccinimide ester (MBS). Lastly, the aptamers with a thiol termination (Apt-SH) are linked to the maleimide functional group.

6.B.4 Solution Preparation

An artificial cerebral-spinal fluid (aCSF) buffer was prepared and used as the solution for baseline measurements (no analyte) as well as the buffer for varying concentrations of the target molecules. The aCSF contained magnesium and calcium ions and was buffered to pH 7.4 through a dropwise addition of hydrochloric acid (HCl). The concentrations of all salt components are listed in **Table 6.S2**.

6.B.5 Microfluidic Setup

The fluidic channels were designed in AutoCAD software and a silicon template was created using photolithography, over which PDMS was cured for 6 hours at 60 °C to create the channels. The fluidic system included a pressure generator (Elveflow AF1 Mk2), flow rate sensor (Elveflow MFS4), and multiplex pneumatic valve switch (Elveflow Distributor MUX) capable of delivering up to eight different solutions. The valve was chosen because of its fast switching time (about 150 ms) and minimal mechanical noise, thereby reducing the effect of a flow rate disruption that would in turn affect the electrical reading of the FETs. The system was controlled using the Elveflow smart interface GUI, which interfaces the pressure generator with a thermal flow rate sensor (Elveflow MFS). In **Figure 6.3C,** a representation of the fluidic system is shown, in which reservoirs are filled with buffers that contain different concentrations of analyte or different pH values. Tygon tubing was used to connect the solution reservoirs to the flow meter, which was then connected to the PDMS channel *via* polyethylene (PE) tubing (Instech Laboratories, Plymouth Meeting, PA), all tubing having an internal diameter of 0.7 mm. Both inlet and outlet of the PDMS channel were punched using a 0.7 mm biopsy punch, which allowed the insertion of the PE tubing. A photo of the channel

on a 3-FET fluidic substrate is shown in **Figure 6.3B**. We positioned the gate electrode at the outlet of the channel for all measurements for consistency.[52] A poly(methyl methacrylate) (PMMA) press was designed to affix the PDMS channel to the chip to prevent leaking.

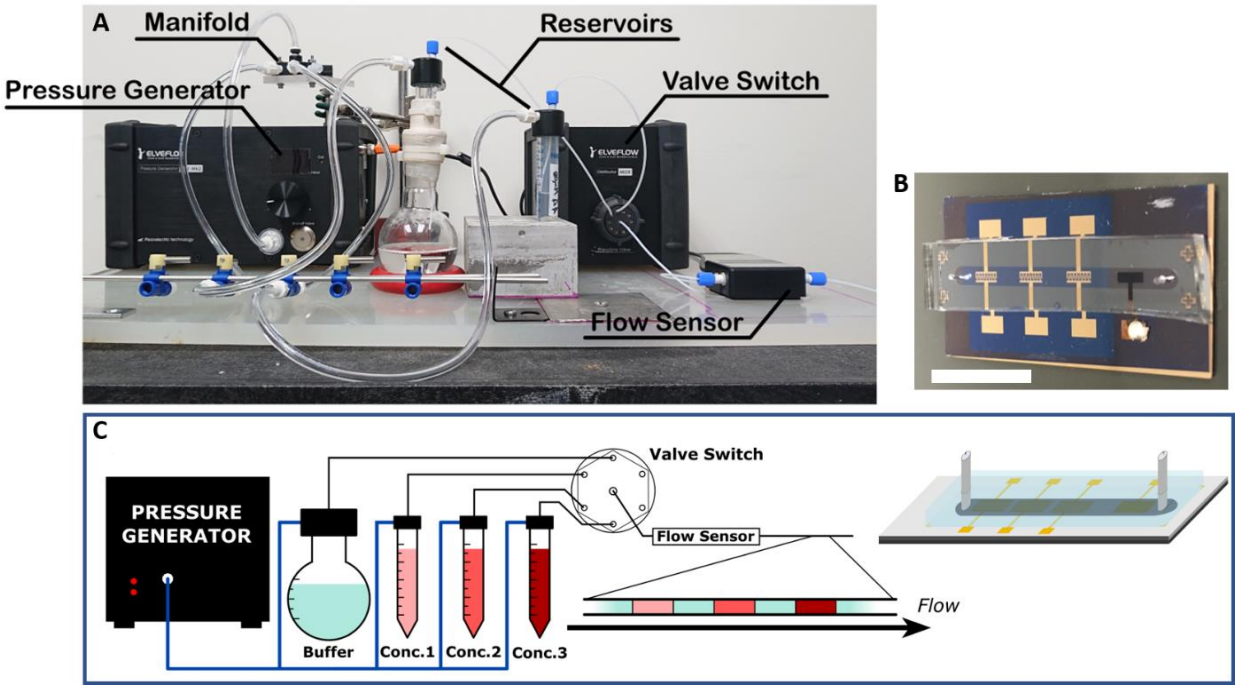

Figure 6.3. (A) Photographs of fluidic hardware setup for 2 solutions and **(B)** fluidic field-effect transistors with polydimethylsiloxane (PDMS) channel. Scale bar is 1 cm. **(C)** Schematic of flow system sending multiple concentrations of target solution in sequence.

6.B.6 Electrical Measurements and Custom Multi-Field-Effect Transistor Hardware

For the measurements involving characterization of the aptamer-target binding reversibility and kinetic parameters, a commercial silicon characterizer (Keithley 4200A-SCS, Tektronix, Beaverton, OR) was used to measure I_d and apply the operational voltages (V_{gs} and V_{ds}). In these measurements, a single FET was measured at any given time. Both V_{ds} and V_g were held constant while the I_d was monitored over time (i-t measurements). A probe station (Signatone, Gilroy, CA) was used to contact the electrodes of the FET. A photo of the setup with contacts, PDMS channel, and PMMA press is shown in **Figure 6.S4**. The applied

V_{ds} was 10 mV, with the V_{gs} chosen such that I_d stabilization would be achieved at an I_d on the order of 100 nA (**Figure 6.S9**). This was a priority because the magnitude of the signals resulting from small concentrations of target binding could be on the order of 1-0.1 nA.[89] A baseline drift of less than ± 1 nA per minute was ideal, which often required a stabilization time (through constant application of V_{ds} and V_{gs}) of up to 8-12 hours per FET. A typical V_{gs} under the conditions of these fluidic experiments was between 200-400 mV. The fastest time resolution for this operational mode per the instrumentation was ~3 s^{-1}.

To measure multiple FETs simultaneously, we developed a custom multi-FET measurement system (MFMS), working in collaboration with the lab of Miguel Alcañiz-Fillol at the Universidad Politécnica de Valencia in Valencia, Spain. The hardware, with accompanying software programmed in *MATLAB 2021a* (MathWorks, Natick, MA), measures four FETs and allows the user to program custom voltage sweeps. The time resolution of our FET measurements was also enhanced by the implementation of our MFMS, with each voltage step as fast as 200 µs. A constant V_{ds} was applied (typically 1-10 mV) while sweeping the V_{gs} over a range of 0 to 300 mV. Further detail of the hardware's design and capabilities is included in supporting information.

6.B.7 Data Processing

In the case of i-t measurements, the absolute change in drain current (ΔI_d) was used to quantify the effect of aptamer-target binding. To obtain kinetic terms, exponential one-phase adsorption and desorption models were fitted to the I_d curves using GraphPad Prism 7.04 (GraphPad Software Inc., San Diego, CA) (**Figure 6.5**).

Calibrated response (CR) as a metric for measuring FET response was applied to the data collected by our MFMS, which measured I_d while sweeping V_{gs}. This method is further described in the supporting information.[53] A real-time control GUI was developed in *MATLAB 2021a* which allowed us to calculate CR at each step of V_{gs} as it was applied by the MFMS.

6.C Results and Discussion

6.C.1 Aptamer Binding Reversibility

In the fluidic experiment to investigate target unbinding from the surface-functionalized aptamers, solutions were flowed with a constant flow rate over the FET while monitoring I_d given constant applications of V_{ds} and V_{gs}. First, aCSF buffer was flowed, followed by a "plug" of the buffer containing a concentration of serotonin or dopamine, then lastly returning to the pure buffer. As the target reaches the FET surface, the I_d increases and eventually reaches a plateau, at which the number of bound versus unbound forms of the aptamer are at equilibrium based on the concentration of the target molecule in solution.[54] When returning to the buffer alone, the signal decreases back to baseline current. (**Figure 6.4A**). We also carried out experiments to optimize the flow rate, where the association and dissociation of target analytes were observed at varying flow rates. In a case where the association is diffusion-limited, which is to say the concentration of the molecule is significantly different at the FET's surface due to the aptamer binding and depleting the solution faster than the flow carries more molecules above the surface, the time needed to reach the equilibrium plateau is proportional to the flow rate.[55] Once reaching sufficient flow rates to leave the diffusion-limited regime and instead function in a kinetic-limited regime,

where the binding affinity of the aptamers to the target is the primary factor for equilibration time, increasing the flow rate will no longer shorten the time to reach equilibrium. Flow rates of 50, 100, 200, 300, 400, and 500 μL/min were investigated. The equilibrium time was much slower when flowed at 50, 100 and 200 μL/min, but after reaching at least 300 μL/min the association time was constant (**Figure 6.S6**). For the majority of all subsequent experiments, unless specifically noted, the chosen flow rate was set at 300 μL/min. Using higher flow rates had an increased risk of encountering leaks between the PDMS channel and the FET surface.

In the traces of I_d collected in these i-t experiments, we observed the reversibility of the aptamer-FET devices as the target unbinds from the aptamer. Previous measurements of our aptamer-FETs, in which concentrations of target were titrated (mixed *via* pipet) into a stationary well of buffer and allowed to diffuse to the FET surface, increased the concentration monotonically but were not able to observe the process of target desorption in real time (**Figure 6.4A-B, D**).[38,42,45] This reversibility is crucial to the sensor as an analytical method to measure the rise and fall of neurotransmitters during a transient event. Furthermore, the same FET was able to be used in repeated measurements and demonstrated the same sensitivity for a given concentration. For example, **Figure 6.S7** shows the repeated measurement of 10 nM serotonin on a FET functionalized with the serotonin aptamer. In this experiment, each signal had a magnitude of about 5 nA for subsequent measurements at this same concentration. The aptamer FETs maintained their sensitivity while under the flow of aCSF buffer for measurements over the course of about 20 hours, after which signals were no longer observed in the presence of target molecules. Upon inspection of the FET surfaces after prolonged measurements, we observed salt crystallization forming at the junctions between the substrate surface and the PDMS channel

walls, which we suspect contributed to their loss of functionality. In a previous study, the fouling of the FETs was investigated by measuring the performance of serotonin aptamer FETs before and after incubating in brain tissue for up to 4 hr.[38] In this case, the reproducibility of the signal was demonstrated. The matter of fouling is not trivial in the case

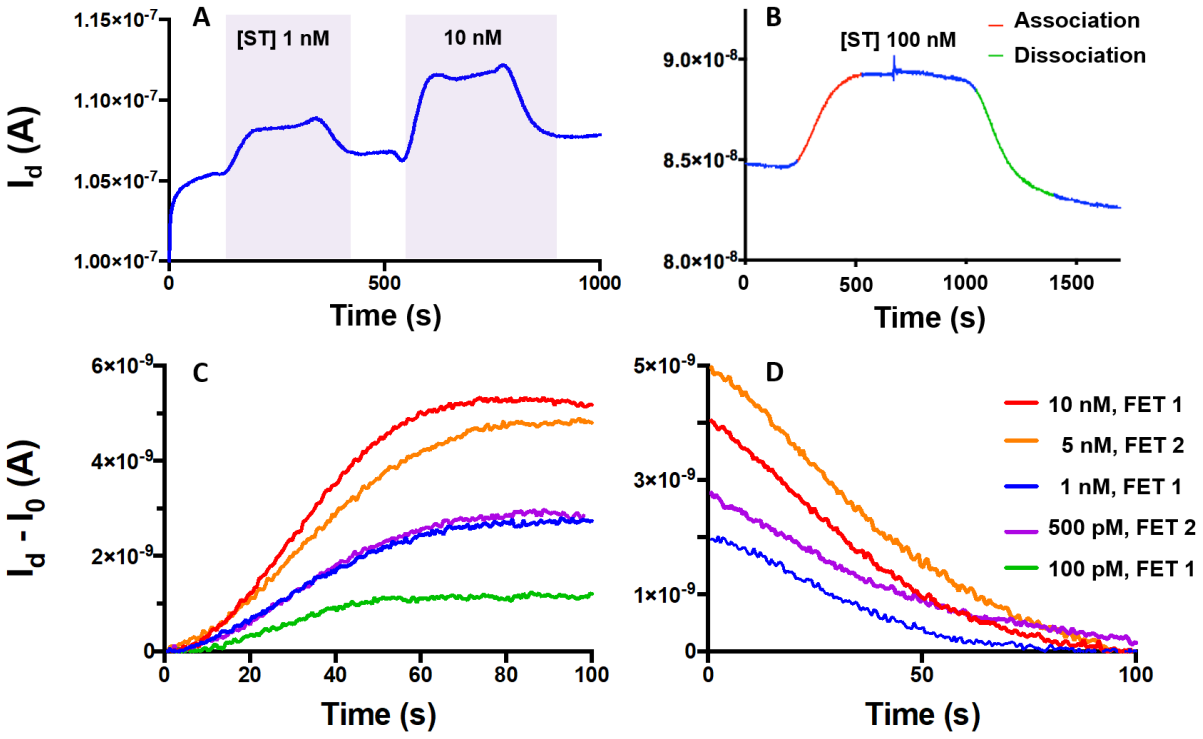

Figure 6.4. (A) Trace of drain current (I_d) measured over time showing the addition of 1 nM then 10 nM serotonin (ST). **(B)** Association and dissociation of 100 nM ST. **(C)** Baseline subtracted association and **(D)** dissociation of various ST concentrations on several field-effect transistors (FETs). Each experiment was carried out in artificial cerebral-spinal fluid buffer with a flowrate of 300 µL/min.

of implantable devices for chronic measurements,[56] however the aptamer FETs demonstrate the necessary consistency in physiological environments for shorter term measurements. Further work can investigate means of passivation and longevity for longer experiments.

Similarly in regards to fouling, at high enough concentrations, nearing 1 μM serotonin, the FETs began to exhibit behavior in which the current did not reach an equilibrium plateau, but rather continuously increased (**Figure 6.S8**). After this behavior was observed, we found that the FETs could not be rinsed and restored to their previous responsiveness with target binding and unbinding. We interpret this result to mean that the aptamer FET surfaces, including the APTMS spacer molecules, may incur additional non-specific interactions and this surface fouling hinders the function of the aptamers.[57] However, we anticipate that this constraint does not limit the aptamer-FET method for our intentions of measuring neurotransmitters because these concentrations far exceed the physiological concentrations of serotonin in the brain (for example, basal levels are on the order of nM in mouse and rat models).[11,58]

6.C.2 Aptamer Binding Kinetics in Flow

Using our fluidic approach, we investigated aptamer binding affinity through a kinetic model. The equilibrium dissociation constant, (K_D) is a value that expresses the binding affinity inversely and is the concentration at which half of the aptamers are in a bound state at equilibrium.[59] In terms of kinetics, K_D can also be expressed as a ratio of the rate constants for dissociation, k_{off}, over that for association, k_{on}, where $K_D = \frac{k_{off}}{k_{on}}$. We observe the time for unbinding of the target to be independent of the molecule's concentration (**Figure 6.4D**), which supports our use of the one-phase dissociation model for kinetics.[60] Using this model, we obtain the rate constants k_{on} and k_{off} by fitting the exponential equations to our I_d curves (**Figure 6.5)**. This kinetic K_D is specific to our flow system, the aptamers being in their functionalized state on the substrate, and the concentrations of the ions in the medium

(aCSF). As part of their characterization, the K_D of the aptamers free in solution was obtained *via* fluorescent displacement assays.[38] Although measured using different approaches, we found that the values obtained for K_D of the aptamers on our FETs were on the same order

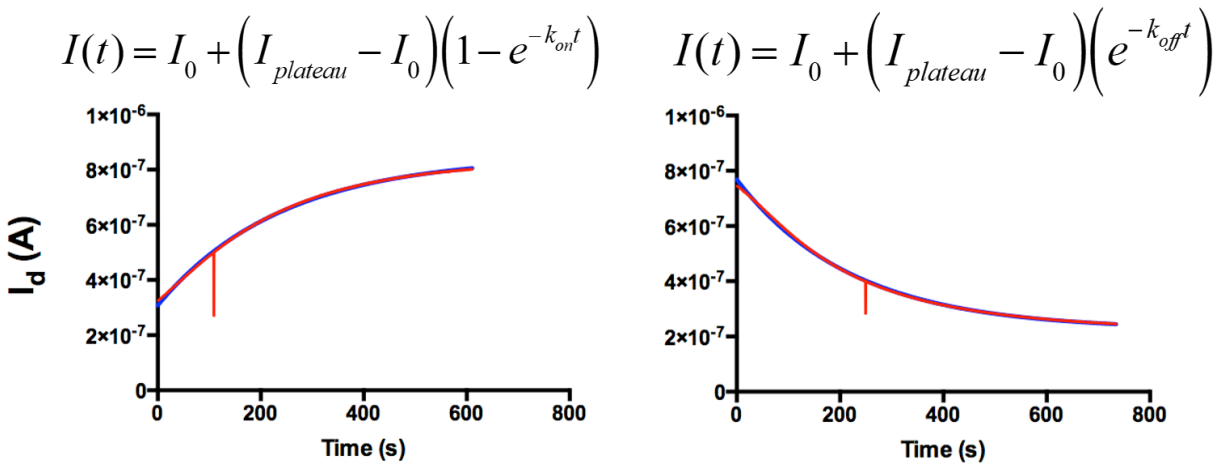

Figure 6.5. Fitting association (left) and dissociation (right) of dopamine (10 µM) with exponential equations (blue line) to obtain parameters of k_{on} and k_{off}. R^2 values for association and dissociation are 0.997 and 0.999, respectively. The spike in the data (red line) seen at drain current (I_d) of 500 nA is an artifact of the Keithley measurement platform changing current scale. The experiment was carried out in artificial cerebral-spinal fluid buffer with a flowrate of 300 µL/min.

of those determined for the aptamers in solution (**Table 6.1**). This comparison suggests that tethering the aptamers to the planar surface does not significantly alter their target affinity after functionalization. Note that the K_D measured in this system is applicable to the system itself and values are comparative given the specific parameters, including the channel dimensions. The agreement of K_D calculated from kinetic parameters measured on-chip compared to solution-based methods was also observed by Merriman and colleagues using their single-molecule nanoelectrodes functionalized with aptamers for the SARS-CoV-2 N and S gene proteins.[89] Continued experiments could bolster this evidence.

In practice, implantable aptamer FET probes will not be subjected to flow, but rather exposed to an environment where molecules diffuse to the sensor surface. The sensor dynamics of target binding/unbinding and thus the rate of change in the signal given a concentration of serotonin (which also changes in time) is a complex system. Using FETs functionalized with the serotonin aptamer, we carried out an experiment to resolve "transient events" of different time spans (**Figure 6.6**). While flowing solutions at

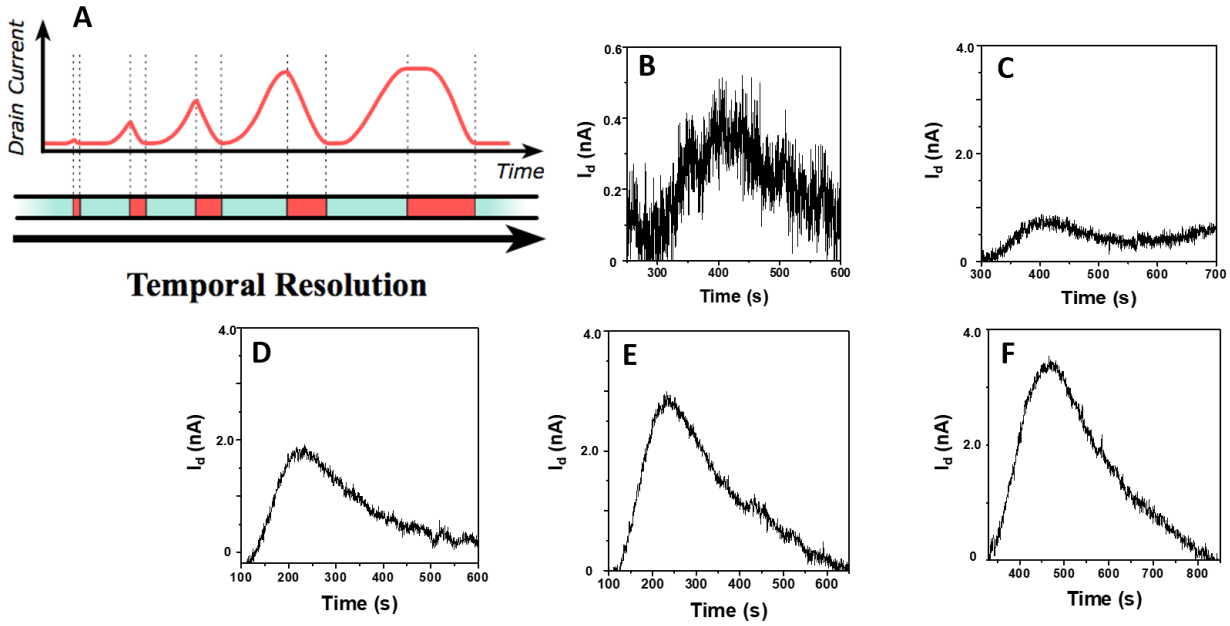

Figure 6.6. (A) Experimental design to resolve "events" of varying durations of flowing 20 nM serotonin at 100 µL/min over a FET functionalized with serotonin aptamer; **(B)** 12 s, **(C)** 30 s, **(D)** 60 s, **(E)** 90 s, and **(F)** 120 s. The applied voltages were 100 mV and 10 mV for V_{gs} and V_{ds}, respectively.

100 µL/min, which falls in the diffusion-limited regime, we determined the time for the sensor to reach equilibrium in 20 nM serotonin to be ~460 s. In these conditions, we resolved a measurable I_d signal, about 0.4 nA above baseline, from a 12 s plug of serotonin, mimicking a neurotransmission event. Although the matter of calibrating for quantification is a complex matter,[61,62] in part because an *in vivo* measurement is done on top of a basal presence of

neurotransmitters, in principal if one knew the association rate constant of the system, one could approximate the change in concentration by using the slope of the signal increase.[63]

As noted above, the In_2O_3 aptamer-FETs have demonstrated high sensitivity to their target and the capability to measure several orders below the aptamer's K_D.[38] In the process of identifying and isolating aptamers, multiple sequences have been found that bind to the same target, which still enable measurement of physiologically relevant concentrations. These sequences may have significant structural differences,[64] however one systematic approach to tuning an aptamer's K_D, described by Armstrong and Strouse,[65] involves adjusting base pairs in the stem-loop region of the aptamer. In the SELEX method, the aptamer-target binding resulting in a favorable stem closure leads to the aptamer being displaced from the column. In addition to the target-aptamer interaction, the strength of the stem closure is also influential in the favorability of this process. Thus, it was hypothesized that altering the base pairs in the stem (for instance A-T instead of G-C) would result in a lower binding affinity, which they demonstrated between variations of an ATP-selective aptamer.

From a kinetics standpoint, one factor that would be connected to the observed difference in K_D is if the aptamers demonstrated different values of k_{off}, indicating a faster or slower dissociation rate. As faster dissociation rates are critical to our sensor's temporal limits, the fluidic FET platform opens a strong means to optimize sensor response times by comparing alternate sequences for the same target in their surface-functionalized configuration.

Table 6.1. Dissociation constant (K_D) of aptamers obtained from fluidic FET experiments (substrate) verses those obtained from aptamers free in solution.

	N values	K_D (Substrate)	K_D (Solution)
Dopamine	2	240 ± 30 nM*	150 nM
Serotonin	3	30 ± 20 nM*	30 nM

*Error values are standard deviations

6.C.3 The Multiplexed Field-Effect Transistor Measurement System

In order to increase the strengths of our aptamer FETs as an analytical technique, we have the need to measure multiple FETs on the same chip, which provide replicate measurements, multiple targets, and controls. To achieve this goal, we developed what I will refer to as the multiplexed FET measurement system (MFMS) (**Figure 6.7A**). The MFMS has a temporal resolution of 200 μs per sample, can apply voltage biases in programmable sweeps, and measures four FETs simultaneously (this translates to sweeping all channels at 5 Hz with 1000 points per sweep, or 50 Hz at 100 points per sweep). A deterministic hold-time with a set V_{gs} is incorporated in the sweep based on the specified sample frequency. This sampling rate is sufficient for capturing fast chemical processes such as the release of neurotransmitters across a synapse.

As previously discussed with regards to FET drift and stabilization time, minimizing the noise performance of the MFMS was critical since the magnitude of signals caused from the trans-impedance variations of the biosensors can be reflected in variations in I_d on the order of less than 1 nA. Two aspects included in our system to aid in noise reduction were

the use of a 6.2 V battery for the power supply and low noise operational amplifiers in the analog signal processing. In terms of current resolution, the available scales (determined by shunt resistor selection) are 200 nA, 500 nA, 1 μA, and 10 μA, leading to a resolution of 6 pA, 15 pA, 30 pA, and 300 pA, respectively. This range is comparable to the limits of the Keithley 4200A-SCS silicon characterizer that was used for the reversibility and kinetics investigations discussed above.

To validate the MFMS's ability to measure our FETs accurately, we compared the I_d response as a function of sweeping V_{gs} using both the Keithley and our custom hardware. On three unfunctionalized FET substrates (solely dodecanethiol passivation on the gold electrodes), we applied a sweep of V_{gs} from 0 to 200 mV in steps of 10 mV (given a constant V_{ds} of 2 mV). Shown in **Figure 6.7B**, we observe that the MFMS's I_d values display slightly greater linearity than those obtained using the Keithley (99.74% mean R^2 vs. 98.76% mean R^2), primarily at 5 μA, which is due to the Keithley automatically changing scale as the current increases above this point. In terms of repeatability of the measurements, we observe that compared to the Keithley, our MFMS sweeps drift upwards. This drift stops after about 10 s of continuous sweeping. We believe the likely cause of this is the manner in which the MFMS applies V_{ds} continuously (which leads to the charging of the In_2O_3),[66] as opposed to the "intermission" between the Keithley measurements, when no biasing is applied. A more in-depth discussion of how the MFMS applies voltage biases is covered in the supporting information.

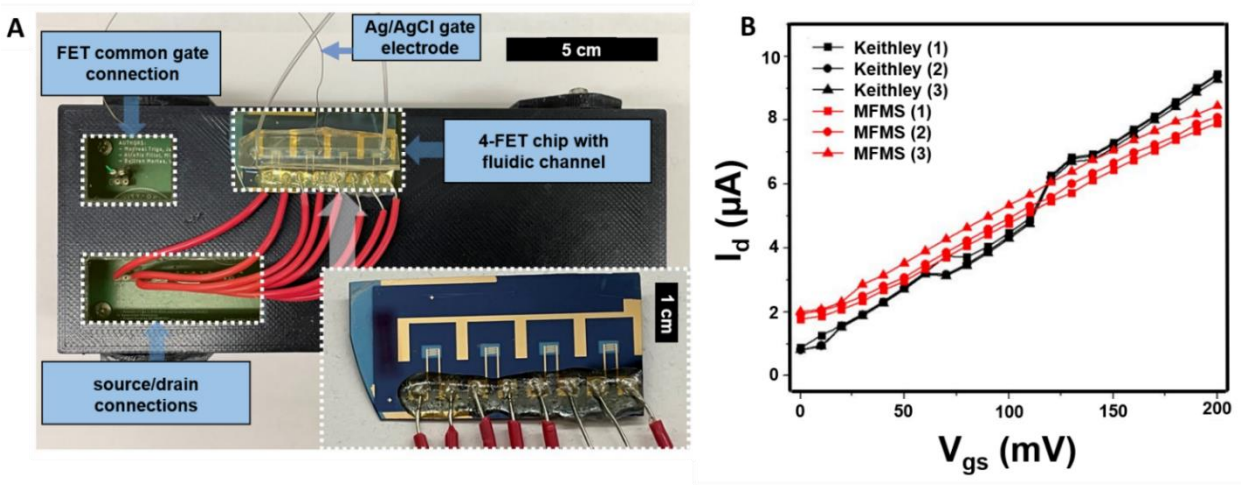

Figure 6.7. (A) Photo of the multi-field-effect transistor (FET) measurement system (MFMS) with fluidic 4-FET chip experiment. **(B)** Validation of MFMS drain current (I_d) measurements (red), in comparison to commercial instrument Keithley 4200A-SCS (black). The mean standard deviation of the sweeps is 71 nA and 221 nA for the Keithley and MFMS, respectively.

6.C.4 Multiplexed Measurements of pH on Four Field-Effect Transistors

We tested the MFMS's functionality by measuring I_d response of four FETs simultaneously as they were exposed to solutions of varying pH. The In_2O_3 surface was functionalized with a 1:9 mixture of APTMS to PTMS and gold electrodes were passivated with dodecanthiol. A fluidic channel was placed over a 4-FET chip (**Figure 6.7A**) and a silver/silver chloride (Ag/AgCl) wire was inserted in the center of the channel to function as the common gate electrode for all FETs. Contacts between the MFMS terminals and the FET electrodes were made with wires and silver epoxy. Each FET was biased with a constant 1 mV V_{ds}, a V_{gs} sweep of 0 to 200 mV in steps of 25 mV every 250 ms, and a hold time of 750 ms (hold V_{gs} of 0 mV). These parameters result in a total sweep time of 3 s. Solutions of 1× PBS with pH from 7.4 to 5.5 and back in steps of 0.5 pH were flowed sequentially over the FET array (**Figure 6.8A)**.

Examining the CR of each FET at a V_{gs} of 100 mV, an increase in CR is seen with decreasing pH; CR then returns to baseline values after the solution returns to the initial pH 7.4 pH. Between the 4 FETs, we see a delay in the response time for the signal to change after a new solution is introduced, a result of the direction of our substrate relative to the direction of flow (here FET 4 is the closest to the inset and FET 1 is positioned at the outlet of the fluidic channel).

The response of our In_2O_3 FETs to changes in pH has been previously characterized.[44,47] The amine termination of the APTMS creates a pH sensitive surface which deprotonates at high pH (pKa ~10.6). Despite this pKa being greater than the pH range we measured, the FETs display sensitivity to the changes in electronic environment contributed to by the variance in degree of polarity of the surface layer[67] and orientation of water molecules at the interface.[68]

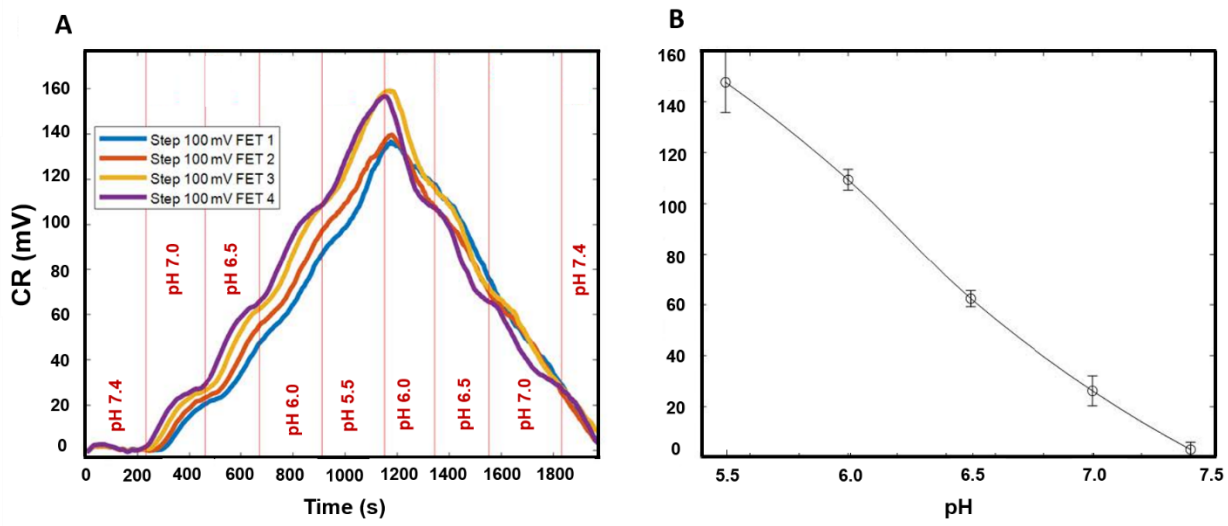

Figure 6.8. (A) Calibrated response (CR) for a multiplexed measurement of 4 field-effect transistors (FETs) as solutions of different pH are flowed over through the fluidic channel at a V_{gs} of 100 mV. Sample rate is 333 mHz. **(B)** Calibration curve of CR versus pH from the measurement of the 4 FETs. Error bars are sample standard deviation.

Overall, the simultaneous 4-FET measurement of pH using our MFMS validated measuring functional FET surfaces.

6.C.5 Preliminary Measurement of Multiple Neurotransmitters Simultaneously

We extended our experiments using the 4-FET MFMS to surfaces functionalized with aptamers for different neurotransmitters, specifically serotonin and glutamate. On the 4-FET substrate, the sensors were set up in pairs, using the serotonin aptamer on one FET alongside a second FET functionalized with a "scrambled sequence" (the same number of each oligonucleotide base in a different order) as a control. Similarly, the remaining 2 FETs were functionalized with the glutamate aptamer and a scrambled control sequence for glutamate. The control sequences allow a measurement with the same surface chemistry, but without conformational changes from target binding, providing a way to account for drift or other mechanical noise from the solution injections. Due to the scale of the FET substrate being sufficiently large, the aptamer solutions were drop-cast in quantities of 50 μL onto the individual FET channels during the functionalization procedure and did not mix.

A PDMS well containing 200 μL of aCSF buffer was situated over the FET array and different concentrations of either serotonin or glutamate were pipetted. The FETs were biased at 1 mV V_{ds} and V_{gs} swept from 0 to 250 mV in steps of 25 mV each 250 ms. Between sweeps, 0 mV V_{gs} was applied for a hold time of 1250 ms (the complete sweep, including hold time, was programmed for 4 s).

The CR at V_{gs} of 175 mV over the course of the target additions is shown in **Figure 6.9,** baselined to the drift of the corresponding control FETs. Each addition event, depicted with vertical lines, indicate 10 μL injections of either aCSF buffer (as a control) or aCSF containing one of the neurotransmitters. Upon injecting 100 nM serotonin (effectively a concentration

of 4.6 nM in 220 µL), the peak signal corresponding to the FET functionalized with serotonin aptamer is 6 mV, above a peak-to-peak noise of 1 mV. The remaining 3 FETs do not appear to respond to addition of the molecule, suggesting the signal is a direct result of the aptamer binding on the active FET. Upon the injection of glutamate (10 µL of 100 nM glutamate, effectively 4.4 nM) the glutamate active FET responds with a peak voltage of 5 mV above 0.5 peak-to-peak noise. Based on these results, we have achieved a multiplexed FET measurement with distinct sensor functionality selective to the desired neurotransmitter.

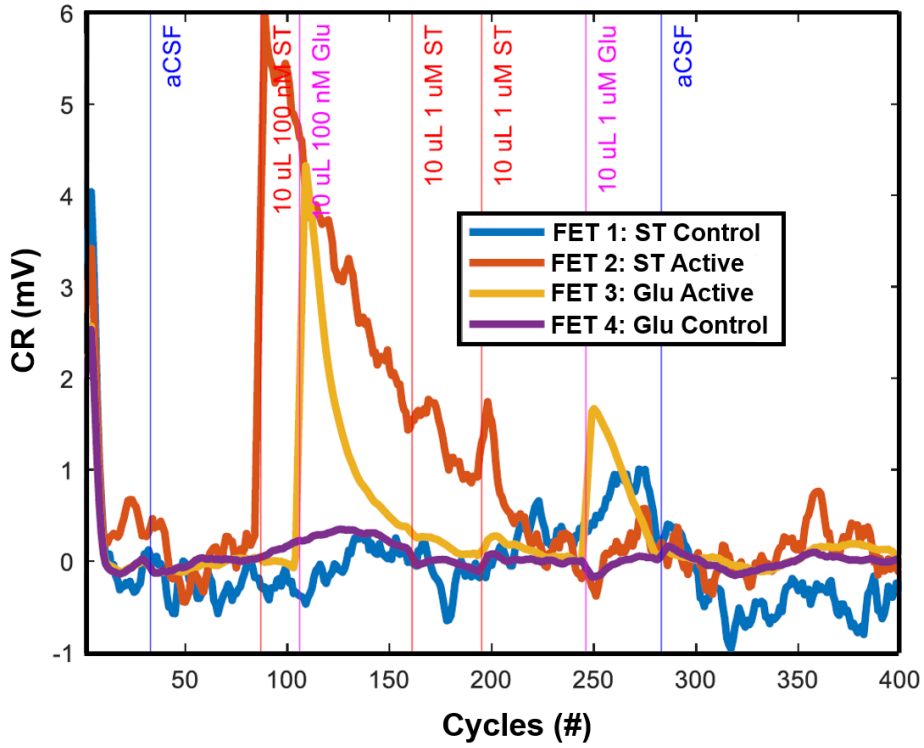

Figure 6.9. Calibrated response (CR) at gate-source voltage (V_{gs}) = 175 mV of 4 field-effect transistors (FETs) functionalized with either serotonin (ST) aptamer, glutamate (Glu) aptamer, or scrambled control sequences for either. The experiment was carried out in artificial cerebral-spinal fluid (aCSF) buffer. Data has been baselined relative to the corresponding control FETs.

In this preliminary experiment, we note that saturation may have occurred as increasingly high concentrations yielded smaller responses than the initial addition. (84 nM

ST and 42 nM Glu). Further experiments that utilize the flow system to rinse the substrate with buffer (as opposed to the monotonic addition) can be repeated to combine multianalyte measurements with investigations of the sequences' dissociations.

6.D Conclusions and Prospects

Aptamer FETs are a promising method to add to the means of studying neurotransmission as it relates to behavior. The access to target selection by identifying aptamers as recognition units taken together with the high sensitivity of In_2O_3 FETs provides the selectivity and low detection limits for resolving transient events. The aspect that must be further studied is in regards to the time response of the sensors. In the previous discussion, I addressed one approach to seeking faster aptamer dissociation rates, which is to alter the aptamer itself, particularly the base pairs in the stem region, and use sequences that demonstrate higher K_D and faster $k_{off.}$ The effectiveness of this strategy can be optimized using a flow system such as the one I have described, which has enabled dynamic measurement of neurotransmitters at biologically relevant concentrations.

Another approach to influencing target desorption is related to the operational voltages involved in the FET measurement. Numerous studies showing how voltage pulses can manipulate DNA adsorption,[69] orientation,[70,71] hybridization,[72,73] and melting[74] on surfaces provide motivation for investigating how modulation of V_{ds} and V_{gs} may affect aptamer binding kinetics of our sensors. The custom hardware and software of our MFMS enables a direct lead-in to future experiments to study how voltage modulation influences aptamer binding-unbinding because of the capability to program unique voltage sweeps.

Nonetheless, our aptamer FETs have been employed in a preliminary experiment measuring *in vivo*, where the neuroprobes functionalized with serotonin aptamer were implanted in awake mice and a change in signal was observed following stimulation and release of serotonin in the brain.[75] Improving the temporal limits will only improve the ability to resolve subtle fluctuations that may be occurring.

Towards further improving our implementation of aptamer FETs as an analytical technique, the need for monitoring multiple FETs simultaneously has been addressed. We have prototyped and tested a platform which measures 4 FETs simultaneously. The platform is significantly smaller and more lightweight than the commercial probe station. This improvement is valuable when looking towards studies in awake animals, where compact hardware that creates minimal disruption to the experimental environment is crucial. Using what we have learned, a future platform to measure an even greater number of FETs can be designed.

Initial experiments demonstrate effective multi-analyte selectivity detection when functionalizing FETs with different sequences. As we think towards the work done in FET miniaturization, such as is necessary for *in vivo* studies, one challenge will be in optimizing "addressable chemistry" to functionalize different aptamers to FETs which are only tens of μm apart, for multi-analyte measurements using neuroprobes. Work is being done to translate an electrochemical method of activating molecules to control functionalization spatially on the In_2O_3 surface, such as the procedure carried out by Curreli and coworkers on In_2O_3 nanowires.[76] In devices prepared by Merriman et. al in 2022, single molecule nanoelectrode arrays were functionalized by directing the desired molecule using dielectrophoresis.[89] This manner of trapping the molecule between micro or nanoelectrodes

has the advantage of short preparation times, able to be completed in ~10 s. Looking to the future, expanding our multiplexing capacity not only bolters the analytical method by increasing controls and replicates, but allows the incorporation of more aptamers for otherwise difficult to measure targets, all on one 50 μm silicon probe.

The high sensitivity of the aptamer FETs lends itself to potential in "bedside" monitoring devices, in which small sample volumes are optimal. An example of this is an aptamer-based device to detect biomarkers from bacteria indicating the onset of sepsis, which can be a life-threatening condition and continuous monitoring can improve patient outcomes.[77] Other aptamers have been developed that recognize pathogenetic cells as a whole.[78] Aside from early detection of harmful biomarkers, an example of controlled drug release in feedback with continuous monitoring of vancomycin, an antibiotic, using electrochemical aptamer biosensors was demonstrated by the Plaxco group at the University of California, Santa Barbara.[79] The portable, lightweight MFMS we developed in the interest of monitoring multiple FETs simultaneously is also an ideal size for this form of instrumentation.

Another avenue of aptamer sensor miniaturization, in cases where fluidic sample handling protocols are not necessary, is their use in wearable devices.[80] In 2023, Ye et al. reported on a wearable device to sense oestradiol, a female reproductive hormone, using aptamer displacement measured using sensitive gold nanoparticle electrodes.[81] Devices such as these with applications in fertility and pregnancy testing are in demand.

A question one might have after discussing the exciting avenues of aptamer technology is why we have yet to see a commercialized aptamer platform.[82] Several challenges exist that must be addressed to fully translate the recognition units to their

greater uses. One matter is in regards to how the specific aptamer-target binding interactions are strongly related to variables such as pH, temperature, and ionic strength, which are more difficult to control in a sensing environment such as a wearable device.[83] These complex, multivariate relationships concerning the binding mechanisms are overall a mystery for many aptamers. As more researchers seek to investigate aptamer mechanisms from other perspectives, including computation,[84,85] greater understanding may open the way for the development of analytical devices operational to wider communities.

6.E Supplementary Materials

6.E.1 Field-Effect Transistor Fabrication

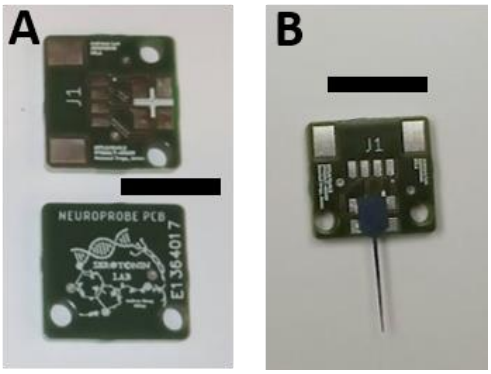

Figure 6.S1. (A) Neuroprobe printed circuit board without and **(B)** with the neuroprobe. Scale bars are 1 cm.

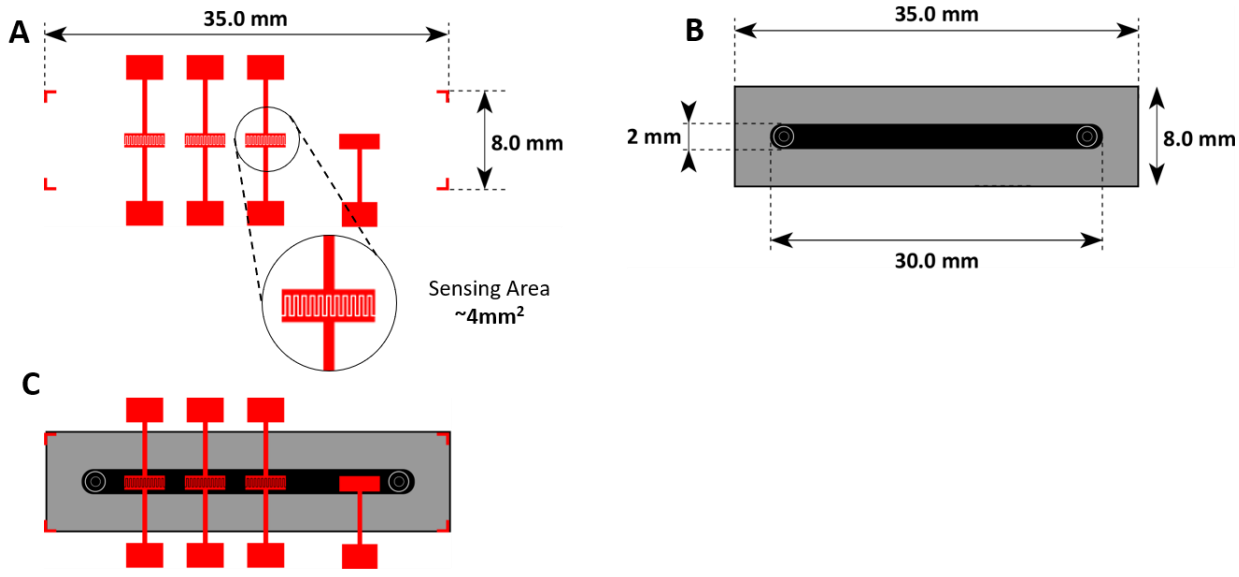

Figure 6.S2. (A) Dimensions of the microfluidic field-effect transistor (FET) chips, zoomed in to show interdigitation. The non-interdigitated electrode on the right end is the gate electrode. **(B)** Polydimethylsiloxane (PDMS) channel dimensions. **(C)** The FETs and PDMS channel superimposed.

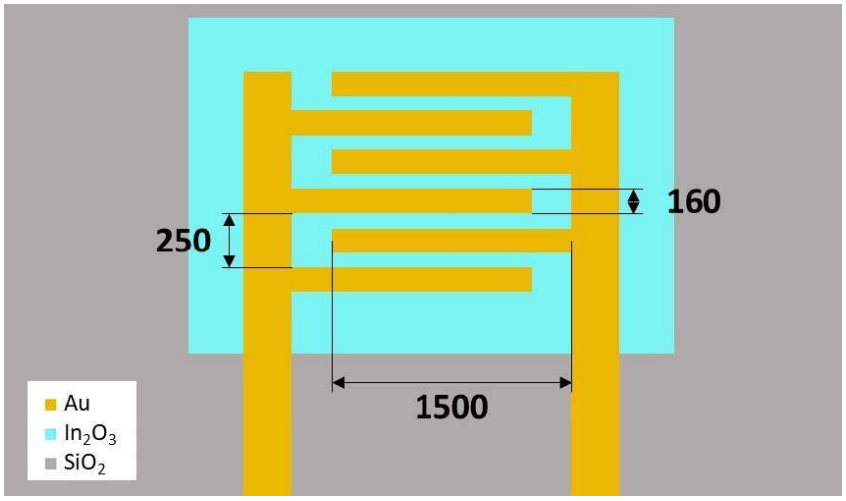

Figure 6.S3. Source and drain geometry of the four-field-effect transistor chips over In_2O_3 channel. Units are in μm. Channel effective length L = 45 μm. Channel effective width W = 6.5 mm. Channel effective area A_{CH} = 0.3 mm^2.

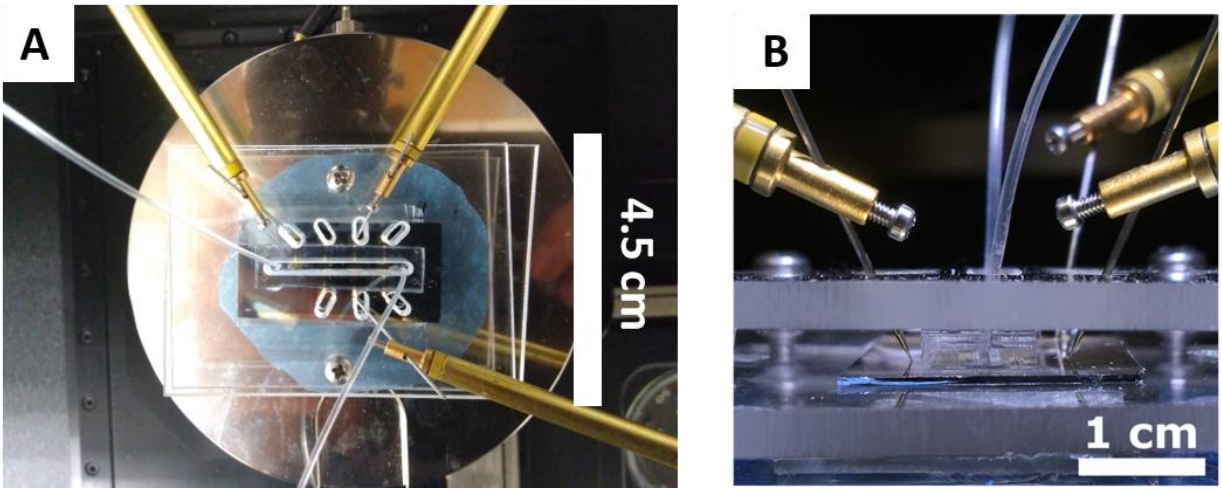

Figure 6.S4. Photo of three-field-effect transistor chip with the poly(methyl methacrylate) press and polydimethylsiloxane fluidic channel while electrodes are contacted by the probe station from **(A)** above and **(B)** from the side view.

6.E.2 Aptamer Sequences[38]

Dopamine and serotonin aptamers were selected and screen for selectivity in phosphate-buffered saline (PBS) with 2 mM $MgCl_2$, pH 7.4. Sequence for glutamate may be available in the future pending publication.

Table 6.S1. Aptamer sequences

Target	Sequence
Serotonin	5'-/5ThioMC6-D/CG ACT GGT AGG CAG ATA GGG GAA GCT GAT TCG ATG CGT GGG TCG
Dopamine	5'-/5ThioMC6-D/CG ACG CCA GTT TGA AGG TTC GTT CGC AGG TGT GGA GTG ACG TCG

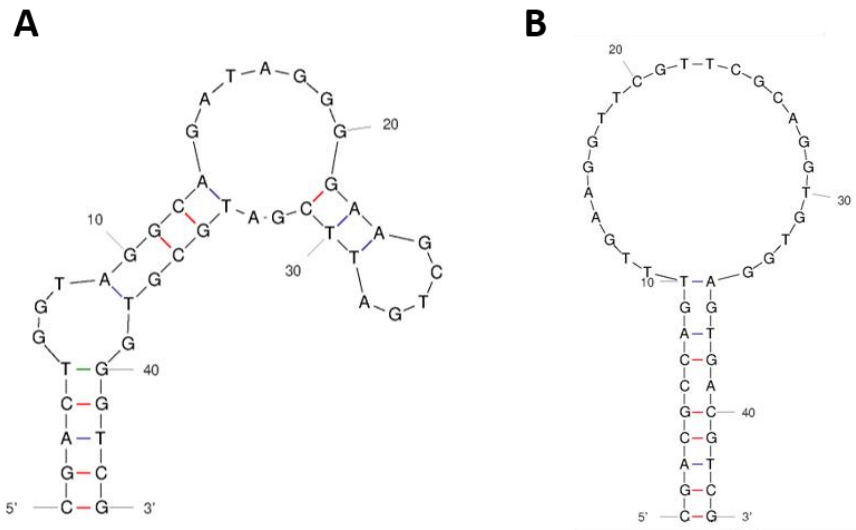

Figure 6.S5. Approximated conformations for the **(A)** serotonin and **(B)** dopamine aptamers calculated using mfold software[86-88] under conditions of 1× PBS buffer with 2 mM Mg^{2+}, at 25 °C.

6.E.3 Fluidic Experiments

Table 6.S2. Composition of artificial cerebrospinal fluid buffer, 1× strength with calcium and magnesium ions.

Chemical	Concentration (mM)	Vendor , Catalogue #
Sodium chloride	147.0	Fluka, 73575
Potassium chloride	3.5	Fluka, 05257
Sodium phosphate monobasic	1.0	Fluka, 17844
Sodium bicarbonate	2.5	Fluka, 88208
Calcium chloride	1.0	Sigma Aldrich, 499609
Magnesium chloride	1.2	Sigma Aldrich, 449172

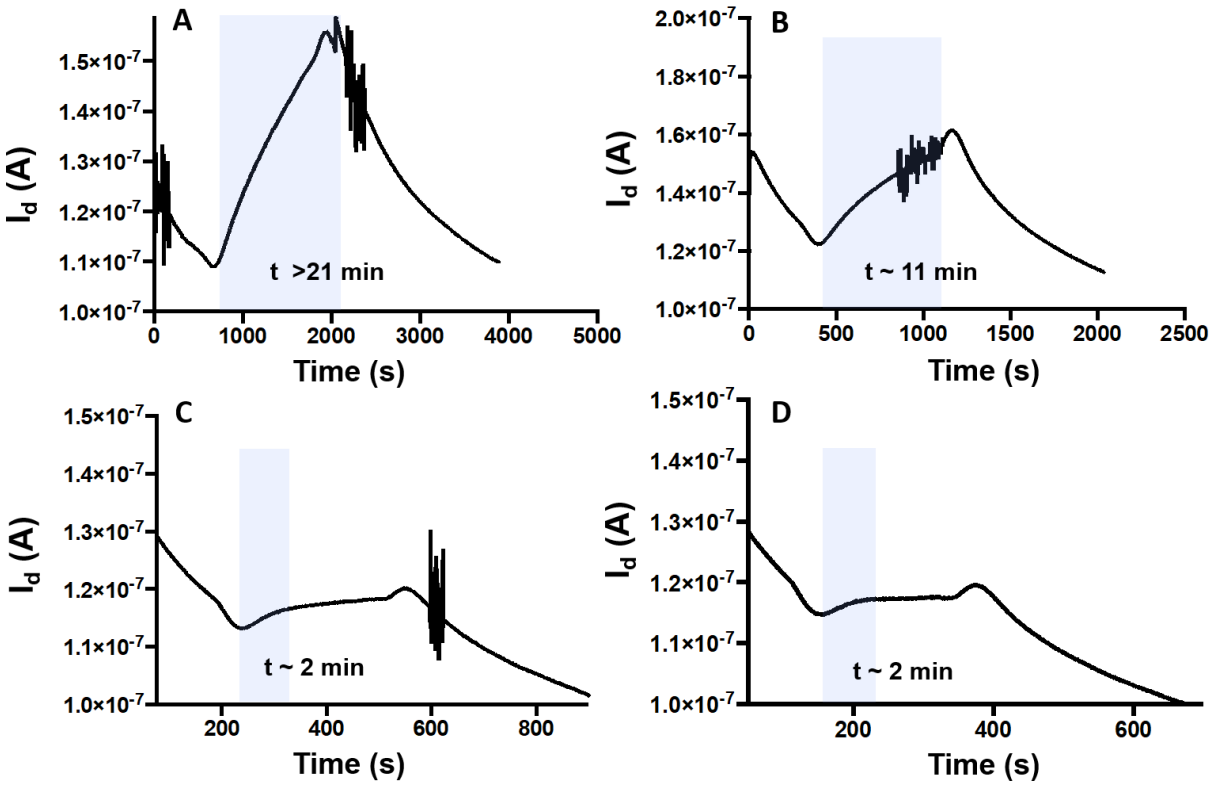

Figure 6.S6. (A) Measurements of drain current (I_d) showing association time to equilibrium of 10 nM serotonin in artificial cerebral-spinal fluid using a flowrate of 50 µL/min, **(B)** 100 µL/min, **(C)** 300 µL/min, and **(D)** 400 µL/min. Noise in the signal is an artifact of the measurement platform.

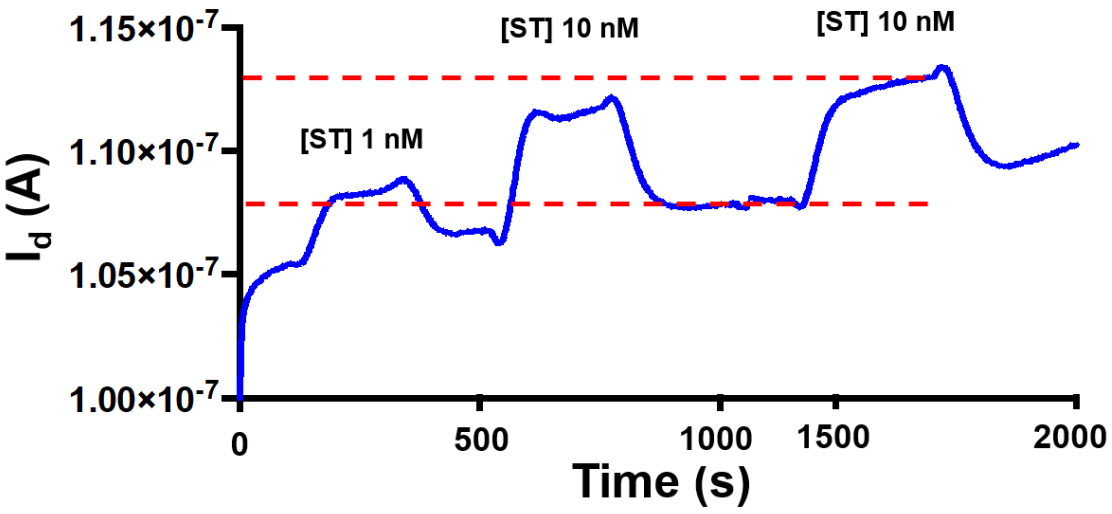

Figure 6.S7. Fluidic experiment of association and dissociation of serotonin (ST) in artificial cerebral-spinal fluid buffer on a field-effect transistor (FET) functionalized with the ST aptamer. The magnitude of the change in drain current (I_d) for 10 nM ST is ~5 nA. The applied voltages were 375 mV and 10 mV for gate-source voltage (V_{gs}) and drain-source voltage (V_{ds}), respectively. The flow rate was 300 µL/min.

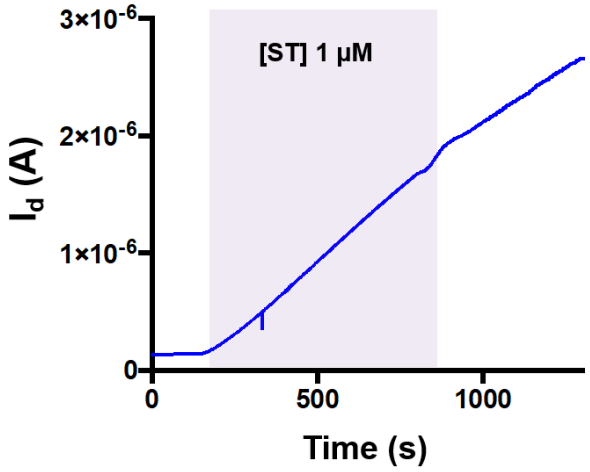

Figure 6.S8. Oversaturation of a field-effect transistor functionalized with the serotonin (ST) aptamer following the flow of 10 µM serotonin at 300 µL/min, after which a reintroduction of pure artificial cerebral-spinal fluid did not reduce the current. The applied voltages were 320 mV and 10 mV for gate-source voltage (V_{gs}) and drain-source voltage (V_{ds}), respectively.

6.E.4 Field-Effect Transistor Stabilization

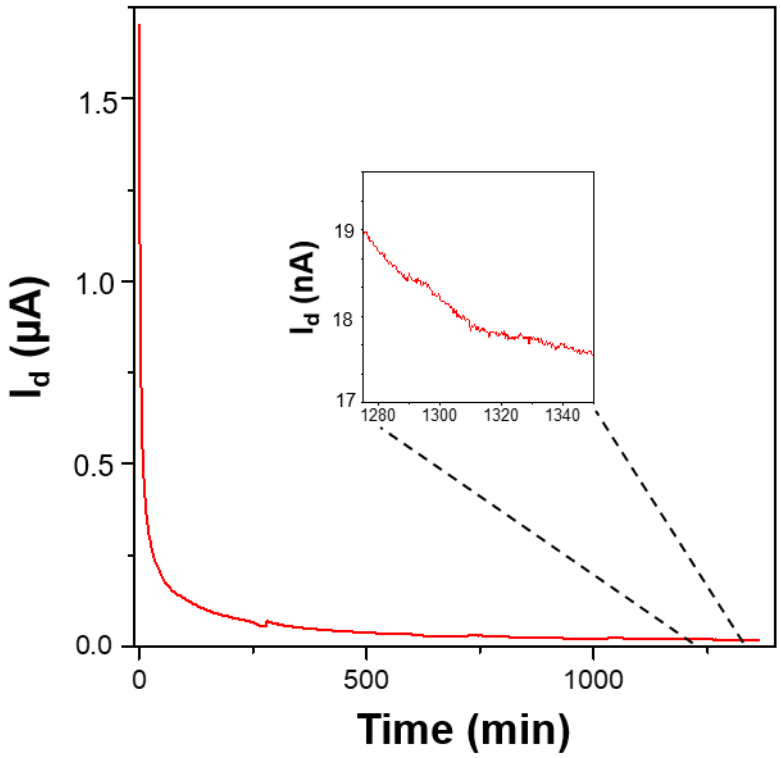

Figure 6.S9. Stabilization of the drain current (I_d) of a field-effect transistor (functionalized with serotonin aptamer) in flow (200 μL/min) while under the constant applications of 10 mV drain-source voltage (V_{ds}) and 100 mV gate-source voltage (V_{gs}) over the course of 24 h. It is possible to reach drifts of less than 2 nA per hour (inset). Measurement and voltage application performed by commercial instrument Keithley 4200A-SCS.

6.E.5 Calibrated Response[8]

Calibrated response (CR) as a metric reduces the magnitude of differences between multiple field-effect transistors (FETs) that, in part, arise from device-to-device variation. In this method, the drain current (I_d) is measured while sweeping the gate voltage (V_{gs}) given a constant drain voltage (V_{ds}). A baseline curve, with no target molecule present, is collected first. Then, a comparison is made between the baseline and the I_d curve after aptamer-target binding in accordance with **Equation 6.S1**, which also considers the change in I_d at it varies with V_{gs}.

$$CR\ (mV) = \frac{\Delta I}{\frac{dI_d}{dV_{gs}}} \qquad \text{Equation 6.S1}$$

6.E.6 Specifications of Hardware and Design Principals for Multi-Field-Effect Transistor Measurements

In the multi-FET measurement system (MFMS) presented in this work, the instrumentation was been designed to allow the "simultaneous" multiplexing of four channels in a common-gate topology. More technically, FETs are read sequentially at 200 µs per sample. Each channel, connected to a biosensor, has two independent voltage sources coming from a 12-bit SPI-controlled digital-to-analog converter (DAC) MAX5725. Each channel read-out is digitalized by its 16-bit analog-to-digital-converter (ADC) with an SPI interface AD7988. The SPI master and core of MBMS is a microcontroller ATSAMD11D14A, which communicates with the PC, where the Graphic User Interface (GUI) is hosted and running, through a UART-USB interface.

To minimize noise in the system, the MFMS is supplied by a 6.2 V battery, obtaining from there the 5 V for the communications with the PC, and 3.6 V from an LDO MIC5219. Digital and analog 3.3 V supplies are obtained from LD39015M LDOs from the former 3.6 V supply. Physically isolated electrically connected digital and analog ground planes are designed in the layout of the device. USB communication galvanic isolation is implemented using the ADUM4160 digital isolator. On analog signal processing, low-noise operational amplifiers OPAx376 have been used. Both the DAC and the ADCs use the REF2030 reference IC to obtain their 3 V reference.

With our aptamer FET arrays, which are gated through the electrolyte solution in which they are measured, we note that any gate voltage (V_{gs}) is applied to all FETs through the solution. Because of this connectivity, our approach implements a "common-gate" topology. The gate electrode is connected to a virtual ground (V_{vgnd}) with a constant voltage equal to half of the supply voltage of the system, so that $V_{gs} = V_{vgnd} - V_s$, where V_s is the potential at the source electrode of a FET. The current we wish to measure, I_d, is directly proportional to the difference between source and drain potentials (V_{ds}). In the case of a "common-source" topology, V_{ds} would be held constant while sweeping V_{gs}. In our system, V_{ds} is obtained by applying the necessary potential at the drain (V_d) relative to the changing V_s in order to maintain the desired V_{ds}, presented as $V_{ds} = V_d - V_s$. In other words, the gate electrode is functioning as the "reference" of the system, and V_d and V_s change accordingly to apply the desired V_{gs} and V_{ds} biases.

To measure the current, a shunt resistor functions as negative feedback on an operational amplifier. An overvoltage is produced on the shunt resistor by I_d, which is measured by an instrumentation amplifier (INA333 with 10× gain). The output is first

filtered with an analog filter with a 3 kHz cut off before going to the ADC. To amplify the current to appropriate scales depending on the sensor response, shunt resistor selection can be done in real time through a GPIO expander, commanding a TMUX1111 analog multiplexer per channel. As described in the main text, the scales available are 200 nA, 500 nA, 1 μA, and 10 μA, with a resolution at each scale of 6 pA, 15 pA, 30 pA, and 300 pA, respectively.

6.F References

(1) Chorlian, D. B.; Porjesz, B.; Cohen, H. L. Measuring Electrical Activity of the Brain ERP Mapping in Alcohol Research. *Alcohol Health Res. World* **1995**, *19*, 315–320.

(2) Schmid, S. M.; Hollmann, M. Bridging the Synaptic Cleft: Lessons from Orphan Glutamate Receptors. *Sci. Signal.* **2010**, *3*, 28.

(3) Scimemi, A.; Beato, M. Determining the Neurotransmitter Concentration Profile at Active Synapses. *Mol. Neurobiol.* **2009**, *40*, 289–306.

(4) Ma, P.; Chen, P.; Tilden, E. I.; Aggarwal, S.; Oldenborg, A.; Chen, Y. Fast and Slow: Recording Neuromodulator Dynamics Across Both Transient and Chronic Time Scales. *Sci. Adv.* **2024**, *10*, 1–17.

(5) Bach-y-Rita, P.; Aiello, G. L. Nerve Length and Volume in Synaptic vs Diffusion Neurotransmission: A Model. *Neuroreport* **1996**, *7*, 1502–1504.

(6) Grace, A. A. Phasic versus Tonic Dopamine Release and the Modulation of Dopamine System Responsivity: A Hypothesis for the Etiology of Schizophrenia. *Neuroscience* **1991**, *41*, 1–24.

(7) Sourkes, T. L. Magendie and the Chemists: The Earliest Chemical Analyses of the Cerebrospinal Fluid. *J. Hist. Neurosci.* **2002**, *11*, 2–10.

(8) Nakatsuka, N.; M. Andrews, A. Differentiating Siblings: The Case of Dopamine and Norepinephrine. *ACS Chem. Neurosci.* **2017**, *8*, 218–220.

(9) Hugo, V.; Castro, C.; Lucía, C.; Valenzuela, L.; Carlos Salazar Sánchez, J.; Pardo Peña, K.; López Pérez, S. J.; Ibarra, J. O.; Morales Villagrán, A. An Update of the Classical and

Novel Methods Used for Measuring Fast Neurotransmitters During Normal and Brain Altered Function. *Curr. Neuropharmacol.* **2014**, *12*, 490–508.

(10) Khan, A. S.; Michael, A. C. Invasive Consequences of Using Micro-Electrodes and Microdialysis Probes in the Brain. In *Trends in Analytical Chemistry*; Elsevier, **2003**, *22*, 503-508.

(11) Justice, J. B. Quantitative Microdialysis of Neurotransmitters. *J. Neurosci. Methods* **1993**, *48*, 263–276.

(12) Abdalla, A.; W. Atcherley, C.; Pathirathna, P.; Samaranayake, S.; Qiang, B.; Peña, E.; L. Morgan, S.; L. Heien, M.; Hashemi, P. In Vivo Ambient Serotonin Measurements at Carbon-Fiber Microelectrodes. *Anal. Chem.* **2017**, *89*, 9703–9711.

(13) Ewing, A. G.; Bigelow, J. C.; Wightman, R. M. Direct in Vivo Monitoring of Dopamine Released from Two Striatal Compartments in the Rat. *Science* **1983**, *221*, 169–171.

(14) Stamford, J. A.; Kruk, Z. L.; Millar, J.; Wightman, R. M. Striatal Dopamine Uptake in the Rat: In Vivo Analysis by Fast Cyclic Voltammetry. *Neurosci. Lett.* **1984**, *51*, 133–138.

(15) Rodeberg, N. T.; Sandberg, S. G.; Johnson, J. A.; Phillips, P. E. M.; Wightman, R. M. Hitchhiker's Guide to Voltammetry: Acute and Chronic Electrodes for in Vivo Fast-Scan Cyclic Voltammetry. *ACS Chem. Neurosci.* **2017**, *8*, 221–234.

(16) Day, J. J.; Roitman, M. F.; Wightman, R. M.; Carelli, R. M. Associative Learning Mediates Dynamic Shifts in Dopamine Signaling in the Nucleus Accumbens. *Nat. Neurosci.* **2007**, *10*, 1020–1028.

(17) Hart, A. S.; Rutledge, R. B.; Glimcher, P. W.; Phillips, P. E. M. Phasic Dopamine Release in the Rat Nucleus Accumbens Symmetrically Encodes a Reward Prediction Error Term. *J. Neurosci.* **2014**, *34*, 698.

(18) Owesson-White, C.; Belle, A. M.; Herr, N. R.; Peele, J. L.; Gowrishankar, P.; Carelli, R. M.; Mark Wightman, R. Cue-Evoked Dopamine Release Rapidly Modulates D2 Neurons in the Nucleus Accumbens During Motivated Behavior. *J. Neurosci.* **2016**, *36*, 6011–6021.

(19) Swamy, B. E. K.; Venton, B. J. Carbon Nanotube-Modified Microelectrodes for Simultaneous Detection of Dopamine and Serotonin in Vivo. *Analyst* **2007**, *132*, 876–884.

(20) Shin, H.; Oh, Y.; Park, C.; Kang, Y.; U. Cho, H.; D. Blaha, C.; E. Bennet, K.; L. Heien, M.; Young Kim, I.; H. Lee, K.; Pyo Jang, D. Sensitive and Selective Measurement of Serotonin in Vivo Using Fast Cyclic Square-Wave Voltammetry. *Anal. Chem.* **2019**, *92*, 774–781.

(21) Movassaghi, C. S.; Perrotta, K. A.; Yang, H.; Iyer, R.; Cheng, X.; Dagher, M.; Fillol, M. A.; Andrews, A. M. Simultaneous Serotonin and Dopamine Monitoring Across Timescales by Rapid Pulse Voltammetry with Partial Least Squares Regression. *Anal. Bioanal. Chem.* **2021**, *413*, 6747–6767.

(22) Roberts, J. G.; Sombers, L. A. Fast-Scan Cyclic Voltammetry: Chemical Sensing in the Brain and Beyond. *Anal. Chem.* **2018**, *90*, 490–504.

(23) Engstrom, R. C.; Strasser, V. A. Characterization of Electrochemically Pretreated Glassy Carbon Electrodes. *Anal. Chem.* **2002**, *56*, 136–141.

(24) Frey, O.; Holtzman, T.; Mcnamara, R. M.; Theobald, D. E. H.; van der Wal, P. D.; de Rooij, N. F.; Dalley, J. W.; Koudelka-Hep, M. Enzyme-Based Choline and L-Glutamate Biosensor Electrodes on Silicon Microprobe Arrays. *Biosens. Bioelectron.* **2010**, *26*, 477–484.

(25) Ou, Y.; Buchanan, A. M.; Witt, C. E.; Hashemi, P. Frontiers in Electrochemical Sensors for Neurotransmitter Detection: Towards Measuring Neurotransmitters as Chemical Diagnostics for Brain Disorders. *Analytical Methods* **2019**, *11*, 2738–2755.

(26) P. Lowry, J.; R. Ryan, M.; D. O'Neill, R. Behaviourally Induced Changes in Extracellular Levels of Brain Glutamate Monitored at 1 s Resolution with an Implanted Biosensor. *Anal. Commun.* **1998**, *35*, 87–89.

(27) Wassum, K. M.; Tolosa, V. M.; Wang, J.; Walker, E.; Monbouquette, H. G.; Maidment, N. T. Silicon Wafer-Based Platinum Microelectrode Array Biosensor for Near Real-Time Measurement of Glutamate in Vivo. *Sensors* **2008**, *8*, 5023–5036.

(28) Wassum, K. M.; Tolosa, V. M.; Tseng, T. C.; Balleine, B. W.; Monbouquette, H. G.; Maidment, N. T. Transient Extracellular Glutamate Events in the Basolateral Amygdala Track Reward-Seeking Actions. *J. Neurosci.* **2012**, *32*, 2734–2746.

(29) Tolosa, V. M.; Wassum, K. M.; Maidment, N. T.; Monbouquette, H. G. Electrochemically Deposited Iridium Oxide Reference Electrode Integrated with an Electroenzymatic Glutamate Sensor on a Multi-Electrode Arraymicroprobe. *Biosens. Bioelectron.* **2013**, *42*, 256–260.

(30) Chatterjee, D.; Gerlai, R. High Precision Liquid Chromatography Analysis of Dopaminergic and Serotoninergic Responses to Acute Alcohol Exposure in Zebrafish. *Behav. Brain Res.* **2009**, *200*, 208–213.

(31) Watson, C. J.; Venton, B. J.; Kennedy, R. T. In Vivo Measurements of Neurotransmitters by Microdialysis Sampling. *Anal. Chem.* **2006**, *78*, 1391–1399.

(32) Yang, H.; Thompson, A. B.; McIntosh, B. J.; Altieri, S. C.; Andrews, A. M. Physiologically Relevant Changes in Serotonin Resolved by Fast Microdialysis. *ACS Chem. Neurosci.* **2013**, *4*, 790–798.

(33) Jing, M.; Zhang, P.; Wang, G.; Feng, J.; Mesik, L.; Zeng, J.; Jiang, H.; Wang, S.; Looby, J. C.; Guagliardo, N. A.; Langma, L. W.; Lu, J.; Zuo, Y.; Talmage, D. A.; Role, L. W.; Barrett, P. Q.; Zhang, L. I.; Luo, M.; Song, Y.; Zhu, J. J.; Li, Y. A Genetically Encoded Fluorescent Acetylcholine Indicator for in Vitro and in Vivo Studies. *Nat. Biotechnol.* **2018**, *36*, 726–737.

(34) Sun, F.; Zeng, J.; Jing, M.; Zhou, J.; Feng, J.; Owen, S. F.; Luo, Y.; Li, F.; Wang, H.; Yamaguchi, T.; Yong, Z.; Gao, Y.; Peng, W.; Wang, L.; Zhang, S.; Du, J.; Lin, D.; Xu, M.; Kreitzer, A. C.; Cui, G.; Li, Y. A Genetically Encoded Fluorescent Sensor Enables Rapid and Specific Detection of Dopamine in Flies, Fish, and Mice. *Cell* **2018**, *174*, 481–496.

(35) Tuerk, C.; Gold, L. Systematic Evolution of Ligands by Exponential Enrichment: RNA Ligands to Bacteriophage T4 DNA Polymerase. *Science* **1990**, *249*, 505–510.

(36) Yang, K. A.; Pei, R.; Stojanovic, M. N. In Vitro Selection and Amplification Protocols for Isolation of Aptameric Sensors for Small Molecules. *Methods* **2016**, *106*, 58–65.

(37) Yang, K.; Mitchell, N. M.; Banerjee, S.; Cheng, Z.; Taylor, S.; Kostic, A. M.; Wong, I.; Sajjath, S.; Zhang, Y.; Stevens, J.; Mohan, S.; Landry, D. W.; Worgall, T. S.; Andrews, A. M.; Stojanovic, M. N. A Functional Group–Guided Approach to Aptamers for Small Molecules. *Science* **2023**, *380*, 942–948.

(38) Nakatsuka, N.; Yang, K.-A.; Abendroth, J. M.; Cheung, K. M.; Xu, X.; Yang, H.; Zhao, C.; Zhu, B.; Rim, Y. S.; Yang, Y.; Weiss, P. S.; Stojanović, M. N.; Andrews, A. M. Aptamer-Field-Effect Transistors Overcome Debye Length Limitations for Small-Molecule Sensing. *Science* **2018**, *362*, 319–324.

(39) Ikebukuro, K.; Kiyohara, C.; Sode, K. Electrochemical Detection of Protein Using a Double Aptamer Sandwich. *Anal. Lett.* **2004**, *37*, 2901–2909.

(40) Radi, A. E.; Abd-Ellatief, M. R. Electrochemical Aptasensors: Current Status and Future Perspectives. *Diagnostics* **2021**, *11*, 1–33.

(41) Tang, T.; Liu, X.; Li, C.; Lei, B.; Zhang, D.; Rouhanizadeh, M.; Hsiai, T.; Zhou, C. Complementary Response of In_2O_3 Nanowires and Carbon Nanotubes to Low-Density Lipoprotein Chemical Gating. *Appl. Phys. Lett.* **2005**, *86*, 103903.

(42) Rim, Y. S.; Bae, S. H.; Chen, H.; Yang, J. L.; Kim, J.; Andrews, A. M.; Weiss, P. S.; Yang, Y.; Tseng, H. R. Printable Ultrathin Metal Oxide Semiconductor-Based Conformal Biosensors. *ACS Nano* **2015**, *9*, 12174–12181.

(43) Kim, J.; Rim, Y. S.; Chen, H.; Cao, H. H.; Nakatsuka, N.; Hinton, H. L.; Zhao, C.; Andrews, A. M.; Yang, Y.; Weiss, P. S. Fabrication of High-Performance Ultrathin In2O3 Film Field-Effect Transistors and Biosensors Using Chemical Lift-Off Lithography. *ACS Nano* **2015**, *9*, 4572–4582.

(44) Chen, H.; Rim, Y. S.; Wang, I. C.; Li, C.; Zhu, B.; Sun, M.; Goorsky, M. S.; He, X.; Yang, Y. Quasi-Two-Dimensional Metal Oxide Semiconductors Based Ultrasensitive Potentiometric Biosensors. *ACS Nano* **2017**, *11*, 4710–4718.

(45) Cheung, K. M.; Yang, K. A.; Nakatsuka, N.; Zhao, C.; Ye, M.; Jung, M. E.; Yang, H.; Weiss, P. S.; Stojanović, M. N.; Andrews, A. M. Phenylalanine Monitoring via Aptamer-Field-Effect Transistor Sensors. *ACS Sens.* **2019**, *4*, 3308–3317.

(46) Wang, B.; Zhao, C.; Wang, Z.; Yang, K.-A.; Cheng, X.; Liu, W.; Yu, W.; Lin, S.; Zhao, Y.; Cheung, K. M.; Lin, H.; Hojaiji, H.; Weiss, P. S.; Stojanović, M. N.; Tomiyama, A. J.; Andrews, A. M.; Emaminejad, S. Wearable Aptamer-Field-Effect Transistor Sensing System for Noninvasive Cortisol Monitoring. *Sci. Adv.* **2022**, *8*, 1–15.

(47) Aroonyadet, N.; Wang, X.; Song, Y.; Chen, H.; Cote, R. J.; Thompson, M. E.; Datar, R. H.; Zhou, C. Highly Scalable, Uniform, and Sensitive Biosensors Based on Top-Down Indium Oxide Nanoribbons and Electronic Enzyme-Linked Immunosorbent Assay. *Nano Lett.* **2015**, *15*, 1943–1951.

(48) Ghosh, S. S.; Kao, P. M.; McCue, A. W.; Chappelle, H. L. Use of Maleimide-Thiol Coupling Chemistry for Efficient Syntheses of Oligonucleotide-Enzyme Conjugate Hybridization Probes. *Bioconjug. Chem.* **2002**, *1*, 71–76.

(49) Vig, J. R. Ultraviolet-Ozone Cleaning of Semiconductor Surfaces. *U.S. Army Electronics Technology and Devices Laboratory* **1992**, 25.

(50) Correa-Puerta, J.; Del Campo, V.; Henríquez, R.; Häberle, P. Resistivity of Thiol-Modified Gold Thin Films. *Thin Solid Films* **2014**, *570*, 150–154.

(51) Ruiz-Villalba, A.; van Pelt-Verkuil, E.; Gunst, Q. D.; Ruijter, J. M.; van den Hoff, M. J. Amplification of Nonspecific Products in Quantitative Polymerase Chain Reactions (QPCR). *Biomol. Detect. Quantif.* **2017**, *14*, 7–18.

(52) Baldwin, A.; Hudson, T.; Meng, E. A Calorimetric Flow Sensor for Ultra-Low Flow Applications Using Electrochemical Impedance. In *2018 IEEE Micro Electro Mechanical Systems (MEMS)*; IEEE, **2018**, 361–364.

(53) Ishikawa, F. N.; Curreli, M.; Chang, H. K.; Chen, P. C.; Zhang, R.; Cote, R. J.; Thompson, M. E.; Zhou, C. A Calibration Method for Nanowire Biosensors to Suppress Device-to-Device Variation. *ACS Nano* **2009**, *3*, 3969–3976.

(54) Johnson, K. A. Transient-State Kinetic Analysis of Enzyme Reaction Pathways. In *The Enzymes*; Sigman, D. S., Ed.; Academic Press, **1992**, *20*, 1–61.

(55) Strieder, W.; Aris, R. Diffusion Limited Reactions. In *Variational Methods Applied to Problems of Diffusion and Reaction*; Strieder, W., Aris, R., Eds.; Springer Berlin Heidelberg: Berlin, Heidelberg, **1973**; 42–58.

(56) Hanssen, B. L.; Siraj, S.; Wong, D. K. Y. Recent Strategies to Minimize Fouling in Electrochemical Detection Systems. *Rev. Anal. Chem.* **2016**, *35*, 1–28.

(57) Reimhult, E.; Höök, F. Design of Surface Modifications for Nanoscale Sensor Applications. *Sensors (Switzerland)* **2015**, *15*, 1635–1675.

(58) Caespi, F.; Martini, K. F.; Marsden, C. A. Measurement of Extracellular Basal Levels of Serotonin in Vivo Using Nafion-Coated Carbon Fibre Electrodes Combined with Differential Pulse Voltammetry. *Neuroscience* **1988**, *27*, 885–896.

(59) Moestrup, S.; Lauffenburger, D. A.; Linderman, J. J. *Receptors. Models for Binding, Trafficking, and Signaling* **1996**, *398*.

(60) Hoare, S. R. J. Analyzing Kinetic Binding Data. In *Assay Guidance Manual, Eli Lilly & Company and the National Center for Advancing Translational Sciences*; **2021**.

(61) Rong, G.; Corrie, S. R.; Clark, H. A. In Vivo Biosensing: Progress and Perspectives. *ACS Sens.* **2017**, *2*, 327–338.

(62) Downs, A. M.; Gerson, J.; Leung, K. K.; Honeywell, K. M.; Kippin, T.; Plaxco, K. W. Improved Calibration of Electrochemical Aptamer-Based Sensors. *Sci. Rep.* **2022**, *12*, 5535.

(63) Holdgate, G. A. Kinetics, Thermodynamics, and Ligand Efficiency Metrics in Drug Discovery. In *Comprehensive Medicinal Chemistry III* **2017**, *2*, 180–211.

(64) Costello, A. M.; Elizondo-Riojas, M. A.; Li, X.; Volk, D. E.; Pillai, A. K.; Wang, H. Selection and Characterization of Vimentin-Binding Aptamer Motifs for Ovarian Cancer. *Molecules* **2021**, *26*, 6525.

(65) Armstrong, R. E.; Strouse, G. F. Rationally Manipulating Aptamer Binding Affinities in a Stem-Loop Molecular Beacon. *Bioconjug. Chem.* **2014**, *25*, 1769–1776.

(66) Ramón, M. E.; Akyol, T.; Shahrjerdi, D.; Young, C. D.; Cheng, J.; Register, L. F.; Banerjee, S. K. Fast and Slow Transient Charging in Various III-V Field-Effect Transistors with Atomic-Layer-Deposited-Al_2O_3 Gate Dielectric. *Appl. Phys. Lett.* **2013**, *102*, 1–5.

(67) Vaécha, R.; Rick, S. W.; Jungwirth, P.; De Beer, A. G. F.; De Aguiar, H. B.; Samson, J. S.; Roke, S. The Orientation and Charge of Water at the Hydrophobic Oil Droplet - Water Interface. *J. Am. Chem. Soc.* **2011**, *133*, 10204–10210.

(68) Gonella, G.; Backus, E. H. G.; Nagata, Y.; Bonthuis, D. J.; Loche, P.; Schlaich, A.; Netz, R. R.; Kühnle, A.; McCrum, I. T.; Koper, M. T. M.; Wolf, M.; Winter, B.; Meijer, G.; Campen, R. K.; Bonn, M. Water at Charged Interfaces. *Nat. Rev. Chem.* **2021**, *5*, 466–485.

(69) Fixe, F.; Branz, H. M.; Louro, N.; Chu, V.; Prazeres, D. M. F.; Conde, J. P. Electric-Field Assisted Immobilization and Hybridization of DNA Oligomers on Thin-Film Microchips. *Nanotechnology* **2005**, *16*, 2061.

(70) Rant, U.; Arinaga, K.; Fujita, S.; Yokoyama, N.; Abstreiter, G.; Tornow, M. Electrical Manipulation of Oligonucleotides Grafted to Charged Surfaces. *Org. Biomol. Chem.* **2006**, *4*, 3448–3455.

(71) Kelley, S. O.; Barton, J. K.; Jackson, N. M.; McPherson, L. D.; Potter, A. B.; Spain, E. M.; Allen, M. J.; Hill, M. G. Orienting DNA Helices on Gold Using Applied Electric Fields. *Langmuir* **1998**, *14*, 6781–6784.

(72) Y. Wong, I.; A. Melosh, N. Directed Hybridization and Melting of DNA Linkers Using Counterion-Screened Electric Fields. *Nano Lett.* **2009**, *9*, 3521–3526.

(73) Cabeça, R.; Rodrigues, M.; Prazeres, D. M. F.; Chu, V.; Conde, J. P. The Effect of the Shape of Single, Sub-Ms Voltage Pulses on the Rates of Surface Immobilization and Hybridization of DNA. *Nanotechnology* **2009**, *20*, 015503.

(74) Vernick, S.; Trocchia, S. M.; Warren, S. B.; Young, E. F.; Bouilly, D.; Gonzalez, R. L.; Nuckolls, C.; Shepard, K. L. Electrostatic Melting in a Single-Molecule Field-Effect Transistor with Applications in Genomic Identification. *Nat. Commun.* **2017**, *8*, 1–9.

(75) Zhao, C.; Cheung, K. M.; Huang, I.-W.; Yang, H.; Nakatsuka, N.; Liu, W.; Cao, Y.; Man, T.; Weiss, P. S.; Monbouquette, H. G.; Andrews, A. M. Implantable Aptamer–Field-Effect Transistor Neuroprobes for in Vivo Neurotransmitter Monitoring. *Sci. Adv.* **2024**, *7*, 7422.

(76) Curreli, M.; Li, C.; Sun, Y.; Lei, B.; Gundersen, M.; Thompson, M.; Zhou, C. Selective Functionalization of In_2O_3 Nanowire Mat Devices for Biosensing Applications. *J. Am. Chem. Soc.* **2005**, *127*, 6922–6923.

(77) Liu, L.; Han, Z.; An, F.; Gong, X.; Zhao, C.; Zheng, W.; Mei, L.; Zhou, Q. Aptamer-Based Biosensors for the Diagnosis of Sepsis. *J. Nanobiotechnology* **2021**, *19*, 1–22.

(78) Chang, Y. C.; Yang, C. Y.; Sun, R. L.; Cheng, Y. F.; Kao, W. C.; Yang, P. C. Rapid Single Cell Detection of Staphylococcus Aureus by Aptamer-Conjugated Gold Nanoparticles. *Sci. Rep.* **2013**, *3*, 1–7.

(79) Dauphin-Ducharme, P.; Yang, K.; Arroyo-Currás, N.; Ploense, K. L.; Zhang, Y.; Gerson, J.; Kurnik, M.; Kippin, T. E.; Stojanovic, M. N.; Plaxco, K. W. Electrochemical Aptamer-Based Sensors for Improved Therapeutic Drug Monitoring and High-Precision, Feedback-Controlled Drug Delivery. *ACS Sens.* **2019**, *4*, 2832–2837.

(80) Kim, J.; Campbell, A. S.; de Ávila, B. E.-F.; Wang, J. Wearable Biosensors for Healthcare Monitoring. *Nat. Biotechnol.* **2019**, *37*, 389–406.

(81) Ye, C.; Wang, M.; Min, J.; Tay, R. Y.; Lukas, H.; Sempionatto, J. R.; Li, J.; Xu, C.; Gao, W. A Wearable Aptamer Nanobiosensor for Non-Invasive Female Hormone Monitoring. *Nat. Nanotechnol.* **2024**, *19*, 330–337.

(82) Wu, Y.; Belmonte, I.; S. Sykes, K.; Xiao, Y.; J. White, R. Perspective on the Future Role of Aptamers in Analytical Chemistry. *Anal. Chem.* **2019**, *91*, 15335–15344.

(83) Cho, E. J.; Lee, J.-W.; Ellington, A. D. Applications of Aptamers as Sensors. *Annu. Rev. Anal. Chem.* **2009**, *2*, 241–264.

(84) Xu, G.; Zhao, J.; Yu, H.; Wang, C.; Huang, Y.; Zhao, Q.; Zhou, X.; Li, C.; Liu, M. Structural Insights into the Mechanism of High-Affinity Binding of Ochratoxin A by a DNA Aptamer. *J. Am. Chem. Soc.* **2022**, *144*, 7731–7740.

(85) Zhang, H. L.; Lv, C.; Li, Z. H.; Jiang, S.; Cai, D.; Liu, S. S.; Wang, T.; Zhang, K. H. Analysis of Aptamer-Target Binding and Molecular Mechanisms by Thermofluorimetric Analysis and Molecular Dynamics Simulation. *Front. Chem.* **2023**, *11*, 1–12.

(86) Zuker, M. Mfold Web Server for Nucleic Acid Folding and Hybridization Prediction. *Nucleic Acids Res.* **2003**, *31*, 3406–3415.

(87) SantaLucia, Jr. A Unified View of Polymer, Dumbbell, and Oligonucleotide DNA Nearest-Neighbor Thermodynamics. *Proc. Natl. Acad. Sci. U.S.A.* **1998**, *95*, 1460-1465.

(88) Peyret, N. Prediction of Nucleic Acid Hybridization: Parameters and Algorithms PhD dissertation, Wayne State University, Department of Chemistry, Detroit, MI, **2000**.

(89) Fuller, C. W.; Padayatti, P. S.; Abderrahim, H.; Adamiak, L.; Alagar, N.; Ananthapadmanabhan, N.; Baek, J.; Chinni, S.; Choi, C.; Delaney, K. J.; Dubielzig, R.; Frkanec, J.; Garcia, C.; Gardner, C.; Gebhardt, D.; Geiser, T.; Gutierrez, Z.; Hall, D. A.; Hodges, A. P.; Hou, G.; Jain, S.; Jones, T.; Lobaton, R.; Majzik, Z.; Marte, A.; Mohan, P.; Mola, P.; Mudondo, P.; Mullinix, J.; Nguyen, T.; Ollinger, F.; Orr, S.; Ouyang, Y.; Pan, P.; Park, N.; Porras, D.; Prabhu, K.; Reese, C.; Ruel, T.; Sauerbrey, T.; Sawyer, J. R.; Sinha, P.; Tu, J.; Venkatesh, A. G.; VijayKumar, S.; Zheng, L.; Jin, S.; Tour, J. M.; Church, G. M.; Mola, P. W.; Merriman, B. Molecular Electronics Sensors on a Scalable Semiconductor Chip: A Platform for Single-Molecule Measurement of Binding Kinetics and Enzyme Activity. *Proc. Natl. Acad. Sci. U.S.A.* **2022**, *119*, 1–12.

(90) Venton, B. J.; Cao Q. Fundamentals of Fast-Scan Cyclic Voltammetry for Dopamine Detection. *Analyst* **2020**, *145*, 1158-1168.

(91) Inglut, C. T.; Gaitan, B.; Najafali, D.; Lopez, I. A.; Connolly, N. P.; Orsila, S.; Perttilä, R.; Woodworth, G. F.; Chen, Y.; Huang, H. C. Predictors and Limitations of the Penetration Depth of Photodynamic Effects in the Rodent Brain. *Photochem. Photobiol.* **2020**, *96*, 301–309.

CHAPTER 7

Conclusions and Prospects

7.A Research Summary

In this thesis, I have discussed my research projects, having a wide range of applications in which nanoscience contributes immensely. The theory, characterization, and control of nanoscale processes has enhanced our understanding of and ability to influence systems at the macroscale.

In the case of germanium surface functionalization, we demonstrated tuning the work function of the material by depositing monolayers of carborane isomers, formed through self-assembly.[1] Concerning the interface of nano-functionalized surfaces with biological systems, we developed two devices for the application of gene editing. Using the cell-squeezing approach to permeabilize cells, we enhanced the antifouling properties of a microfluidic channel by assembling lipid bilayers formed from lipid bicelle nanostructures.[2] The second device employed a piezo-electric transducer to manipulate cells as they passed through a glass capillary, permeabilizing the cells as they sheared along the channel walls.[3] Another project related to the growing research in personalized medicine was a "catch and release" nanoparticle-based platform with the aim of isolating and selectively releasing malignant cells.[4] We utilized gold nanoparticles, over which we have achieved a high degree of control, directing their size and shape,[5] for their plasmonic properties to convert light to

heat. The capability to screen patient samples and culture cells displaying specific markers, such as cancerous cells, is of interest for developing patient-specific treatments.[6]

7.B Aptamer Technology

Sensitivity, selectivity, sampling time, sample volume requirements, precision, reproducibility, or cost effectiveness;[7] an advisor of mine during undergraduate studies, Dr. Joseph Aldstadt at the University of Wisconsin, Milwaukee, often reminded me of a conundrum when it came to analytical methods. "You get to choose two."

This statement is clearly hyperbole and an unsatisfactory limitation, but the relationship of these analytical properties, while far from mutually exclusive, is such that any technique possesses varying merits that must be considered for a given experiment. Towards the application of uncovering the mysteries of chemical transmission and thought, we would seek an analytical method that achieves a high degree on all of these fronts. Aptamer field-effect transistors (FETs) are our approach to multi-analyte measurements.[8] In my work, I sought to investigate the time responses of our sensors and developed portable hardware for measuring multiple FETs simultaneously. The multi-FET measurements will open the way for future studies to characterize many aptamer sequences and program customizable voltage sweeps to modulate aptamer binding kinetics.[9] As discussed in the work, another application of this technology is in the area of "bedside" monitoring instrumentation[10] and wearable sensors,[11] both instances that involve continuous measurement in a complex environment. The fabrication methods for miniaturization of aptamer FETs along with our ability to multiplex measurements will lead to more experiments characterizing the aptamers for use in this analytical method.

7.C Closing Thoughts on Nanoscience and Nanotechnology

Although the primary focus of my thesis research has been on biomedical applications, nanomaterials and control of nanoscale processes is the driving force behind much of our everyday technology. Famously, in 1965, Gordon Moore made an observation leading to his prediction, now referred to as Moore's Law, that the number of transistors per microchip doubled every two years.[12] While this trend has shown to be true up to the 2020s, it is estimated by some that this rate of advances is reaching a plateau.[13] Some hypothesize that there are unavoidable limitations, such as that as transistors become increasingly small, they begin to display different electronic properties, along with theoretical limits of working with countable numbers of atoms.[14] To circumvent this, approaches to designing new types of transistor architectures include creating new 3-dimensional materials using precise methodology to control the deposition of extremely thin layers.[15]

Another avenue where nanomaterials are enabling important strides revolves around the issue of energy. With our increasing demands of power globally, the ability to convert solar energy efficiently, even in cloudy conditions, is a significant source of renewable energy.[16] Nanomaterials are being employed to improve the efficiency of electron transfer for capturing solar energy.[17–19] Aside from the conversion of solar energy to electric, means of energy storage still presents challenges. To meet our power demands, materials that have high storage capacity ideally must also be able to charge and dispense energy rapidly.[20,21] A large amount of research is being done on battery materials to address this issue, with a promising avenue being in the nano-morphology of the materials themselves changing where charges are stored.[22]

When I first began my education at UCLA, nanoscience was very much a mystery to me. The California NanoSystems Institute (CNSI) housed many phenomenal instruments that I felt lucky to have access to. I did not know that a project to synthesize gold nanostars would lead to utilizing the scanning electron microscope, or that I would examine the uniformity of an indium oxide layer using atomic force microscopy. Although these advanced methods of experimentation require sophisticated, state-of-the art instrumentation, nanoscience exists all around us. In my time as a graduate student, I became involved in CNSI's nanoscience outreach program. The mission statement of this group is to bring nanoscience education to young students as well as the general public. A big aspect of this program involves educating elementary through high school teachers on experiments they can do in their classrooms to explore the nanoworld. In a simple experiment where one deposits a drop of oil on the surface of a bowl of water, the thickness of a monolayer of oil can be calculated just from measuring the diameter of the film.[23] To me, this illustrates how concepts of self-assembly and the scale of a lipid molecule, both nanoscience concepts used in real research, can be effectively put into perspective for someone who might previously think of nanoscience as a strictly technical field. I believe nanoscience will become increasingly accessible in the coming years and we will see incredible ingenuity to address some of the greatest challenges we face.

7.D References

(1) Serino, A. C.; Anderson, M. E.; Saleh, L. M. A.; Dziedzic, R. M.; Mills, H.; Heidenreich, L. K.; Spokoyny, A. M.; Weiss, P. S. Work Function Control of Germanium through Carborane-Carboxylic Acid Surface Passivation. *ACS Appl. Mater. Interfaces* **2017**, *9*, 34592–34596.

(2) Belling, J. N.; Heidenreich, L. K.; Hyeon Park, J.; Kawakami, L. M.; Takahashi, J.; Frost, I. M.; Gong, Y.; Young, T. D.; Jackman, J. A.; Jonas, S. J.; Cho, N.-J.; Weiss, P. S. Lipid-Bicelle-Coated Microfluidics for Intracellular Delivery with Reduced Fouling. *ACS Appl. Mater. Interfaces* **2020**, *12*, 45744–45752.

(3) Belling, J. N.; Heidenreich, L. K.; Tian, Z.; Mendoza, A. M.; Chiou, T.-T.; Gong, Y.; Chen, N. Y.; Young, T. D.; Wattanatorn, N.; Hyeon Park, J.; Scarabelli, L.; Chiang, N.; Takahashi, J.; Young, S. G.; Stieg, A. Z.; De Oliveira, S.; Jun Huang, T.; Weiss, P. S.; Jonas, S. J. Acoustofluidic Sonoporation for Gene Delivery to Human Hematopoietic Stem and Progenitor Cells. *Proc. Natl. Acad. Sci., U.S.A.* **2020**, *117*, 10976–10982.

(4) Vinnacombe-Willson, G. A.; Chiang, N.; Scarabelli, L.; Hu, Y.; Heidenreich, L. K.; Li, X.; Gong, Y.; Inouye, D. T.; Fisher, T. S.; Weiss, P. S.; Jonas, S. J. In Situ Shape Control of Thermoplasmonic Gold Nanostars on Oxide Substrates for Hyperthermia-Mediated Cell Detachment. *ACS Cent. Sci.* **2020**, *6*, 2105–2116.

(5) Scarabelli, L.; Sánchez-Iglesias, A.; Pérez-Juste, J.; Liz-Marzán, L. M. A "Tips and Tricks" Practical Guide to the Synthesis of Gold Nanorods. *J. Phys. Chem. Lett.* **2015**, *6*, 4270–4279.

(6) Maughan, T. The Promise and the Hype of 'Personalised Medicine.' *New Bioethics* **2017**, *23*, 13–20.

(7) Valcarcel, M.; Rios, A. The Hierarchy and Relationships of Analytical Properties. *Anal. Chem.* **1993**, *65*, 781-787.

(8) Nakatsuka, N.; Yang, K.-A.; Abendroth, J. M.; Cheung, K. M.; Xu, X.; Yang, H.; Zhao, C.; Zhu, B.; Rim, Y. S.; Yang, Y.; Weiss, P. S.; Stojanović, M. N.; Andrews, A. M. Aptamer-Field-Effect Transistors Overcome Debye Length Limitations for Small-Molecule Sensing. *Science* **2018**, *362*, 319–324.

(9) Fixe, F.; Branz, H. M.; Louro, N.; Chu, V.; Prazeres, D. M. F.; Conde, J. P. Electric-Field Assisted Immobilization and Hybridization of DNA Oligomers on Thin-Film Microchips. *Nanotechnology* **2005**, *16*, 2061.

(10) Amen, M. T.; Pham, T. T. T.; Cheah, E.; Tran, D. P.; Thierry, B. Metal-Oxide FET Biosensor for Point-of-Care Testing: Overview and Perspective. *Molecules* **2022**, *27*, 7952.

(11) Kim, J.; Campbell, A. S.; de Ávila, B. E.-F.; Wang, J. Wearable Biosensors for Healthcare Monitoring. *Nat. Biotechnol.* **2019**, *37*, 389–406.

(12) Moore, G. E. Cramming More Components onto Integrated Circuits. *Electronics* **1965**, *38*, 114–117.

(13) Shalf, J. The Future of Computing Beyond Moore's Law. *Philosophical Transactions of the Royal Society A: Mathematical, Physical and Engineering Sciences* **2020**, *378*, 1–15.

(14) Schaller, R. R. Moore's Law: Past, Present and Future. *IEEE Spectr.* **1997**, *34*, 52–59.

(15) Wang, X.; Liu, C.; Wei, Y.; Feng, S.; Sun, D.; Cheng, H. Three-Dimensional Transistors and Integration Based on Low-Dimensional Materials for the Post-Moore's Law Era. *Materials Today* **2023**, *63*, 170–187.

(16) Kelly, N. A.; Gibson, T. L. Increasing the Solar Photovoltaic Energy Capture on Sunny and Cloudy Days. *Solar Energy* **2011**, *85*, 111–125.

(17) Banin, U.; Waiskopf, N.; Hammarström, L.; Boschloo, G.; Freitag, M.; Johansson, E. M. J.; Sá, J.; Tian, H.; Johnston, M. B.; Herz, L. M.; Milot, R. L.; Kanatzidis, M. G.; Ke, W.; Spanopoulos, I.; Kohlstedt, K. L.; Schatz, G. C.; Lewis, N.; Meyer, T.; Nozik, A. J.; Beard, M. C.; Armstrong, F.; Megarity, C. F.; Schmuttenmaer, C. A.; Batista, V. S.; Brudvig, G. W. Nanotechnology for Catalysis and Solar Energy Conversion. *Nanotechnology* **2021**, *32*, 042003.

(18) Yu, K.; Chen, J. Enhancing Solar Cell Efficiencies Through 1-D Nanostructures. *Nanoscale Res. Lett.* **2009**, *4*, 1–10.

(19) Ali, N.; Hussain, A.; Ahmed, R.; Wang, M. K.; Zhao, C.; Haq, B. U.; Fu, Y. Q. Advances in Nanostructured Thin Film Materials for Solar Cell Applications. *Renewable and Sustainable Energy Reviews* **2016**, *59*, 726–737.

(20) Lee, S. C.; Jung, W. Y. Analogical Understanding of the Ragone Plot and a New Categorization of Energy Devices. *Energy Procedia* **2016**, *88*, 526–530.

(21) Manthiram, A. A Reflection on Lithium-Ion Battery Cathode Chemistry. *Nat. Commun.* **2020**, *11*, 1550.

(22) Yan, Y.; Kim, H.-S.; Cook, J. B.; Robbennolt, S.; Dunn, B.; Tolbert, S. H. Mesoporous MoO2 Thin Films for High Rate Li^+ Storage: Effect of Crystallinity and Porous Structure. *Solid State Sci.* **2022**, *129*, 106890.

(23) Wang, D. N.; Stieglitz, H.; Marden, J.; Tamm, L. K. Benjamin Franklin, Philadelphia's Favorite Son, Was a Membrane Biophysicist. *Biophys. J.* **2013**, *104*, 287–291.